



**TIAGO MANUEL  
RODRIGUES  
DA SILVA**

**ANÁLISE NUMÉRICA E EXPERIMENTAL PARA O  
DESENVOLVIMENTO DE UMA PROTEÇÃO SOLAR  
COM INCORPORAÇÃO DE MATERIAIS DE  
MUDANÇA DE FASE**







**TIAGO MANUEL  
RODRIGUES  
DA SILVA**

**ANÁLISE NUMÉRICA E EXPERIMENTAL PARA O  
DESENVOLVIMENTO DE UMA PROTEÇÃO SOLAR  
COM INCORPORAÇÃO DE MATERIAIS DE  
MUDANÇA DE FASE**

Tese apresentada à Universidade de Aveiro para cumprimento dos requisitos necessários à obtenção do grau de Doutor em Sistemas Energéticos e Alterações Climáticas, realizada sob a orientação científica do Doutor Romeu da Silva Vicente, Professor Associado do Departamento de Engenharia Civil da Universidade de Aveiro e coorientação da Doutora Maria Fernanda da Silva Rodrigues, Professora Auxiliar do Departamento de Engenharia Civil da Universidade de Aveiro.



“Most people say that it is the intellect which makes a great scientist. They are wrong: it is character.” – Albert Einstein



## **o júri**

presidente

**Prof. Doutor Mário Guerreiro Silva Ferreira**  
Professor Catedrático da Universidade de Aveiro

vogais

**Prof. Doutora Inês Flores-Colen**  
Professora Auxiliar do Instituto Superior Técnico da Universidade de Lisboa

**Prof. Doutor Miguel Ângelo Dias Azenha**  
Professor Auxiliar da Universidade do Minho

**Prof. Doutor Nelson Amadeu Dias Martins**  
Professor Auxiliar da Universidade de Aveiro

**Prof. Doutor Nuno Manuel Monteiro Ramos**  
Professor Auxiliar da Faculdade de Engenharia da Universidade do Porto

**Prof. Doutor Romeu da Silva Vicente**  
Professor Associado da Universidade de Aveiro



## **agradecimentos**

O presente trabalho resulta do meu esforço pessoal, em que a colaboração que me foi prestada assumiu um papel importante, por isso, gostaria de aqui expressar o meu reconhecimento e sinceros agradecimentos a todos os que me ajudaram a realizar este objetivo pessoal.

Agradeço ao meu orientador Professor Doutor Romeu Vicente pela partilha de conhecimento, dedicação e disponibilidade que apresentou desde que trabalho com ele. Além de meu orientador, tem sido um amigo pessoal e de trabalho, sempre disponível para me ajudar e dar conselhos para a vida. Obrigado pela ajuda e paciência nos períodos menos bons. Espero que possamos continuar a trabalhar desta forma durante muito mais tempo.

Agradeço à minha coorientadora Professora Doutora Fernanda Rodrigues pela sua disponibilidade e ajuda durante estes anos.

Agradeço ao Professor Doutor António Samagaio, pela sua disponibilidade e apoio, o qual disponibilizou de forma incondicional o espaço para a realização da campanha experimental deste trabalho.

Agradeço ao Professor Doutor Victor Ferreira pela sua amizade, disponibilidade e perguntas pertinentes. Obrigado pelo suporte e voto de confiança dados no meu período inicial de investigação.

Agradeço a todos os meus amigos e colegas de trabalho, pelo incentivo e preocupação ao longo da realização deste trabalho. Aos funcionários do Departamento de Engenharia Civil, pela sua disponibilidade e ajuda, em especial ao Vítor Rodrigues pela ajuda prestada no laboratório para preparação da campanha experimental.

Agradeço à minha família, pela forma como me acompanharam e ajudaram na conclusão de mais uma importante etapa da minha vida. Um agradecimento especial aos meus pais e sogros, por tudo que têm feito por mim, pela sua disponibilidade, preocupação e por me tornarem o que sou hoje.

Finalmente, um agradecimento muito especial à minha esposa, Cláudia Amaral, pelo seu carinho, amizade, compreensão e incondicional apoio que sempre demonstrou. Muito obrigado pelas conversas e palavras de coragem nos momentos menos bons da vida e por todo o incentivo dado. À minha filha, Lara Silva, que com a sua forma de viver, repleta de alegria e de carinho, tem sido sempre um motivo de força e de energia, a qual está sempre disposta a nos dar um sorriso e com isso nos alegrar o dia.

A ti, estou eternamente grato.





**palavras-chave**

armazenamento de energia térmica (TES), calibração numérica, conforto térmico interior, eficiência energética, fluxo de calor, material de mudança de fase (PCM), simulação numérica, proteção solar, validação com métodos estatísticos.

**resumo**

O sector dos edifícios é o maior consumidor final de energia na União Europeia. O maior consumo de energia neste sector está associado principalmente ao recurso de sistemas ativos para a climatização dos espaços interiores – aquecimento e arrefecimento. Atualmente, o desenho arquitectónico exterior de escritórios e de edifícios comerciais recorre sistematicamente ao uso de vãos envidraçados e de soluções translúcidas, que aumenta significativamente as perdas térmicas nestas zonas.

Os sistemas de armazenamento de energia térmica, utilizando materiais de mudança de fase nos edifícios, é um tema atualmente muito investigado e com rápido desenvolvimento tecnológico. A incorporação de materiais de mudança de fase é atualmente uma solução avançada que permite melhorar o desempenho térmico do edifício, inclusive na aplicação em vãos envidraçados e soluções de proteção solar.

O presente trabalho apresenta e analisa a campanha experimental e simulação numérica de um sistema de proteção solar que incorpora materiais de mudança de fase. A campanha experimental é composta por dois compartimentos lado a lado, e cada um deles tem duas proteções solares – um dos compartimentos com a incorporação de materiais de fase e no outro sem. Ambos os compartimentos foram sujeitos a condições climáticas exteriores similares numa região de clima mediterrâneo durante a estação de verão e de inverno. A fachada orientada a sul é um vão envidraçado, o qual tem aplicado o sistema de proteção solar.

De acordo com os critérios de validação analisados, os resultados do modelo numérico foram considerados calibrados e validados.

Os resultados obtidos provam o potencial dos materiais de mudança de fase na regulação térmica e na otimização da eficiência energética dos espaços interiores dos edifícios.



**keywords**

window shutter, phase change material (PCM), energy performance, heat flux, indoor thermal comfort, numerical simulation, thermal energy storage (TES), statistical validation.

**abstract**

The building sector is the largest final end-use consumer of energy in the European Union. The large energy consumption of the building sector is mainly resourcing to active systems for cooling and heating of indoor spaces. Presently, the external envelopes of offices and commercial buildings are systematically composed by large glazed areas, which lead to substantial heat losses through these zones.

Thermal Energy Storage systems (TES), using phase change materials (PCM) in buildings, are widely investigated technologies and a fast developing research area. The use of phase change materials (PCMs) is presently an advanced solution to improve the energy performance of building components, namely the glazing and window shutter protections solutions.

The present work presents and discusses a numerical and experimental testing of a thermal energy system that contains phase change materials. The testing apparatus is composed by two side-by-side compartments that have two similar windows shutters, one containing PCMs and the other considered as a reference solution, without PCMs. The internal compartments were submitted to similar weather conditions in a Mediterranean climate during the summer and winter season, and the south oriented facade is a glazed area that incorporates the window protection systems.

According the used acceptance criteria, the results of the numerical model presented a good agreement and reliability and were considered calibrated with well prediction data.

The results reveal the PCM potential for the thermal regulation of indoor spaces as well as improving the energy efficiency of indoor building spaces.





3.1.4	Test cell material properties .....	70
3.2	System description .....	70
3.2.1	Dimensions, external characteristics and schematic constitution .....	70
3.2.2	PCM aluminium blade filling .....	72
3.2.3	System rotation .....	73
3.3	Work functionalities – Window shutter configurations .....	73
3.4	Development of a new window shutter typology .....	76
<b>4</b>	<b>Experimental apparatus</b>	<b>77</b>
4.1	Test cell composition .....	79
4.2	Location and orientation .....	80
4.3	Test cell shading .....	81
4.4	Measurement and monitoring data .....	82
4.5	Experimental constraints and limitations .....	83
4.5.1	PCM losses .....	83
4.5.2	Thermal bridges .....	84
4.5.3	Heat flux through compartments .....	85
4.6	Results .....	85
4.6.1	External Conditions .....	86
4.6.1.1	Overall .....	86
4.6.1.2	Summer .....	87
4.6.1.3	Winter .....	89
4.6.2	Indoor temperatures .....	91
4.6.2.1	Summer .....	91
4.6.2.2	Winter .....	95
4.6.3	Heat flux .....	98
4.6.3.1	Summer .....	98
4.6.3.2	Winter .....	102
<b>5</b>	<b>Numerical simulation</b>	<b>105</b>
5.1	Two-dimensional model .....	107
5.2	Mesh Definitions .....	108
5.3	Imposed conditions .....	112
5.4	Numerical definitions .....	114
5.4.1	Materials .....	115
5.4.2	Cell zones and boundary conditions .....	115
5.4.3	Models, solidification and melting .....	117
5.4.4	Solution methods and controls .....	120
5.4.5	Solution initialization .....	121

---

5.4.6	Calculation parameters .....	122
5.4.7	Points of the numerical domains for the results analysis ....	123
5.5	Numerical results.....	123
5.5.1	Summer week .....	123
5.5.2	Winter week .....	130
5.6	Numerical validation.....	135
5.6.1	Summer week .....	138
5.6.2	Winter week .....	148
<b>6</b>	<b>Conclusions</b>	<b>161</b>
6.1	Final remarks .....	163
6.2	Past research and studies.....	163
6.3	Prototype definitions and development.....	164
6.4	Experimental results.....	164
6.4.1	Summer week .....	165
6.4.2	Winter week .....	165
6.5	Numerical results.....	166
6.5.1	Summer week .....	166
6.5.2	Winter week .....	167
6.6	Economic analysis.....	168
6.7	Future work .....	169
	<b>References</b>	<b>171</b>





---

LIST OF FIGURES

Figure 1 Flow diagram of the experimental work methodology .....	7
Figure 2 Flow diagram of the numerical work methodology .....	8
Figure 3 Mainly results for different windows using (a) Method 1; (b) Method 2; (c) Method 3.....	12
Figure 4 (a) Perfect window for summer; (b) Perfect window for winter ...	13
Figure 5 Route for energy efficiency to a single glazing.....	14
Figure 6 Methods for thermal energy storage .....	15
Figure 7 (a) Heat storage as sensible heat leads to a temperature increase when heat is stored (b) Latent heat storage for the case of solid-liquid phase change.....	16
Figure 8 Classes of materials that can be used as thermal storage material.....	18
Figure 9 Classification of energy storage materials.....	18
Figure 10 System description of the ventilated PV-DSF system .....	23
Figure 11 Operations modes of the PV-DSF system .....	24
Figure 12 Schematic of the prototype facade .....	25
Figure 13 Buildings composition of the different models simulated numerically .....	26
Figure 14 Validation of the simulated model .....	27
Figure 15 Indoor temperatures for the simulated models and measured experimental data .....	28
Figure 16 Experimental test cell with the two glazing systems (DGU_PCM and DGU_CG) .....	28
Figure 17 PMV and PMV* vs. time at 0.75m from DGU (08:00 – 20:00) (a) Summer, (b) Winter, (c) Mid-season warm period and (d) Mid-season cold period .....	30
Figure 18 Vertical cross section of a glazing system with prismatic solar reflector and PCM cavity .....	32
Figure 19 Interior and exterior surface temperature. Test with 1000 [W.m <sup>-2</sup> ] and 24°C indoor and outdoor air temperature .....	32
Figure 20 Scheme of the computational grid (glass panes and PCM layer)	34

---

Figure 21 Outdoor testing setup .....	36
Figure 22 Comparison between the calculated heat losses, heat gains and solar gains for winter.....	37
Figure 23 Comparison between the calculated heat losses, heat gains and solar gains for summer .....	37
Figure 24 Comparison between the calculated heat losses, heat gains and solar gains of the optimized system for winter .....	38
Figure 25 PCM-filled glass window scheme and boundary conditions.....	39
Figure 26 Indoor surface temperatures for (a) summer – overcast and rainy days; (b) summer – sunny days; (c) winter – overcast and rainy days; (d) winter – sunny days .....	40
Figure 27 Prototype composition .....	41
Figure 28 Outdoor experimental testing and prototype.....	42
Figure 29 Numerical model geometry .....	43
Figure 30 (a) Test cell; (b) Venetian blind; (c) System scheme and measurement positions .....	45
Figure 31 Comparison of the experimental and numerical results of the overall solar and visible transmittance data.....	46
Figure 32 (a) Analysed sun protections – Conventional and PCM blind; (b) PCM-slats .....	46
Figure 33 Office in Karlsruhe with the PCM blind protection.....	47
Figure 34 Comparison of the measured indoor temperatures.....	48
Figure 35 PCM blinds prototype and main results .....	49
Figure 36 Cross section of the PCM wall scheme .....	50
Figure 37 Test room scheme.....	50
Figure 38 Interior temperature of the room for the selected days .....	53
Figure 39 Ratio of solar energy gain and total efficiency during the heating season .....	53
Figure 40 Trombe wall schematic: (a) vertical section; (b) horizontal section .....	54
Figure 41 PCM macrocapsule .....	54
Figure 42 Switching process using (a) thermochromic, (b) electrochromic (c) electrochromic and (d) thermochromic laminated glass .....	56

---

Figure 43 GlassX Schematic .....	56
Figure 44 Schematic of the PCM-shutter.....	58
Figure 45 Physical model schematic for a) 9 a.m. to 5 p.m. and b) for 5p.m. to 9a.m.....	58
Figure 46 Total stored and released energy comparison during a complete daily cycle.....	59
Figure 47 Roller window shutter system composition.....	60
Figure 48 Comparison between the four models of the window shutter system .....	61
Figure 49 Heat flux for different PCM layer thickness.....	61
Figure 50 Differential Scanning Calorimeter (DSC) – Perkin® Elmer 4000 .	66
Figure 51 DSC results of test #4.....	67
Figure 52 Window blade filled with PCM .....	68
Figure 53 Some solutions to seal the PCM macrocapsules .....	68
Figure 54 (a) Aluminium blade end cap; (b) Window blade with epoxy on the external surface.....	69
Figure 55 Application of the thermal insulation material at the window shutter .....	69
Figure 56 Window shutter external dimensions.....	71
Figure 57 Window shutter scheme.....	71
Figure 58 (a) Shutter blades heating to the PCM filling; (b) Shutter blade filled with PCM .....	73
Figure 59 Window shutter system rotation (a) rotation system; (b) rotation parts and (c) modelled picture .....	73
Figure 60 Window shutter closed position (energy storage) (a) Overall scheme; (b) Detailed position; (c) Window shutter position during daytime .....	74
Figure 61 Window shutter opened position (a) Overall scheme; (b) Detail position; (c) Window shutter position during the night period .....	74
Figure 62 Window shutter intermediate position (a) Overall scheme; (b) Detail position; (c) Window shutter position during the night or day period.....	75

Figure 63 Window shutter applied in outdoor test cell and external dimensions .....	79
Figure 64 Test cell composition .....	80
Figure 65 Test cell location and orientation .....	81
Figure 66 Diagram of the chamber showing the probes and sensors positions and quantities .....	82
Figure 67 Data logger setup .....	83
Figure 68 Thermal bridges and heat losses of reference compartment (a) West side; (b) East side; (c) Overall test cell.....	84
Figure 69 Measured external temperature, R.H. and average daily solar radiation.....	86
Figure 70 Overall wind orientation and intensity.....	87
Figure 71 External climate conditions of the test compartments – Temperature, daily average R.H. and solar radiation.....	88
Figure 72 Wind orientation and intensity from 02-08-2013 to 09-08-2013	89
Figure 73 Outdoor air temperature, relative humidity and average daily solar radiation .....	90
Figure 74 Outdoor wind orientation and intensity from 28-01-2014 to 06-02-2014 .....	90
Figure 75 Indoor air temperatures, external air temperature and the daily solar radiation on selected days .....	92
Figure 76 Measured data of the indoor air temperature in the test cell and the external air temperature and daily solar radiation.....	93
Figure 77 Indoor temperature reduction between both compartments for each time step.....	94
Figure 78 Indoor air temperatures for both compartments, outdoor air temperature and daily solar radiation .....	96
Figure 79 Indoor air temperature for both compartments, outdoor air temperature and daily solar radiation – 3 day period .....	96
Figure 80 Indoor air temperature comparison and temperature reduction between compartments.....	98
Figure 81 Overall heat flux through the internal partition wall, indoor air temperatures in both compartments and external average solar radiation.....	99

---

Figure 82 heat flux and indoor air temperatures for the compartment with the PCM shutter and external average solar radiation. ....	100
Figure 83 Heat flux and indoor air temperatures for the reference compartment and external average solar radiation. ....	102
Figure 84 Heat flow of the internal partition.....	103
Figure 85 DesignModeler 2D picture .....	108
Figure 86 Mesh evaluation form .....	110
Figure 87 Mesh evaluation (a) Mesh elements number vs. standard deviation; (b) Mesh average quality vs. standard deviation; (c) Mesh min element quality vs. standard deviation.....	111
Figure 88 Model mesh – overall geometry and close-up to the exterior window boundary .....	112
Figure 89 Equivalent temperature profile, $T_{eq}$ , for the summer season ....	114
Figure 90 Equivalent temperature profile, $T_{eq}$ , for the winter season .....	114
Figure 91 (a) List of materials; (b) Example of the PCM properties definitions .....	115
Figure 92 (a) Cell zones of the numerical models; (b) Boundary conditions of the numerical domains.....	116
Figure 93 Boundary condition of the south-facing facade .....	117
Figure 94 Selected models for the calculation process .....	117
Figure 95 Viscous model definitions.....	119
Figure 96 Solidification and melting menu .....	120
Figure 97 Definitions of the solution methods, (b) the relaxation option values and (c) solutions controls.....	121
Figure 98 Menu of the solution initialization .....	122
Figure 99 Calculation parameters of the 2D models.....	122
Figure 100 Point coordinates of the temperature results .....	123
Figure 101 Temperature profiles in both compartments from the 2 <sup>nd</sup> to 9 <sup>th</sup> August .....	124
Figure 102 Temperature profiles in both compartments from the 2 <sup>nd</sup> to the 5 <sup>th</sup> of August .....	125
Figure 103 Temperature contours at 0h (3 <sup>rd</sup> August) for the (a) reference compartment; (b) PCM compartment.....	126

---

Figure 104 Temperature contours at 6h (3 <sup>rd</sup> August) for the (a) reference compartment; (b) PCM compartment .....	126
Figure 105 Temperature contours at 12h (3 <sup>rd</sup> August) for the (a) reference compartment; (b) PCM compartment .....	127
Figure 106 Temperature contours at 18h (3 <sup>rd</sup> August) for the (a) reference compartment; (b) PCM compartment .....	128
Figure 107 Temperature contours at 24h (3 <sup>rd</sup> August) for the (a) reference compartment; (b) PCM compartment .....	129
Figure 108 Contours of the temperatures differences between both compartments at (a) 0h; (b) 6h; (c) 12h, and (d) 18h .....	129
Figure 109 Temperature profiles in both compartments from the 31 <sup>th</sup> January to 4 <sup>th</sup> February .....	130
Figure 110 Temperature profiles in both compartments from the 1 <sup>st</sup> to 4 <sup>th</sup> of February .....	131
Figure 111 Temperature contours at 10h (3 <sup>rd</sup> February) for the (a) reference model; (b) PCM model .....	132
Figure 112 Temperature contours at 13h (3 <sup>rd</sup> of February) for the (a) reference model; (b) PCM model .....	132
Figure 113 Temperature contours at 16h (3 <sup>rd</sup> of February) for the (a) reference model; (b) PCM model .....	133
Figure 114 Temperature contours at 19h (3 <sup>rd</sup> of February) for the (a) reference model; (b) PCM model .....	133
Figure 115 Temperature contours at 22h (3 <sup>rd</sup> of February) for the (a) reference model; (b) PCM model .....	134
Figure 116 Contours of the temperatures differences between both compartments at (a) 10h; (b) 13h; (c) 16h; (d) 19h and (e) 22h .....	135
Figure 117 Experimental temperatures Vs. Numerical temperatures for the (a) Reference compartment (b) PCM compartment.....	139
Figure 118 Plot of the daily Coefficient of Variation of the Root Mean Square Error .....	140
Figure 119 Plot of the daily Normative Mean Bias Error (NMBE) .....	141
Figure 120 Plot of the daily Goodness of Fitness (GOF) .....	141
Figure 121 Box whisker mean (BWM) plot of the reference compartment	143
Figure 122 Box whisker mean (BWM) plot of the PCM compartment .....	143

---

Figure 123 Comparison of the numerical results with the experimental data for the period between the 2 <sup>nd</sup> and 9 <sup>th</sup> of August .....	144
Figure 124 Comparison of the numerical and experimental data for the period of the 5 <sup>th</sup> to the 8 <sup>th</sup> August .....	146
Figure 125 Thermal profiles for one day cycle (5 <sup>th</sup> August).....	148
Figure 126 Filtered signal of the experimental indoor temperatures for the numerical comparison.....	149
Figure 127 Winter results: experimental temperatures Vs. numerical temperatures for the (a) Reference compartment and (b) PCM compartment.....	150
Figure 128 Plot of the daily Coefficient of Variation of the Root Mean Square Error.....	151
Figure 129 Plot of the daily Normative Mean Bias Error (NMBE) .....	152
Figure 130 Plot of the daily Goodness of Fitness (GOF).....	152
Figure 131 Box whisker mean (BWM) plot of the reference compartment	153
Figure 132 Box whisker mean (BWM) plot of the PCM compartment.....	154
Figure 133 Comparison of the numerical results with the experimental data for the period between the 28 <sup>th</sup> of January and 4 <sup>th</sup> of February .....	154
Figure 134 Comparison of the numerical and experimental data for the period of the 1 <sup>st</sup> to 4 <sup>th</sup> February: (a) for the reference compartment; (b) for the PCM compartment and (c) for both compartments .....	157
Figure 135 Thermal profiles for one day cycle (3 <sup>rd</sup> of February).....	158





---

LIST OF TABLES

Table 1 Comparison of energy savings potential for three windows types .	12
Table 2 Comparison of different types of PCMs: advantages and disadvantages.....	19
Table 3 Thermal performance results summary of PV-DSF system under different modes.....	24
Table 4 Comparison between experimental and numerical data.....	35
Table 5 Comparison of the overall solar and visible transmittance for the glazing without shading under OCS .....	45
Table 6 GlassX crystal main technical data .....	57
Table 7 Physical and thermal properties of PCM RT28HC® .....	65
Table 8 DSC results for the different imposed conditions; .....	67
Table 9 Thermal and physical properties of the aluminium macrocapsules	67
Table 10 Thermal and physical properties of the insulation material .....	69
Table 11 Material properties introduced in the numerical model definitions .....	70
Table 12 Test cell shading for three different daytime for all seasons.....	81
Table 13 PCM quantities and losses .....	83
Table 14 Test cell shading for 3 different daily hours in summer period....	88
Table 15 Comparison of the temperature values and time delay between compartments.....	94
Table 16 Indoor air temperatures and time delays of both compartments between the 28 <sup>th</sup> and the 31 <sup>th</sup> January .....	97
Table 17 Design points and results of the output parameters.....	111
Table 18 Index calibration tolerances from the most used standards.....	136
Table 19 Values of the selected statistical indexes for the summer period analysed (2 <sup>nd</sup> – 9 <sup>th</sup> August) .....	138
Table 20 Statistical indexes for each testing day .....	140
Table 21 Numerical versus experimental results .....	145
Table 22 Values of the selected statistical indexes for the analysed winter period (28 <sup>th</sup> January to 4 <sup>th</sup> February) .....	149

Table 23 Statistical indexes for each testing day ..... 150  
Table 24 Numerical versus experimental results..... 155

---

**NOMENCLATURE**
Abbreviation

<i>A</i>	<i>Area</i>	$[m^2]$
<i>a-Si</i>	<i>Amorphous silicon</i>	
$A_{c,d}$	<i>Duct cross-section</i>	$[m^2]$
$A_g$	<i>Surface area of the glazing</i>	$[m^2]$
$A_{mush}$	<i>Mushy zone constant</i>	
<i>BIPV</i>	<i>Building integrated photovoltaic</i>	
<i>BWM</i>	<i>Box whisker mean</i>	
<i>C</i>	<i>Heat capacity</i>	$[kJ.K^{-1}]$
<i>CAGR</i>	<i>Compound annual growth rate</i>	
<i>CFD</i>	<i>Computational Fluid Dynamics</i>	
$C_p$	<i>Specific heat capacity</i>	$[kJ.kg^{-1}.K^{-1}]$
<i>CSC</i>	<i>Clear sky conditions</i>	
<i>CVRMSE</i>	<i>Cumulative root mean square error</i>	
<i>DGU_CG</i>	<i>Conventional double glazing unit with clear glass</i>	
<i>DGU_PCM</i>	<i>Double Glazing Unit with PCM</i>	
<i>DSC</i>	<i>Differential Scanning Calorimetry</i>	
<i>DSF</i>	<i>Double-skin facade</i>	
<i>E</i>	<i>Energy</i>	$[J]$
$E_{g,d}$	<i>Daily solar energy gain</i>	$[J.day^{-1}]$
$E_{g,m}$	<i>SEG per month</i>	$[J.month^{-1}]$
$E_{h,m}$	<i>Electricity consumption of the heaters per month</i>	$[J.month^{-1}]$
$E_{i,d}$	<i>Daily solar energy incidence</i>	$[J.day^{-1}]$
$E_{i,m}$	<i>Solar energy incident per month</i>	$[J.month^{-1}]$
<i>EU</i>	<i>European Union</i>	
<i>g</i>	<i>Solar transmittance</i>	
$g_e$	<i>Solar transmittance of the solar spectrum</i>	
$g_l$	<i>Solar transmittance of the visible spectrum</i>	
<i>GOF</i>	<i>Goodness of fitness</i>	
<i>h</i>	<i>Sensible enthalpy</i>	$[kJ.kg^{-1}]$
$h_0$	<i>Natural convection</i>	$[W.m^{-2}.K^{-1}]$
<i>HDPE</i>	<i>High-density polyethylene</i>	
$h_e$	<i>Exterior heat transfer convection coefficient</i>	$[W.m^{-2}.K^{-1}]$
<i>HVAC</i>	<i>Heating, ventilation, and air conditioning</i>	

$I$	Solar radiation	$[W.m^{-2}]$
IEA	International energy agency	
$I_i$	Solar radiation incident	$[W.m^{-2}]$
$I_t$	Transmitted solar irradiance heating	$[W.m^{-2}]$
$I_t$	Solar radiation transmitted in NTG	$[W.m^{-2}]$
$\vec{J}_j$	Diffusion flux of species $j$	$[kg.m^{-2}.s^{-1}]$
$k$	Thermal conductivity	$[W.m^{-2}.K^{-1}]$
$k_{eff}$	Effective conductivity	$[W.m^{-2}.K^{-1}]$
$k_t$	Turbulent thermal conductivity	$[W.m^{-2}.K^{-1}]$
$L_{air}$	Air layer	$[m]$
LCA	Life-cycle analysis/assessment	
$L_f$	Latent heat storage capacity	$[kJ.kg^{-1}]$
$L_g$	Glass layer	$[m]$
$L_{PCM}$	PCM layer	$[m]$
$L_{sh}$	Shutter layer	$[m]$
$m$	Mass	$[kg]$
$\dot{m}_a$	Air mass flow	$[Kg.s^{-1}]$
MBE	Mean bias error	
$M_i$	Record values of the experimental campaign	
Mtoe	Million tonnes of oil equivalent	
$N$	Number of days for each month	$[days]$
NIR	Near-infrared range	$[\mu m]$
NMBE	Normative mean bias error	
NTG	Novel Triple Glass	
NZEB	Nearly-zero energy buildings	
OSC	Overcast sky conditions	
$P$	Pressure	$[Pa]$
$p_c$	Cooling rating factor	$[kWh.m^{-2}]$
PCM	Phase Change Materials	
$p_h$	Heating rating factor	$[kWh.m^{-2}]$
PMV	Predicted Mean Vote	
PMV*	Modified predicted mean vote	
PRMSE	Percentage root mean square error	$[\%]$
PV	Photovoltaic	
PV-DSF	Photovoltaic double-skin facade	
PVC	Polyvinyl chloride	
PVCC	Photovoltachromic	
$q$	Overall heat flux	$[W.m^{-2}]$

---

$Q$	Net heat flux	$[W.m^{-2}]$
$\dot{Q}$	Solar heat gain	$[W.m^{-2}]$
$q_{cin}$	Convection heat flux between the indoor air and the indoor glass surface	$[W.m^{-2}]$
$q_{cout}$	Convection heat flux between the internal and external glass surface	$[W.m^{-2}]$
$q_{gc}$	Conduction heat flux between the inside and outside glass surface	$[W.m^{-2}]$
$q_{rg,out}$	Net radiation from glass surface to the outdoor air conditions	$[W.m^{-2}]$
$q_{rin,g}$	Net radiation between the glass surface and room surface	$[W.m^{-2}]$
$Q_s$	Solar radiation	$[W.m^{-2}]$
$q_r$	Net radiation heat flux	$[W.m^{-2}]$
$R^2$	Correlation factor	
$RH$	Relative humidity	$[\%]$
$RMSE$	Root Mean Square Error	
$RSEG$	Ratio of Solar Energy Gain	
$S$	Solar radiation	$[W.m^{-2}]$
$S$	Mushy zone	
$SBS$	Styrene butadiene-styrene	
$SEG$	Solar energy gain	$[J]$
$S_h$	Heat transfer from chemical reactions	$[W.m^{-2}]$
$SHGC$	Solar Heat Gain Coefficient	
$S_i$	Temperatures values of the numerical model	$[K]; [^{\circ}C]$
$SSPCM$	Shape-Stabilized PCM	
$STD$	Standard deviation	
$T$	Temperature	$[K]; [^{\circ}C]$
$T_0$	Air temperature	$[K]; [^{\circ}C]$
$T_{a,lv}$	Air temperature at the lower vents	$[K]; [^{\circ}C]$
$T_{a,uv}$	Air temperature at the upper vents	$[K]; [^{\circ}C]$
$T_e$	External air temperature	$[K]; [^{\circ}C]$
$T_{eq}$	Equivalent temperature	$[K]; [^{\circ}C]$
$TES$	Thermal Energy Storage	
$T_f$	Melting/solidification range	$[K]; [^{\circ}C]$
$T_{fp}$	PCM flash point	$[K]; [^{\circ}C]$
$T_i$	Indoor air temperature	$[K]; [^{\circ}C]$
$TIM$	Transparent insulation material	
$U$ -value	Thermal transmittance values	$[W.m^{-2}. K^{-1}]$

---

## Nomenclature

---

$v$	Velocity	$[m.s^{-1}]$
$XPS$	Extruded polystyrene	
$Y_j$	Mass fraction	
$\Delta H$	Enthalpy difference	$[kJ.kg^{-1}]$
$\Delta h$	Latent heat of fusion	$[kJ.kg^{-1}]$
$\Delta Q$	Sensible Heat capacity	$[kJ.kg^{-1}]$
$\Delta T$	Thermal difference between the final and initial temperature	$[K]; [^{\circ}C]$
$\Delta V$	Volume expansion	$[\%]$

### Greek symbols

$\vec{v}$	Velocity vector	$[m.s^{-1}]$
$\vec{v}_p$	Pull velocity	$[m.s^{-1}]$
$ \bar{\Delta} $	Average	
$a$	Solar absorption coefficient	
$\beta$	Liquid volume fraction	
$\varepsilon$	Small constant for calculation of the mushy zone	
$\eta$	Efficiency	$[\%]$
$\eta_{T,d}$	Daily total efficiency	
$\lambda$	Thermal conductivity	$[W.m^{-1}.K^{-1}]$
$\mu$	Dynamic viscosity	$[kg.m^{-1}.s^{-1}]$
$\nu$	Kinematic viscosity	$[m^2.s^{-1}]$
$\rho$	Mass density	$[kg.m^{-3}]$
$\rho_l$	Mass density liquid phase	$[kg.m^{-3}]$
$\rho_s$	Mass density solid phase	$[kg.m^{-3}]$
$\sigma$	Standard deviation	
$\tau_{S,tot}$	Overall solar transmittance	
$\tau_{V,tot}$	Overall visible transmittance	
$\bar{\tau}$	Stress tensor parameter	
$\vec{v}$	Velocity vector	$[m.s^{-1}]$
$v_m$	Air duct mean velocity	$[m.s^{-1}]$
$\vec{v}_p$	Pull velocity	$[m.s^{-1}]$

# **CHAPTER 1**

## **1 Introduction**

This section introduces the work overview and the main objectives.

The framework for energy efficient building solutions is contextualized and the thesis organization is presented. The work methodology for the experimental campaign and for numerical analysis is presented.

---





## 1.1 Overview

Presently, the environmental concerns and the energy efficiency are two widely compatible main research topics. According with the International Energy Agency (IEA) the buildings sector in the European Union is currently the single largest final end-use consumer of energy [1]. The energy consumption of this sector is 470 Mtoe (million tonnes of oil equivalent) of 1194 Mtoe which represents about 40% of the total energy consumption [1]. Not considering the emissions associated with the electricity use in the building sector, the CO<sub>2</sub> emissions represent 12% of the total CO<sub>2</sub> emissions produced in 2011 [1].

According with the International Energy Agency [1] the global primary energy consumption will rise in average at an annual rate of 1.2% through 2035 and as the building sector is the largest energy consumer, it is imperative to improve the energy efficiency of the building sector and decrease the energy consumption [1, 2]. By 2035 it is expected that the energy consumption in the building sector increases 29%, which represents an average annual rate of 1%. So, the energy performance and energy consumption of the building sector is targeted in advanced studies and policy making by the European Union and other developed countries [1, 3]. The European Union, to minimize and to improve the energy efficiency of the building sector has applied some policies and established goals, such as [4-6]:

- The Energy Service Directive and Renewables Directive proposes respectively a 9% of energy savings by 2016 and 20% increased use of renewable energy sources by 2020;
- All new buildings by 2020 must be nearly-zero energy buildings (NZEBs) and after 2018 new public buildings should be NZEBs;
- The Energy strategy of the European Union added targets for 2020, known as "20-20-20" that have the objective of 20% reduction of greenhouse gas emissions, comparatively to the 1990 levels, increase of 20% of energy production from renewable energy sources, and decrease of 20% of energy consumption;
- Besides the Energy Strategy, the EU added individual rules and directives for each member for the use of renewable sources and to improve the energy efficiency until 2020.

The reduction of the energy consumption for cooling and heating and the reduction of the energy needs are crucial to achieve the proposed targets [2]. Considering the importance of the existing buildings recent studies show that a

good building refurbishment combined with correct operation and installation of monitoring devices with well-designed active systems, can improve the buildings energy efficiency up to 60% [1, 7].

Nowadays, the external glazing envelope, mainly in offices and commercial spaces, are systematically composed by large glazed areas that lead to increase the energy consumption of the building and to visual discomfort to their occupants [8-10]. In terms of energy efficiency and indoor thermal regulation, these areas are presently an object of high-end research and application for enhancing building envelope [8, 11, 12].

Many studies, prototypes and developments have been done in the last years to increase the thermal and energy efficiency of windows. The improvements of the thermal performance of windows and glazed areas have been resourcing to new materials, new geometries and shapes and to the use of new techniques and technology in the glazing production.

The use of phase change materials (PCMs) is currently a promising solution to improve the energy performance of building elements considering their capacity to store and release energy. This capacity contributes to minimize the maximum and minimum indoor air temperature peaks and to reduce the buildings energy demand [13-16]. According the marketsandmarkets report, in 2013 the phase change material market was 407M€ and it is expected to grow to 1015M€ by 2018 and 1300M€ by 2019, which represents a compound annual growth rate (CAGR) of 20.1%. According to this report, the major PCM applications are the building and construction sector, the cold storage, HVAC, textile and the thermal energy storage systems. The Bio-based PCM is considered to have the higher growth until 2019 because of the environmental issues supported by European policies [17, 18].

## 1.2 Objectives and thesis structure

The main goal of this thesis is to research and to evaluate the thermal performance of a window shutter with phase change materials.

The main objectives could be summarized by:

1. Development of a window shutter system that contains phase change materials;
2. Development of a window shutter testing apparatus (with and without PCM)  
- quantification over the thermal behaviour and energy demand;

3. Results comparison of the reference window shutter versus the PCM window shutter;
4. Numerical simulation and validation of the window shutter;
5. Improvement of the thermal performance of the window shutter resorting to numerical models;
6. Thermal amplitude reduction of the indoor space of the building and reduction of the maximum and minimum indoor temperatures;
7. Indoor thermal regulation of the indoor spaces of the building.

The thesis is structured into 6 chapters. In the following sub-sections will be detailed each chapter, identifying main expected results.

#### Introduction and state-of-art

The chapter 1 and 2 allowed and supported the development of the next sections. The knowledge of other experimental and numerical research works, studies and PCM constituted important background to identify relevant parameters that should be recorded for the experimental testing and numerical analysis. In these chapters it was identified:

- Energy efficiency trends according the present policies and rules;
- Building construction solutions namely glazing with incorporation of PCMs;
- PCMs integration methods and types used in the buildings elements and components;

The main expect results were:

- Increasing of the knowledge in the scope of studies and research on buildings energy efficiency, PCM incorporation in building components and numerical developments;
- Background creation to support the next sections, more precisely the experimental testing and instrumentation setup and the numerical development of the window shutter with PCM;

#### Experimental apparatus

The chapter 3 a 4 presents the prototype developed and the experimental campaign.

The experimental testing is a crucial step and indispensable for the present work. The recorded data from the experimental instrumentation is fundamental

and has an important role for the validation and calibration of the numerical models. These chapters focus on the prototype development, experimental testing and instrumentation.

The main expected results were:

- Experimental instrumentation and recorded data of outside environment and indoor temperature, relative humidity and heat flow between compartments;
- Monitoring of the thermal behaviour inside of each compartment (reference and the PCM window shutter compartment);
- Identification of parameters and definitions that could improve the thermal behaviour of the PCM window shutter and can be used for the numerical validation.

The use of the recorded data from different weather seasons to understand the effect on the window shutter thermal behaviour for all seasons. Besides the experimentally recorded data, this work step includes data treatment using signal-filtering tools.

#### Numerical simulation and validation

In chapter 5 is developed the numerical model.

Resourcing to the experimental data, the numerical studies were developed and characterized. The aim of these numerical simulations is to characterize the thermal performance of the window PCM shutter.

The numerical validation was carried out using the recorded thermal data to compare with the numerical simulations based on statistical indexes. The results of the statistical indexes quantify the validation of the numerical results.

The main expected results were:

- Analysis and discussions of numerical simulations results;
- Validation of the numerical results with the experimental data;
- Validation of the numerical results according the statistical indexes.

### 1.3 Work methodology

The experimental procedure follows the work method presented in Figure 1. The test cell was located in Aveiro, Portugal, a region with a Mediterranean

climate. Considering the weather database available (from the weather station at the University of Aveiro) the adequate melting temperature of the PCM was chosen.

According to the selected PCM the shape of the window shutter blade (used as a macrocapsule) was defined and also the material. With the components of the window shutter prepared the system was assembled and applied in the outdoor test cell.

Two compartments compose the test cell and each one has two window shutters installed (two filled with PCM for one compartment and the other two without PCM). The test cell and the exterior surrounding were instrumented and the measured data is analysed and discussed further on.

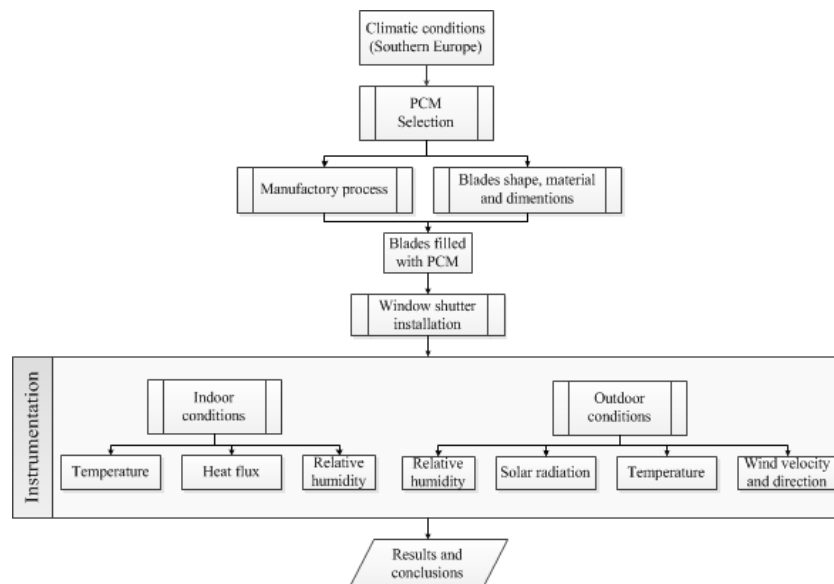


Figure 1 Flow diagram of the experimental work methodology

At the end of the first stage, the numerical analysis was carried out. As presented in Figure 2 the numerical model is based on the experimental apparatus. The geometry, the inputs weather conditions and the materials data of the experimental data was used to define the numerical models.

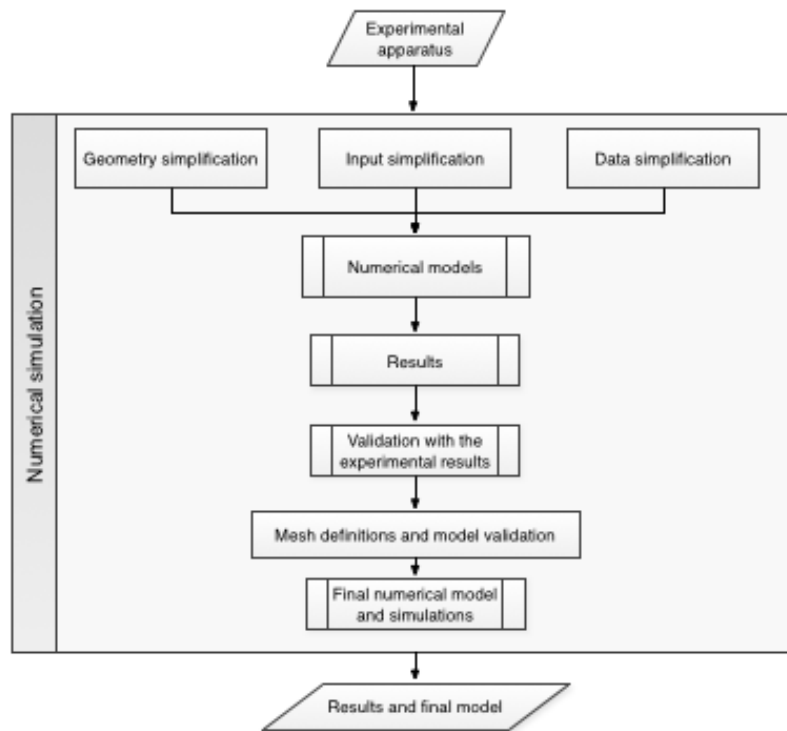


Figure 2 Flow diagram of the numerical work methodology

The results of the numerical simulation were analysis and discussed. The numerical model was validated comparing the numerical results with the experimental data. To quantify the agreement between the numerical and experimental data it was used statistical indexes.

# CHAPTER 2

## 2 Energy efficiency solutions applied in windows and glazings facades

The scope of this chapter is to present a state-of-art on other research studies and works in the field of the energy efficient windows and glazings boundaries envelope solutions.

The following section presents a extensive review on numerical and experimental studies, prototypes, techniques and final products applied in translucent and glazing systems, mainly focusing on solutions with phase change materials. The section is divided into three main sub-sections: *i)* the present challenges of building glazing solutions, *ii)* the phase change materials definitions and *iii)* the applications and studies of energy efficient glazing and windows.

---





## 2.1 Challenges and future role of glazed areas in buildings

Large glazed areas dominate currently the new building design and as most authors of previous research explain and discuss there are still many challenges and concerns to improve the glazed areas of the building envelope. There are four main concerns that constitute challenges that must be considered to improve the thermal behaviour of the translucent areas: the window frame, type and number of glass panes, building orientation and building geometry.

The use of materials with low thermal conductivity (frame and glass panes) should also assure good mechanical strength in respect to safety of indoor spaces intrusion. In the last years the most typical window frame material used in South-western Europe is aluminium, however nowadays the use of PVC and other composite materials are growing, with the advantage of presenting lower thermal conductivity, with still good mechanical behaviour.

Window glass materials and the glass layers composition influence significantly the thermal performance and the U-value of the window solution. The resource to glass with integrated solar reflection (i.e. prismatic glass) can enhance the thermal performance of the window for different seasons because the solar radiation is reflected according to the solar angle of incidence. To improve the thermal performance of the windows it is commonly used multiple glass layers and gaps filled with gas (i.e. argon, krypton and air) or filled with other insulation materials that have good optical properties that do not compromise natural lighting.

The building orientation and the building geometry are many times overlooked in the initial stage. However, these features associated to glazing areas are most relevant to improve the thermal comfort and temperature asymmetry of indoor building spaces. The use of natural resources, such as the direct solar radiation, wind and shading strategies can be proposed in the building design to improve its energy performance.

Grynning, et al. [19] discussed what types of windows will be used in future buildings and tested and analysed the effect of the heat losses and the heat gains in a typical office building located in Norway. They used the building energy simulation software – EnergyPlus – and tested different thermal transmittance values (U-Value) and solar heat gain coefficients (SHGC). They identified the common energy performance rating methods: Danish method [20], Spanish method [21], Italian method [22] and the Canadian method [23]. To evaluate the energy performance of the windows in their work, the authors used three different approaches: *i)* using the ISO 18292:2011 [24] standards that suggested a

calculation procedure for the energy performance of fenestration systems for residential buildings, *ii*) a useful gain method proposed by the authors and *iii*) the method of combined cooling and heating demand of the building.

The first method (ISO 18292:2011) calculates two rating factors: the cooling rating factor –  $p_c$  [ $\text{kWh}\cdot\text{m}^{-2}$ ] and the heating rating factor –  $p_h$  [ $\text{kWh}\cdot\text{m}^{-2}$ ]. The rating factor indicates how the window performance changes the energy demand of the building. The second method, proposed by them, analysed a useful gain factor. This factor combines the heat losses of the window system and the solar heat gains allowing to evaluate the energy performance of the window. The third method evaluated the window performance of the building according the heating and cooling needs. This method is in function of U-value and SHGC (solar heat gain coefficient).

The main results carried out by them using the EnergyPlus simulations with the present methods are shown in Figure 3 and Table 1.

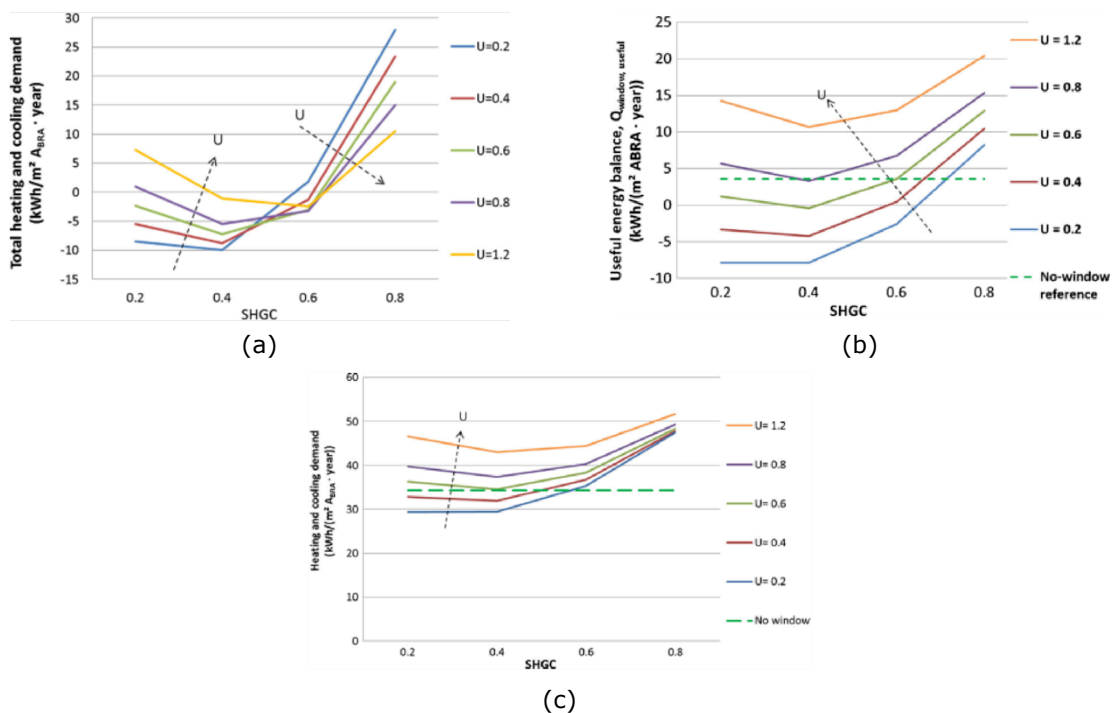


Figure 3 Mainly results for different windows using (a) Method 1; (b) Method 2; (c) Method 3 [19]

Table 1 Comparison of energy savings potential for three windows types

	Energy savings potential [ $\text{kWh}\cdot\text{m}^{-2}$ Year]		
	Method 1	Method 2	Method 3
2-window U-value/SHGC = 1.2/0.50	-2	12	45 (10)
3-window U-value/SHGC = 0.8/0.34	-4	4	35 (3)
4-window U-value/SHGC = 0.4/0.28	-7	-4	32 (-3)

Taken the overall results Grynning, et al. [19] conclude that:

- The three models present incoherent results, as showed in Table 1.
- The method 1 presents high potential for energy savings. In this method, the SHGC under 0.6 with any U-Value presents cooling and heating demands below zero.
- For method 1 the optimum combination is SHGC of 0.4 and U-value smaller than  $0.8 \text{ [W.m}^{-2}.\text{k}^{-1}]$ .
- For method 2, the window with the highest energy gain is the solution with  $U\text{-value} < 0.4$  and  $SHGC < 0.6$ .
- The results of all methods match for the same combination of U-Value and optimal SHGC: solar heat gain coefficient of 0.4.
- The discrepancy of the results between all methods is highest for the double-pane window and smaller for the four-pane window solutions.
- The energy savings can increase 5% to 15% (depends on SHGC) if the U-value is reduced from  $1.28 \text{ [W.m}^{-2}.\text{k}^{-1}]$  to  $0.8 \text{ [W.m}^{-2}.\text{k}^{-1}]$ .

Ye, et al. [25] presents the route for the perfect window. As they explain the ideal active/passive smart window can minimize the energy consumption in summer and winter by adjusting their reflection.

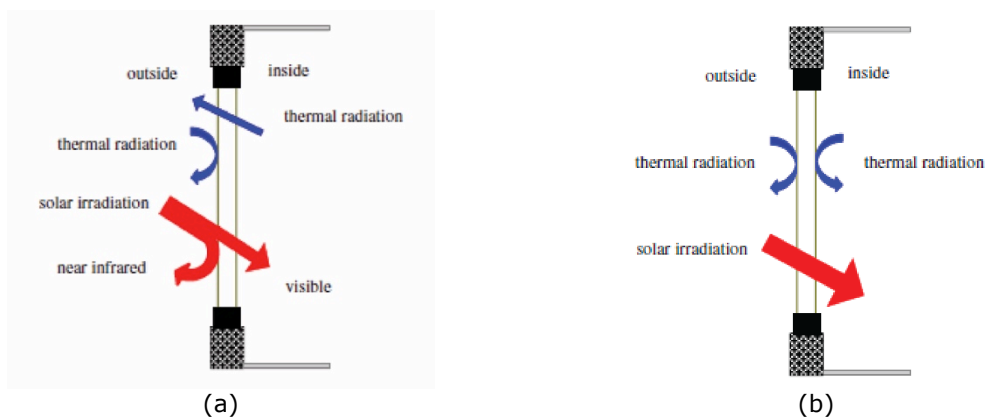


Figure 4 (a) Perfect window for summer; (b) Perfect window for winter [25]

The most typical wavelength in the Earth surface is between  $0.25$  and  $2.5 \mu\text{m}$ . This wavelength values included the near-infrared (NIR) range  $0.7\text{-}2.5 \mu\text{m}$  and visible part  $0.4\text{-}0.7\mu\text{m}$ . As they explain, the typical heat transfer coefficient of the glass is poor and equal to  $5.6\text{-}6.4 \text{ [W.m}^{-2}.\text{k}^{-1}]$ . The heat transmittance is high for the visible and NIR wavelength, for these reasons the glazing losses heat in winter.

In their work, Ye, et al. [25] refer that to improve the energy efficiency of single glazing chromogenic technology (which included electrochromic, photochromic, thermochromic and gasochromic technologies) should be used. This type of window change their solar spectrum properties mainly the NIR spectrum. The thermochromic windows use phase change material and change automatically their optical properties according to the imposed temperatures.

They created a schematic flow diagram with the route of energy efficiency to a single glazing (see Figure 5).

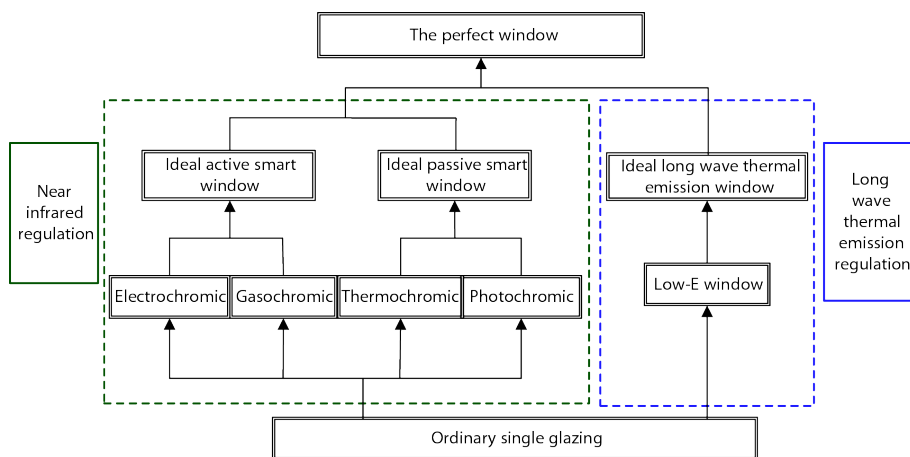


Figure 5 Route for energy efficiency to a single glazing [25]

Using this approach they tested the performance of a passive smart window [26] and created a physical model of a room. The room has  $4 \times 3.3 \times 2.8 \text{ m}^3$  and is located in the middle of a building with a southern wall and one window ( $1.5 \times 1.5 \text{ m}^2$ ) exposed to the external conditions.

They considered some assumptions to carry out the studies for five different cities: Haerbin, Beijing, Shanghai, Guanzhou and Kunming, all cities in China, but represent different climates.

The main conclusions and results obtained expressed that:

- The regulation of the solar spectrum of a passive/smart window depends on mainly of the absorption rather than the reflection;
- The effect of the long wave emissivity in summer is insignificant but is an important factor for energy savings in winter;
- The ideal passive smart window can improve the energy efficiency in summer, however is not so efficient in winter. Therefore, the active smart window can contribute for the temperature regulation in interior of the building for winter and summer season.

The energy efficiency and energy consumption can be enhanced if the solar spectrum response properties and the long wave emission properties are well defined.

## 2.2 Phase Change Materials

Most studies of phase change materials (PCMs) have received more attention in applications for opaque building solutions [27]. Therefore, solutions that use phase change materials to improve the energy efficiency of the glazing areas and transparent/translucent areas have been carried out in the last 20-25 years with promising results [28]. The introduction of phase change materials in building elements is an efficient method for improving the thermal energy storage capacity in latent form and the thermal inertia of glazing areas [29, 30]. Many studies and research challenges of PCM into glazing or windows solutions can be found in the literature [27-45], where some of them are explained in detail in the next subsections. There are many research and constructive solutions regarding the use of phase change materials that was first mainly applied into wallboards and renders (i.e. see [46-53]). There are also many research works and prototypes using PCMs into translucent components, to enhance the thermal performance and the indoor comfort of buildings.

### 2.2.1 Definition and operation principles

Thermal energy storage, also referred to as heat and cold storage, have two main possible methods for energy storage: physical process and chemical process (see Figure 6).

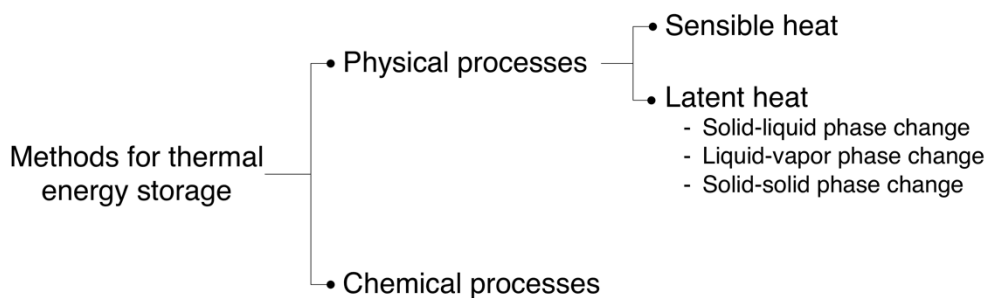


Figure 6 Methods for thermal energy storage

As Zhu, et al. [54] suggested, one of the most advanced technology to increase the energy efficiency in the building sector is the thermal energy storage systems using phase change materials (PCMs). One of the most interesting features of the PCMs is that they can store energy in the latent heat form as well as sensible heat as common materials.

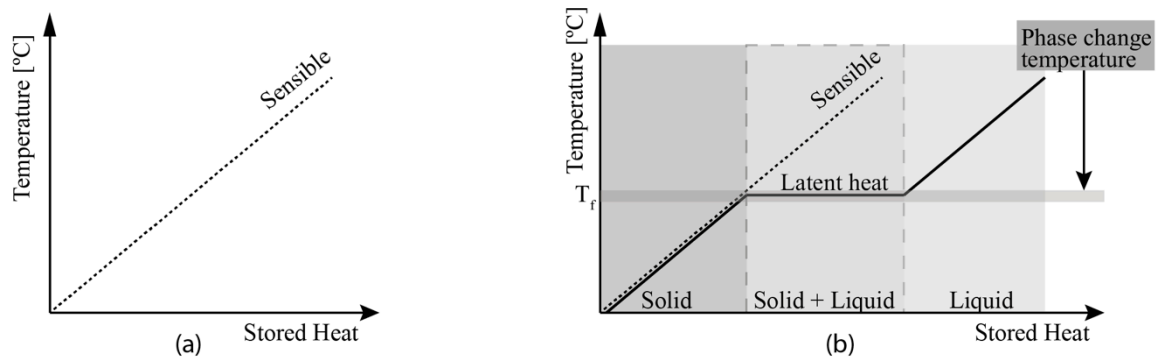


Figure 7 (a) Heat storage as sensible heat leads to a temperature increase when heat is stored  
 (b) Latent heat storage for the case of solid-liquid phase change

As Figure 7.a shows, the sensible property is a linear function and the increase of temperature leads to a stored heat increase. This process represents the sensible heat and can be given by:

$$\Delta Q = C \cdot \Delta T = m \cdot c \cdot \Delta T \quad (2.1)$$

The heat capacity  $C$  is given by the amount of material and by the mass specific heat capacity of the material ( $c$ ). The mass of storage material is represented by  $m$  and the  $\Delta T$  represents the thermal difference between the final and initial temperature. Each material has a different heat capacity  $C$ , so the sensible heat is influenced by the materials properties and by the imposed temperature. The sensible heat storage is the most common method for heat storage [15].

Another method for thermal energy storage is the latent heat physical process. This method uses the phase change process of the material to store energy, in the latent form. Usually these types of materials have associated a small volume change, less than 10%, when the phase change process occurs. As Figure 7.b shows, for a solid – liquid phase change, when the temperature of phase change is reached the temperature of the PCM is constant and the stored heat increases. Besides the range temperature of the phase change process, the PCM behaviour is the same of a common material, storing heat by sensible heat process [15]. The stored heat for the phase change process is calculated from the enthalpy difference  $\Delta H$  between the solid and liquid phase:

$$\Delta Q = \Delta H \quad (2.2)$$

Materials with solid-liquid phase change, store and release energy, in latent form, are commonly referred as latent heat storage material, *phase change material (PCM)* or *Thermal Energy Storage Material*.

When the temperature of PCM increases the material changes phase from solid to liquid, in opposite side, when the temperature of PCM decreases the material changes phase from liquid to solid. The first process is an endothermic reaction, the PCM stores energy, and the second process is an exothermic reaction, the PCM releases the stored energy.

The improvement of the thermal performance of the building due to the incorporation of PCMs into building envelope system depends on:

- Climate conditions;
- Solar radiation;
- Operating indoor temperature;
- Thermal properties of the materials;
- Design parameters such as shading, configuration and orientation of the system;
- Amount and type of PCM.

These systems require a complex and dynamic thermal behaviour simulation to estimate the energy efficiency of this type of systems, according to the features listed above.

### 2.2.2 Classification and types of PCMs

There are many types of phase change materials depending on their properties: Thermal properties; Physical properties; Chemical properties; Kinetic properties; Economical values; Encapsulation type (see Figure 8).

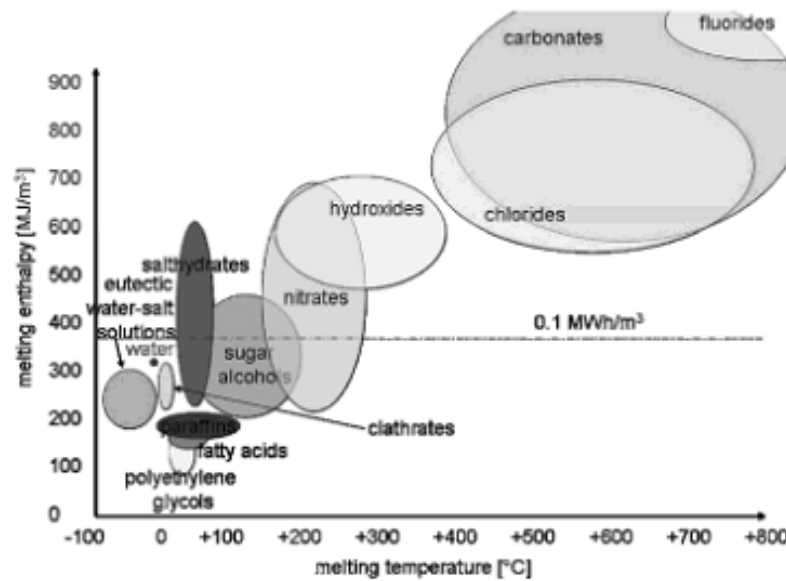


Figure 8 Classes of materials that can be used as thermal storage materials [15]

The concept of phase change material (PCM), or thermal energy storage (TES) material, is associated with the energy storage in solid-liquid phase change. These types of materials have been studied during the last 40 years, mainly the hydrated salts, paraffin waxes, fatty acids and eutectics of organic and non-organic compounds [55].

It is consensual in the literature to divide PCMs into three main groups: solid-solid, solid-liquid and liquid-gas, according to their chemical composition [56] or in two main groups, according their chemical properties: organic and inorganic [13, 57, 58] (see Figure 9).

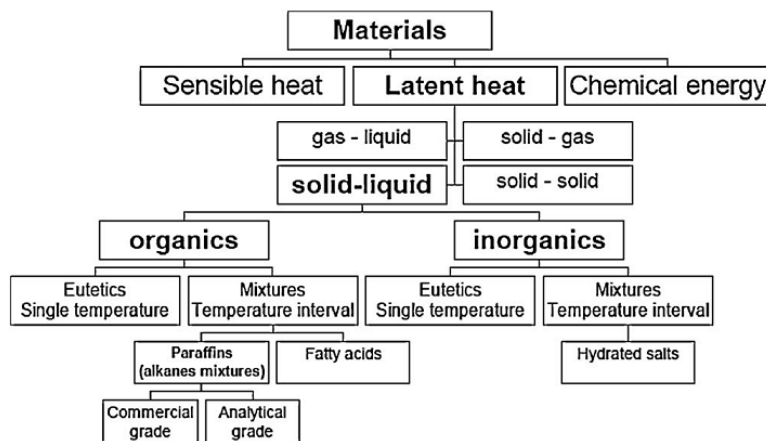


Figure 9 Classification of energy storage materials [59]

Table 2 presents the typical groups and sub-groups of PCMs according to their chemical composition indicating their main advantages and disadvantages [13, 55, 56, 60-65].



Table 2 Comparison of different types of PCMs: advantages and disadvantages

	<b>Sub-Group</b>	<b>Advantages</b>	<b>Disadvantages</b>
<b>Organic compounds</b>	Paraffins	<ul style="list-style-type: none"> <li>• can be directly incorporated;</li> <li>• can be impregnated into porous buildings materials;</li> <li>• chemically stable and inert;</li> <li>• do not suffer from supercooling;</li> <li>• non-corrosive;</li> <li>• non-toxic;</li> </ul>	<ul style="list-style-type: none"> <li>• low thermal conductivity (typically <math>0.2 \text{ W.m}^{-1}.\text{K}^{-1}</math> for paraffins);</li> <li>• large volume change during the phase change (paraffins);</li> <li>• Non-paraffins are three times more expensive than paraffins;</li> <li>• some are flammable.</li> </ul>
	Non-paraffins (fatty acids, esters, alcohols, glycols)	<ul style="list-style-type: none"> <li>• high thermal energy storage (latent heat of fusion);</li> <li>• wide range of melting temperatures;</li> <li>• low vapour pressure in phase change process;</li> <li>• do not suffer phase segregation;</li> <li>• good thermal performance after large thermal cycles;</li> <li>• excellent melting and freezing properties (non-paraffins).</li> </ul>	
<b>Inorganic compounds</b>	Salt hydrates	<ul style="list-style-type: none"> <li>• usually high thermal energy storage (latent heat of fusion);</li> <li>• good thermal conductivity;</li> </ul>	<ul style="list-style-type: none"> <li>• corrosive to most metals;</li> <li>• supercooling and phase segregation;</li> <li>• loss of thermal performance after large thermal cycles;</li> <li>• Requires support and container;</li> <li>• Cannot be directly incorporated;</li> </ul>
	Metallics	<ul style="list-style-type: none"> <li>• less expensive;</li> <li>• non-flammable.</li> </ul>	
<b>Inorganic eutectics or eutectic mixtures</b>	Organic-organic	<ul style="list-style-type: none"> <li>• sharp melting points;</li> <li>• usually high volumetric storage density.</li> </ul>	<ul style="list-style-type: none"> <li>• some suffer from super-cooling effect;</li> <li>• low total latent heat capacity.</li> </ul>
	Inorganic-inorganic		
	Inorganic-organic		

The limitations of the organic PCMs can be minimized using metallic containers and matrix structures to improve the thermal conductivity or if the volume expansion is a limitation, plastic containers or different container geometries can be used [13].

### 2.2.3 Types of PCMs incorporation

The solar energy storage and efficiency of the phase change materials in building elements depends on many factors and according the followed references one of the major features that influences the energy performance is the encapsulation method [15, 29]. There are 3 main types of PCMs encapsulation: *i)* direct incorporation (mixing) or shape-stabilized PCM (SSPCM), *ii)* macroencapsulation and *iii)* microencapsulation.

#### *2.2.3.1 Direct incorporation or shape-stabilized PCM (SSPCM)*

There are three main methods for the direct impregnation and incorporation of PCM into other components/materials [13]: during the manufacturing, after the manufacturing and based on a mixing slurry [66, 67]. The procedure for one of the PCM incorporation method is described by Feldman, et al. [66]. The shape-stabilized PCM (SSPCM) makes use of a mixing slurry that is composed by supporting materials (matrix) and working substances that incorporate the phase change material [56]. After the complete mixing process the mixture solidifies and the PCM is enclosed in the supporting material. Despite minimizing the leakage problem, the advantage of the SSPCM is the high density of the PCM (above 80%) that leads to high energy storage capacity of this solution [56, 68].

The most common supporting materials found in the literature are high-density polyethylene (HDPE) and styrene butadiene– styrene (SBS). Sari [69] states that no leakage of the phase change material by using HDPE as supporting material is observed. Xiao *et al.* [70] made the same remark for SBS. Zhang *et al.* [71] report that the PCM mixes better into SBS than in HDPE, but the shape-stabilized PCM is more rigid when using HDPE. The thermal conductivity of a shape-stabilized PCM is not very high, which is a problem in latent heat storage systems. The most complete study on those additives has been made by Zhang *et al.* [72]. They found that most efficient conducting material was ex-foliated graphite. The conductivity of their shape stabilized PCM evolved from  $0.150 \text{ W}\cdot\text{m}^{-1}\cdot\text{K}^{-1}$  to  $0.229 \text{ W}\cdot\text{m}^{-1}\cdot\text{K}^{-1}$  by adding 10% weight graphite into the mixture. Zhang *et al.* [72] developed a model to predict the thermal conductivity of the material from its composition.

Some references mentioned that the direct impregnation of the PCM into gypsum, concrete or other porous materials can deteriorate the mechanical properties of the container.

The direct incorporation of PCM has broad scope of applications, such as:

- Concrete mixture with PCMs that is designated mainly by thermo-concrete [73-79];
- Wallboard solutions with PCM [46, 47, 50, 67, 80-97];
- Foams with PCM [71, 98-100];
- Ceiling panels [101, 102].

#### *2.2.3.2 Macroencapsulation*

The simplest phase change materials encapsulation method is the macroencapsulation, which comprises the inclusion of PCM in some form of package or container such as tubes, pouches, spheres, panels, etc. These containers can serve directly as heat exchangers and be incorporated into building construction products.

The macroencapsulation method allows to store large PCM quantities and the macrocapsules can have different shapes according to the building element in which they could be incorporated. Besides these advantages, the macrocapsules can improve the thermal behaviour of the PCM, improves material compatibility with the surrounding, creating a barrier and contain the external volume change of PCMs [15].

Some applications of the PCM macroencapsulation:

- Bricks and blocks [52, 53, 103, 104];
- Air conditioning system and heat exchangers [105, 106];
- Flooring systems [107-109];
- Ceiling/roof [101, 110];
- Ventilated facade systems [42, 111].

#### *2.2.3.3 Microencapsulation*

The PCM microencapsulation is a widely used technique to incorporate phase change materials into building element components mainly in wallboards and concrete.

To enhance the integration capabilities of PCMs into existing and new products, some commercial companies base their solution on microencapsulated PCM. The PCM microcapsules are composed by microscopic polymer capsules with a diameter of some micrometres [112, 113]. These capsules have a spherical shape and the PCM is enclosed inside of the microcapsule [113]. The material selection of polymer capsule has to be taken to avoid chemical reactions between the microcapsules and the building materials [112]. As Kuznik, et al. [112] stated the PCM microcapsule quality is evaluated by the ratio between the mass of the capsules and the total mass of the powder.

The main advantages of the use of microencapsulated PCM are: a) the easy incorporation into conventional building materials; b) increase of the heat transfer area; c) lack of protection needed against their destruction and loss of properties; d) good control of the volume change when the phase change occurs [55, 113-117].

The coated particles can then be incorporated in any material matrix that is compatible with the encapsulating film [113].

The disadvantage of this method is the low heat transfer rate due to the polymer shell (microcapsules) that have a low thermal conductivity values [56, 118]. More studies and building solutions of microencapsulated technology used into wallboards and concrete can be found in literature [48, 64, 75, 88, 119-123].

### 2.2.4 Buildings components using phase change materials

The list of research studies using phase change materials into building applications is extensive, therefore the main review works focus on the opaque buildings components [13, 54, 55, 60-65, 77, 112, 124-132]. However the glazed areas and the shading devices have a significant role over the energy building consumption, so many research studies and prototype development in the last years have increased the thermal and the energy efficiency of this translucent boundary. A previous review on the research and development of transparent insulation systems focus on transparent insulation materials (TIMs) was published by Wong, et al. [133]. The following sub-section presents a review of windows and glazing energy efficient solutions, mainly using phase change materials in glazing and shadings building solutions.

## 2.3 Windows and glazings energy efficient solutions

The glazed areas and the shading devices have a significant role over the energy building consumption, so many research studies and prototypes have been

developed in the last years to increase the thermal and the energy efficiency of this boundary. The improvement of the thermal performance through the glazing area of the building can be attained resorting to new materials, geometries and new techniques to produce solutions with higher energy efficiency. New approaches, as the building orientation and the use of natural resources, as wind and solar radiation could decrease the energy needs and improve the energy transfer of these boundaries. Recent research and experimental tests could be found in the references: venetian blinds [9, 134-138], windows with roller blinds/shades [139-142], louver shadings devices [143-145], internal shading [146] and overhangs [147].

### 2.3.1 Ventilation method

Peng, et al. [10] presents an experimental study of the thermal performance of a novel ventilated building-integrated photovoltaic (BIPV) double-skin facade (DSF) (Figure 10). This photovoltaic (PV) DSF system is composed by a double glazing with an airflow duct between these two layers. The external layer/glass is composed by amorphous silicon (a-Si) and PV panel, so a-Si PV module allows to see through the glazing layer. The second layer (number 6, Figure 10) – indoor layer – allow the window to be opened inwardly for collect and transfer the external air to the internal air if needed.

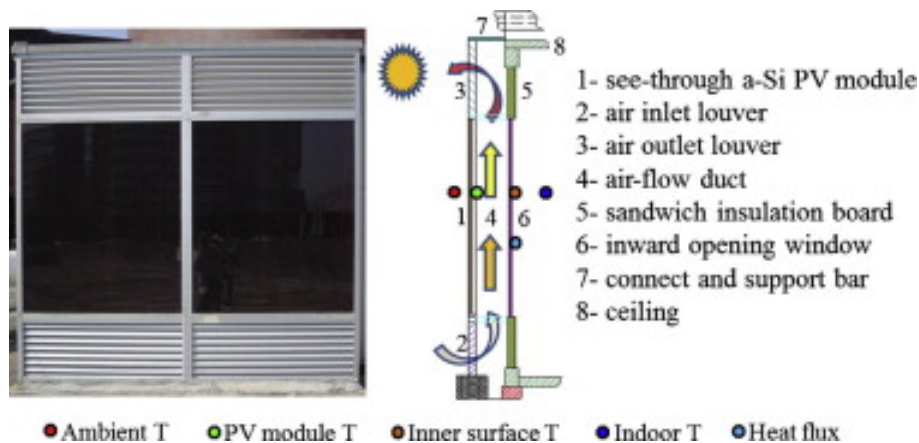


Figure 10 System description of the ventilated PV-DSF system [10]

The PV module of the ventilated PV-DSF system has (1.1x1.3x0.006m) and the inlet and outlet air louver has (1.1x0.5m). The airflow duct has 0.4 meters of depth.

The PC-DSF system has four operation modes by opening and closing different inlet and outlet louvers (see Figure 11) and the system tested under three different ventilation conditions: ventilated, natural-ventilated and non-ventilated.

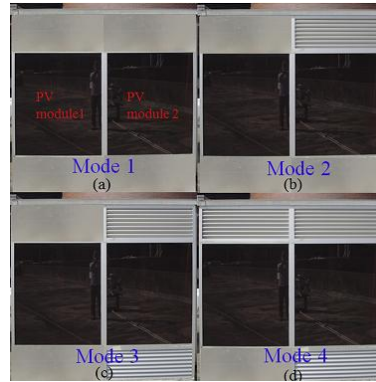


Figure 11 Operations modes of the PV-DSF system [10]

Peng, et al. [10] compared the results of the different operating modes and the different ventilation types to find an optimum operating strategy of the PV-DSF system:

- Mode 1: Studies of the passive heating effect in winter
- Mode 2: Comparison of the thermal performance between non-ventilated and naturally-ventilated conditions;
- Mode 3: Comparison of the thermal performance between ventilated and non-ventilated conditions;
- Mode 4: Comparison of the thermal performance between ventilated and naturally-ventilated conditions.

They compared the temperature profiles, heat gains and heat losses, solar heat gain coefficient (SHGC) and the U-Value of the PV-DSF system (see the results summary in Table 3).

Table 3 Thermal performance results summary of PV-DSF system under different modes [10]

<b>Modes</b>		<b>Mode 1</b>	<b>Mode 2</b>	<b>Mode 3</b>	<b>Mode 4</b>
SHGC		0.19	0.15/0.13	0.13/0.10	0.17/0.15
U-value	[W.m <sup>-2</sup> .K <sup>-1</sup> ]	5.9	3.2/3.6	3.4/4.6	3.8/4.7
Indoor temperature	[°C]	28.3	26.9/24.7	26.9/23.5	29.1/25.3
PV module temperature	[°C]	40.4	38/36.7	39.3/35.8	43.9/41
Heat gain	[W.m <sup>-2</sup> ]	108.6	50/45	53.3/42.1	75.8/70.2

Using the experiments and the obtained results, they suggested some operation strategies to improve the PV-DSF working and they conclude:

- The PV-DSF system generate electricity but also reduces the heat gains and heat losses through the building envelope;

- The ventilation duct benefits was demonstrated using a thermal imaging;
- The air temperature at the inlet louver is 2.2-2.3°C less than at that outlet louver;
- The ventilated PV-DSF had the best perform in terms of SHGC;
- The non-ventilated PV-DSF is the most effective in terms of heat losses;
- The PV-DSF is more appropriate for buildings and houses placed in tropical and subtropical climate zones, according the experimental campaign in Hong Kong;

**Advantages:** The PV-DSF system generates electricity and allows the sun light cross through the window. The system take advantage of the window geometry and their functionality is more adequate for tropical and subtropical climate zones. The PV-DSF system has four different operation modes according to the user needs.

**Disadvantages:** Peng, et al. [10] declares that during the day in winter season the airflow duct collects energy by the sun. However, to release the stored energy to the interior of the room, the window must be opened. This is a disadvantage since the window must be operated manually to release the heat into the room. This type of PV module has a future potential to be used in buildings but actually has low energy efficiency and is expensive to produce.

Diarce, et al. [42] presented an experimental and numerical study of a ventilated active facade with the incorporation of PCM in its external layer.

In their study, they design and tested an experimentally prototype facade with 2.7x2.7m<sup>2</sup> of area applied in a typically PASLINK test cell. They evaluated and discussed the PCM effect by the solidification and melting process and the thermal performance of the ventilated facade.

Five layers as shown in Figure 12 compose the prototype facade.

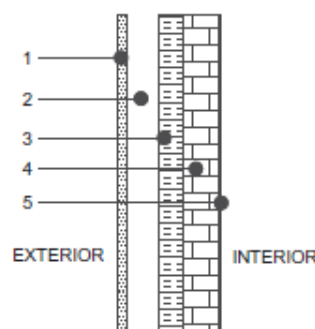


Figure 12 Schematic of the prototype facade [42]

The external layer – layer 1 (thickness of 20mm) – includes the phase change material incorporated into aluminium macrocapsules that is in contact with the external conditions and with the ventilated air gap (layer 2, thickness 60mm). The insulation material (50mm) is extruded polystyrene (layer 3) and is in contact with the layer 2 and layer 4 – brickwork wall composed by thick hollow common bricks. The layer 5 is in contact with the interior of the test cell (inner layer) and is made by plasterboard with 2mm of thickness. The PCM used in the first layer was the Rubitherm<sup>®</sup> RT35 (melting temperature 28°C to 35°C). The quantity of PCM in this layer was 50kg and the phase change enthalpy of the PCM is 135 kJ.kg<sup>-1</sup>.

The PASLINK test cell was located in Vitoria-Gasteiz, Spain and the temperature of every layer was measured using PT100 probes. The total PT100 probes used in the experimental test was thirty-two: fifteen probes in PCM layer (layer 1), twelve probes at layer 2 (air gap) and five probes in the remaining layers.

The PASLINK test cell was modelled numerically in Design Builder<sup>®</sup> software and to analyse different building solutions Diarce, et al. [42] created four different traditional facades models. These models represent the most common construction of buildings in Mediterranean regions – S1, S2, S3, and S4 – which composition is presented in Figure 13.

ID	DETAIL	LAYER DESCRIPTION	THICKNESS
S1	EXT.       INT.	Mortar-limestone	2 cm
		Limestone masonry	50 cm
		Gypsum plastering	1,5 cm
S2	EXT.       INT.	Face brick	12,5 cm
		Air gap	6 cm
		Double hollow brick	7 cm
		Gypsum plaster	1 cm
S3	EXT.       INT.	Face brick	12,5 cm
		Injected polyurethane	6 cm
		Double hollow brick	7 cm
		Gypsum plaster	1 cm
S4	EXT.       INT.	Face brick	12,5 cm
		Air gap	6 cm
		Double hollow brick	7 cm
		Glass fibre insulation	4 cm
		Gypsum plaster	1 cm

Figure 13 Buildings composition of the different models simulated numerically [42]

Diarce, et al. [42] present and discuss the results divided into three sections: experimental, simulation validation and simulation results of the tested models.

The experimental results showed that for days with high radiation the temperature of the circulating air increased the test cell indoor temperature in average about 10°C to 12°C. These results can be used to improve the thermal



behaviour of the internal space of the building. As they explained, the ventilated facade without PCM can also warm up the air, however the PCM effect extends the heated period. When the solar radiation drops the ventilated facade with PCM keeps the indoor air temperature warming up after 2.5 hours above 2°C. The authors estimated that the energy efficiency of the ventilated active facade with PCM increased 10% to 12%, compared with the same model without PCM.

Diarce, et al. [42] calibrated and validated the simulated model with the experimental results with success. The largest deviation between both models was 0.5°C and the mean values 0.2°C. Figure 14 presents the comparison of the results between the experimental PASLINK test cell and the simulated model.

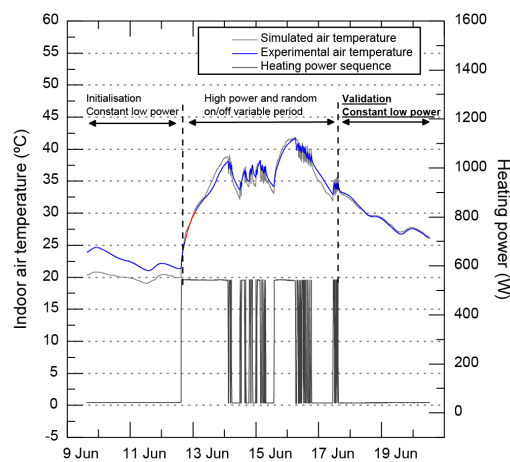


Figure 14 Validation of the simulated model [42]

The temperatures obtained in the simulated models show that the ventilated facade with PCM has high thermal inertia compared with the other models. The thermal amplitude of this model is 0.2°C – 0.7°C, smaller than S1 model 0.5°C to 1.3°C (analysed model with higher thermal inertia). However, when the solar radiation is higher, the indoor temperature during the daylight hours at the S2, S3 and S4 model is higher 2°C than the prototype – Figure 15 shows the temperatures results during 9 days (6 March to 14 March) for the simulated models and for the experimental ventilated facade with PCM.

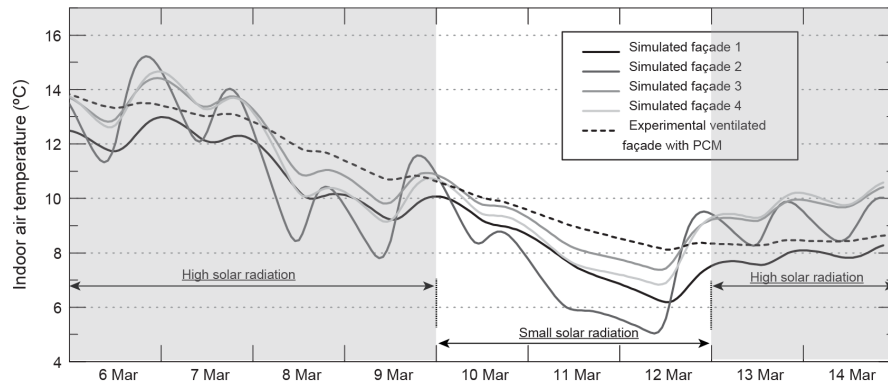


Figure 15 Indoor temperatures for the simulated models and measured experimental data (adapted from [42])

To conclude, they suggested for further work the evaluation and the optimization of the airflow rate through the ventilated chamber and the utilization of PCMs with different melting temperatures.

### 2.3.2 Glazing

Goia, et al. [30] proposed a prototype of a simple PCM glazing system (DGU\_PCM). They compared, during six months, relevant thermophysical properties and thermal performance (such as temperature, heat flux, and transmitted solar irradiance) between a simple PCM glazing system and the typical double glazed unit with common clear glass. Through numerical analysis, they improved the innovative PCM glazing system according the thermal comfort requirements.



Figure 16 Experimental test cell with the two glazing systems (DGU\_PCM and DGU\_CG) [30]

Two layers (8mm and 6 mm) of glass compose the double glazed unit with PCM (DGU\_PCM) and the air cavity (15mm) between the two layers was filled with commercial paraffin (RT35). The DGU\_PCM element area is about 1m<sup>2</sup>

(1.4x0.72m), inserted in an experimental test cell with 3.6m wide, 5.4 long and 3.0 high. The PCM was introduced into the air cavity and the volume of the PCM was 13dm<sup>3</sup> ( $\approx$ 13kg of RT35). They performed a Differential Scanning Calorimetry (DSC) analysis to characterize the thermal properties of the PCM. According the DSC analysis the latent heat of fusion ( $\Delta h$ ) is about 145 kJ.kg<sup>-1</sup> and the melting temperature about 34°C with a temperature range of 10°C [30]. The optical properties of the glazing prototype were evaluated by Goia, et al. [35] revealing that the light and solar transmittance increases when the PCM is completely melted, for example, with a normal incidence angle the solar transmittance of the visible spectrum ( $g_v$ ) and of the solar spectrum ( $g_e$ ) changes from the solid state (S) for the liquid state (L):  $g_e^S = 0.46$ ;  $g_v^S = 0.55$ ;  $g_e^L = 0.75$ ;  $g_v^L = 0.85$ .

The set point of the indoor air temperature was 26°C in summer, 23°C in mid-season and 20°C in winter. The test cells were oriented to the south, with direct solar radiation and without any shading device. They evaluated the comfort conditions using the predicted mean vote (PMV) method and calculated the thermal performance according to the ISO 7730 [148], ISO 15251 standards [149] and the Fanger theory [150].

The external and internal conditions were measured using 40 sensors connected to a data logger. As the standard PMV does not take into account the direct solar radiation influence, they calculated the modified predicted mean vote (PMV\*) (eq. (2.3)) considering the effect of the transmitted solar irradiance heating to the facade,  $I_t$ :

$$PMV^* = PMV + \Delta PMV \quad (2.3)$$

$$\Delta PMV = I_t \times 0.0024 \quad (2.4)$$

According to the standard EN 15251 [149] the thermal quality of the indoor environment is classified by: *i*) class A:  $-0.2 \leq PMV \leq +0.2$ , *i*) class B:  $-0.5 \leq PMV \leq +0.5$  and *i*) class C:  $-0.7 \leq PMV \leq +0.7$ . The thermal discomfort condition is achieved when the PMV or PMV\* is below or above these ranges.

Goia, et al. [30] analysed the PCM glazing system based on *i*) the visual appearance and temperature in glazing surface, *ii*) the results of hourly PMV and PMV\* values and *iii*) the spatial distribution of PMV\* values in the area for each indoor thermal quality class.

The results showed that the PCM melted completely from 14h to 16h and at the end of this process the surface temperature grows from 31-32°C to 39-40°C.

## 2.3 Windows and glazings energy efficient solutions

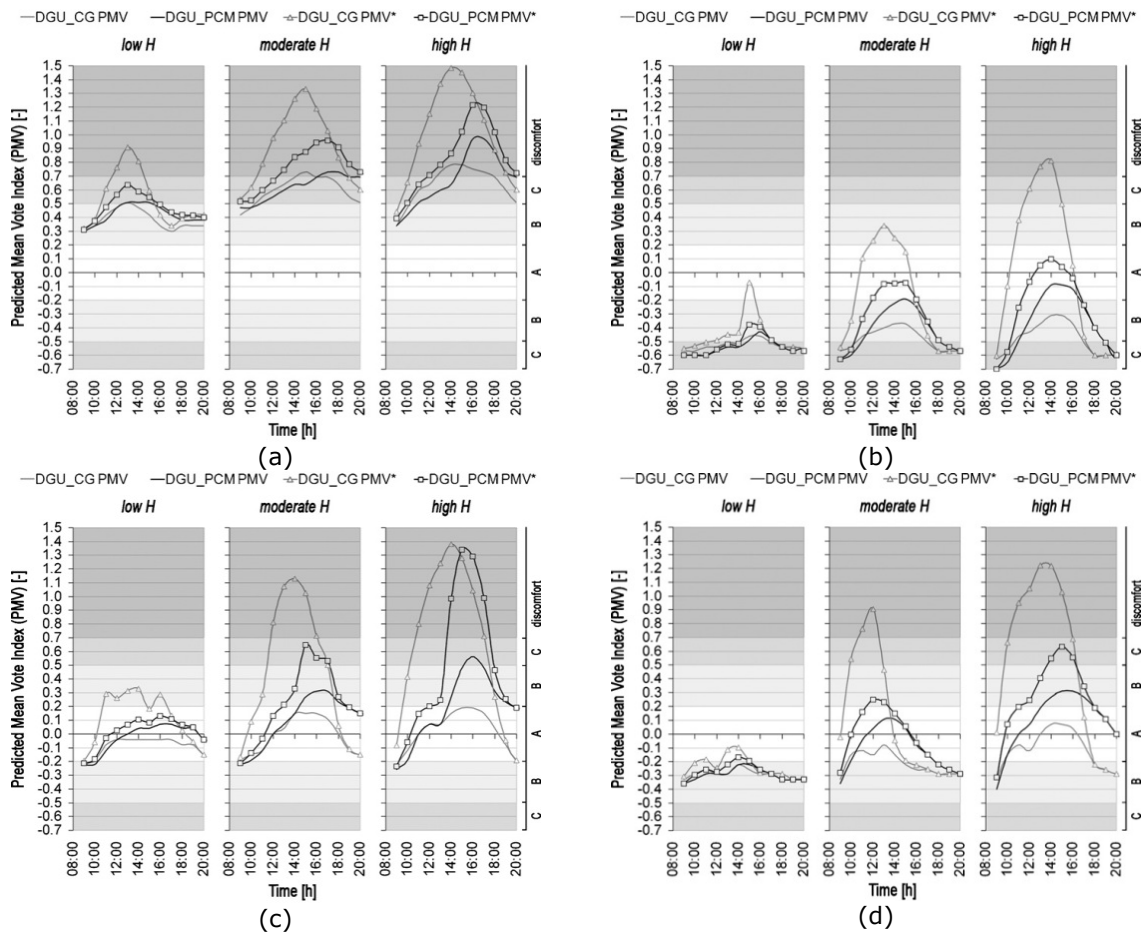


Figure 17 PMV and PMV\* vs. time at 0.75m from DGU (08:00 – 20:00) (a) Summer, (b) Winter, (c) Mid-season warm period and (d) Mid-season cold period [30]

Figure 17 shows the summary results of PMV and PMV\* values of both models (DGU\_PCM and DGU\_CG) for winter (low H – low daily solar irradiations conditions), summer (High H) and mid seasons (Moderate H).

Figure 17.a – summer (cooling) season – The PMV and PMV\* values in DGU\_PCM are significantly lower than DGU\_CG for all boundary conditions. The differences of the peak values are constant and approximately -0.3. For moderate and high daily solar irradiation (H) the PMV is above 0.7 for both models (discomfort range). In case of PMV\* results, for high solar irradiation the values exceeded the comfort range during 9 hours.

Figure 17.b – winter (heating) season – With low irradiation conditions the PMV and PMV\* values are most of the time in class C (discomfort range) for both cases. The PMV\* peak value of DGU\_CG model reached class A during two hours but the DGU\_PCM model only reached class B. For moderate irradiation conditions, the DGU\_PCM model presents 5 hours in class A while DGU\_CG model only presents 2 hours. The biggest difference between both models is for high solar irradiation. The DGU\_PCM model keeps between the comfort range during

the daytime, however the DGU\_CG model reached the discomfort range (> class C) between 12:00 to 13:00.

Figure 17.c – mid season (warm period) – The presented results for low solar irradiation levels show that both model are in comfort area. For moderate solar irradiation, the DGU\_PCM model has better thermal behaviour because the DGU\_CG model has values in discomfort range between 11:00 to 16:00. With high solar irradiance, both models reached discomfort PVM\* values but the DGU\_PCM model has better thermal behaviour than DGU\_CG. The discomfort range it reached at 14:00 for the DGU\_PCM model and it reached at 11:00 for the DGU\_CG model.

Figure 17.d – mid season (cold period) – The PMV\* results for this season are similar to the winter season. For low H both models stabilized within the various comfort classes. For moderate and high irradiance, the DGU\_CG presents some PMV\* values in the discomfort range (2hours for moderate H and 5 hours for high H).

Goia, et al. [30] concluded that the indoor conditions reached by the application of the DGU\_PCM solution increased considerably the thermal comfort comparatively to the conventional solution (DGU\_CG) for the most time of the different seasons. They suggested *i)* the application of PCM with lower melting temperature for cold climates and winter season and *ii)* the application of PCM with high melting temperature for hot climates and summer.

**Advantages:** The glazing configuration is easily manufactured, has low production cost and has a simple configuration.

**Disadvantages:** The prototype is for a fixed window. Testing this prototype in a real building environment is needed to evaluate the increase of the thermal comfort. During the solid state the PCM is not a clear layer, so the user cannot see through the window. This system does not have any application or strategy to use the stored energy to increase the energy efficiency or thermal comfort in the interior of the building.

Grynning, et al. [151] conducted an experimental study of a commercial glazing system with an integrated solar reflection (prismatic glass, as presented by Christoffers [152]) and a PCM filled cavity. The window has 1.44m<sup>2</sup> of area composed by four layers and the PCM cavity has 23mm of thickness as shown in Figure 18. Grynning, et al. [151] presents some preliminary results important for future experimental work. As Grynning, et al. [151] explained, thermal transmittance (U-Value) and solar heat gain coefficient cannot be completely

defined in this test because the introduction of dynamic properties in the glazing system makes the characterization a complex task.

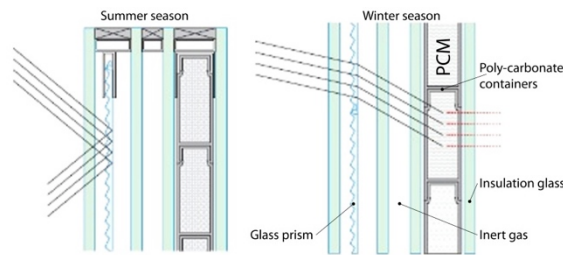


Figure 18 Vertical cross section of a glazing system with prismatic solar reflector and PCM cavity [Adapted from [151]].

The authors tested the glazing system with PCM using an environmental chamber with imposed climatic conditions in both sides of the glazing system and measured the heat flux, the temperature and the solar radiation using four heat flux meters, ten k-type thermocouples and two pyranometers. The climatic chamber allows imposing temperatures between  $-20^{\circ}\text{C}$  to  $+80^{\circ}\text{C}$ , relative humidity between 20 to 95% and in addition can apply rain and solar radiation. In their experiment they tested the glazing system with PCM in nine different scenarios:  $24^{\circ}\text{C}$  and  $20^{\circ}\text{C}$  indoor air temperature,  $24^{\circ}\text{C}$  and  $10^{\circ}\text{C}$  outdoor air temperature and the solar irradiation defined with  $500 [\text{W}\cdot\text{m}^{-2}]$  and  $1000 [\text{W}\cdot\text{m}^{-2}]$  for 1, 2, 4 and 8 hours. The U-Value of this glazing system is  $0.5 [\text{W}\cdot\text{m}^{-2}\cdot\text{K}^{-1}]$  and the fully optical and thermal properties of the glass system are presented in Table 6, page 57.

They conclude that the temperature stratification is higher than expected probably because the non-linear behaviour of the PCM, for example, the scenario with solar irradiance of  $1000 [\text{W}\cdot\text{m}^{-2}]$  and indoor and outdoor air temperature defined as  $24^{\circ}\text{C}$ , the temperature difference between the up and down of the surface is about  $4^{\circ}\text{C}$  to  $6^{\circ}\text{C}$  (exterior surface) and  $2^{\circ}\text{C}$  (interior surface) (see Figure 19).

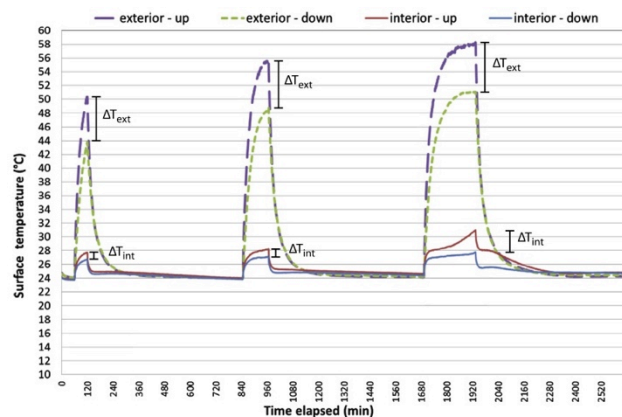


Figure 19 Interior and exterior surface temperature. Test with  $1000 [\text{W}\cdot\text{m}^{-2}]$  and  $24^{\circ}\text{C}$  indoor and outdoor air temperature [151]

**Advantages:** For office buildings it is a good solution because usually these are strongly glazed spaces, so the presented glazing system can work together with conventional or more conventional glazing solutions, allowing to operate the windows when needed.

**Disadvantages:** The study does not simulate the real day conditions because the cycle experiment was tested during 1h to 8h in the climatic chamber. The PCM needs more time to stabilize the temperature and more time to store and release the energy. This is a fixed solution and the PCM in solid state is translucent, so the light crosses through the window but the user cannot see through.

Gowreesunker, et al. [27] evaluated experimentally and numerically the performance of a PCM-glazing, including the thermal and optical characterization of the PCM. For this experiment, they selected the RT27 with latent heat capacity of  $184 \text{ kJ.kg}^{-1}$  provided by Rubitherm<sup>®</sup> manufacturer. The thermal testing of the PCM RT27 was carried out and explained by Gowreesunker, et al. [27] and Zhang, et al. [153] using the T-history method and the enthalpy method. The phase change material and the reference samples were submitted to a step temperature between  $14^{\circ}\text{C}$  to  $37^{\circ}\text{C}$  and they evaluated the stored and released heat behaviour as well as the enthalpy value.

The optical characteristics were analysed to evaluate the solar heating potential of the RT27 for solar glazing. They measured the transmittance spectrum, using a lambda spectrophotometer, for a wavelength from 200nm to 1600nm for three different PCM conditions: liquid, solid and transition phase. This wavelength included the ultraviolet, visible and part of near infrared range. Therefore, they evaluated the optical characterization experimentally using a photometer/environmental chamber.

The experimental studies were carried out for irradiation of  $950 \text{ [W.m}^{-2}\text{]}$ ,  $550 \text{ [W.m}^{-2}\text{]}$  and  $260 \text{ [W.m}^{-2}\text{]}$  and for imposed temperatures between  $13^{\circ}\text{C}$  and  $29^{\circ}\text{C}$ . For these conditions, the transmittance results of the standard double glazed unit range between 0.53-0.56 and 0.47 for the PCM-glazing solution.

To validated the technical characterization and the developed relations in this study, Gowreesunker, et al. [27] simulated the double PCM glazed unit using a CFD analysis with ANSYS<sup>®</sup> Fluent<sup>®</sup> software.

Gowreesunker, et al. [27] concluded that:

- The optical thickness of the PCM decreases with the temperature rise;
- The PCM-glazed is translucent in liquid phase and transparent in solid state;

- Under stable conditions, the visual PCM transmittance is 90% (liquid phase) and 40% (solid phase);
- A successful relationship was developed using some equations that allow representing the radiation behaviour into PCM for 350nm to 850nm wavelength. For further work, they recommended extended the same approach to others wavelength spectrums;
- The PCM increased the thermal inertia of the solution. However, this phenomenon is valid during the phase change process. When the PCM is liquid the overheating risk increased.

Goia, et al. [28] present a numerical model to evaluate the PCM effect in a glazed system configuration. The main objective of their work was to develop a simple method to simulate a PCM glazing system, considering the environmental conditions.

The numerical model is divided in two sub-models: to solve the heat transfer process and to calculate the solar irradiance transmitted and absorbed. Both models were based on a 1D nodal approach without considering the heat and shortwave radiation. They considered three nodes at the glass layers and five in PCM layer, as shown in Figure 20. Each PCM node can be in a single phase (solid or liquid) or in a transition phase (solid and liquid).

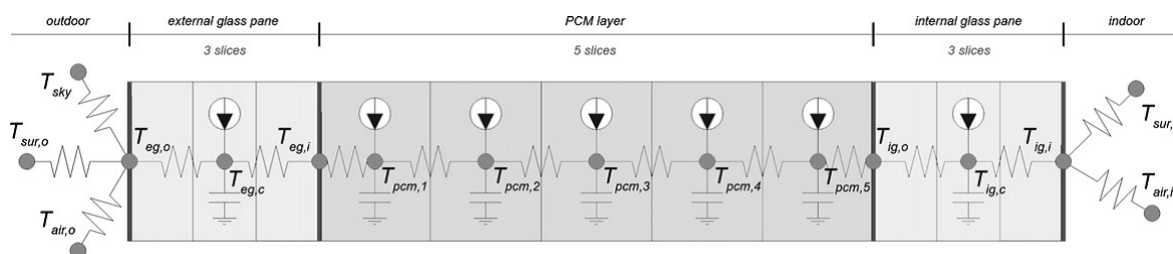


Figure 20 Scheme of the computational grid (glass panes and PCM layer) [28]

The thermal results were calculated numerically using the energy conservation equation of each node. Goia, et al. [28] adopted eight premises in their numerical definitions, such as the nodes of the layers are homogeneous; the glass surface is a grey body for the infrared wavelength; they neglected the convection in liquid PCM; the thermo-physical properties of the PCM that depends on their temperature; the optical properties of the glass that depends on the incident angle of indication.

To validate the numerical model, Goia, et al. [28] tested experimentally a PCM glazing prototype (1.4m x 1.15m) composed by two layers of glass (6mm and 8mm) and one PCM layer (paraffin, 15mm thick with melting temperature of



35°C). The data acquisition was carried out using 40 probes (thermocouples, heat flux meters and pyranometers) with a time step of 5 minutes during 1 year.

The physical model was evaluated and validated quantitatively, comparing the hourly values of the temperature, surface heat flux and transmitted solar irradiance. To quantify the agreement between the measured and simulated data the authors used: *i*) the percentage root mean square error (PRMSE), *ii*) the root mean square error (RMSE), *iii*) the average,  $|\bar{\Delta}|$ , of the difference between the experimental and the numerical data and *iv*) its standard deviation, STD  $|\bar{\Delta}|$ . The quantified values are presented in Table 4.

Table 4 Comparison between experimental and numerical data [28]

	season	PRMSE	RMSE	$ \bar{\Delta} $	STD $ \bar{\Delta} $
Surface temperature [°C]	S & W	7.1%	1.7	1.1	1.3
	summer	6.0%	1.9	1.4	1.2
	winter	8.1%	1.5	0.9	1.2
Transmitted surface heat flux [W.m <sup>-2</sup> ]	S & W	–	14.9	11.4	9.5
	summer	–	17.9	13.3	11.9
	winter	–	11.1	9.6	5.5
Transmitted solar irradiance [W.m <sup>-2</sup> ]	S & W	–	20.3	6.5	19.3
	summer	–	27.6	10.4	25.6
	winter	–	7.9	2.7	7.5

The results obtained by Goia, et al. [28] show a good agreement between *i*) the model and the experimental data of the transmitted solar irradiance, *ii*) the indoor surface temperatures and *iii*) the solar transmittance, reflectance and absorptance coefficients of the PCM. As they explained, the results in Table 4 present good accuracy because the values of the RMSE and  $|\bar{\Delta}|$  are lower than the maximum value of the variable. The poorest agreement is for the summer season due to the transmitted solar irradiance and the best agreement for the winter season. As Goia, et al. [28] explain the small discrepancies results between the experimental and numerical data can be justified by the premises considered.

Weinläder, et al. [34] carried out an experimental and numerical studies of a double glazing unit resorting to three different PCMs manufactured by Rubitherm®– two salt hydrates (S27 and L30) and one organic paraffin (RT25). The melting temperatures of the PCMs (RT25, S27 and L30) is respectively 25°C, 27°C and 30°C, and the latent heat capacity 147 kJ.kg<sup>-1</sup>, 190 kJ.kg<sup>-1</sup> and 270 kJ.kg<sup>-1</sup> respectively. The thermal property of the PCMs was modelled numerically using the explicit finite difference method. The optical properties of the three

PCMs were determined using the calculated values of the complex spectral refractive indices and the mean effective scattering coefficients.

The PCMs were filled into a transparent plastic container that was placed behind a typical double glazing unit with an air gap of 10mm, as presented in Figure 21. The thicknesses of the plastic containers have different values according the filled PCM used. The PCM RT25 containers have 12mm, the PCM S27 8.6mm and the PCM L30 10mm.

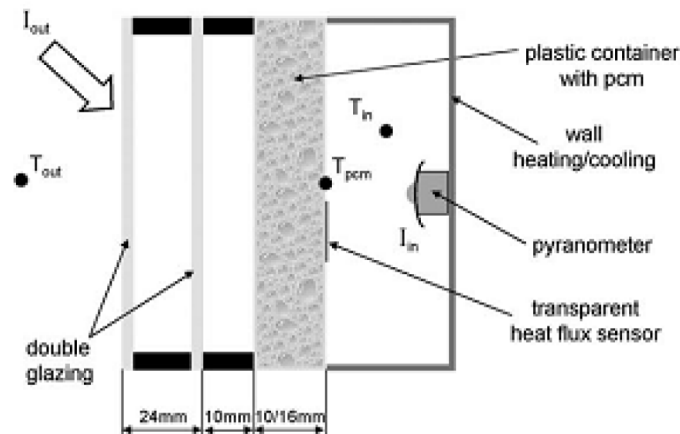


Figure 21 Outdoor testing setup [34]

The experimental results, more precisely the values of the temperatures ( $T$ ), heat fluxes and transmitted solar radiation ( $I$ ) were used to calibrate and validate the numerical model. The validated models used the climatic data of a reference year for Würzburg, Germany, to investigate the system performance of the facade panel with PCM with south orientation. Each system with the different PCM but with the same thickness (12mm) were analysed and the system performance results for the winter and the summer were presented.

For the winter conditions (considered November to February), the PCM models presented better results in comparison with the singular double glazing. The heat losses of the double glazing with 12mm of PCM RT25 reduced about 30% compared to the normal double glazing system. The facade panel with the PCMs revealed to store additional solar radiation gains compared with the double glazing system, more precisely 21% (RT25), 29% (S27) and 31% (S30).

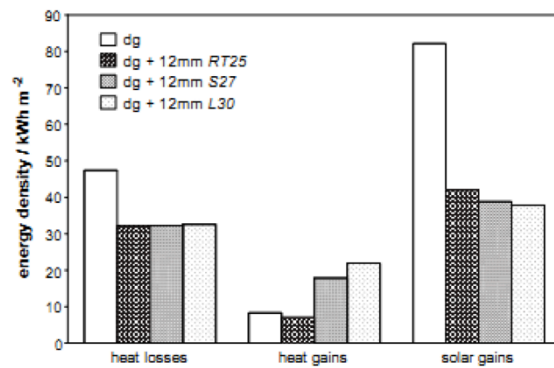


Figure 22 Comparison between the calculated heat losses, heat gains and solar gains for winter [34]

Figure 22 depicts the calculated results between November to February of the heat losses, heat gains and solar gains. These results show that the incorporation of PCM can reduce the solar gains and the heat losses and increases the heat gains. Analysing the calculated results of the hourly mean values of the total energy flow and the hourly mean values of the surface temperature the authors concluded that: *i*) the double glazing has high heat losses during the night and also high energy gains during the day and *ii*) the double glazing with PCM presents lower heat losses at night and also lower energy gains during the day.

Similar simulations for the winter season were made for the summer season (June to September). In this case, the PCM models presented once again lower heat losses and solar gains and high heat gains, as shown in Figure 23. The facade panels with PCM reduced the solar gains up to 50% that helps to minimize the indoor overheating. However, analysing the indoor surfaces temperatures Weinsläder, et al. [34] concluded that the PCM system presented lower thermal comfort in the rooms. As they explained, during the day the PCM system presented lower surface mean temperatures, however during the evening and at the night, the surface temperatures remained higher leading to lower thermal comfort for this period.

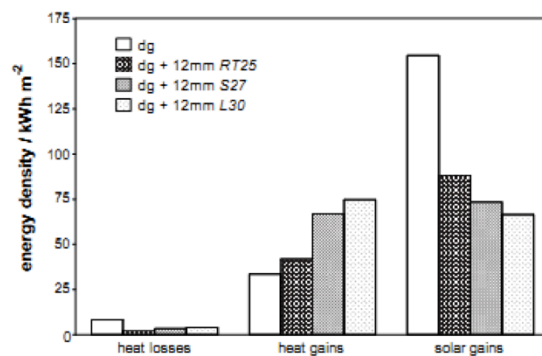


Figure 23 Comparison between the calculated heat losses, heat gains and solar gains for summer [34]

Using the calibrated model and the calculated results for the winter and the summer period, the authors carried out a system optimization to determine the right quantity of PCM to guarantee that all PCM material is used to store and release energy (not partially liquid fraction). Using the analysed parameters the selected PCM was the PCM S27 with 6mm of thickness, which presents similar or better results than the 12mm thickness. Comparing the results of both models for the winter (see Figure 24) the optimized system presents lower heat losses, higher heat gains and higher solar gains (in this case the 12mm model stores 13% of solar radiation energy against 8% of the optimized solution).

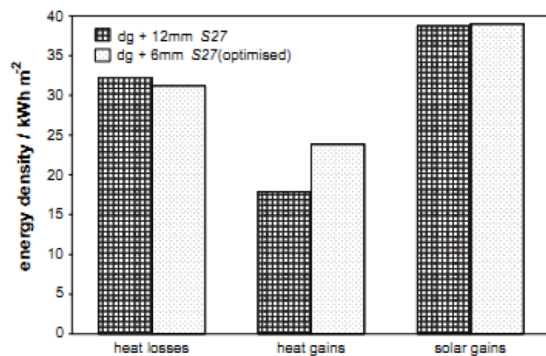


Figure 24 Comparison between the calculated heat losses, heat gains and solar gains of the optimized system for winter [34]

Li, et al. [36] analysed the thermal behaviour of a PCM-filled glass windows for a hot and cold climate. As they explain, the most used solutions in the building transparent facade are the insulated glass windows with dry air or inert air in the air gap of the double glazing. These types of windows usually have heat transfer coefficients ranging from 1.63 to 3.1 [ $\text{W}\cdot\text{m}^{-2}\cdot\text{K}$ ]. In their experiment, the authors compared the PCM-filled glass windows with the conventional insulated double glass with heat transfer coefficient of 2.6 [ $\text{W}\cdot\text{m}^{-2}\cdot\text{K}$ ] and solar transmittance of 83.6%.

The PCM-filled glass window is composed by three main layers: glass ( $L_g$ ), PCM/air ( $L_{air}/L_{PCM}$ ) and glass ( $L_g$ ) (see Figure 25). The thickness of each layer is 0.005m ( $L_g$ ) and 0.014 ( $L_{air}$  or  $L_{PCM}$ ) and the length-width size is  $0.5\times 0.5\text{m}^2$ . The external surface is submitted to solar radiation conditions ( $Q_s$ ), air temperature ( $T_0$ ) and natural convection ( $h_0$ ). The indoor air temperatures ( $T_i$ ) were set to 18°C (winter) and 26°C (summer).

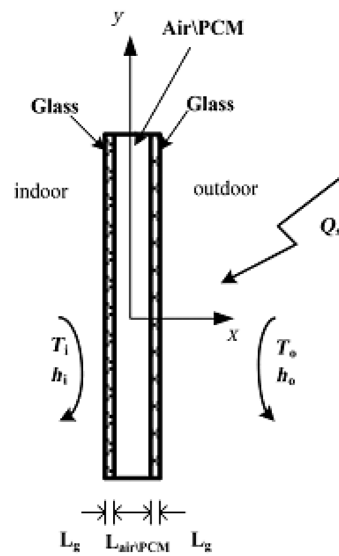


Figure 25 PCM-filled glass window scheme and boundary conditions [36]

In order to carry out the numerical studies, Li, et al. [36] used the commercial computational fluids dynamic (CFD) software ANSYS Fluent. To simulate the solidification-melting process they used the enthalpy-porosity method of Fluent software [154]. The liquid fraction was calculated using the enthalpy balance gradually approximation method. Two PCMs (salt hydrates) were chosen to be tested according to the climatic conditions of Nanjing, China. One is the  $\text{CaCl}_2 \cdot 6\text{H}_2\text{O}$  which has  $192 \text{ kJ.kg}^{-1}$  of latent heat capacity and melting temperature ranging from of  $27^\circ\text{C}$  to  $29^\circ\text{C}$ . The other is the  $\text{Na}_2\text{SO}_4 \cdot 10\text{H}_2\text{O}$  which has  $254 \text{ kJ.kg}^{-1}$  of latent heat capacity and the melting range is  $30^\circ\text{C}$  to  $32^\circ\text{C}$ . The thermal conductivity of these PCMs at the solid/liquid state is  $1.09/0.54 \text{ W.m}^{-1}.\text{K}^{-1}$  and  $0.554/0.45 \text{ W.m}^{-1}.\text{K}^{-1}$  respectively.

In this numerical research, Li, et al. [36] analysed four climatic conditions (two for winter and two for summer): *i*) overcast and rainy days and *ii*) sunny days. According to these weather data conditions they simulated the different windows solutions (conventional and the PCM-filled glass windows) and compared the surface temperatures results.

Considering the designation “window 1” for the insulated glass windows, “window 2” for the PCM-filled glass windows with  $\text{CaCl}_2 \cdot 6\text{H}_2\text{O}$  and “window 3” for the PCM-filled glass windows with  $\text{Na}_2\text{SO}_4 \cdot 10\text{H}_2\text{O}$  the temperatures results on the internal surface are presented in Figure 26.

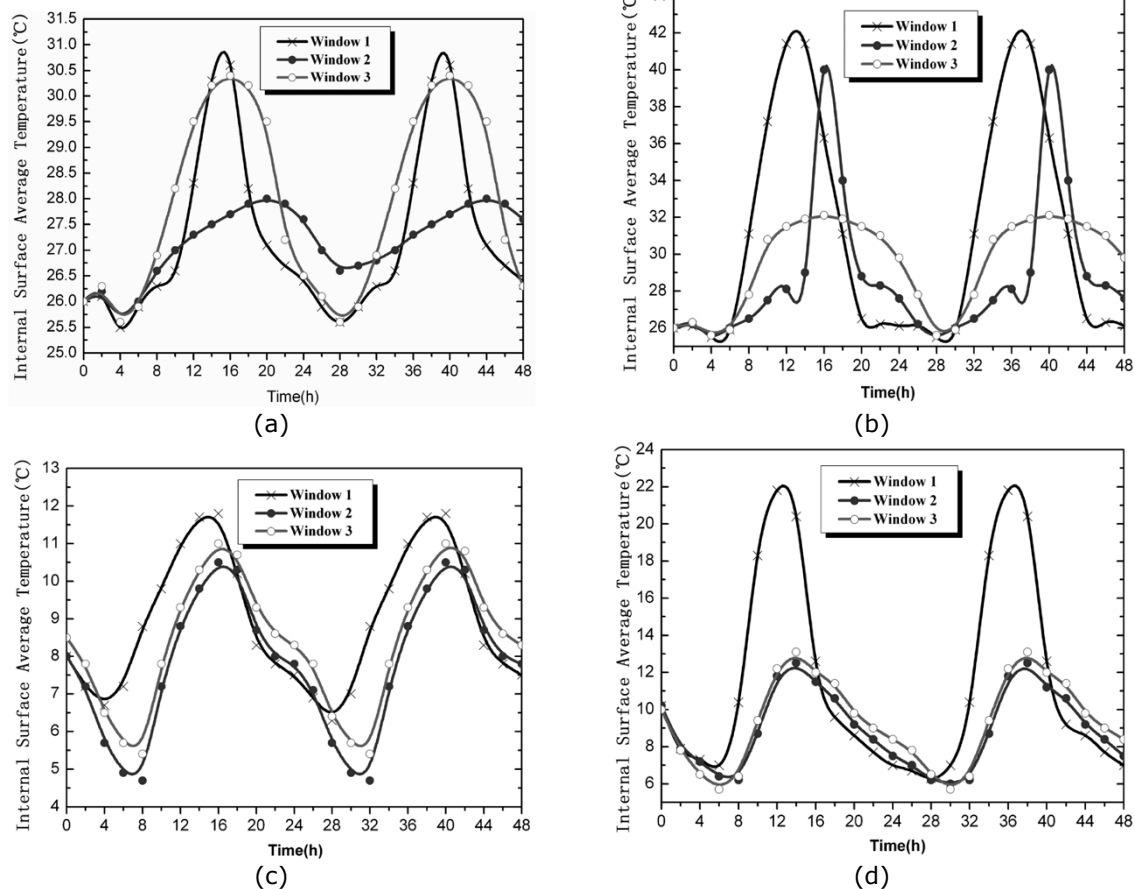


Figure 26 Indoor surface temperatures for (a) summer – overcast and rainy days; (b) summer – sunny days; (c) winter – overcast and rainy days; (d) winter – sunny days [36]

The thermal regulation effect of the PCMs models in winter (Figure 26 c and d) were not as expected. As the authors explain, during this period there was no phase change as a result of the high melting temperatures of the PCMs. The minimum temperatures reached in winter are similar for all windows but the maximum temperature of the insulated glass windows can reach about 10°C more compared with the PCM-filled glass windows.

The internal surface temperatures for the summer conditions show significant thermal improvement by the PCM effect (Figure 26 a and b). For the overcast and rainy days (Figure 26.a) the “window 2” solution presents best results but for the sunny days the “window 3” solution shows best thermal regulation effect. These results reveal the importance of the correct selection of the melting temperatures of PCMs.

The PCM of the window 3 can store more energy than the PCM of the “window 2” solution. However this feature can be taken if the correct conditions are applied.

For the overcast and rainy days, the PCM with lower melting temperature works better because the imposed temperatures are not so high to melt the PCM of the “window 3” solution (which have higher melting temperature). On the other hand for the sunny days the higher imposed temperatures melt the PCM of the “window 2” solution faster and after this time the surface internal temperature increases. In these conditions, the PCM of the window 3, which has higher melting temperature, works better and decreases 12°C the maximum temperature peaks compared to the reference window (without PCM).

In general, the PCM-filled glass windows models obtained better results for the summer period and worst for the winter period. The main factor that rules the results is the melting temperature of the PCMs according the imposed external climatic conditions.

Cannavale, et al. [155] presented an experimental study of a photovoltachromic (PVCC) system for the dynamic solar control in buildings.

Manz, et al. [31] presented a window system composed by two main layers: transparent insulation material and translucent phase change material. In their experimental work they used a salt hydrate phase change material with latent capacity of 192 [kJ.kg<sup>-1</sup>] and a melting temperature of 26.5°C. Figure 27 shows the prototype composition used in the experimental testing.

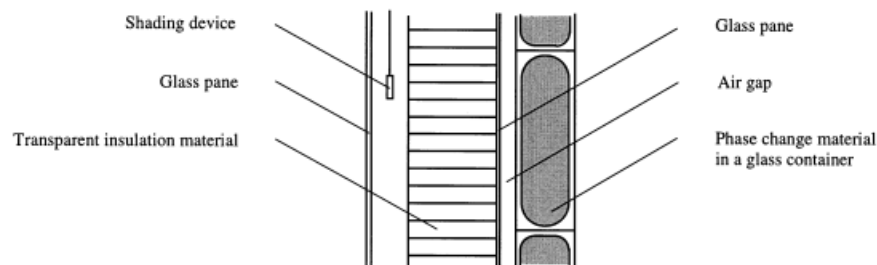


Figure 27 Prototype composition [31]

The authors carried out four main studies:

- i) Optical and thermal modelling of the materials. As Manz, et al. [31] explain, the optical properties of the materials depend strongly of the wavelength, so they divided the incident solar radiation into 20 wavelength. The optical and thermal properties of the transparent insulation material and translucent phase change material were tested. In order to simulate the optical behaviour of the PCM they used a Monte Carlo technique;
- ii) Experimental investigation of the optical material properties. In a spectrophotometer the authors tested experimentally the optical

properties of samples of: glass container, PCM and PCM filled into the glass container;

- iii) Outdoor experimental investigation of the prototype. The prototype was installed in an outside test cell and was experimentally tested. Figure 28 shows the outdoor experimental test cell and the prototype before its installation into the test cell;
- iv) Numerical simulation. A modular system simulation program was used to analyse the prototype behaviour. They compared the measured data with the simulation results. The numerical simulation allows to study and to analyse the prototype submitted to different climatic conditions or indoor boundary conditions.

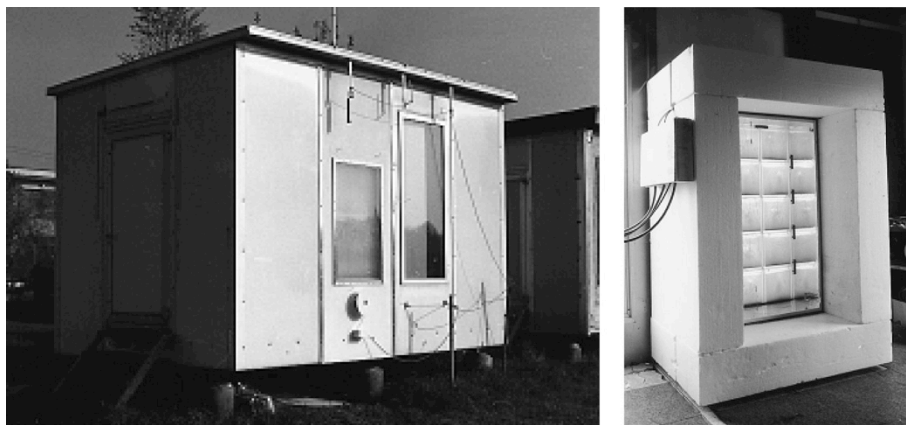


Figure 28 Outdoor experimental testing and prototype [31]

The results of the prototype indicate that the energy gains are promising. The measured and simulated data agreed well. The advantage of the use of phase change materials was demonstrated, therefore the selected PCM backscattered the solar radiation in the solid state that leads to heat and light losses. In their experiment, Manz, et al. [31] conclude that the decrease of the melting temperature of the PCM from 26.5°C to 21°C enhanced the prototype performance.

Wang, et al. [12] evaluated the total heat flux through a glazing surface according to three main factors: *i)* the influence of the radiation transmittance; *ii)* the effect of the convection heat transfer coefficient; and the *iii)* influence of the thermal amplitude between the temperature of the interior space and the surface.



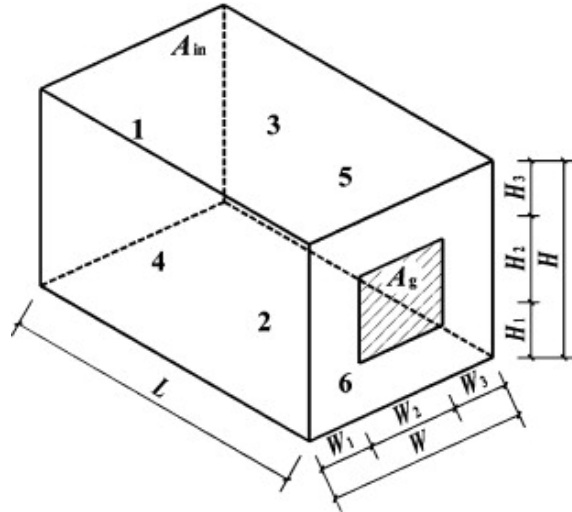


Figure 29 Numerical model geometry [12]

For the long wavelength radiation heat flux analysed, Wang, et al. [12] assumed all surfaces 1-6 as isothermal except the  $A_g$  surface (surface area of the glazing) (see Figure 29). The glass of the surface area was assumed as transparent diffused-grey surface.

The overall heat flux,  $q$ , was calculated as present in eq. (2.5) and the heat balance of the glazing is given by eq. (2.6).

$$q = \frac{Q}{A_g} \quad (2.5)$$

$$q_{rin,g} + q_{cin} = q_{rg,out} + q_{count} + q_{\tau} = q_{gc} + q_{\tau} = q \quad (2.6)$$

Where:  $Q$  represents the net heat flux;  $q_{rin,g}$  the net radiation between the glass surface and the room surface;  $q_{cin}$  the convection heat flux between the indoor air and the indoor glass surface;  $q_{rg,out}$  the net radiation from glass surface to the outdoor air conditions;  $q_{count}$  the convection heat flux between the internal and external glass surface;  $q_{\tau}$  the net radiation heat flux and  $q_{gc}$  the conduction heat flux between the inside and outside glass surface.

Wang, et al. [12] developed a mathematical model for the heat transfer that evaluated with good agreement the effect of *i)* the glass properties; *ii)* the convection heat transfer coefficient; *iii)* the surfaces temperatures; and *iv)* the air temperature. The main results show that:

- The influence of the solar radiation through the glass is significant for the heat flux increment;

- If the difference of temperatures, between the surface and the air (from the inside to the outside of the room) do not exceed 2°C, therefore the total heat flux effect can be neglect;
- The convection heat transfer coefficient do not effect significantly the overall heat flux;
- Heat transfer is improved by the solar radiation in winter but has an adverse effect in summer.

### 2.3.3 Internal shading devices

Gomes, et al. [9] determined both solar and visible properties of a glazing system with venetian blinds using a net radiation method. They compared the numerical results with the experimental data measured from an outdoor test cell.

As they explained there are different methods to calculate the solar optical properties of glazing layers [156-163]. Considering the properties of the venetian blinds in the model many authors used the ray tracing method [164, 165] or the net radiation method [166-170]. According the mentioned bibliography Gomes, et al. [9] estimated numerically the optical properties of venetian blinds using the net radiation method and compared the results with the experimental data carried out in a test cell. The measurements of the outdoor test cell included the illuminance and irradiance fluxes and the calculations of the visible and solar transmission properties of the experimental apparatus. In their experiment, Gomes, et al. [9] implemented a venetian control strategy to improve the day lighting but reducing the direct solar radiation.

The dimensions of the test cell are 3.5m length and 2.5m height with 0.2m of total gap. The location of the test cell is the National Laboratory of Civil Engineering in Lisbon and the glazing and shading system are oriented to south (Figure 30.a). From the external to the internal layer, the glazing system is composed by 5mm of single clear glass; an outer air gap and a venetian blind of 50mm; an inner air gap; and a 6-16-5mm double glazing with a spectral low emissivity coating (see Figure 30.b and Figure 30.c).

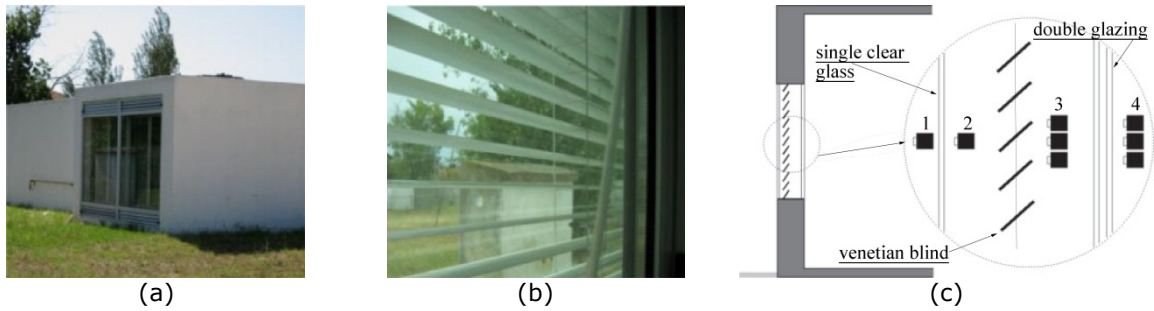


Figure 30 (a) Test cell; (b) Venetian blind; (c) System scheme and measurement positions [adapted from [9]]

The positions of the irradiance and illuminance sensors are presented in Figure 30.c. It was used four different system configurations: no shading, full shading (blind closed, slats at  $90^\circ$ ), 50% of shading (slats at  $45^\circ$ ) and venetian blind open (slats at  $0^\circ$ ).

Using the net radiation method, Gomes, et al. [9] presented the equations to evaluate the solar and visible optical characteristics of the multilayer system. They considered in their calculations the total radiation (reflected, absorbed and transmitted), the interactions of incident (solar and visible) radiation with the glazing and shading system and they considered the venetian blind shading device.

The numerical, analytical and experimentally results of the overall solar ( $\tau_{s,tot}$ ) and visible transmittance ( $\tau_{v,tot}$ ) for the glazing without shading under overcast sky conditions (OCS) was compared (see results at Table 5).

Table 5 Comparison of the overall solar and visible transmittance for the glazing without shading under OCS

	$\tau_{v,tot}$	$\tau_{s,tot}$
Experimental	0.35	0.15
Numerical	0.34	0.15
Analytical	0.34	0.15

To evaluate the accuracy of the developed venetian blind model the results of the simulation studies were compared with the other typically recognized models, EnergyPlus [171] and ISO 15099 [166] and presented in Gomes, et al. [172].

In their paper, Gomes, et al. [9] presented graphs with the numerical and experimental data, such as irradiance and illuminance under clear sky conditions (CSC) and OCS for the models without blinds and with venetian blind slats of  $0^\circ$ ,  $45^\circ$  and  $90^\circ$ . The comparison of the overall solar and visible transmittance for different venetian blind slats is shown in Figure 31. As expected, when the light

obstruction increases (high blind slat angle) the overall solar and the visible transmittance values decrease.

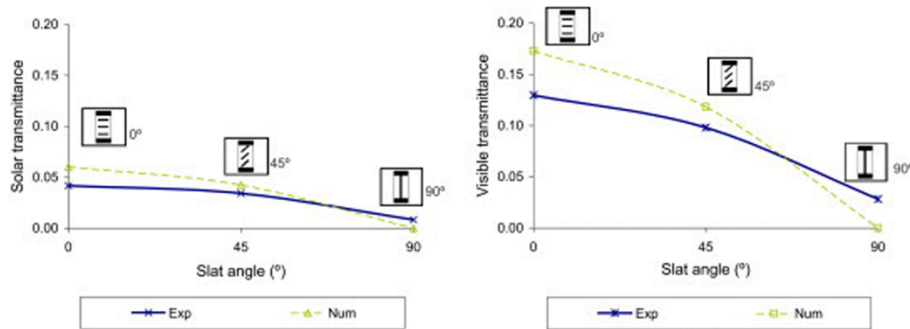


Figure 31 Comparison of the experimental and numerical results of the overall solar and visible transmittance data

They concluded that the developed model can be used to simulate different system configurations, such as glazing and/or shading devices (including venetian blinds) and the model can be introduced into building energy simulations and building design tools. The numerical results were compared with the experimental data and for overcast sky conditions. For these conditions they got excellent fitting results, but for the clear sky conditions the comparison of the results presented some discrepancies. A venetian blind control strategy was used and they concluded that it is more important for southern European regions. To help designers and users to improve the thermal and daylighting indoor conditions they presented some design plots with information about how to adjust the slat orientation of the venetian blinds.

Weinlaeder, et al. [44] tested experimentally between 2008 to 2010 an interior sun protection, that is composed by vertical slats filled with phase change materials and it was applied in four office buildings.

They analysed two similar conventional sun protections composed by vertical slats (filled with PCM or empty) (see Figure 32.a). The vertical slat is made of polycarbonate with an indoor gap of 12mm between the shading device and the double glazing and it was covered with a highly reflective white fabric (see Figure 32.b).

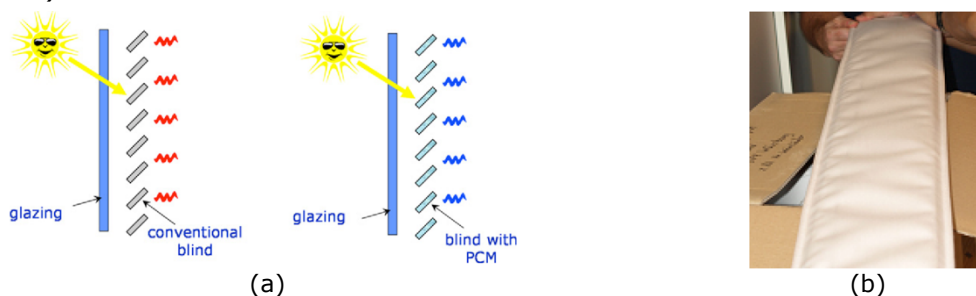


Figure 32 (a) Analysed sun protections – Conventional and PCM blind; (b) PCM-slats [44]

The PCM used was the Dorken Delta<sup>®</sup> Cool 28 which is a salt hydrate with latent heat of  $188\text{kJ}\cdot\text{kg}^{-1}$  and melting temperatures of  $26^{\circ}\text{C}$  to  $30^{\circ}\text{C}$  (average of  $28^{\circ}\text{C}$ ). The hollow polycarbonate blind is filled with PCM, which represents about 17kg of PCM per square meter.

In a first approach, the PCM and reference prototypes were tested in a laboratory to determine the solar heat gain coefficient (g-values) and the transient behaviour in case of incident solar radiation. The laboratory apparatus is composed by two controlled chambers and one solar radiation unit (up to  $1000\text{W}\cdot\text{m}^{-2}$ ) that simulates the indoor and outdoor temperatures. Once finished the laboratory tests that proved the PCM potential, the authors carried out a full-scale of the PCM blind into four offices.

The offices are located in Karlsruhe and in Kassel (each location has two offices: one with a PCM blind and the other a conventional blind). In the first region, the test room has westward orientated and about 50% is window area. In the second region the tested office has southeast orientated and 40% of glazing area. The indoor activity and the blinds control strategy of the test rooms (reference and with PCM) were similar. Figure 33 shows the Karlsruhe office with the PCM blind. To simulate the internal gains, electrical heaters of 500W were used between 9a.m. to 5p.m that resulted in  $28^{\circ}\text{C}$  operative indoor temperature during this period. Weinlaeder, et al. [44] presents the results of the system performance for the two main seasons: summer and winter.

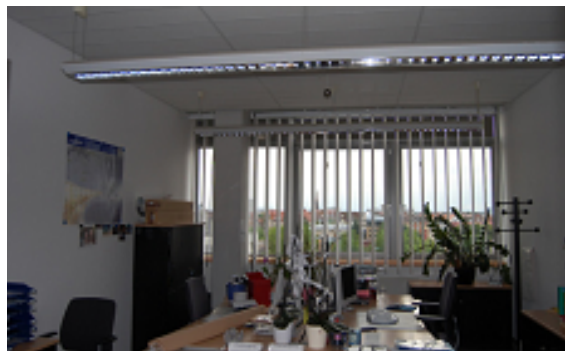


Figure 33 Office in Karlsruhe with the PCM blind protection [44]

The results of the summer period of the Karlsruhe office shows that the PCM test room decreases the maximum indoor temperatures  $2^{\circ}\text{C}$ , from  $34^{\circ}\text{C}$  to  $32^{\circ}\text{C}$  as presented in Figure 34. Analysing the results during long periods, Weinlaeder, et al. [44] concluded that the PCM in the blind slats never melt completely if during the night the stored energy by the PCM is not completely released.

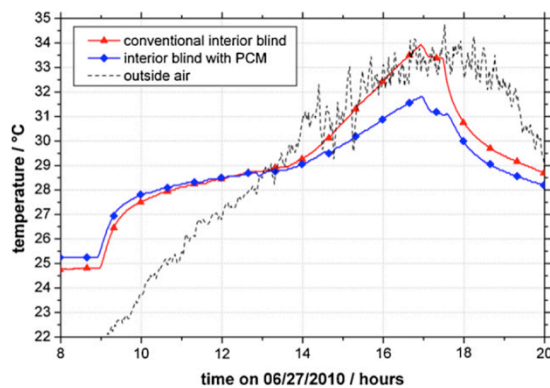


Figure 34 Comparison of the measured indoor temperatures [44]

To evaluate the system performance of the PCM energy releasing during the night, Weinlaeder, et al. [44] tested the office with the opened windows during the night and with a ventilation system that adds an additional air flow of  $300 \text{ [m}^3\cdot\text{h}^{-1}\text{]}$ . The measured temperatures on the blind surface of the reference system dropped  $14^\circ\text{C}$ , but the PCM blind surface remained up to  $26^\circ\text{C}$ . These results revealed that the PCM could not release the total stored energy during the night period, even with additional night ventilation.

Weinlaeder, et al. [44] concluded that the results measured in both regions for summer and winter periods revealed advantages of the PCMs slats use comparing with the typical window blind shading. The authors recommended to install the PCM blind combined with mechanical ventilation to improve the system performance. However, a disadvantage identified by the users of the offices with the PCM blind verified that the indoor natural illumination decreased. With their work, Weinlaeder, et al. [44] showed the great potential of the PCM to reduce the cooling loads and to increase the thermal comfort of the buildings indoor spaces.

Merker, et al. [173] presents a prototype that was developed within the project "Innovative PCM-Technology" funded by company Warema and ZA Bayer. In their study an internal blind with PCM (melting temperature of  $25^\circ\text{C}$ ) were used to absorb the solar radiation and to release the stored energy to the interior of the room. As the authors explain, the internal blinds without PCM cannot effectively prevent the excess internal solar loads from the incident solar radiation through the glazing. However, if external blinds are used there are two big disadvantages: *i)* they are more susceptible to external weather conditions, so the construction costs will be higher because more mechanical stability is needed; and *ii)* is more difficult to clean and maintain. During the day, the PCM stores large quantities of energy (from the solar incident radiation) that consequently delays the fast increase of temperature inside of the building. Otherwise, the stored heat by the PCM is released during the night period.

Figure 35 shows the developed prototype with the internal PCM blinds and the temperature values obtained.

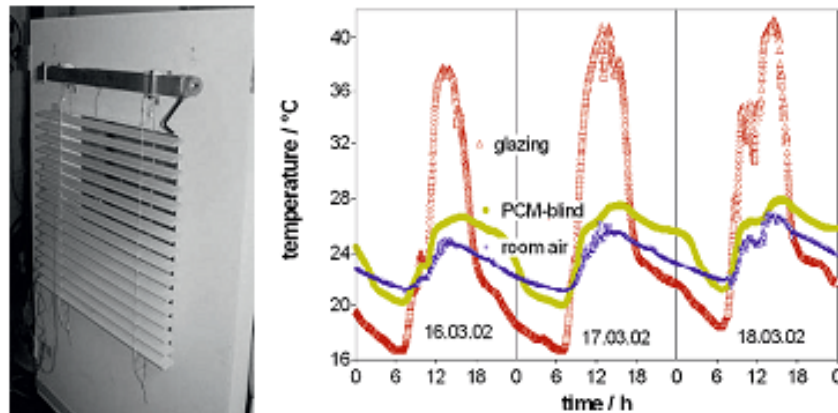


Figure 35 PCM blinds prototype and main results [173]

The main conclusion taken by the author, from the analysis of the results and of the further numerical studies carried out show:

- The PCM blind temperatures decreased 10°C and the time delay increased 3h;
- The indoor air temperature was 2°C lower;
- The numerical results show that the operative temperature of the room decreased 3°C and a time shift of the heat release from noon to the evening;
- Strongly improving of the thermal comfort through the working hours;

To conclude, in their study the authors present interesting thermal results by the PCM incorporation. The internal blinds are small size, so the PCM material is a great solution that improves the thermal behaviour of these solutions. To enhance the discharge during the night, [173] it is recommended to resort to a forced convection on the blinds.

#### 2.3.4 Trombe wall

Kara and Kurnuç [29] developed an experimental study of the performance of a PCM trombe wall with a novel triple glass (NTG) and a plasterboard containing PCMs. They built a test room in Erzurum, Turkey and tested the south-facing external wall during one year using the outdoor conditions to evaluate the performance of the solution. A NTG and PCM wall (plasterboard containing PCMs) composed the external wall solution. The PCM introduced in the plasterboard was the Rubitherm® GR41 and GR35, which is granulated encapsulated paraffin. The

NTG is composed by Prismsolar<sup>®</sup> glass that transmits the most of the sunlight in winter and reflects it in summer. Kara and Kurnuç [29] developed this study to improve the trombe wall system and overcome two main disadvantages of the conventional trombe wall: *i)* store solar energy using sensible heat, so a thicker or massive masonry wall is necessary and *ii)* the overheating during the summer when it is used with conventional glass. As shown in Figure 36 the trombe wall has an upper and lower air vent. Connected to the upper air vent is an air duct with a fan that is used to introduce the heat stored by the PCM wall into the test room.

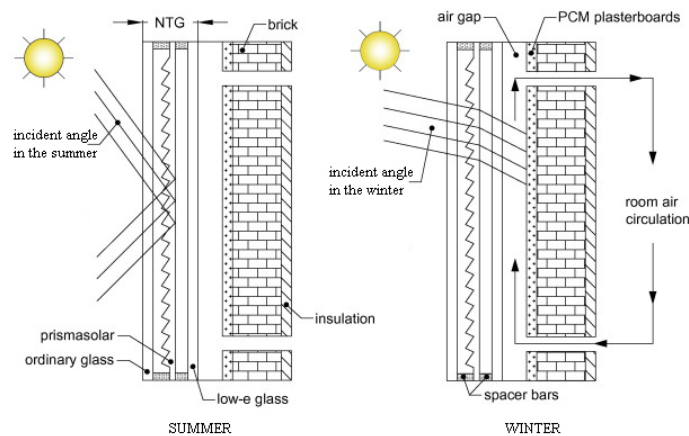


Figure 36 Cross section of the PCM wall scheme [adapted from [29]]

As explained, the melting temperature of the PCM is an important factor to be taken into account. The air temperature supplied from the PCM wall should be greater than 22°C and closer to 50°C, so they selected the GR35 and GR41, which has 13-41°C and 13-51°C melting temperature range and compared experimentally the thermal performance. Figure 37 shows the experimental test room configuration.

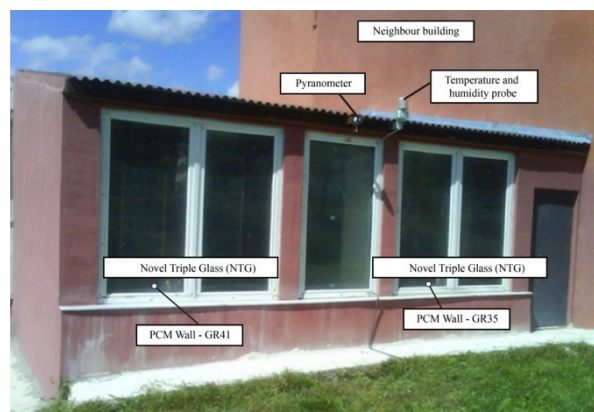


Figure 37 Test room scheme [adapted from [29]]



The internal temperature of the test room was set between 20°C and 23°C using an electrical heater with a digital thermostat. Both test rooms are instrumented with: air temperature sensors, heat flux meters (on the glass and wall), pyranometers, surface temperature probes, soil temperature sensors and anemometer. The digital controller activates the fans when the maximum melting temperature of the PCMs is reached. In case of GR41 the fan switches on when the surface temperature of the plasterboard is 45°C and for GR35 the fan switches on at 35°C.

Using the measured data, they determined the heat load and the ratio of solar energy gain (RSEG) of the test room using the following equations. The solar transmittance, g-value, was calculated with the use of eq. (2.7):

$$g(t) = \frac{I_t(t)}{I_i(t)} \quad (2.7)$$

Where  $I_i(t)$  is the solar radiation incident and  $I_t(t)$  is the solar radiation transmitted through the NTG. The air mass flow rate ( $\dot{m}_a$ ) between the air gap and the air duct to the interior of the room was calculated as shown in eq. (2.8).

$$\dot{m}_a = \rho_a v_m A_{c,d} \quad (2.8)$$

Using the air mass flow, ( $\dot{m}_a$ ), the solar heat gain,  $\dot{Q}(t)$  – heat rate extracted from the wall to the room – calculated according the eq. (2.9). The  $T_{a,uv}(t)$  and  $T_{a,lw}(t)$  represent the air temperature at the upper and lower vents respectively. The other parameters of these equations (eq. (2.8) and eq. (2.9)) represents:

$\rho$  - specific mass of the air

$v_m$  - mean velocity of the air duct

$A_{c,d}$  - Duct cross-section

$c_{p,a}$  - specific heat of the air

$$\dot{Q}(t) = \dot{m}_a c_{p,a} [T_{a,uv}(t) - T_{a,lw}(t)] \quad (2.9)$$

To determine the RSEG (eq. (2.16)), Kara and Kurnuç [29] determined first the daily solar energy incidence,  $E_{i,d}$  [J/day], and the daily solar energy gain – SEG,  $E_{g,d}$  [J/day], according to eq. (2.10) and eq. (2.11).

$$E_{i,d} = \int I_i(t) A_{s,NTG} dt \quad (2.10)$$

$$E_{g,d} = \int \dot{Q}_g(t) dt \quad (2.11)$$

Using these values, they calculated *i*) the daily total efficiency,  $\eta_{T,d}$  – eq. (2.12) *ii*) the SEG per month,  $E_{g,m}$  [J/month] – eq. (2.13) and *iii*) the solar energy incident per month,  $E_{i,m}$  [J/month] – eq. (2.14).

$$\eta_{o,d} = \frac{E_{g,d}}{E_{i,d}} \quad (2.12)$$

$$E_{g,m} = \sum_{i=1}^n E_{g,d} \quad (2.13)$$

$$E_{i,m} = \sum_{i=1}^n E_{i,d} \quad (2.14)$$

Where  $n$  represents the number of days for each month. The total solar heat gain,  $\sum E_{g,m}$  (eq. (2.15)) was calculated considering both PCMs walls.

$$\sum E_{g,m} = E_{g,m,GR41} + E_{g,m,GR35} \quad (2.15)$$

The heat load per month provided by the test room is represented by the denominator of eq. (2.16), where  $E_{h,m}$  represent the electricity consumption of the heaters per month.

$$RSEG = \frac{\sum E_{g,m}}{E_{h,m} + \sum E_{g,m}} \quad (2.16)$$

The ratio of solar energy gain represents the heat load fraction provided by both walls.

Kara and Kurnuç [29] analysed and presented some results for each day from October 2008 to October 2009.

The wall with GR35 PCM presents better total efficiency than GR41 PCM wall. From October to the end of February, the daily total efficiency of the GR35 PCM wall changed from 22% to 37% and for the same period the GR41 PCM wall between 20% and 33%. The air temperature of the upper vent in both PCM walls is similar.

The interior comfort temperature in the room, 22°C, is exceeded during the winter season (see Figure 38). The use of a regulation system of the air to the interior of the room is necessary. So, an adjustable air fan controlled according to

the PCM wall temperature can improve the room temperature because the stored energy can be introduced into the room more progressively. Another solution to avoid the overheating in the winter season is the use of gypsum boards with PCM in the range of 22°C to 24°C applied in the ceiling or cell envelope walls. As they explained, this possible solution with the fans control allows the PCM to collect the exceeding energy during the day and releases the stored energy during the night.

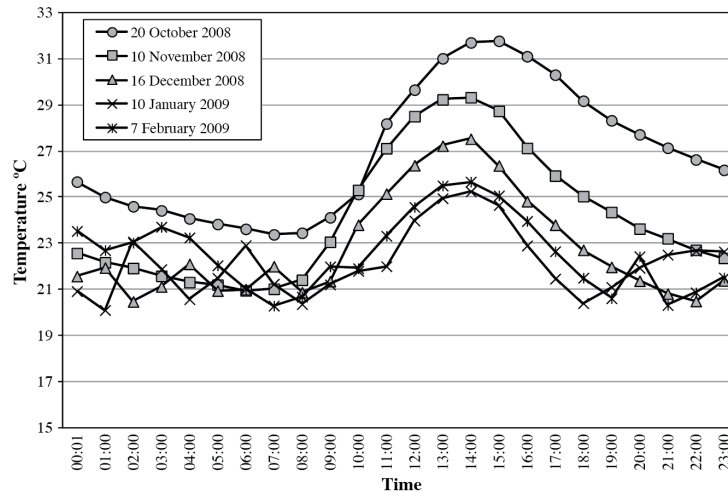


Figure 38 Interior temperature of the room for the selected days [29]

The daily and monthly results analysed show that the wall with the PCM GR35 has higher energy performance than PCM GR41 wall. The solar energy gain decreased to zero in April and May because the solar transmittance of the novel triple glass, as previously explained. The summary result, presented in Figure 39, shows the contribution of the PCM walls.

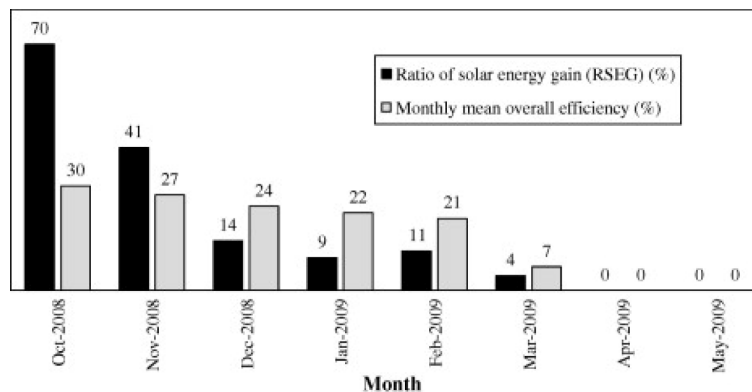


Figure 39 Ratio of solar energy gain and total efficiency during the heating season [29]

The results show that the heat load provided by the PCM wall in October and November was 70% and 41% respectively. The RSEG values decrease for the following months because the heat load requirements increased. Analysing the

results on an annual basis, the ratio of solar energy gains from the PCM wall provided 14% of the heat load demand.

Zalewski, et al. [174] presented experimental testing results of a composite trombe wall that incorporates phase change materials. For testing a small-scale trombe composite wall was built and submitted to real weather conditions. The energy performance of the testing wall was evaluated resorting to: *i)* the heat flux meters, *ii)* the temperature probes and *iii)* the enthalpy balance.

The experimental scheme and geometry of the tested wall is shown in Figure 40.

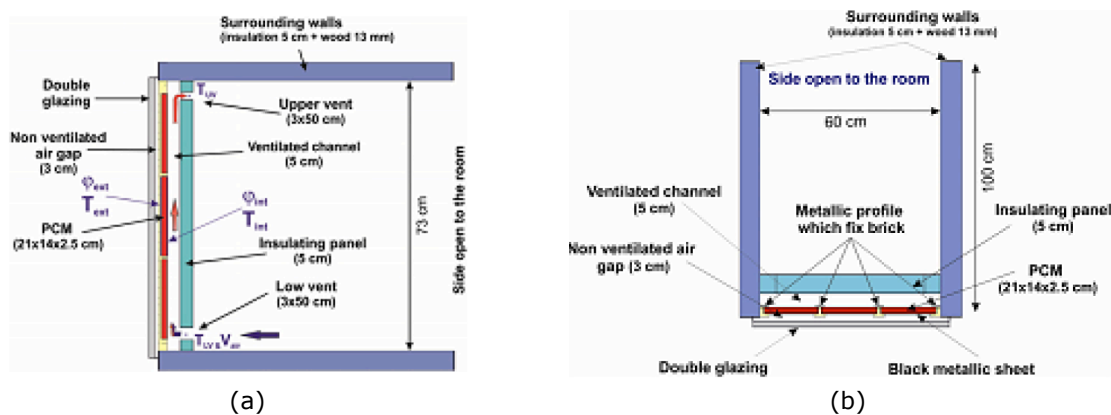


Figure 40 Trombe wall schematic: (a) vertical section; (b) horizontal section [174]

As shown in Figure 40, the surrounding walls are composed by insulation material (5cm) and wood (13cm). The window trombe wall is composed by three main layers: *i)* an external double glazing; *ii)* a PCM wall and; *iii)* an insulating panel. The air gap of 3cm between the first and second layer is non-ventilated. The air gap of 5cm between the PCM wall and the insulating panel is ventilated and has two openings of 5x50cm (lower and upper vent) to improve the energy transfer between the imposed conditions and the indoor room environment. The PCM storage wall has an energy exchange area of 60x73cm and is made of polyolefin macrocapsules of 21x14x2.5cm, as shown in Figure 41.



Figure 41 PCM macrocapsule [174]

The experimental campaign was carried out in northern France during two weeks of spring (April 22 to May 5 2008) using a pyranometer, thermocouples, flux meters and one anemometer.

The authors presented many outputs: heat fluxes, temperatures and time delay. The more relevant conclusions and results were:

- The temperature differences between the upper and the lower vents are significant, mainly when the solar heat flux increases, so the free convection is dominant since air velocities are lower than  $25\text{cm}\cdot\text{s}^{-1}$ ;
- Using a cross-correlation function the authors estimated the time delay of the absorbed flux and the transmitted flux. The authors state, the tested PCM wall of 2.5cm releases the stored energy after 2:40h which represents half of the time compared with a 15cm thick concrete wall studied by Zalewski, et al. [175];
- The PCM wall reached the maximum temperatures of 50 to 60°C and the maximum air temperature at the upper vent was 40°C;
- The results reveal the PCM effect releasing the stored heat after 2:00 am at a heat flux rate of  $25\text{W}\cdot\text{m}^{-2}$ ;
- After 24 days of experimental testing the total solar irradiance through the glazing was  $78\text{ kWh}\cdot\text{m}^{-2}$ . The PCM wall absorbed 49% of this incident solar energy ( $37.7\text{ kWh}\cdot\text{m}^{-2}$ ) and the energy release from the PCM wall was  $23.5\text{ kWh}\cdot\text{m}^{-2}$ , which means that 68% of the absorbed energy is recover.

### 2.3.5 Commercial based products

The company Gesimat has different switchable glass products using different techniques: electrochromic, electrothermic, electrotropic and thermochromic laminated glass. The first approach using electrochromic laminated glass used a small DC voltage to switch the light and heat transmittance of the glass (see Figure 42.a). The second glass is similar to the previous latter but changes the glass transparency using different colour temperature (Figure 42.b). The electrotropic laminated glass (Figure 42.c) allows the user to choose the glass transduced or mate, increasing the privacy and decreasing the heat flow in this glass. This glass has two switching choices, digital (manual typology) and gradual switching (automatic function). The thermochromic laminated glass (Figure 42.d) changes the light transmittance according to the temperature of the glass pane. Special substances that are strong coloured at high temperature and less coloured for small temperatures allow this feature [176].



Figure 42 Switching process using (a) thermochromic, (b) electrochromic (c) electrochromic and (d) thermochromic laminated glass

**Advantages:** Based on advanced technological and ergonomic solution. Adapts the glass properties according to the imposed conditions changing the light and heat transmittance properties. It can be introduced into existing buildings and is compatible with different windows frames.

**Disadvantages:** It still an expensive technology and an expensive product. A specific professional with knowledge in this field and technology is needed to install the glass.

The GlassX crystal is a triple insulation glazing unit that contains phase change materials. The GlassX is composed by three main layers, as shown in Figure 43 [177].

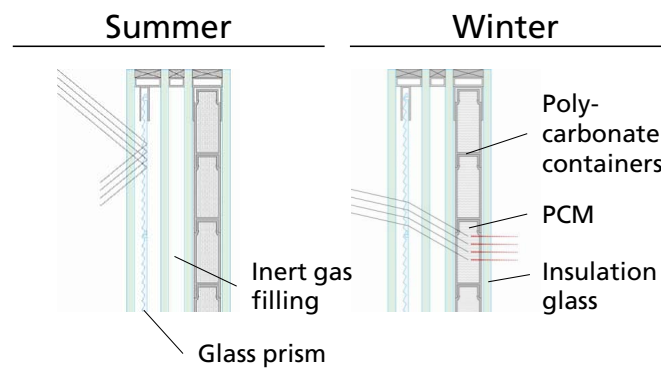


Figure 43 GlassX Schematic [177]

The first layer is the prismatic pane that reflects the solar radiation in the summer (when the temperature is above of 35°C) and transmits through this layer in the winter (when the temperature drops 35°C). The second layer is composed by inert gas that insulates this layer and improves the thermal behaviour through this boundary. The last and third layer is the polycarbonate containers with PCM. The PCM used in this system is a salt hydrate with melting temperature of 26°C to 30°C and a heat capacity of 1185Wh.m<sup>-2</sup>.

With this composition, the system presents an excellent thermal insulation – U-value of  $0.40 \text{ W.m}^{-2}.\text{k}^{-1}$ .

The GlassX integrates 3 main functionalities: transparent heat insulation, protection against overheating, can store and release energy through a passive method. The GlassX crystal details and composition can be seen in Table 6.

Table 6 GlassX crystal main technical data [177]

Glass 1	Tempered safety glass	
Air gap 1-2	Air gap with prim glass and inert gas	
Glass 2	Tempered safety glass with low-E	
Air gap 2-3	Air gap with inert gas	
Glass 3	Tempered safety glass with low-E	
Air gap 3-4	Gap with PCM containers	
Glass 4	Tempered safety glass with ceramic silkscreen printing	
Thickness	$7.9 \times 10^{-2} \text{ cm}$	
Max. Height	2.8m	
Max. width	1.5m	
Storage capacity	$1185 \text{ Wh.m}^{-2}$	
Storage temperature	26-30°C	

Besides the GlassX crystal base system there are also four similar systems based on the GlassX technology: the GlassX prism, the GlassX comfort, the GlassX comfort slim and the GlassX comfort store.

### 2.3.6 Window shutter

Soares, et al. [178] evaluated the potential of a PCM-shutter containing phase change materials. In their study, numerical studies were carried out to analyse the influence of the imposed external and internal conditions and the heat transfer coefficients of the system performance.

The PCM-shutter system is composed by five main layers, as shown in Figure 44.

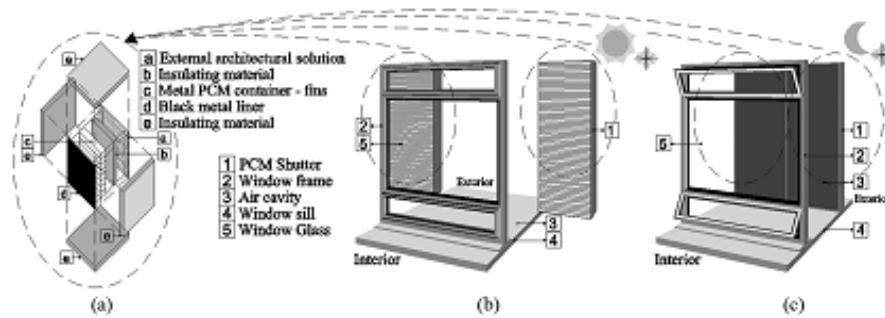


Figure 44 Schematic of the PCM-shutter [178]

The imposed external conditions were taken from the national climatic data of the SOLTERM<sup>®</sup> software. It was used the climatic data of Coimbra, Portugal – solar radiation and external air temperature – considering the hourly data taken from a monthly average during January. The external heat convection coefficient was considered equal to  $25 \text{ W.m}^{-2}.\text{K}^{-1}$ , the indoor temperature was considered constant and equal to  $18^\circ\text{C}$  and the indoor heat transfer coefficient was estimated using empirical correlations.

To simplify the numerical analysis the authors considered some premises and used a two dimensional physical 2D model, as can be seen in Figure 45.

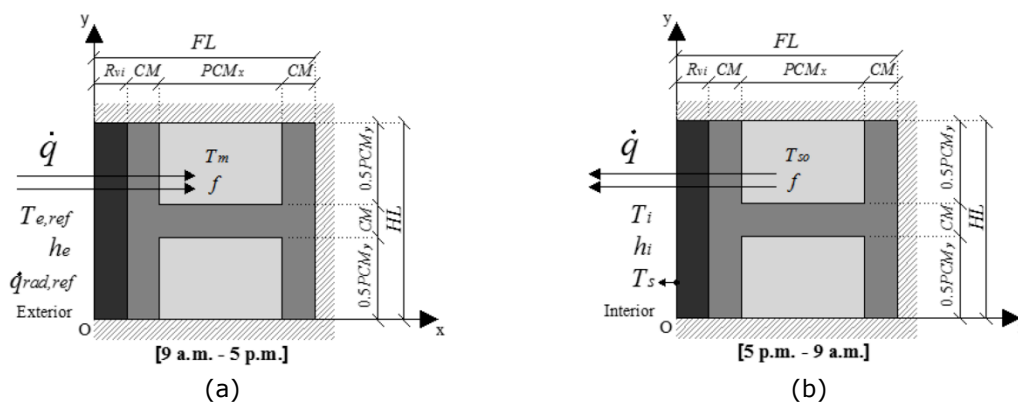


Figure 45 Physical model schematic for a) 9 a.m. to 5 p.m. and b) for 5p.m. to 9a.m. [178]

The PCM considered for this study was an organic paraffin (n-Octadecane  $\text{CH}_3(\text{CH}_2)_{16}\text{CH}_3$ ). The latent heat is  $243\text{kJ}.\text{kg}^{-1}$  and the thermal conductivity for the solid and liquid state is  $0.358$  and  $0.148\text{W}.\text{m}^{-1}.\text{K}^{-1}$ , respectively.

To simulate the phase change behaviour and to carry out the numerical simulations, Soares, et al. [178] used mathematical models and equation formulations proposed by many authors: [47, 179-185]. The results of the parametric analysis focused on two main fields that influence the system performance: the fins distance and the thermal properties (outdoor conditions, indoor conditions and PCM thermophysical properties). The authors compared a



numerical study of the total energy storage and release of the PCM system against other materials.

The results show that the outdoor air temperature and the solar radiation heat flux has a large influence over the melting process of the PCM. The indoor temperature and the heat transfer coefficient in the inner surface during the night is a relevant factor to the PCM solidification process. To improve the energy release of the PCM it becomes necessary to increase the internal heat transfer coefficient. The melting temperature of the PCM has a significant effect in the total energy storage and release of the system. The correct melting temperature for the used climatic conditions is 20°C and during a complete daily cycle can store and release 2501.3 kJ. Comparing the total storing and releasing energy of the system using different typical materials during a complete daily cycle, the PCM system stores and releases 2.5 times more compared with other materials, as presented in Figure 46.

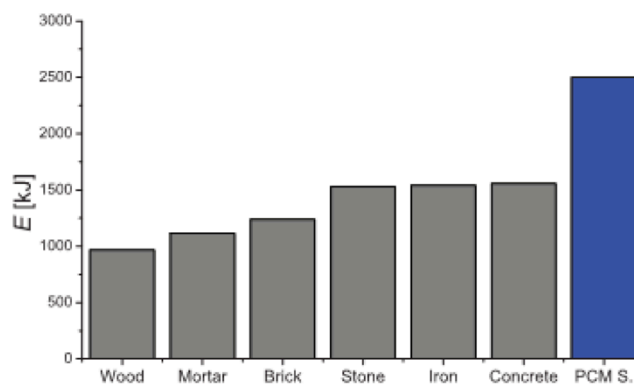


Figure 46 Total stored and released energy comparison during a complete daily cycle [178]

Alawadhi [45] evaluated the thermal analysis of a typical roller window shutter incorporating phase change materials. In his research, they replaced the foam fill in slats by three different PCMs and compared the results.

The configuration of the analysed blind system is presented in Figure 47 and is composed by three main layers (indoor to outdoor) with 1.5m height: glass, air cavity and PCM slats or foam slats. The outdoor layer surface was submitted to thermal conditions that simulate the weather conditions of Kuwait city during the hottest month (June). On the indoor layer surface were applied free floating conditions, which means that none condition was applied. The thickness of the air gap and glass is constant and equal to  $L_a=0.15\text{m}$  and  $L_g=0.005\text{m}$ . The thickness of the shutter layer,  $L_{sh}$ , with PCM ranges from 0.01m to 0.03m and with foam is 0.02m.

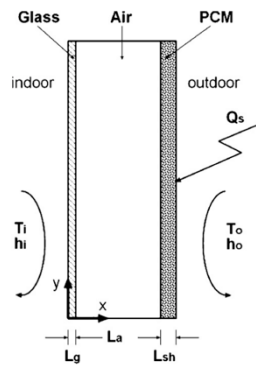


Figure 47 Roller window shutter system composition [45]

Considering the materials thermal properties and some assumptions, Alawadhi [45] developed the equations for the heat transfer in all domains and the equations for the equivalent specific heat of the PCM. Using the equations and the boundary conditions, the author defined the numerical model and analysed the roller window shutter. The numerical model was validated and verified according to the guide for the verification and validation of computational fluid dynamics simulations principles [186].

The first analysed model was the typical roller window shutter that is composed by the foam filled slats. The results show that operative temperature in the computational domains changes between 23.6°C and 61.4°C, so according to these temperatures the author selected three PCMs (organic paraffin) to be tested: n-Octadecane, n-Eicosane and P116. The melting temperature of these PCMs is 27°C, 37°C and 47°C, and the latent heat capacity is 243.5kJ.kg<sup>-1</sup>, 241kJ.kg<sup>-1</sup> and 225kJ.kg<sup>-1</sup>, respectively.

Alawadhi [45] presented the temperature contours and the heat flux profiles during different periods of a day, as well as the results of the optimized model with different P116 PCM thickness. For the first numerical models the thickness of the PCM/foam layer was the same and equal to 0.02m.

According to heat flux behaviour of the tested PCMs, Figure 48, shows the P116 PCM lower heat flux through the tested timeframe of 24 hours compared with the other PCMs. The n-Octadecane PCM presented the worst results, because as the author explains, the n-Octadecane melting temperature is closest to the minimum operative temperature, so the PCM melted completely at 9h and after this point the heat flux increased quickly. The P166 PCM has the best and progressive behaviour during the phase change allowing this model to present lower heat flux changes. However, this PCM has a high thermal conductivity, so while the phase change process does not occurs the PCM reacts faster (until 8h). The n-Eicosane PCM melted completely at about 11:30 and until this point the

PCM has a good thermal behaviour, but once again after this point the heat flux increased faster, similar to the n-Octadecane PCM. The foam window shutter system is the model that reacts faster to the imposed conditions during the working hours.

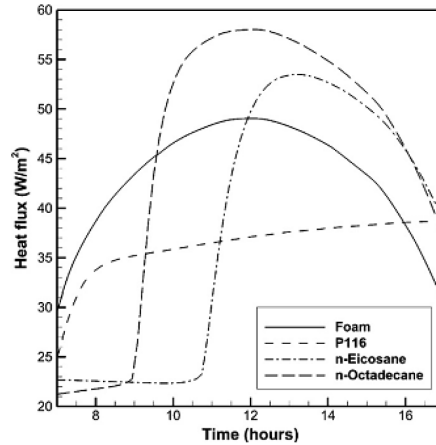


Figure 48 Comparison between the four models of the window shutter system [45]

In order to evaluate the advantage of the PCM the author used an equation to integrate the heat flux and obtained the net heat flux during the working hours. The net heat flux of the foam shutter system is  $43.25 \text{ [W.m}^{-2}\text{]}$ . The results show that the P116 PCM shutter system reduces 16.01% (to  $36.32 \text{ W.m}^{-2}$ ) and the n-Eicosane 12.13% (to  $38.01 \text{ W.m}^{-2}$ ). Therefore, the net heat flux of the n-Octadecane is 4.98% higher (to  $45.41 \text{ W.m}^{-2}$ ) than the reference foam shutter.

Analysing the heat flux and the net heat flux on the indoor surfaces, the optimal quantity of P166 PCM was investigated. For this, the author used four different thickness of the PCM layer: 0.01m, 0.015m, 0.02m and 0.03m. The results show that the layer with 0.03m decreases the net heat flux on the indoor surface 23.29% compared with the foam shutter system. The result of the heat flux during the working hours, presented in Figure 49, shows the significant influence of the PCM quantity.

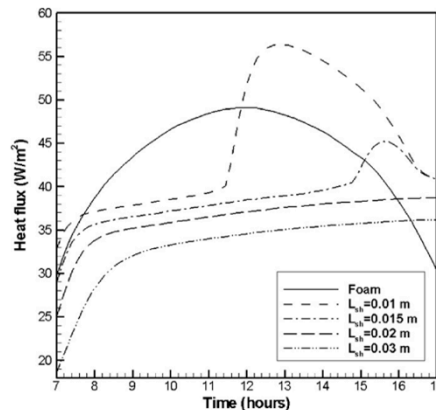


Figure 49 Heat flux for different PCM layer thickness [45]

The presented research work shows the potential benefits of the PCM incorporation in building solutions mainly focused on glazed areas. Using the accumulated knowledge, the main constraints and limitations of the various solutions were essential for the prototype development.

# CHAPTER 3

## 3 Prototype definitions and development

The following section explains and defines the window shutter functionality and composition. The geometry, shape details and used materials for the experimental testing are described in detail.

---



### 3.1 Materials

The main characteristics of the materials that compose the window shutter and the test cell are fully-described in the next sub-sections.

#### 3.1.1 PCM RT28HC®

The PCM was selected according to the weather conditions that it would be submitted to, namely the solar radiation, the thermal amplitude and the temperature peaks of the Aveiro region. The selected PCM was the RT28HC® provided by Rubitherm® GmbH.

The dynamic viscosity is one of the needed input parameters of the materials definitions in the numerical model. To calculate the dynamic viscosity,  $\mu$ , (eq. (3.1)) it was used the PCM kinematic viscosity,  $\nu$ , and the density in liquid phase,  $\rho_l$ , given by the PCM manufacturer datasheet.

$$\nu = \frac{\mu}{\rho} \Leftrightarrow \mu = \nu \cdot \rho \quad (3.1)$$

According to the previous information, the dynamic viscosity at 50°C is 19.8 [kg.m<sup>-1</sup>.s<sup>-1</sup>].

Other main physical and thermal properties of the PCM were given by the supplier and are presented in Table 7.

Table 7 Physical and thermal properties of PCM RT28HC®

$T_f$	Melting/solidification range	[°C]	27 – 29
$L_f$	Latent heat storage capacity $\pm 7,5\%$	[kJ.kg <sup>-1</sup> ]	245
$C_p$	Specific heat capacity	[kJ.kg <sup>-1</sup> .K <sup>-1</sup> ]	2
$\rho_s$	Mass density solid phase	[kg.m <sup>-3</sup> ]	880
$\rho_l$	Mass density liquid phase	[kg.m <sup>-3</sup> ]	770
$\lambda$	Thermal conductivity	[W.m <sup>-1</sup> .K <sup>-1</sup> ]	0.2
$\Delta V$	Volume expansion	[%]	12.5
$T_{fp}$	PCM Flash Point	[°C]	165
$\nu$	Kinematic viscosity at 50°C	[m <sup>2</sup> .s <sup>-1</sup> ]	25.71x10 <sup>-6</sup>

The paraffin PCM RT28HC® belongs to the organic group of PCMs and presents as advantages their compatibility with other typical construction materials and the fact that they are not corrosive. This PCM is chemically inert and does not suffer any supercooling effect. The thermal behaviour of the heat storage and release process is done at a nearly constant temperature and is stable throughout long

and repetitive cycles (good life cycle assessment). Other important chemical property is the chain length of the PCM structure that improves the thermal behaviour and the heat capacity of the PCM. As main disadvantages this type of PCMs presents higher volume expansion (up to 12.5%) and lower thermal conductivity ( $0.2 \text{ W}\cdot\text{m}^{-2}\cdot\text{k}^{-1}$ ).

The thermal behaviour and the total heat capacity of the PCM was verified experimentally with a Differential Scanning Calorimeter (DSC) – Perkin® Elmer 4000 (Figure 50).



Figure 50 Differential Scanning Calorimeter (DSC) – Perkin® Elmer 4000

For the DSC experiment two PCM samples were used – with 6.5mg and 7.8mg – and four testing procedures were defined according the follow procedure:

- Test 1: Hold the PCM sample (6.5mg) 30min at  $10^{\circ}\text{C}$ , heat from  $10^{\circ}\text{C}$  to  $40^{\circ}\text{C}$  at  $0.5^{\circ}\text{C}\cdot\text{min}^{-1}$ , hold for 30min at  $40^{\circ}\text{C}$  and reverse process;
- Test 2: Hold the PCM sample (6.5mg) 30min at  $10^{\circ}\text{C}$ , heat from  $10^{\circ}\text{C}$  to  $40^{\circ}\text{C}$  at  $5^{\circ}\text{C}\cdot\text{min}^{-1}$ , hold for 30min at  $40^{\circ}\text{C}$  and reverse process;
- Test 3: Heat the PCM sample (7.8mg) from  $10^{\circ}\text{C}$  to  $40^{\circ}\text{C}$  at  $5^{\circ}\text{C}\cdot\text{min}^{-1}$  and reverse process;
- Test 4: Heat the PCM sample (6.5mg) from  $10^{\circ}\text{C}$  to  $50^{\circ}\text{C}$  at  $0.5^{\circ}\text{C}\cdot\text{min}^{-1}$  and reverse process.

All samples were tested during four complete cycles melting/solidification and the main results obtained are present in Table 8.



Table 8 DSC results for the different imposed conditions;

Test	Storage Energy – Heating			Release Energy – Cooling			Expected $\Delta H$ [kJ.kg <sup>-1</sup> ] $\pm$ 7.5%
	T <sub>onset</sub> [°C]	T of max Heat Flow [C]	$\Delta H$ [kJ.kg <sup>-1</sup> ]	T <sub>onset</sub> [°C]	T of max Heat Flow [C]	$\Delta H$ [kJ.kg <sup>-1</sup> ]	
1	28.19	29.39	229.80	26.85	27.07	216.68	245
2	28.41	32.38	227.18	25.59	24.67	229.27	
3	28.14	32.31	230.44	25.75	24.29	238.10	
4	28.26	29.22	267.17	25.99	26.19	266.13	

The heat capacity of the PCM given by the supplier has good accuracy comparing with the experimental testing data. However, has others authors refers, i.e. Mehling and Cabeza [15], smaller PCM samples and heating rates should be taken to minimize the error between the measured heat capacity and the real heat capacity.

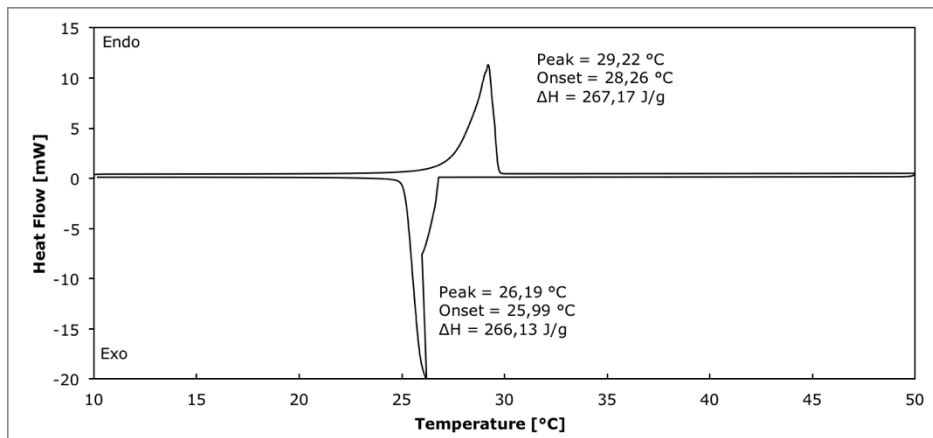


Figure 51 DSC results of test #4

### 3.1.2 Aluminium hollowed blades filled with PCM

The material selected for the window blades is the aluminium because it is one of the most typical materials used in window shutter solutions (in Portugal), as is easy to shape and is lighter than steel. Another relevant factor is the high thermal conductivity of the aluminium that allows the system to react faster under the imposed conditions. Considering these features, the PCM can store and release energy faster during the charging and discharging process. The main thermal and physical properties of the aluminium hollow blades are presented in Table 9.

Table 9 Thermal and physical properties of the aluminium macrocapsules

$C_p$	Specific heat capacity	[kJ.kg <sup>-1</sup> .K <sup>-1</sup> ]	0.91
$\rho_s$	Mass density	[kg.m <sup>-3</sup> ]	2700
$\lambda$	Thermal conductivity	[W.m <sup>-1</sup> .K <sup>-1</sup> ]	230

The interior of the aluminium blades was filled with PCM, as shown in Figure 52. The waterproofness and air tightness of the blades filled with PCM was a challenge and were tested individually for different sealing solutions.

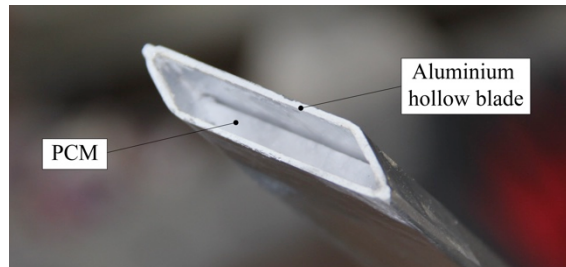


Figure 52 Window blade filled with PCM

The blade sealing needs to fulfil three main technical features: *i)* mechanical resistance – the rotation system is linked to the end of each blade; *ii)* airtightness and water seal – the PCM leakage must be avoided; and *iii)* thermal resistance (up to 70°C) – the window blades with PCM will be submitted to high temperatures and direct solar radiation. Many experiments were done to guarantee the mentioned features using different sealing solutions, such as the use of liquid metal, mounting glue, high temperature resistant epoxy glue, polyurethane glue and high temperature resistant silicon/glue (i.e. see Figure 53).



Figure 53 Some solutions to seal the PCM macrocapsules

In order to optimize the macrocapsule seal and joint, the macrocapsule plug was adapted with an aluminium cap profile (see Figure 54.a) to assure more seal material in this zone. The ends of the blades were hermetically sealed using the aluminium cap glued with silicon and epoxy that support high temperatures. The volume expansion of the PCM is 12.5% higher in the liquid state than in the solid state, so the introduction of the PCM into the window blade was done using the PCM melted and using controlled external conditions (constant temperature of 30°C). The silicon guarantees the PCM airtightness (applied in the internal cut profile) and seal (when in the liquid state) because the selected silicon can resist a

temperatures that range of -50 to 250°C and the chosen epoxy glue gives mechanical resistance that can resist compressive loading up to 300kg.cm<sup>-2</sup> (applied on external surface, Figure 54.b).



Figure 54 (a) Aluminium blade end cap; (b) Window blade with epoxy on the external surface

### 3.1.3 Thermal insulation material

The thermal insulation material applied on both window shutters (reference and with PCM) was extruded polystyrene (XPS). The thermal and physical properties of the insulation material from the ITE50 database [187] are presented in Table 10.

Table 10 Thermal and physical properties of the insulation material [187]

$C_p$	Specific heat capacity	[kJ.kg <sup>-1</sup> .K <sup>-1</sup> ]	1.17
$\rho_s$	Mass density	[kg.m <sup>-3</sup> ]	32
$\lambda$	Thermal conductivity	[W.m <sup>-1</sup> .K <sup>-1</sup> ]	0.037

The application of the thermal insulation material to the windows shutter blades was done using two approaches. Firstly, the insulation layer was applied at the window shutter and after that was cut each by each blade (Figure 55). In this case, the insulation material was fixed to the blades using a double adhesive tape.



Figure 55 Application of the thermal insulation material at the window shutter

However, after some experimental tests, the insulation material fixed with double adhesive tape unstuck from the aluminium blades. The second approach to

apply the insulation material on the window blades, it was cutting the insulation material before and gluing on the windows shutter blades using contact glue. In this case, the application of the insulation material on the window blades needs to be done blade by blade.

The application of the insulation material resorting to this technique did not present any problems later during the experimental testing.

### 3.1.4 Test cell material properties

There are two materials defined and created as a fluid – air and PCM – and six other as solid – aluminium, glass, glass-fibre, polyurethane foam (PU), phenolic and XPS. The properties of each material that composes the test cell and was used for the numerical models are presented in Table 11 – glass, glass-fibre and polyurethane foam (PU) (except the aluminium, PCM and XPS materials that were defined before).

Table 11 Material properties introduced in the numerical model definitions

	Property	Units	Glass	PU Foam	Glass-fibre	Phenolic
$C_p$	Specific heat capacity	[J.kg <sup>-1</sup> .K <sup>-1</sup> ]	830	1045	1045	1000
$\rho_s$	Mass density	[kg.m <sup>-3</sup> ]	2200	40	15	1300
$\lambda$	Thermal conductivity	[W.m <sup>-1</sup> .K <sup>-1</sup> ]	1.4	0.037	0.045	0.3

## 3.2 System description

The main structure of the window shutter is made of aluminium and four similar window shutters were built. The blades of two of the window shutters were filled with PCM ("PCM compartment" – compartment with the PCM window shutter) and the others two were left empty ("Reference compartment" – compartment with the reference window shutter).

The window shutter is composed by insulation material (XPS), aluminium blades filled with PCM (or empty) and two main aluminium structures (one of each side) that supports the rotation system and all components. However, the first experimental test carried out during the summer period presented the window shutter configuration without the insulation material.

### 3.2.1 Dimensions, external characteristics and schematic constitution

Each window shutter has 2.22m of height and 1.71m of width and is composed by 50 aluminium blades, as shown in Figure 56.

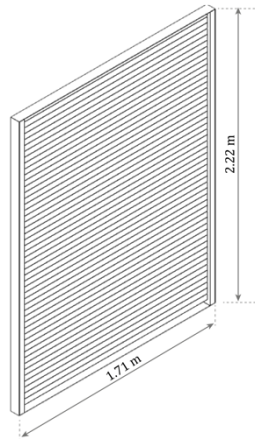


Figure 56 Window shutter external dimensions

The total area of the four window shutters is similar to the total area of the front glazing unit. It is intended to cover overall glazing area to protect the indoor space against the external conditions (mainly from the direct solar radiation).

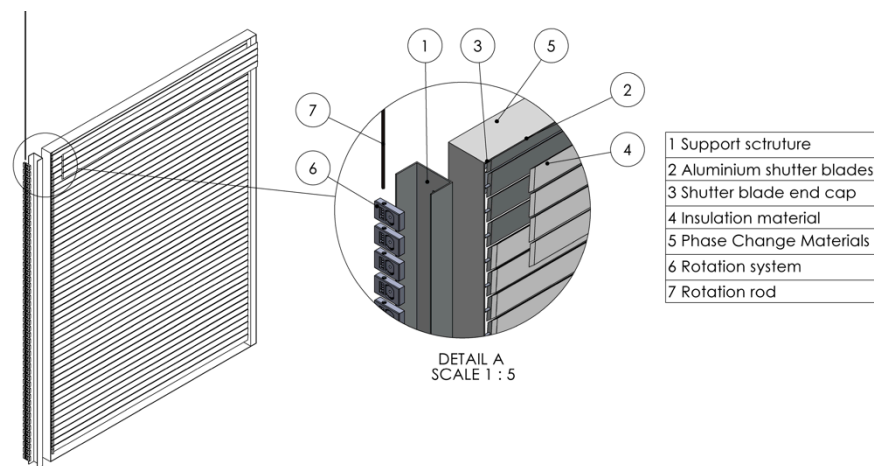


Figure 57 Window shutter scheme

Seven main parts compose the window shutter, as shown in Figure 57:

- Support structure (2x) – Each side of the window shutter (right and left) has a vertical support structure where all components are fixed. One of them has installed internally the rotation system of the windows shutter blades;
- Aluminium shutter blades (50x) – Fifty window blades compose the window shutter. Each of them is filled with PCM (for one compartment and are empty for the other) and on window blade surface the insulation material is applied. Each window blade has two end caps (one of each side) that isolate hermetic the PCM inside of the blade;

- Shutter blade end cap (100x) – The end cap is made of aluminium and is fixed at the end of the window blade using epoxy glue and silicon. This component is extremely important to guarantee no PCM leakage. Besides the hermetic functionality this component needs to be mechanically resistant because it has the rotation axis that will be fixed on the support structure;
- Insulation material (50x) – Each shutter blade has fixed insulation material (1cm of thickness) on the external surface oriented to the internal compartment (considering the window shutter at a closed position). The insulation material will enhance the thermal performance, mainly when the PCM is totally melted;
- Phase change material (50x) – Each shutter blade was filled with PCM RT18HC<sup>®</sup>. The total volume of PCM in each blade is approx. 330ml (290g of PCM);
- Rotation system (50x) – The support structures supports the rotation system with the rotation rod. The window blade is connected to the rotation system that allows the window blade to rotate close to 180°;
- Rotation rod (1x) – The rotation rod cross all rotation system to synchronize the window blades rotation.

#### 3.2.2 PCM aluminium blade filling

At the liquid state the PCM uses 12% more volume than the solid state. Considering this property, the introduction of PCM into the shutter blade was done with the PCM in liquid state. In addition, each shutter blade was previously heated to keep the temperature of the aluminium blades higher than the fusion temperature of the PCM preventing the PCM solidification during the filling process. Figure 58.a and Figure 58.b show the PCM filling process and the final aspect of the PCM in the aluminium shutter blade.

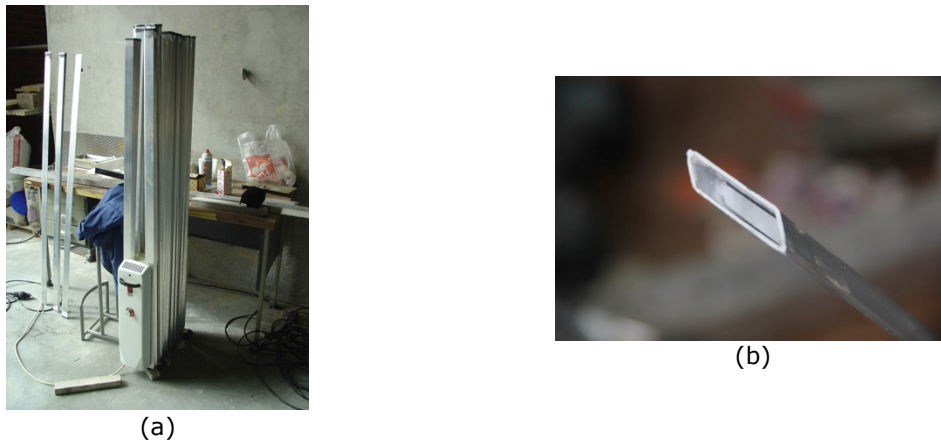


Figure 58 (a) Shutter blades heating to the PCM filling; (b) Shutter blade filled with PCM

To introduce the liquid PCM into the aluminium blade it was used a flexible hose with a stopcock. Besides the visual confirmation of the PCM filling, at the end of the filling process each window blade was weighed and the values recorded to confirm the PCM quantity inserted in each blade. The total weight of each blade with PCM is 840g, where 550g represent the mass of the blade and 290g is the mass of PCM inside of each window blade.

### 3.2.3 System rotation

At each shutter blade (one side) is connected the window rotation system. Figure 59.b shows the parts of the blades rotation scheme. To synchronize the rotation of the blades it was used a rod that crosses all rotation devices. The lock pin fixes each blade to the rotation system. The rotation gear was adapted to allow the window blade to rotate 0 to 180°.

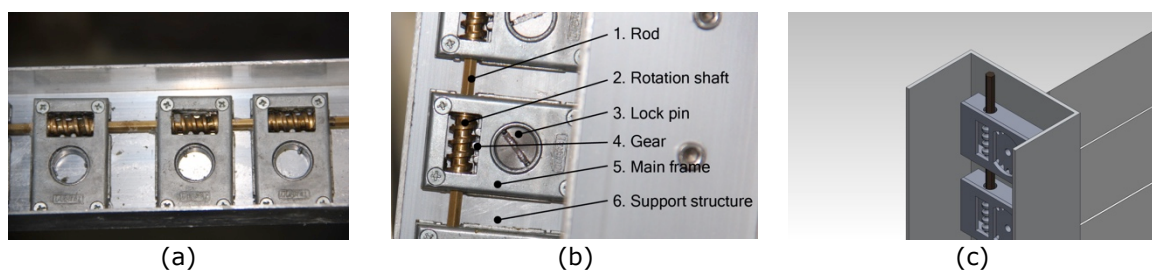


Figure 59 Window shutter system rotation (a) rotation system; (b) rotation parts and (c) modelled picture

Most parts of the rotation system are made of aluminium, however the rod and the rotation shaft that transfer the movement from the rod to the rotation main part, are made of copper alloy. All parts of the rotation system are mounted inside of the main frame and each main frame is fixed on the support structure.

### 3.3 Work functionalities – Window shutter configurations

To improve the system functionality and the thermal behaviour of the compartments the window blades rotate 0 to 180°. According the weather conditions, three main positions can be used: closed (Figure 60), opened (Figure 61) and intermediate (Figure 62).

The following sub-sections explain the work functionality of each position.

- Closed position

For the compartment with the PCM shutter, during the day, the PCM inside of the blades is storing energy, in the latent form, due to the direct solar radiation (see Figure 60). During this period, the insulation material behind the window blades minimizes the internal gains in the interior of the compartment, mainly when the phase change material is completely melted (charged).

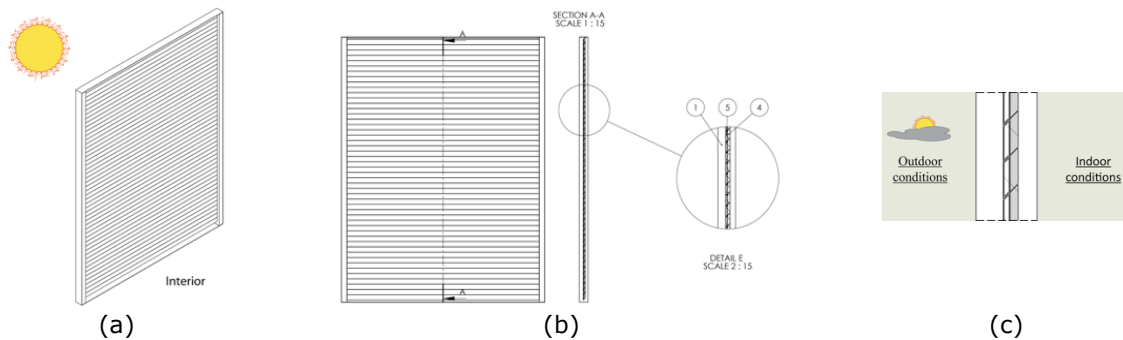


Figure 60 Window shutter closed position (energy storage) (a) Overall scheme; (b) Detailed position; (c) Window shutter position during daytime

- Opened position

During the night period, represented in the Figure 61, the phase change material discharges the stored energy into the interior of the compartment. During this period, the insulation material improves the heat flux direction from the exterior to the interior of the compartment, minimizing the thermal losses to the exterior.

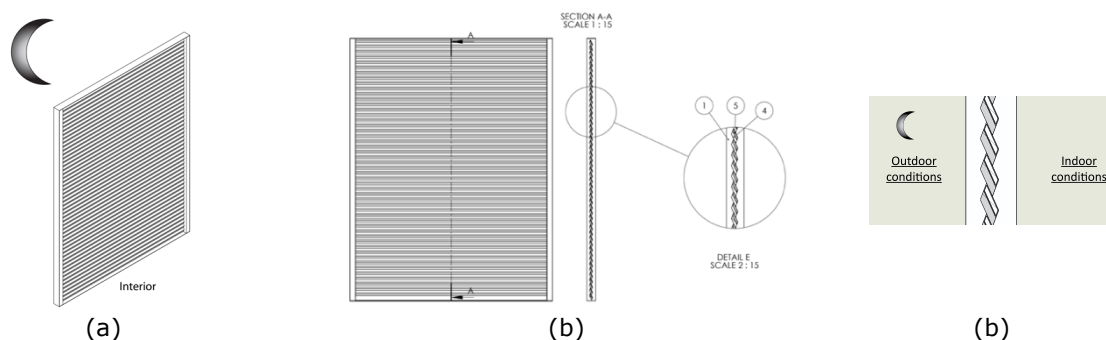


Figure 61 Window shutter opened position (a) Overall scheme; (b) Detail position; (c) Window shutter position during the night period



- Intermediate position

When the natural light is needed for the indoor spaces, the intermediate position is more adequate (Figure 62). In this position, the PCM stores energy without compromising the indoor visibility. However, under some conditions (according to the sun position and intensity) the PCM cannot store so much energy as in the closed position – the PCM does not melted completely.

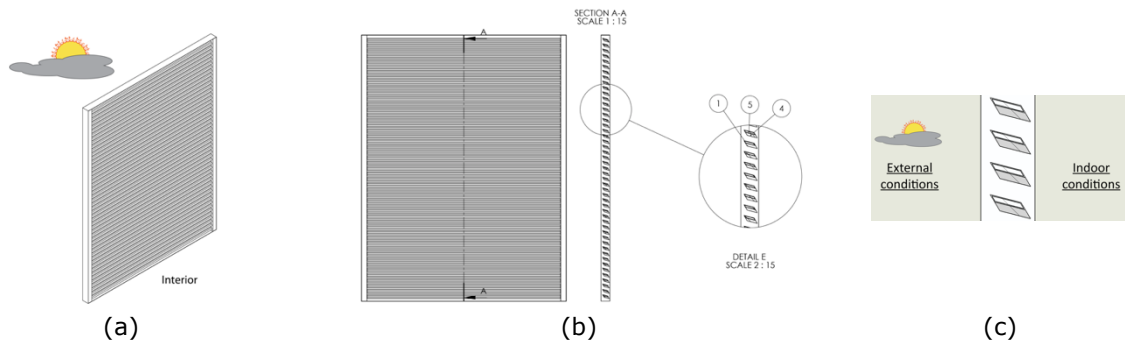


Figure 62 Window shutter intermediate position (a) Overall scheme; (b) Detail position; (c) Window shutter position during the night or day period

In theory, using the intermediate position on a cloudy day the indoor temperature does not increase as much compared with the indoor temperature in a closed position situation. However, during a sunny day, part of the solar energy is absorbed by the PCM, but other quantity is reflected from the windows shutter blades to the indoor space that increases the indoor temperature.

- Summer and winter operating conditions

The position of the window shutter that should be used can be divided into two main groups: for the winter season or heating period and for the summer or cooling period.

For the winter season (heating needs) to improve the energy efficiency the window shutter should be in the next positions:

- During a cloudy day the adequate window shutter position is the intermediate position. This position allows the PCM to store energy without compromising the indoor natural light. According to the external weather conditions on these days, the PCM can store more or less energy, depending on the incident radiation and the external temperature.
- During the night the window shutter is at the opened position. At this position, the window shutter releases the stored energy to the indoor space, minimizing the heating needs of the night period.

For the summer season (cooling needs) the best practice of the window shutter positions are:

- During the day – warm period – the window shutter is at the closed position or in alternative at the intermediate position. In these positions the PCM can store energy during the day.
- During the night, considering that the external temperature does not drop significantly, the position of the window shutter to be more efficient is the closed position. This position helps the PCM to release the stored energy faster to the external environment, allowing the shutter to be ready to fully charge energy during the next day cycle.

### 3.4 Development of a new window shutter typology

A window shutter system was developed and registered using a patent form - PCM Smart Window Protection System (Patent REF: PT 107310). The developed window shutter optimizes the thermal energy transfer between the indoor spaces of the building and the outdoor climate, increasing the thermal comfort of their occupants and consequently enhancing the energy efficiency of the building, by lowering the use of heating and cooling systems. Comparatively to the typical windows systems, the developed window shutter system has the advantage of assuring good thermal performance for any region, by their adaptive features. The system is composed by phase change materials, insulation material, glass and function components. The developed geometry and shape (external and internal) allowing the system to store and release more energy than any other conventional systems. The developed solution can be applied into existing and new buildings.

It is the scope of this development to pursue for partners and enterprises that have a core business in high-energy efficiency window solutions and shading devices.

The developed innovation contributes to increase the energy efficiency of window shutter protection systems resorting to phase change materials that are applied strategically into the window shutter. This is a dynamic and responsive system based on passive solar energy that stores and release energy according to the outdoor weather conditions (temperature and solar radiation) for all seasons.

The full public description of the developed PCM Smart Window Protection System can be found in: <http://goo.gl/AKw4ON> or <https://www.marcasepatentes.pt> (searching by patent number 107310) [188].

# CHAPTER 4

## 4 Experimental apparatus

This section presents detailed information on the experimental testing campaign. Test cell geometry, location and the shading inside of the test cell is described. The monitoring data apparatus, main experimental constraints and limitations are discussed.

The measured data from the experimental campaign is presented and discussed: outdoor weather and boundary conditions, indoor temperatures of the compartments and the heat flux between them.

---



#### 4.1 Test cell composition

The outdoor test cell (Figure 63) used in this experiment was built by COMOD Portuguese Company (model CLIP 05) and the external dimensions of the test cell are 7.00x2.35x2.58m (length x width x height). The internal floor area is 5.17m<sup>2</sup> and the main cell structure was built using galvanized steel profiles of 2mm thickness. The floor, besides the steel structure that supports 250kg.m<sup>-2</sup> maximum load, is composed by 18mm of insulation material with vinyl finish (*"Phenolic Frame"*). The test cell external envelope in contact with the external conditions is composed by 4cm of sandwich panels (insulation material – polyurethane foam) and the roof is composed by sandwich panels with glass fibre and water vapour protection layer (total of 8cm). The cell is divided into two internal compartments (with the same dimensions) with an internal partition wall constituted by a sandwich panel, also with 4cm of insulation material. It was applied additionally 4cm of XPS insulation material on each side of the partition wall to improve the thermal insulation between compartments and to decrease the energy transfer. Ventilation plays an important role that influences the indoor thermal performance, so to guarantee that the test cell boundary conditions are equivalent, a blower door test was carried out in both compartments to calculate the infiltration rate (the obtained values were similar, 0.8h<sup>-1</sup>).



Figure 63 Window shutter applied in outdoor test cell and external dimensions

Figure 63 shows the front facade that is composed by four double glazing windows panes with a dimension of 1.8x2.28m. Each windowpane is composed by two 5mm glass panes with an air gap of 12mm between them (5x12x5mm, layer 1-3, Figure 64). The window shutter system is located behind the double glazing

layer. The details of the composition of the system are presented in Figure 64 where it could be seen the window shutter position and the composition of the overall system.

The structure (layer 4) and the blades (layer 5) of the window shutter are aluminium and the window shutter was fixed behind the double glazing. The window blades were filled with phase change material (RT28HC<sup>®</sup>, layer 6) and the insulation material was added on the blade surface (layer 7). Each window shutter module can rotate the blades individually and synchronized.

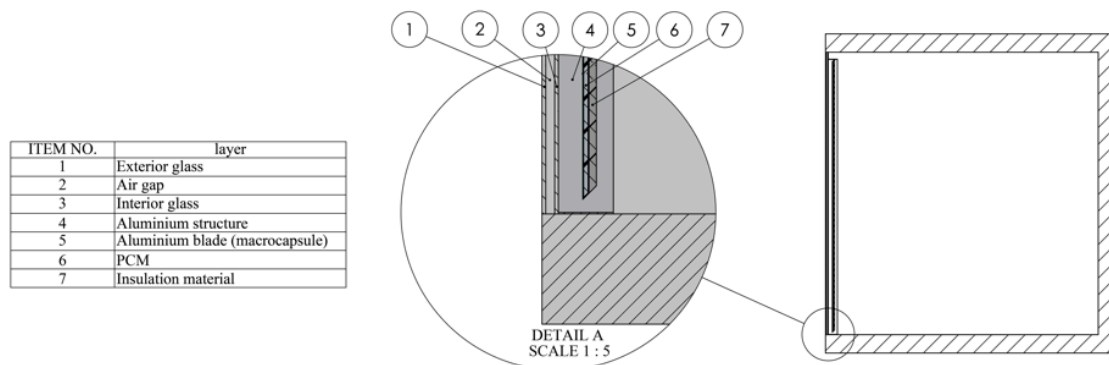


Figure 64 Test cell composition

The geometry and the imposed conditions of both internal compartments are very similar; the difference between them is the composition of the shutter blades: *i*) the reference compartment has an internal window shutter composed with aluminium hollowed blades; *ii*) the PCM compartment has a window shutter composed by the same hollowed blades with paraffin PCM RT28HC<sup>®</sup>.

#### 4.2 Location and orientation

The test cell is located at the University of Aveiro, in Aveiro – Portugal (Figure 65) and the translucent facade is oriented to the south. It was chosen this orientation since large glazed areas oriented to south are challenging in terms of discomfort, leading to asymmetry of the indoor thermal conditions in winter and overheating in summer.



Figure 65 Test cell location and orientation

The test cell is isolated, so it does not have any neighbouring building that could create shadows or other effects that can compromise the similar imposed external conditions of both compartments.

### 4.3 Test cell shading

The test cell shading was analysed resorting to the open source software Google SketchUp. Considering clear sky conditions, during almost the whole period of the day the test cell is submitted to direct solar radiation (as shown in Table 12).

Table 12 Test cell shading for three different daytime for all seasons

Time\Season	Spring (20th March)	Summer (21st June)	Autumn (22nd September)	Winter (21st December)
09h				
13h				
17h				

Both compartments are submitted to similar conditions. The difference between them is at the beginning and at the end of the day, because of the sunrise from the east side (side of the compartment with the PCM shutter) and the sunset is on the side of the reference compartment.



#### 4.4 Measurement and monitoring data

The test compartments were monitored and the following parameters were measured: temperatures, relative humidity, solar radiation and wind velocity. These parameters were collected using two Hukseflux type HFP01 sensors, twelve PT100 probes, one anemometer, two Jumo Hygrometer, one DeltaOHM pyranometer LP03 series and one DeltaOHM HD9007-A1 relative humidity (R.H.) and temperature sensor. The measured data was collected using two ICP I-7015P input modules and two I-7561 modules to transfer data via USB.

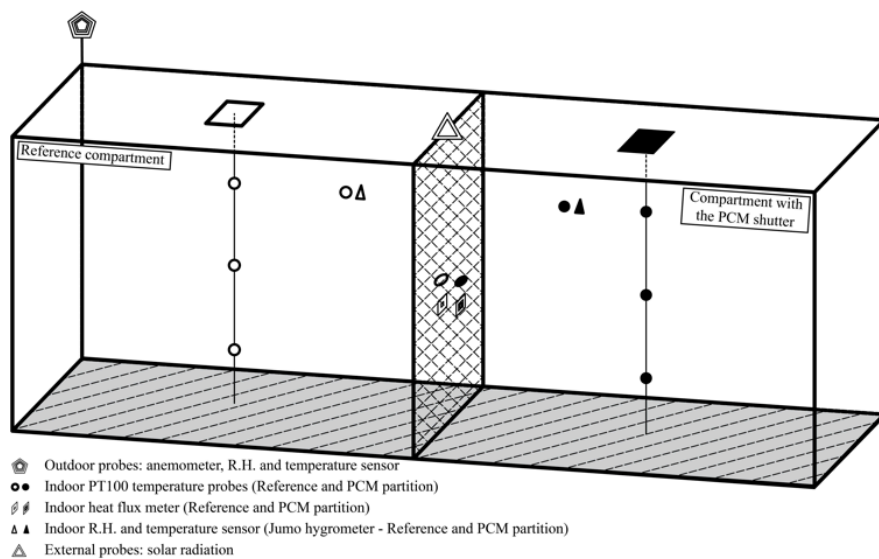


Figure 66 Diagram of the chamber showing the probes and sensors positions and quantities

Figure 66 presents the sensors position and quantities in each compartment. Five PT100 probes, one heat flux meter and one Jumo hygrometer was placed in the interior of each compartment. Above the roof of the test compartments was installed the pyranometer, the anemometer, the hygrometer and the temperature probes.

The sensors were calibrated and the accuracy of each type of sensor is as follows: temperature ( $\pm 0.01^\circ\text{C}$ ), solar radiation ( $\pm 0.1\text{W}\cdot\text{m}^{-2}$ ), relative humidity ( $\pm 0.1\%$ ), heat flux ( $\pm 0.1\text{W}\cdot\text{m}^{-2}$ ) and wind velocity ( $\pm 0.1\text{m}\cdot\text{s}^{-1}$ ).

The modules of the ICP data loggers are connected to the computer and all measured data was continuously saved each 5 minutes.



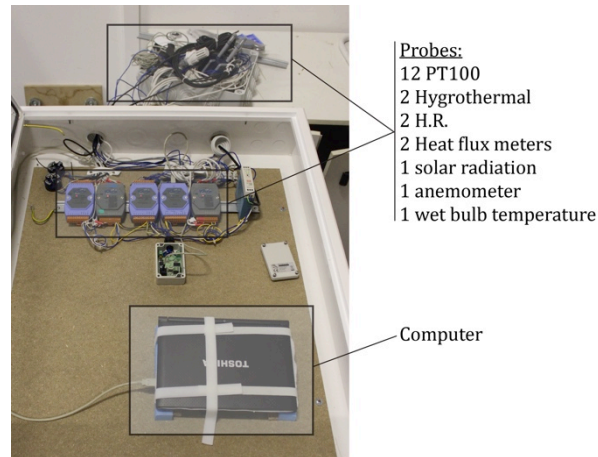


Figure 67 Data logger setup

The experimental data was continuously recorded from June of 2013 until March 2014 and the measured data for the selected seasons (Summer and Winter) was treated and presented in the following sub-sections.

#### 4.5 Experimental constraints and limitations

During the present work some limitations and constraints associated to the window shutter experimental campaign were identified.

##### 4.5.1 PCM losses

As explained in the previous section, the PCM filling into the aluminium blades was a challenge. Besides of all concerns to keep the PCM inside of the shutter blades, during the experimental testing the blades registered PCM losses. At the end of the first experimental test period, 14% loss PCM was registered (between July and November of 2013). Each shutter blade was evaluated and the blades that presented significant PCM losses were repaired and refilled with PCM. At the end of the second experimental testing campaign (winter season) the PCM losses of the aluminium blades were analysed again. The verification tests revealed a 7% PCM leakage. Table 13 presents the PCM quantity for each experimental testing period.

Table 13 PCM quantities and losses

Date	2013/07	2013/11	2013/12	2014/02
Full PCM weight (g)	290.79	290.79	290.79	290.79
Average PCM weight (g)	283.23	242.41	260.02	237.59
PCM Quantity [%]	97	83	89	82
PCM Losses [%]	→	14	→	7

4.5 Experimental constraints and limitations

These results were calculated for the PCM at the solid state. In this condition the specific mass,  $\rho$ , of the PCM is  $770\text{kg}\cdot\text{m}^{-3}$  and resorting to the specific mass equation the total PCM mass inside the blades could be estimated. As shown in the previous table, the maximum PCM quantity inside of the blade is 290g and the PCM average inside of the windows shutter blades is 283g. This means that the windows shutter blades are filled with 97% of PCM at the beginning of the experimental tests (2013/07). At the end of the first experimental test the PCM mass inside of each blade reduced to 242g, which represents losses of 14%. To minimize the PCM losses for the experimental test of the winter season each blade was evaluated before the test and the blades that registered significant PCM losses were fixed. The PCM mass average before the winter experimental test was 260g, which means that each blade is filled with 89% of PCM. At the end of the winter experimental test period the PCM mass was evaluated and it was verified an 7% of PCM loss.

4.5.2 Thermal bridges

As described before, the external opaque envelope of the test cell is insulated using sandwich panels that incorporate 4cm to 8cm of insulation material (PU-Foam). However, using a thermal camera (Testo<sup>®</sup> 875i) thermal bridges were identified where potential heat losses occurred that could not be overlooked (see Figure 68).

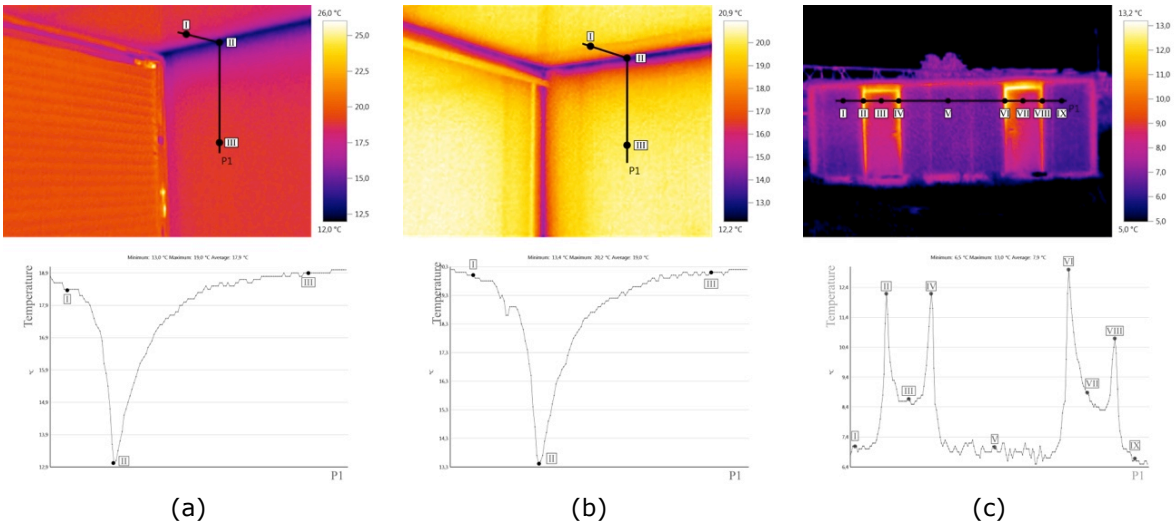


Figure 68 Thermal bridges and heat losses of reference compartment (a) West side; (b) East side; (c) Overall test cell

The thermal images were taken at the end of the day (18h, 2014-02-10), inside of the reference compartment (see Figure 68.a and Figure 68.b) and

outside the test cell (see Figure 68.c). According to the thermal images and the temperature surface profile (line P1) it can be concluded that:

From Figure 68.a), the maximum surface temperature measured by the thermal camera is 19°C (point III). On the edge point between the roof and the external wall (point II) the temperature is 13°C, which represents a temperature difference of 5°C. This external wall is west orientated, so at 18h00 it is hit by direct solar radiation;

From Figure 68.b), once again, there are significant differences between the temperature measured on the wall surface (point III) and the edge (point II) between the partition wall surface and the roof surface. In this case, the partition wall is east orientated and divides from the compartment that contains the PCM shutter. The maximum surface temperature measured is 20.2°C (point I and III) and the minimum temperature is 13.4°C (point II).

From Figure 68.c), observing the thermal image taken from the exterior of the test cell and the results of the temperature profile, it is clear that the doors reveal significant heat losses in respect to other walls surfaces. The average surface temperature of the doors is 9°C (point III and VII) and the minimum wall surface temperature is about 6.5 to 7°C (point I, V and IX). Around the door frame the maximum temperature value reached is about 11 to 13°C (point II, IV, VI and VIII), which represents a temperature difference of 6.5°C comparing to the wall surface temperatures.

#### 4.5.3 Heat flux through compartments

Besides of the concerns to improve the thermal insulation of the internal partition wall that divides the compartments, it was verified that heat flux through compartments occurs. The detailed discussions and explanation of the heat flux results through the compartments is presented in sub-section 4.6.3.

### 4.6 Results

The outdoor test cell was continuously instrumented during the winter and summer seasons. Therefore, it is presented and analysed the results from the 28<sup>th</sup> of January to the 6<sup>th</sup> of February (winter) and from 2<sup>nd</sup> to 9<sup>th</sup> of August (summer).

## 4.6.1 External Conditions

## 4.6.1.1 Overall

Figure 69 presents the measured and recorded weather data: temperature, relative humidity and solar radiation for the period from 24<sup>th</sup> July to 5<sup>th</sup> April. The zone **A** and zone **C** are referred to the summer and winter experimental testing and is discussed in detail in the following sub-sections.

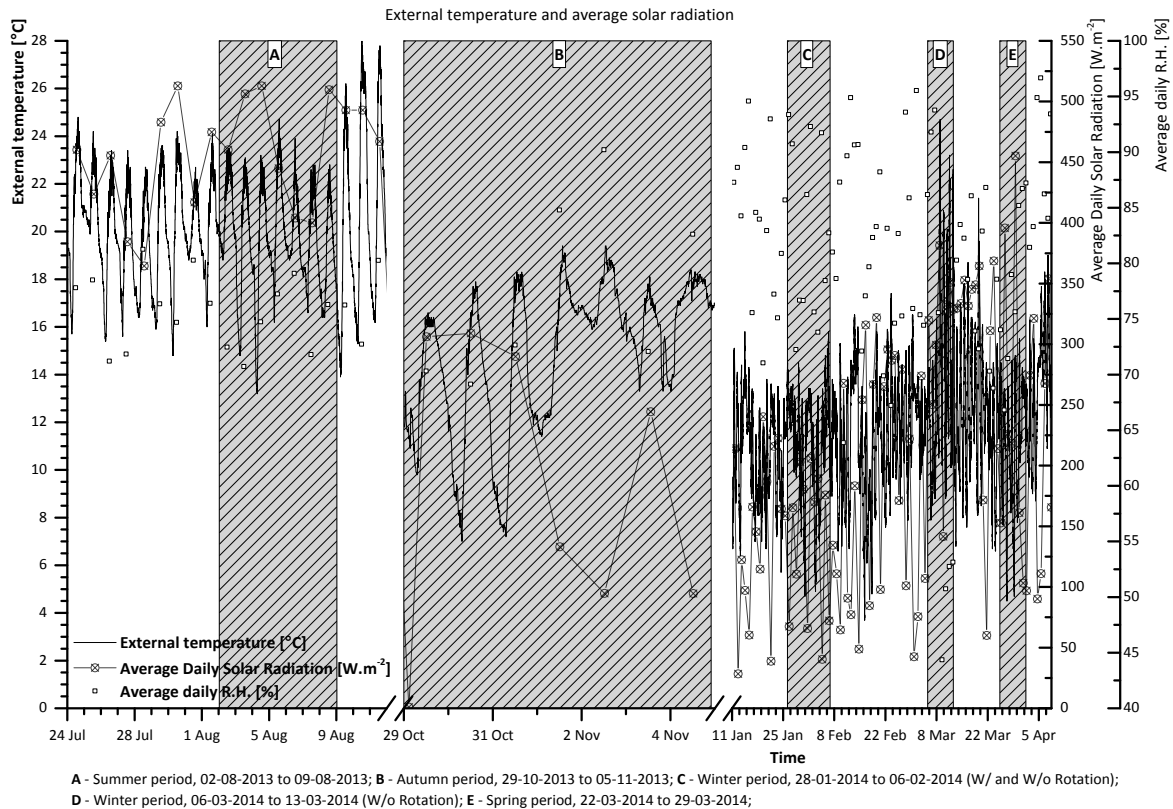


Figure 69 Measured external temperature, R.H. and average daily solar radiation

The external temperature presents high amplitude values – many times a daily thermal amplitude of 10° C. The value of the daily solar radiation indicates this is a thermal parameter with an important role on the final energy balance. During the summer season the daily solar radiation reached 500 [W.m<sup>-2</sup>], however in the winter season this values keep high (reaching in average 250 [W.m<sup>-2</sup>] and in some days 350 [W.m<sup>-2</sup>] to 450 [W.m<sup>-2</sup>]). The data of the relative humidity shows this is a region with high humidity because during the summer the relative humidity ranges from 70% to 80% and during the winter season from 65 % to ≈100%.

The wind intensity and orientation was also analysed and instrumented. The Figure 70 presents the detailed data of the wind intensity (m.s<sup>-1</sup>) and orientation (8 cardinal directions).

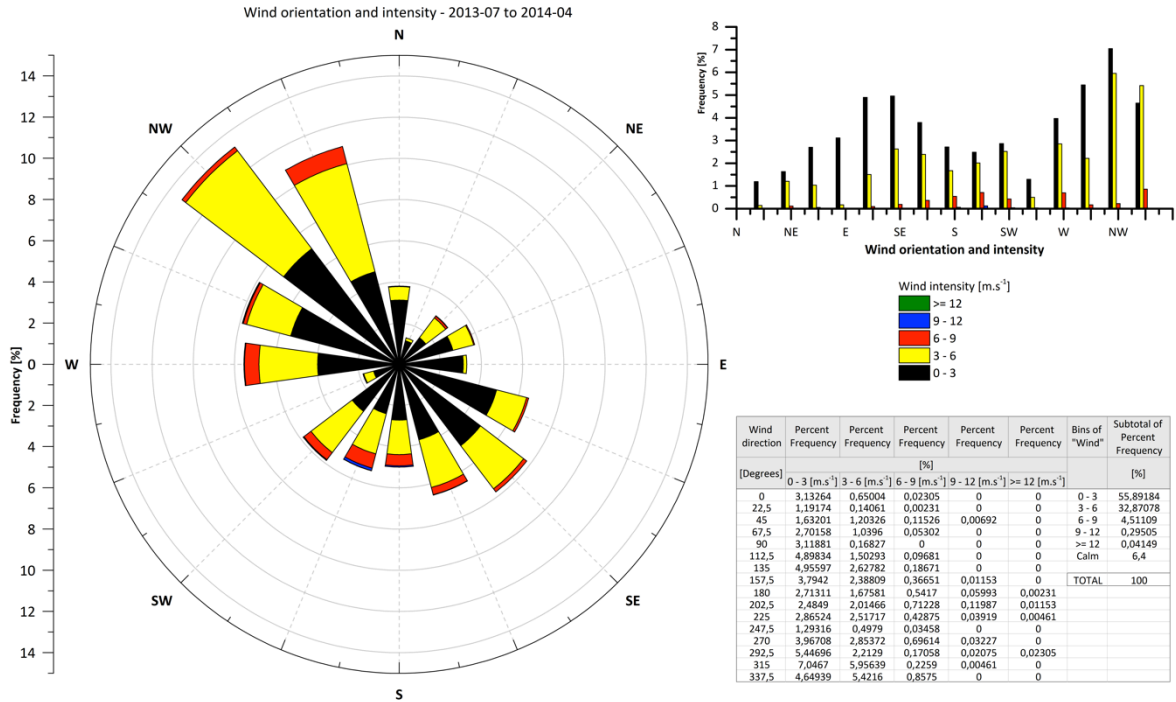


Figure 70 Overall wind orientation and intensity

The results of the wind rose graphic presented in Figure 70 (left side) shows clearly that the northwest (NW) orientation have higher frequency for the selected period. Analysing the presented detail data, the wind intensity with higher frequency is between 0 to 3m.s<sup>-1</sup> that represents ≈55% and 3 to 6m.s<sup>-1</sup> that represents ≈33% of the time. The higher wind intensity (9 – 12m.s<sup>-1</sup>) is predominated from South (S) – Southwest (SW) orientation.

To conclude, these results indicate that the test cell is submitted more frequently hit by northwest orientation wind. So, in theory the test cell is lash to northwest-facing wind, which means that the window glazing (south orientated) to less intends wind gust. However, for the worst wind intensity, the window glazing is more sacrificed, because the higher wind intensity is South – Southwest orientation.

#### 4.6.1.2 Summer

The experimental test campaign was carried out during the summer period of 2013. The solar radiation incidence into both compartments is very similar during the day cycle that is depicted in Table 14. Although, during the morning (between 11h to 13h) the surface of the internal wall partition on the PCM side is submitted to more direct solar radiation.

Table 14 Test cell shading for 3 different daily hours in summer period

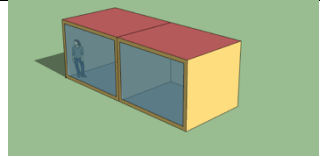
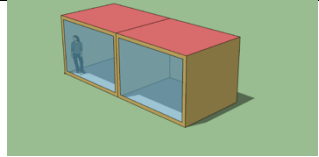
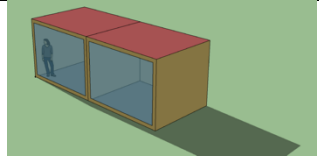
Date/Time	09h	13h	17h
Summer (21 <sup>st</sup> of June)			

Figure 71 shows the external climatic conditions from 2<sup>nd</sup> to the 9<sup>th</sup> of August. The minimum and maximum air temperature are respectively 13.2°C and 24.7°C and the maximum temperature amplitude is 10°C (registered on 4<sup>th</sup> of August). The daily average solar radiation ranges between 237 [W.m<sup>-2</sup>] to 306 [W.m<sup>-2</sup>], the individual maximum peak value reaches 900 [W.m<sup>-2</sup>]. The daily relative humidity does not oscillate significantly and the mean value is about 75%.

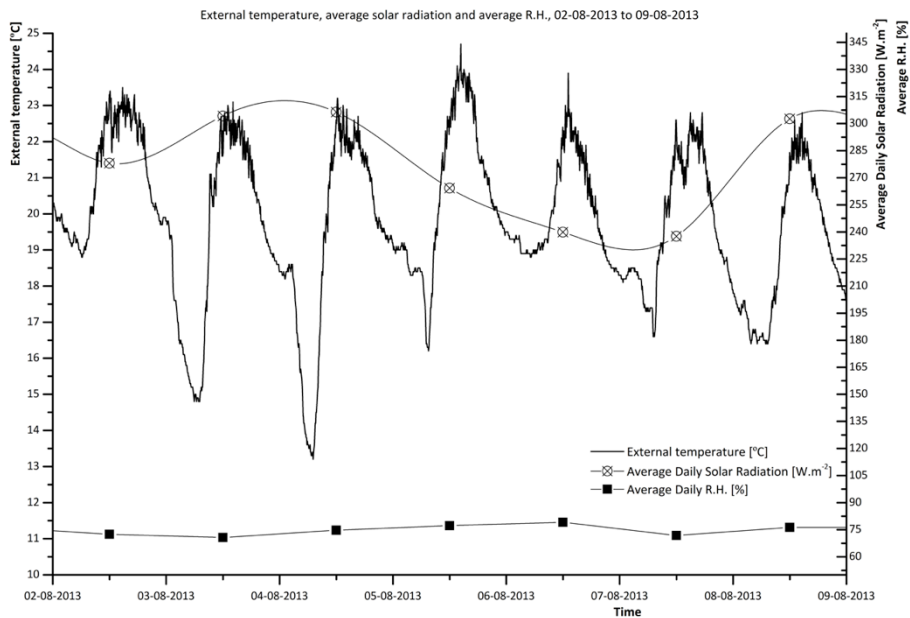


Figure 71 External climate conditions of the test compartments – Temperature, daily average R.H. and solar radiation

During this time interval, the wind orientation was mainly from NW and the wind intensity achieves values between 3 [m.s<sup>-1</sup>] to 6 [m.s<sup>-1</sup>] (about 24% of the time). During this period the percentage of time with the higher wind velocity (6 [m. s<sup>-1</sup>] to 9 [m.s<sup>-1</sup>]) was approx. 4%. These values are presented in Figure 72 with detailed data of the wind orientation and intensity during this period.

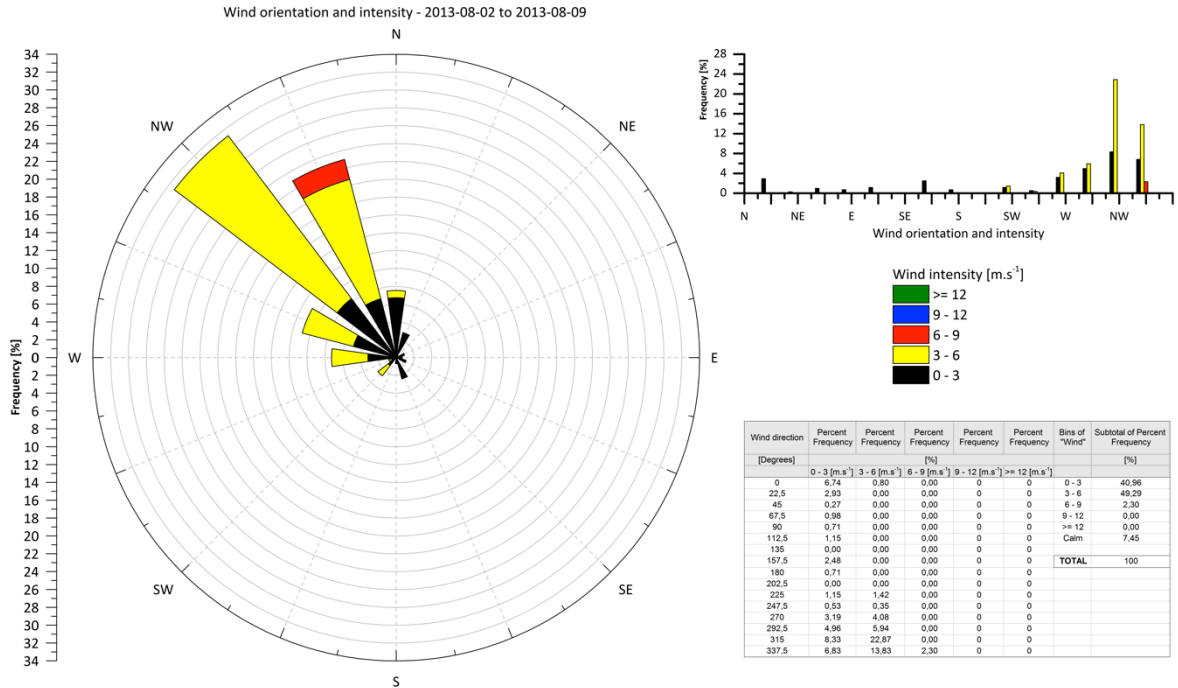


Figure 72 Wind orientation and intensity from 02-08-2013 to 09-08-2013

#### 4.6.1.3 Winter

Figure 73 shows the measured data of the outdoor air temperature, the relative humidity and the average daily solar radiation from the 28<sup>th</sup> January to the 6<sup>th</sup> February. The value of the outdoor air temperature floats from 4.5°C to 14°C, which represents a thermal amplitude of 9.5°C and the relative humidity change between 75% and 95%. During this period the daily average solar radiation ranges from 25 W.m<sup>-2</sup> to 110W.m<sup>-2</sup>. Analysing the values of the average hourly solar radiation, used in graphs of the heat flux results (section 4.6.3, Figure 84), the maximum nominal peak reached was 310W.m<sup>-2</sup>.

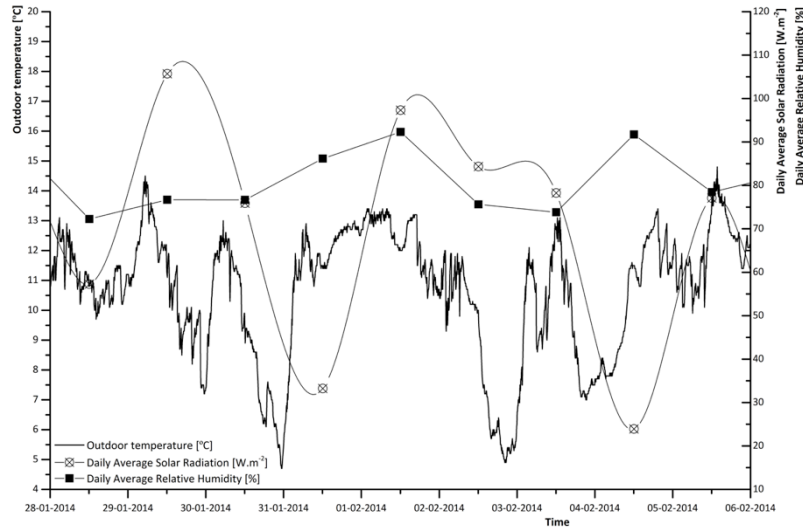


Figure 73 Outdoor air temperature, relative humidity and average daily solar radiation

The wind intensity and orientation was measured and is presented in Figure 74. The values of the wind intensity are in average higher than  $3\text{m}\cdot\text{s}^{-1}$  and have predominant orientation between  $135^\circ$  and  $315^\circ$  (southeast to northwest). As shown in Figure 74, approximately 31% of the time the wind intensity was between  $0$  to  $3\text{m}\cdot\text{s}^{-1}$ , 50% between  $3$  to  $6\text{m}\cdot\text{s}^{-1}$  and 15% between  $6$  to  $9\text{m}\cdot\text{s}^{-1}$ .

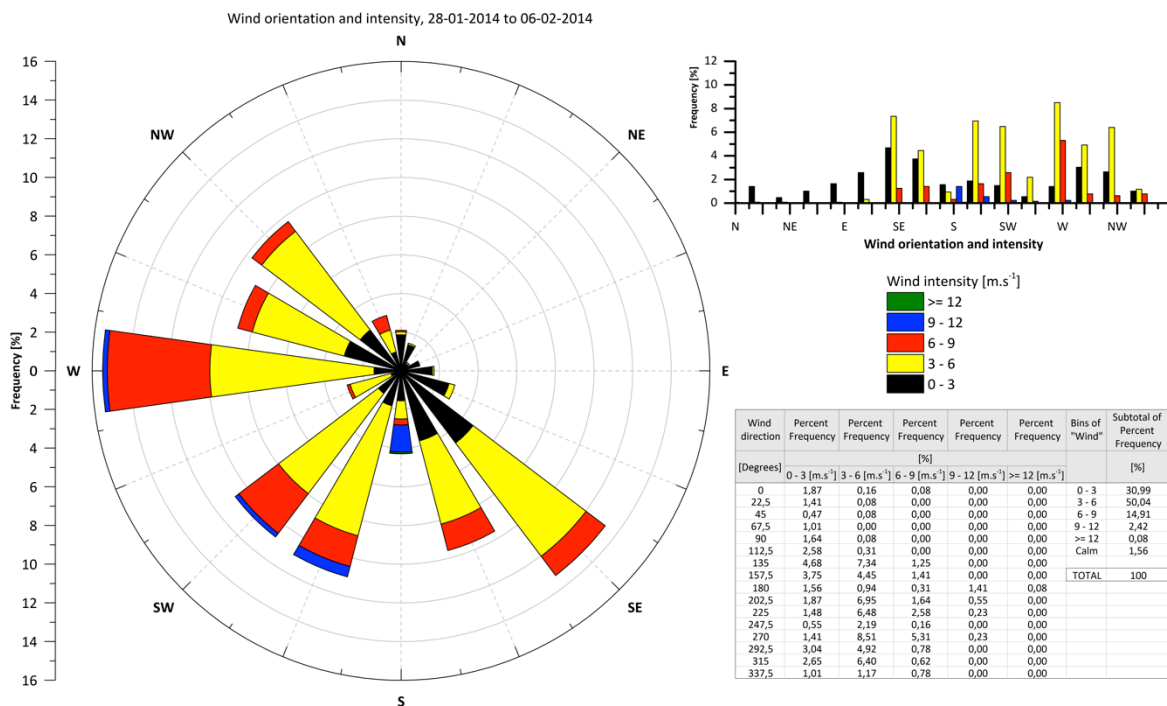


Figure 74 Outdoor wind orientation and intensity from 28-01-2014 to 06-02-2014

The wind intensity and orientation are two parameters that influence the window shutter system performance. If the heat convection coefficient of the external layer of glass is higher, the time for the PCM to release the stored energy



can decrease. However, to evaluate and quantify the thermal influence of these parameters in terms of the overall energy transfer, controlled conditions must be used.

#### 4.6.2 Indoor temperatures

##### 4.6.2.1 *Summer*

The indoor temperature in both compartments is presented and discussed for the time period from 2<sup>nd</sup> to 9<sup>th</sup> of August. During this time of the year the overheating of the compartments is inevitable. This fact was expected in consequence of the cell composition (low inertia and high glazing area) and also due to the high solar radiation in compartments. No cooling system or air renovation is installed inside of the compartments. It must be kept in mind that the shutter blades were in the closed position, so the natural lighting of the compartments was affected. However, the energy consumption of artificial lighting is negligible when compared to the potential PCM energy saving benefit.

Figure 75 shows that the compartments exceed the comfortable indoor air temperature (typically 20°C to 22°C). The maximum air temperature in the reference compartment was approx. 48°C and the minimum temperature was 14°C. The indoor air temperature for the PCM compartment is lower for the maximum temperature peak (approx. 46°C) and is higher for the minimum indoor air temperature (approx. 15°C). More detailed results using a smaller time range will be shown and discussed further on.

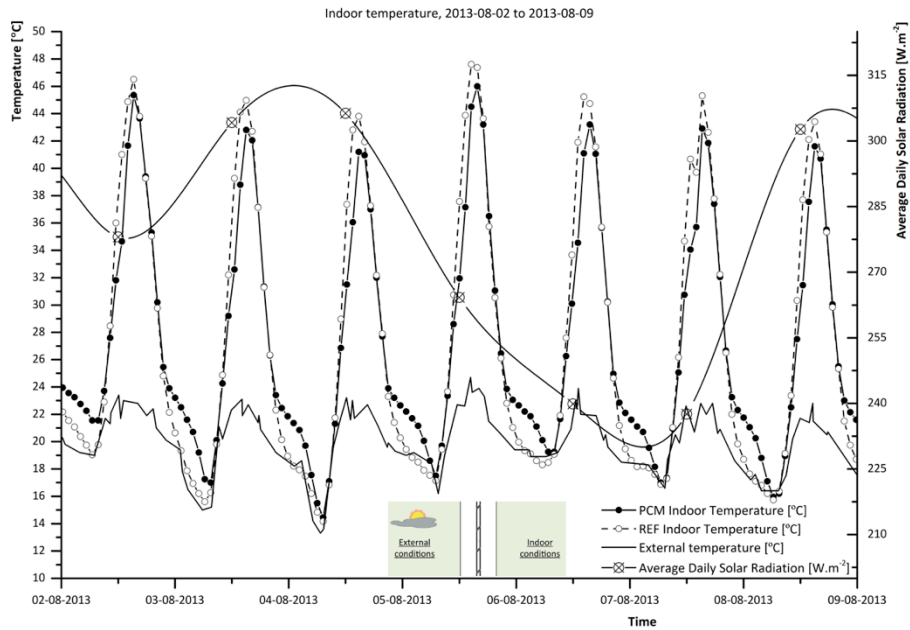


Figure 75 Indoor air temperatures, external air temperature and the daily solar radiation on selected days

The maximum external air temperature was about 25°C and the minimum 13°C. Due to the lower temperatures in respect to the phase change range – 27°C to 29°C – of the PCM, the overheating of the interior of the compartments was increased by the high daily values of the solar radiation that boost significantly the indoor air temperatures. The day with the maximum indoor temperature for both compartments was the 5<sup>th</sup> August. Nevertheless it was not the day with the highest average solar radiation. On this day, the daily solar radiation was 265 [W.m<sup>-2</sup>], not a significant difference to the maximum value of solar radiation of 306 [W.m<sup>-2</sup>] reached on the 4<sup>th</sup> August.

During this test, the position of the shutter blades was the same for both compartments. The window shutter was closed, protecting the indoor compartment from the direct solar radiation. In the compartment with the PCM shutter blades, during the day the PCM stores energy and during the night period the stored energy is released. During the day when the indoor temperature of the compartments is higher and the incident solar radiation on the shutter blades is significant, the PCM stores energy. During the night, when the external temperature drops to the range of 14°C – 18°C, the PCM releases the stored energy and minimizes the temperature drop of the indoor space temperatures in comparison the reference compartment, as shown in Figure 75.

The Figure 76 presents more clearly the results of the indoor temperatures and the PCM effect over the hygrothermal comfort. Looking at the PCM melting range proximity represented in Figure 76 and following the profile of the indoor

temperature, it is clearly visible that the temperature profile slope changes in the compartment with the PCM shutter comparatively to the reference. The temperature in the interior of the PCM shutter blades is not measured, however the effect of the stored and released energy by the PCM changes the behaviour and the slope of the indoor temperature profile. During the energy storage process the PCM changes from the solid to the liquid state and this process occurs when the imposed temperatures to the PCM filled shutter blades is higher than the melting temperature of the PCM. When 100% of the PCM is totally melted and the imposed temperature drops under the fusion temperature of the PCM, the energy release process occurs and the PCM changes state, from liquid to solid.

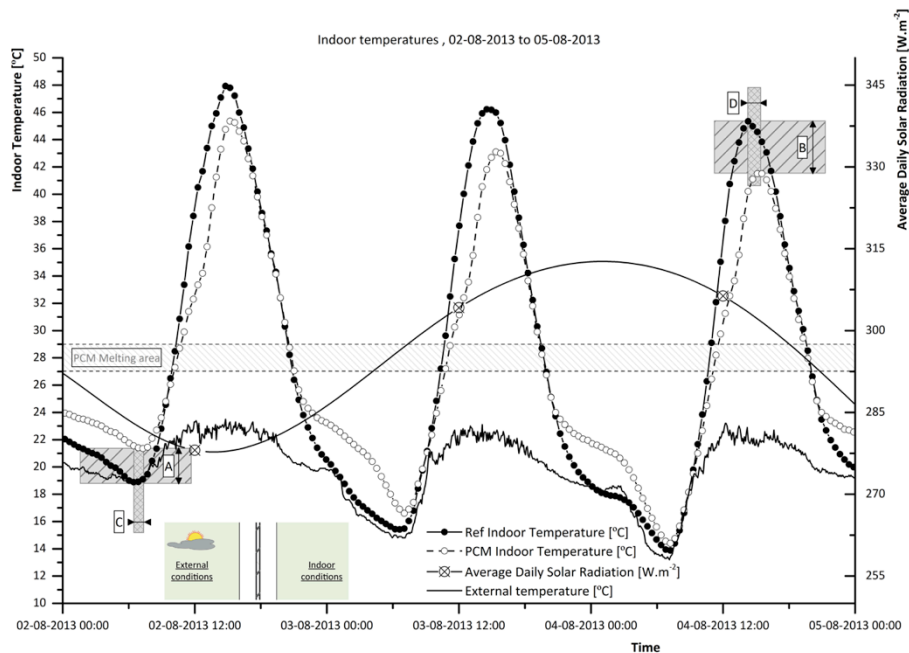


Figure 76 Measured data of the indoor air temperature in the test cell and the external air temperature and daily solar radiation

The PCM benefit is obvious over the indoor temperatures results. In Table 15 and Figure 76 are shown the difference of the maximum and minimum indoor temperature peaks and the time lag between both compartments. Four different aspects are identified - the **A**; **B**; **C**; and **D** zones:

**Zone A:** The minimum temperature difference between both compartments is  $2.32^{\circ}\text{C}$ , which means that the temperature in the reference compartment drops 11% more than the compartment with the PCM shutter.

**Zone B:** The maximum temperature in the reference compartment was  $44.17^{\circ}\text{C}$  and in the compartment with the PCM shutter was  $41.55^{\circ}\text{C}$ , which represents less  $2.62^{\circ}\text{C}$  lower value (about 6%).

**Zone C:** Besides the difference of the minimum temperature attained, the time delay between the two compartments increases 40 minutes, this means that the minimum temperature in the compartment with the PCM shutter is reached 40 minutes after of the minimum temperature in the reference compartment.

**Zone D:** The time lag for the maximum temperature, between the reference compartment and the compartment with PCM shutter, is about 55 minutes, which means that the maximum temperature of the compartment with the PCM shutter is reached after 55 minutes of the reference compartment.

Table 15 Comparison of the temperature values and time delay between compartments

	02-08-2013		03-08-2013		04-08-2013	
	REF	PCM	REF	PCM	REF	PCM
Minimum temperature [°C]	19.03	21.35	15.60	16.60	14.07	14.40
(Zone A) $\Delta T_{\min}$ [°C]	2.32		1.00		0.33	
Maximum temperature [°C]	46.70	45.40	45.07	43.20	44.17	41.55
(Zone B) $\Delta T_{\max}$ [°C]	-1.30		-1.87		-2.62	
Thermal damping [°C]	27.67	24.05	29.47	26,6	30,10	27,15
$\Delta T$ Thermal damping reduction [°C]	3.62		2.87		2.95	
Time of minimum temperature [hh:mm]	06:22	07:02	06:17	07:02	06:57	07:02
Time of maximum temperature [hh:mm] [hh:mm]	14:47	15:22	14:32	15:32	14:17	15:12
(Zone C) Time delay for min temperature [hh:mm]	0:40		0:45		0:05	
(Zone D) Time delay for max temperature [hh:mm]	0:35		1:00		0:55	

As mentioned before, the compartment with the PCM shutter reduced 6% and 11% the values of the maximum and the minimum indoor temperature comparing to the reference compartment respectively. However, the evaluation and the comparison of the indoor temperatures between both compartments, for each time step, reach significant reductions – from -22% to 18%, as shown in Figure 77.

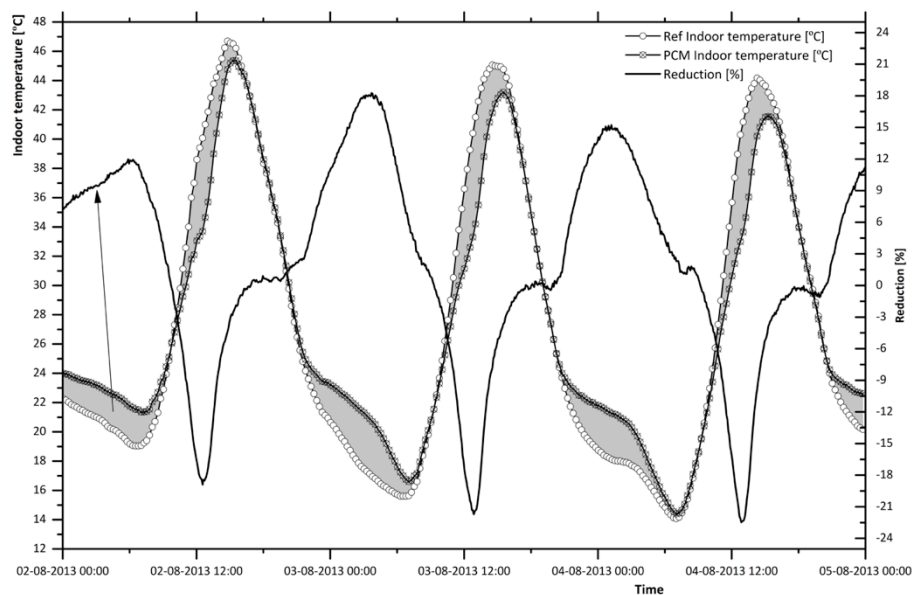


Figure 77 Indoor temperature reduction between both compartments for each time step

During the heating and cooling periods, stored and released energy from the PCM has influenced the indoor temperature and the time delay. The thermal regulation of the indoor spaces in buildings could be achieved with PCM incorporation in building solutions at glazed areas. The PCM could store the excess of solar energy and could decrease the energy needs associated to active cooling systems in the interior of building spaces.

#### 4.6.2.2 *Winter*

The test cell, even in the winter season (between 28<sup>th</sup> January and 6<sup>th</sup> February), recorded in the interior of the compartments high temperatures. The orientation of the glazing to the south and the incident solar radiation with no overhang shading elements, leads to overheating effect in the interior of the compartments leading to high indoor air temperatures.

Figure 78 presents the daily average solar radiation, the outdoor air temperature and the compartments indoor air temperature for the selected time period. The average solar radiation during this period was  $70\text{W}\cdot\text{m}^{-2}$ , the average outdoor air temperature was  $10.4^{\circ}\text{C}$  and the indoor temperatures ranges from  $4.5^{\circ}\text{C}$  to  $52.5^{\circ}\text{C}$ . During the daytime when the phase change material is storing energy, the indoor air temperature difference between compartments is significant. During the analysed time period some days present low solar radiation and for these days the indoor air temperature difference between compartments is less significant. Another feature is the difference of the thermal behaviour of both compartments. The descendant and ascendant temperature slope of the compartment with the PCM shutter changes at about  $21^{\circ}\text{C}$  that reveals the charging and discharging effect of the PCM.

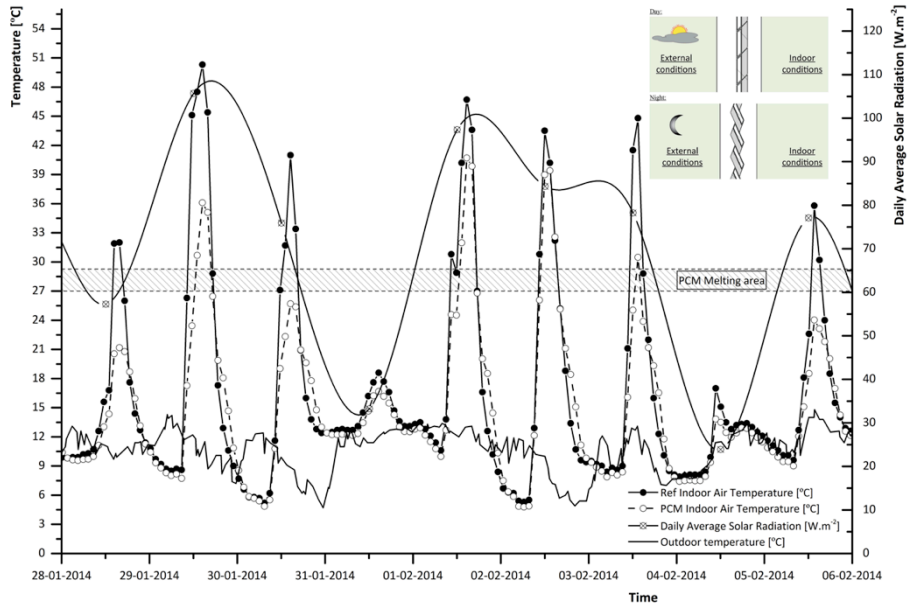


Figure 78 Indoor air temperatures for both compartments, outdoor air temperature and daily solar radiation

Figure 79 and Table 16 present detailed results of the monitored data, more precisely from 28<sup>th</sup> of January to the 31<sup>th</sup> of January. In Figure 79 are identified three main zones that represent and compare the minimum temperature differences (zone **A**), the maximum temperature difference (zone **B**) and the time delay between the maximum temperatures attained (zone **C**) for both compartments.

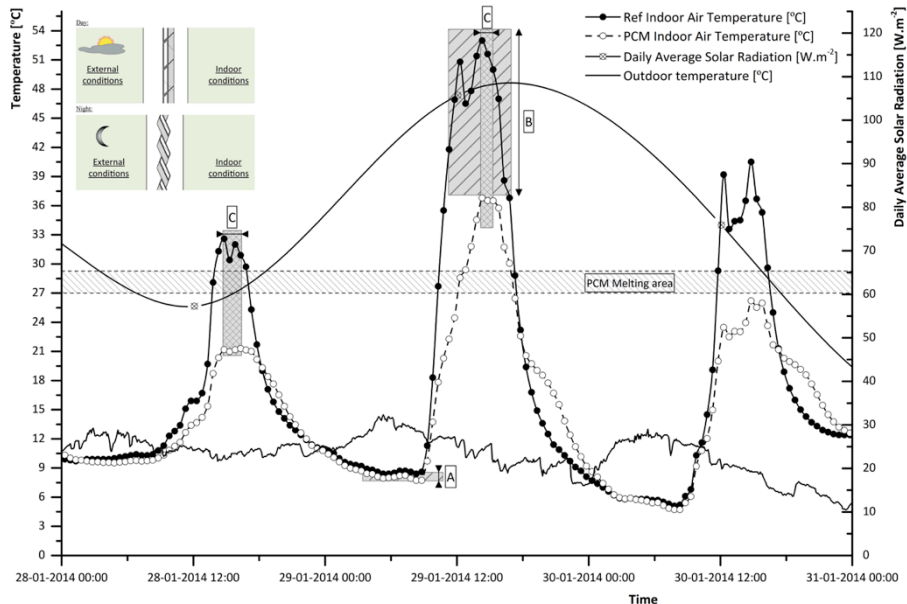


Figure 79 Indoor air temperature for both compartments, outdoor air temperature and daily solar radiation – 3 day period

The compartment with the PCM shutter presents a maximum indoor air temperature of 37.2°C, which is 16.6°C (zone **B**) lower than the indoor air

temperature of the reference compartment that reached 53.8°C. Beyond the maximum air temperature reduction, the compartment with the PCM shutter reveals a time lag to reach the maximum indoor air temperature increased by 50min (zone **C**). During the day the PCM alternates the indoor temperature swing of the compartment since the PCM is storing energy in the latent form that attenuates the maximum air temperature peak, improving the energy efficiency of this indoor space. Analysing the 28<sup>th</sup> and 30<sup>th</sup> of January the maximum indoor air temperatures reached for the compartment with the PCM shutter were 21.4°C and 26.3°C, not overheating, opposite to the reference compartment that reached 32.6°C and 41.5°C respectively.

Considering the minimum indoor air temperatures (zone **A**) reached for both compartments, the compartment with the PCM shutter did not obtain such good results. At the end of the day when the outdoor air temperature drops the behaviour of the temperature profile for the compartment with the PCM shutter is better than the reference compartment because the PCM is releasing the stored energy. After the total PCM discharge it behaves similarly to a typical sensible material with a thermal conductivity of  $[0.2\text{W}\cdot\text{m}^{-2}\cdot\text{C}^{-1}]$ , therefore, the minimum indoor air temperatures of both compartments are similar. For the first two analysed days, the results of the time delay between the minimum temperatures of the zone **A** is 3:45 and 3:15, because for these days the outdoor air temperature are unusual. The outdoor air temperature during these days floats inconstantly and during the night increases smoothly, so the reference compartment reacts faster than the PCM compartment and this factor is the justification for the high time delay between both compartments.

Table 16 Indoor air temperatures and time delays of both compartments between the 28<sup>th</sup> and the 31<sup>th</sup> January

		28-01-2014		29-01-2014		30-01-2014	
		REF	PCM	REF	PCM	REF	PCM
Minimum air temperature	[°C]	9.7	9.5	8.4	7.7	5.1	4.7
(Zone <b>A</b> ) $\Delta T_{\min}$	[°C]	-0.2		-0.7		-0.4	
Maximum air temperature	[°C]	32.6	21.4	53.8	37.2	41.5	26.3
(Zone <b>B</b> ) $\Delta T_{\max}$	[°C]	-11.2		-16.6		-15.2	
Daily amplitude	[°C]	22.9	11.8	45.4	29.5	36.4	21.6
$\Delta_{\text{Amplitude}}$ between temperatures	[°C]	-11.1		-15.9		-14.8	
Time of minimum temperature	[hh:mm]	00:52	04:37	05:07	08:22	07:47	07:57
Time of maximum temperature	[hh:mm]	14:47	16:02	14:12	15:02	14:37	14:42
Time delay at min temperature	[hh:mm]	3:45		3:15		0:10	
(Zone <b>C</b> ) Time delay at max temperature	[hh:mm]	1:15		0:50		0:05	

Figure 80 presents and compares the indoor air temperature for both compartments and shows the temperature profile reduction [%] over time (secondary yy axis). Between midnight and 6 a.m. the indoor air temperatures are similar and the major and most expressive difference of temperatures is during the heating and cooling period of the day cycle. The maximum temperature

reduction provided by the compartment with the PCM shutter is 90% and is reached during the heating period when the PCM is storing energy. When the outdoor and indoor temperature drops below the set point solidification temperature, the PCM releases energy and improves the indoor temperature up to 35%. At the maximum indoor air temperature peak the temperature reduction of the compartment with the PCM shutter is about 30% to 40% over, but for the minimum indoor air temperature the improvement is practically null (both compartments have similar minimal temperatures).

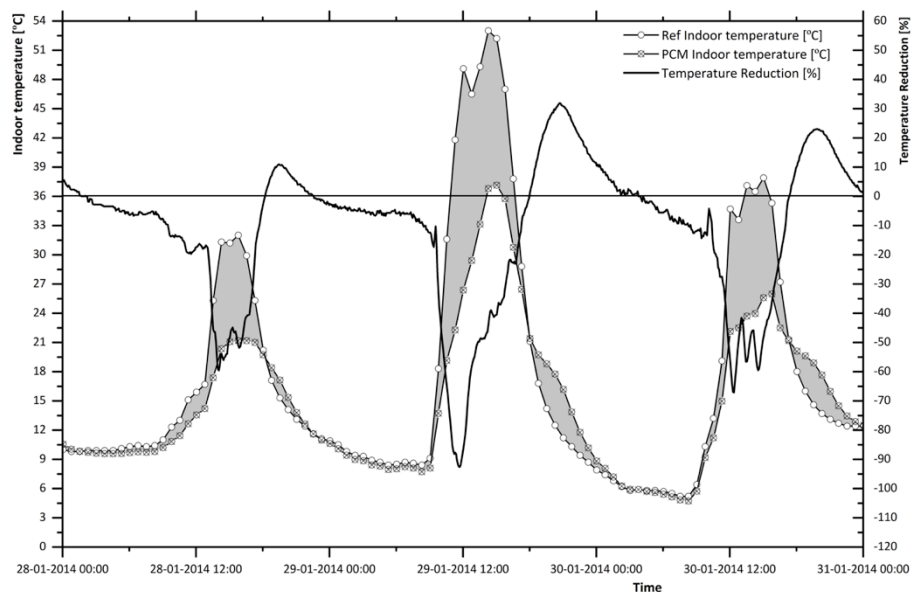


Figure 80 Indoor air temperature comparison and temperature reduction between compartments

### 4.6.3 Heat flux

#### 4.6.3.1 *Summer*

Figure 81 presents the values of the heat flux measured in the interior partition wall that divides compartments; the indoor air temperatures of each compartment and the total horizontal solar radiation. The average hourly solar radiation profile presents significant fluctuations, mainly for the 2<sup>nd</sup> August. Comparing the heat flux through the internal partition wall between the reference compartment and the compartment with the PCM shutter, is clear the difference between both results.



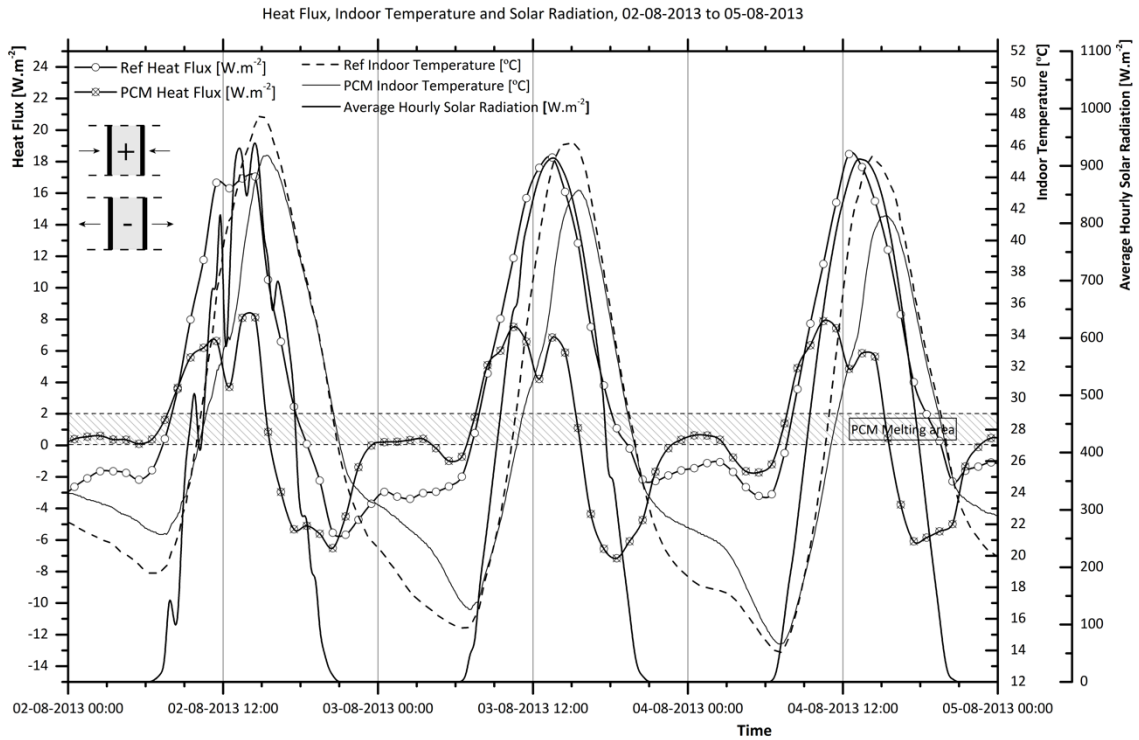


Figure 81 Overall heat flux through the internal partition wall, indoor air temperatures in both compartments and external average solar radiation.

When the indoor air temperature is higher than the surface temperature of the interior partition wall the heat flux is positive and the interior partition wall is storing energy. When the indoor air temperature is lower than the temperature of the interior wall surface, the heat flux presents negative values. The slope of the heat flux gives information on the difference of the temperatures between the surface and the indoor air. During the day (warm temperatures), when the indoor temperature of the compartments increases the heat flux mainly presents positive values. However, analysing and comparing the values of the heat flux for the compartment with PCM shutter versus the reference, the profile behaviour of the heat flux is completely different. Figure 82 presents the results of the heat flux for a typical day cycle (4<sup>th</sup> August) for the compartment with the PCM shutter.

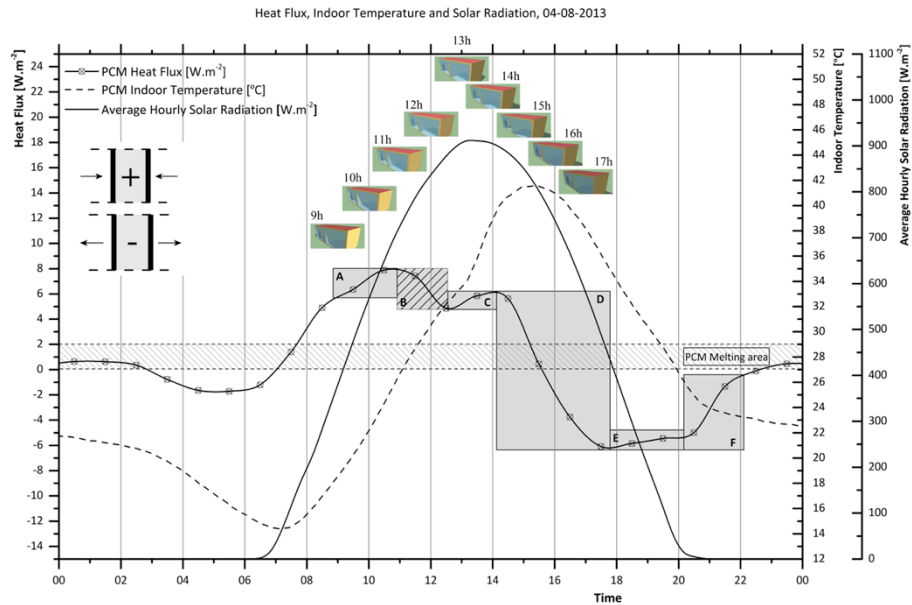


Figure 82 heat flux and indoor air temperatures for the compartment with the PCM shutter and external average solar radiation.

During the night period the solar radiation is neglected and once the indoor air temperature is similar to the surface temperature of the internal wall partition, the heat flux is practically zero. For a more thorough analysis of the results, six main zones (**A** to **F**) are identified and represented in Figure 82:

**A:** The sun rises and the external temperature increases. The indoor air temperature increases and the window shutter has direct solar radiation, however it is identified that the slope of the heat flux at this point changed. The indoor air temperature increases but not so quickly as the surface temperature of the partition wall, so the temperatures difference is lower and the heat flux does not increase strongly. The slope of the heat flux changes because the PCM is storing energy (in latent form) that allows stabilizing the indoor air temperature giving more time for the surface of the internal wall partition to react to the indoor temperature.

**B:** The anterior process keeps on. The PCM is storing energy and at this point the difference of temperature between the wall surface and the indoor air decreases. The explanation is the same of the point **A**. The PCM works as thermal regulator of the indoor space and gives more time to the internal partition wall surface to react. This feature decreases the temperature difference between the surface and the indoor air and consequently the heat flux.

**C:** During this range the heat flux values slightly increase. This is explained because the PCM is completely melted and cannot store more energy in the latent form. At this point the thermal behaviour of the PCM is similar to a common

material. The temperature difference between the indoor air and the internal partition wall surface increases again because the indoor air temperature increases faster than the temperature of the internal surface of the wall partition.

**D:** During this range the external solar radiation and the indoor air temperature decreases. The difference between the indoor air temperature and the partition wall surface temperature drops. During this time the difference between the indoor air temperature and the partition wall surface temperatures will decrease until it is reached the zero value. At this point the heat flux is null, which means that the indoor air temperature and the partition wall surface temperature are the same. After this point the indoor temperature decreases faster than the surface temperature, so the heat flux presents negative values (the partition wall surface temperature is higher than the indoor air temperature). The compartment with the PCM shutter shows negative values than the reference compartment and one of the reasons for that is the influence of the reference compartment. During the daytime, the indoor air temperature of the compartment with the PCM shutter is inferior compared to the reference compartment, however the higher temperature in the reference compartment led to a higher heat flux value during a longer period.

**E:** At this zone the partition wall surface temperature keeps higher than the indoor air temperature, however the difference is less significant.

**F:** At this time the heat flux slope increases strongly because the indoor air temperature is near the PCM phase change temperature range. So, during this time the PCM releases energy and aids to minimize the temperature difference between the partition wall surface and the indoor air temperature, stabilizing the indoor air temperature during part of the overnight period.

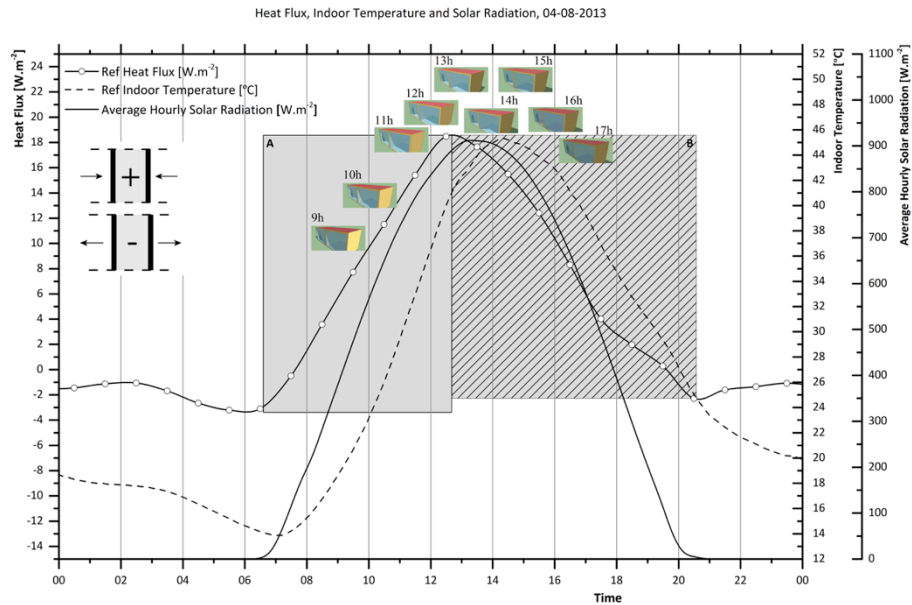


Figure 83 Heat flux and indoor air temperatures for the reference compartment and external average solar radiation.

For the reference compartment the heat flux presents a sinusoidal behaviour. When the external conditions warm up the indoor air, the heat flux increases because the indoor air temperature increases faster than the partition wall surface temperature (zone **A**) and when the external conditions drop the values of the heat flux also decrease (zone **B**) until it is reached the equilibrium conditions (at the end of zone **B**).

Another conclusion that could be taken by analysing Figure 82 and Figure 83 is that the compartment with the PCM shutter is transferring a slight quantity of energy to the reference compartment. Once reached the thermal equilibrium, the heat flux in the compartment with the PCM shutter is positive and at the reference compartment is negative. So, the temperature of the partition wall surface in the reference compartment is higher than the temperature of the reference compartment and is lower than the temperature of the compartment with the PCM shutter.

#### 4.6.3.2 *Winter*

It was selected one day of the recorded data in the winter season – 28<sup>th</sup> January – to analyse the heat flow of the partition wall between both compartments since the results tendency is representative for the winter period. The indoor thermal conditions of both compartments are different, so it was expected that the heat flux results of the partition wall would aid in fully understanding. As shown in Figure 84, heat flux module of the internal wall

partition surface of the reference compartment is higher than the compartment with the PCM shutter.

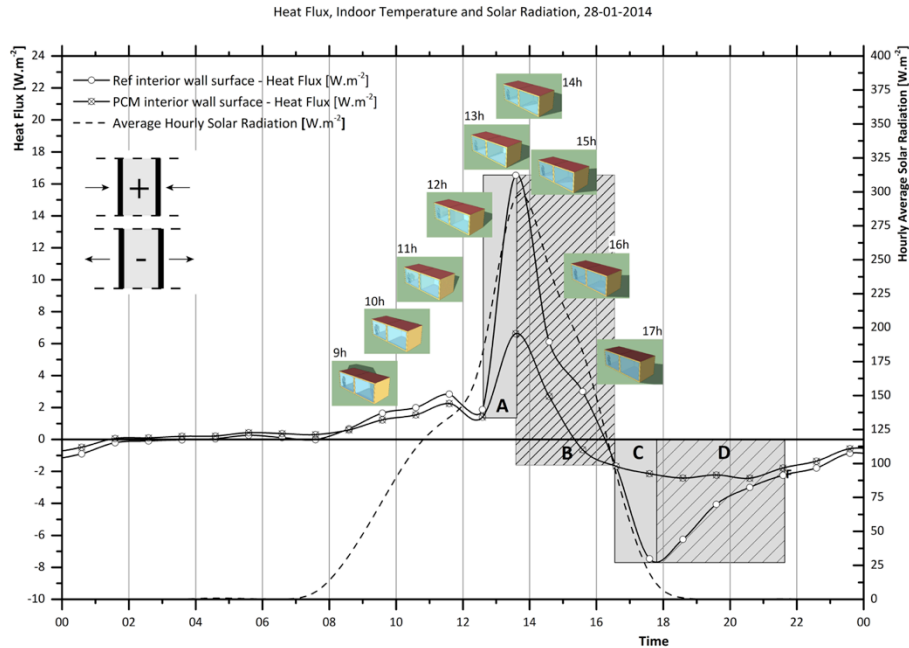


Figure 84 Heat flow of the internal partition

From 22h00 to 9h00 the measured heat flux of the internal wall partition is similar and null, which means that the indoor air temperature of the compartments and the surface temperature are equivalent. For this representative day cycle, there are four main zones represented in Figure 84 that show the major differences between both compartments.

First, when the incident solar radiation increases and consequently the indoor air temperatures – zone **A** – the heat flux of the reference compartment on the internal partition wall surface is higher comparatively to the compartment with the PCM shutter. The stored energy capacity of the internal partition wall between both compartments is the same so the main factor that differentiates the results is the presence of the PCM that stores energy. For the reference compartment the difference of the indoor air temperature and the surface temperature is higher than for the compartment with the PCM shutter. The maximum heat flux on the reference compartment side is  $16 \text{ [W.m}^{-2}]$  and for the compartment with the PCM shutter is  $6.5 \text{ [W.m}^{-2}]$ .

After this point the indoor air temperature and the surface temperature starts to stabilize (zone **B**) and the equilibrium of the temperatures (between the indoor air and the surface) is reached when the heat flux is once again practically null (at about 16h30m).

After this period the heat flux changes its direction (zone **C**) and records negative values, meaning that the indoor air temperature is lower than the surface temperature of the partition wall. The surface temperature of the partition wall is higher than the indoor air temperature of the compartments (zone **C**), so the internal wall releases energy (sensible heat) to the indoor space. Once again, the negative heat flux of the reference compartment is higher, because the difference of the temperatures between the indoor air and the partition wall surface is higher for the reference compartment than the compartment with the PCM shutter.

The indoor air and surface temperature both drop and the heat flux tends to zero (zone **D**). One of the reasons that the compartment with the PCM shutter has low heat flux results is because for this period between 18h00 and 22h30 the PCM is releasing energy to the indoor space. So, the indoor air temperature of the compartments with the PCM shutter does not decrease and is similar to the partition wall surface temperature.

The partition wall is well insulated however at zone **A** and zone **D** the reference compartment affects the compartment with the PCM shutter since the indoor air temperature of the reference compartment is so high that it contributes to increase the indoor air temperature of the compartment with the PCM shutter (zone **A**). On the other hand at zone **D** the indoor temperature in the reference compartment decreases so fast that it contributes to reduce the indoor temperatures of the compartment with the PCM shutter. To fully quantify this energy transfer between compartments a heat flux sensor in the middle of the partition wall should have been installed.

# CHAPTER 5

## 5 Numerical simulation

The numerical models are presented in this section.

A 2D model of the test cell compartment was created to simulate the experimental testing. Measured experimental weather data was used to imposed conditions. The numerical definitions, such as: the mesh, cell zones, boundary conditions and models are also presented in detail.

The results obtained from the equivalent positions points of the experimental testing, are presented and analysed for the selected period, supporting the model calibration.

The numerical models were validated according to the most used statistical methods to improve the quantitative agreement of the measured indoor temperatures and the results of the numerical models.

---





## 5.1 Two-dimensional model

To minimize the computational requirements of the numerical studies and to simplify the numerical model without compromising the results, it was considered the following premises:

- The 2D model represents a cross-section of the test cell that does not consider the structural members of the window shutter, the rotation mechanisms and the back door opening;
- Two 2D models were developed – PCM compartment and the reference compartment – instead of a 3D complex model;
- The external boundary (flat roof, north wall and floor) is composed by one equivalent layer;
- It was not taken into account the geometry imperfections – i.e. door perimeter – the geometry of the numerical model is considered “perfect” while in the experimental model as previously described and proved there are thermal bridges (see more details in [189]);
- It is considered a continuous contact of layers – without any air cavity between them. For example, the insulation material (XPS) applied on the blade surface is perfectly joined (winter analysis). In the case of the experimental prototype the insulation material is in contact with the blade, using thin glue layer between them;
- The distance between each shutter blade is 2mm – in the experimental campaign the distance between each shutter blade is up to 5mm;
- The aluminium blade end caps were not considered – in the experimental prototype, each shutter blade has two end caps made of aluminium;
- It is considered that the shutter blade is completely filled with PCM. According to the PCM manufacturer data sheet, the volume changes 12.5% during the phase change process, so when the PCM is in the solid state, 22% of the internal volume of the shutter blade is occupied by air;
- The numerical model is airtight, so it does not consider the air infiltrations of the test cell.

The 2D models were built with the Solidworks software – as plain surfaces – and the modelled file was exported to the ANSYS DesignModeler. To import correctly the Solidworks geometry to the ANSYS DesignModeler it was enabled the solid, surface and line bodies’ functions and also the DS parameter key. These options consider all geometry definitions created in Solidworks and the parameter

key DS is a string that aids to filter the CAD parameter names to attach. For these models it was considered a 2D analysis type and it was also imported the coordinate system from the original geometry model. The decompose disjoint geometry option was also enabled to allow to decompose a disjoint faces into separate faces.

To simplify the simulation process in Fluent in the DesignModeler it was considered the model as one part with multi-bodies. This approach leads to a simpler model definition, because in this case the interfaces/contact between bodies are identified and created automatically. Considering one part, when the mesh is imported into the ANSYS Fluent, the virtual wall between bodies automatically is considered as coupled, so the thermal energy transfer through the wall is considered. If a multi-parts approach is considered, the contacts between each part are identified automatically, however this contact by default is considered mechanical and the coupled option is not introduced.

In Figure 85 the dimensions and composition of the 2D model used in the winter analysis is shown (for the summer analysis layer 7, XPS is not present).

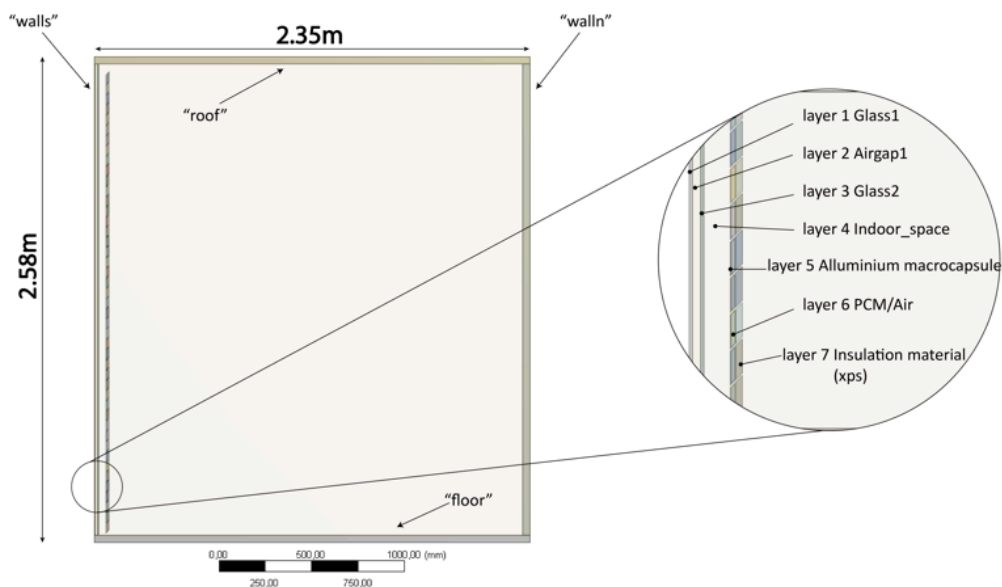


Figure 85 DesignModeler 2D picture

## 5.2 Mesh Definitions

As ANSYS Fluent was chosen to carry out the numerical simulations, the creation of the model mesh was done selecting the CFD physic preference and the Fluent solver, that enables the default values of the mesh properties.

It was used the proximity and curvature advanced size function. This function provides greater control of the sizing functions, such as: the angles between the adjacent mesh elements, the number of the mesh elements and the graduation between the minimum and maximum sizes based on the specific growth rate.

The main defined mesh definitions, are as follows [154]:

- High smoothing: The smoothing attempts to improve the element quality by moving the location of the nodes in respect of the surrounding nodes and elements. The high option increases the number of the smoothing iterations, so the mesh creation is slowest but improved;
- Fine span angle centre: the span angle centre defines the goal for the curvature based on the refinement. With the fine span angle centre enabled the mesh will be subdivided into regions with angles between 36° and 12°.
- Default curvature normal angle: the curvature normal angle is the maximum allowable angle that one element edge is allowed to span. The default value is automatically calculated according the values of the relevance and span angle enter options;
- Default number cells across gap: The number cells across gap option is the minimum number of layers of elements to be generated in the gaps. With the default option selected the corresponding number is automatically calculated according the relevance option;
- Max size and max size face: the maximum size and maximum face size was defined as 500mm. This means that the size function will return to the surface mesher the maximum element sizes up to 500mm.

To improve the mesh element quality it was used refinement controls for the smallest domains and also the triangles method control for all domains. According to this, it was used the refinement control (2x) at the following layers: macrocapsules, PCM and insulation material.

The mesh quality was evaluated using the mesh metric option that allows to view the mesh information and to evaluate the mesh quality. After the mesh generation, it was used and selected two mesh metric options to evaluate and optimize the mesh quality: the "Element Quality" and the "Skewness". When the mesh metric is on, the following mesh information is shown: the values of the min, max, average and standard deviation of the selected method and the number of elements.

The element quality provides a evaluation metric value that ranges between 0 and 1. The higher results correspond to more quality of the element mesh. This mesh control is calculated according the ratio between the volume and the edge length of the analysed element. The mesh metric skewness evaluates how close the mesh element (face or cell) is to the ideal. Once again, the results are presented between the 0 and 1, therefore the values nearest to zero represents best element quality. There are two methods to calculate the skewness values based on:

- equilateral volume (applied only to triangles and tetrahedrons);
- deviation from a normalized equilateral angle (to all cells and face shapes).

In the present work, it was imposed the triangles/tetrahedrons method in all domains, so the calculation of the skewness mess metric is based on the equilateral volume. The equilateral volume is calculated according to the equation (5.1):

$$Skewness = \frac{Optimum\ Cell\ Size - Cell\ Size}{Optimal\ Cell\ Size} \quad (5.1)$$

The mesh metric feature gives the mesh information that allows to optimize the mesh generation, however other quality mesh controls must be used with this feature.

To select the best mesh several parameters feature were assessed, to evaluate crucial inputs and outputs values. Parameters such as, the "min size" and "min face size" of the mesh elements (mesh inputs) and parameters of the mesh metric outputs: min mesh element quality (P1), average quality (P3), mesh elements number (P5) and mesh standard deviation (P4). In sum, after the model generated and the mesh created, the parameter set is attached to the mesh file – as presented in Figure 86.

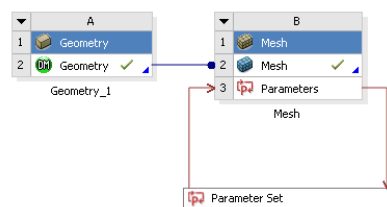


Figure 86 Mesh evaluation form

It was applied 10 steps of the mesh proximity minimum sizes and mesh minimum sizes (P7): 5.12, 2.56, 1.28, 0.64, 0.32, 0.16, 0.08, 0.04, 0.02 and 0.01mm, which represent a step of ½ from the last minimum used size. Using the

results of the output parameters, the Table 17 and the graphs presented in Figure 87 were generated to evaluate, calibrate and validate the mesh quality.

Table 17 Design points and results of the output parameters

Name	P7 [mm]	P4	P3	P1	P5
DP 1	5.12	0.208280	0.82428	0.43629	5.3763E+04
DP 2	2.56	0.103720	0.90412	0.21898	1.3581E+05
DP 3	1.28	0.036292	0.96620	0.53029	2.4388E+05
DP 4	0.64	0.031985	0.96976	0.36651	4.8218E+05
DP 5	0.32	0.026316	0.95936	0.35905	9.1987E+05
DP 6	0.16	0.026188	0.95939	0.42314	9.1982E+05
DP 7	0.08	0.026235	0.95938	0.35661	9.1981E+05
DP 8	0.04	0.026275	0.95937	0.37419	9.1980E+05
DP 9	0.02	0.026064	0.95942	0.42314	9.1987E+05
DP 10	0.01	0.026074	0.95942	0.42314	9.1985E+05

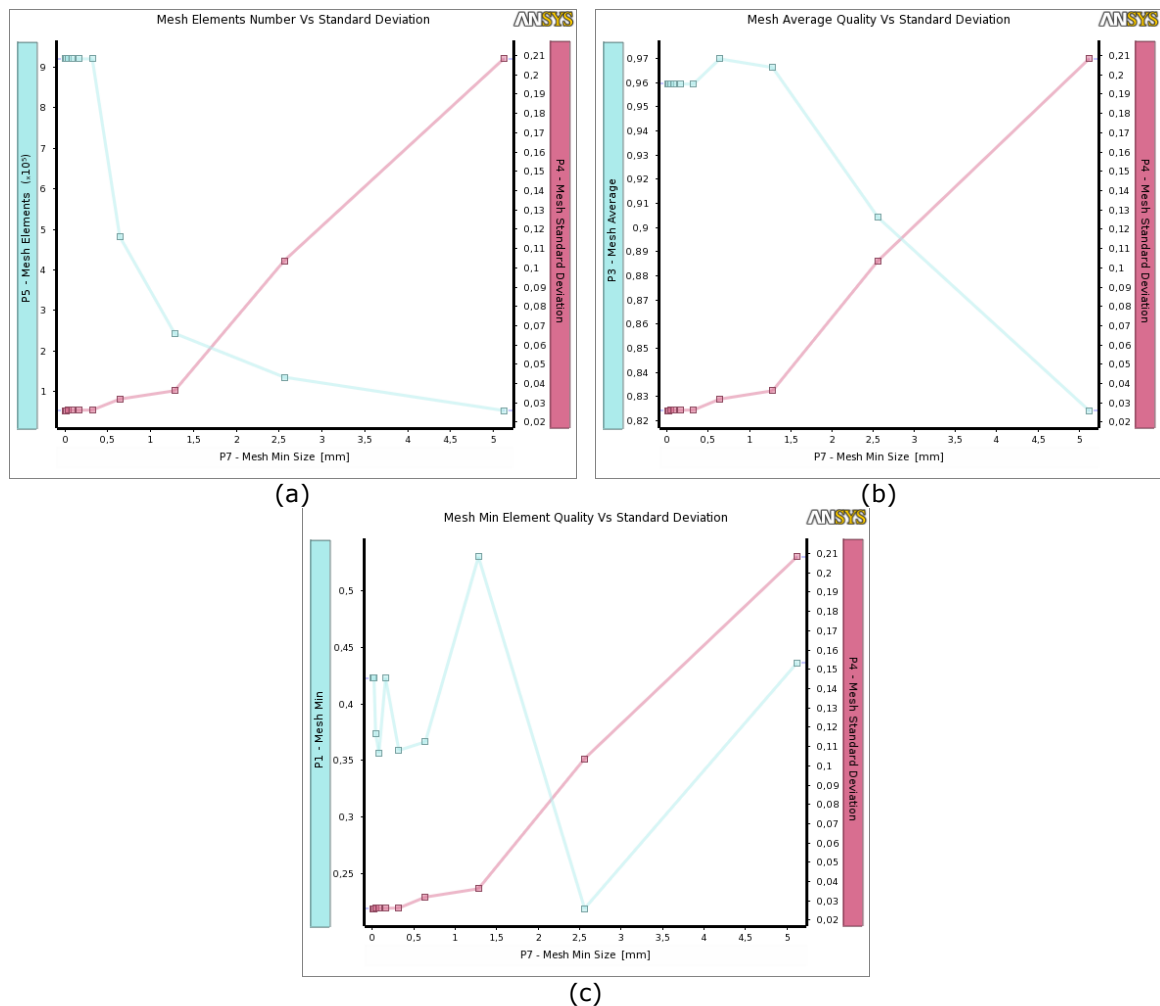


Figure 87 Mesh evaluation (a) Mesh elements number vs. standard deviation; (b) Mesh average quality vs. standard deviation; (c) Mesh min element quality vs. standard deviation

Resourcing to the results presented in Figure 87 and Table 17 it can be concluded that:

- Figure 87.a: The mesh standard deviation (P4) and the mesh elements number (P5) stabilized and converged after the design point 5 (DP5) that uses the minimum mesh size (P7) of 0.32mm;
- Figure 87.b: The DP4 presents the best mesh average quality (P3). Therefore, the DP5 presents also a high average quality and after these design points the results has convergence. So, according to these results the best-selected point is the DP5;
- Figure 87.c: The results of the mesh minimum quality (P1) are irregular and do not present convergence results. The design point with the best minimum mesh element quality is DP3, for which the minimum element quality is 0.53029.

According to these results, the design point 5 (DP5) was selected and used for the ANSYS Fluent simulations. The final and selected mesh geometry is presented in Figure 88.

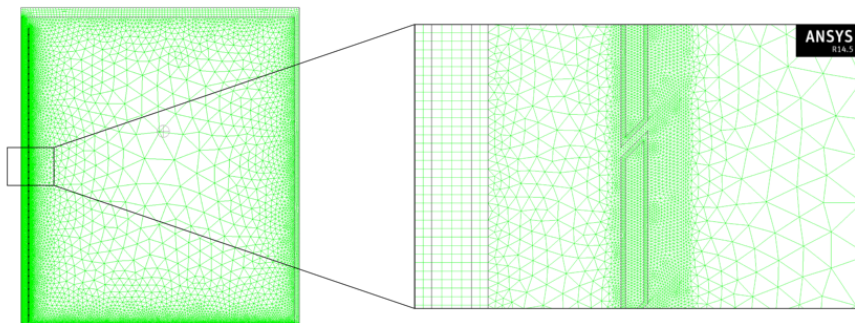


Figure 88 Model mesh – overall geometry and close-up to the exterior window boundary

### 5.3 Imposed conditions

The solar radiation was incorporated in the numerical models resourcing to an equivalent temperature profile. The equivalent temperature profile was calculated according equation (5.2):

$$T_{eq} = T_e + \frac{\alpha \cdot S}{h_e} \quad (5.2)$$

The equivalent temperature was calculated using the recorded weather data (onsite weather station at the campus) for the summer and winter season – more precisely between 2<sup>nd</sup> to 9<sup>th</sup> August and 28<sup>th</sup> January to 4<sup>th</sup> February. The

resourced data was the external air temperature ( $T_e$ ) and solar radiation ( $S$ ). The solar absorption coefficient,  $\alpha$ , was considered as 1 and the exterior heat transfer convection coefficient,  $h_e$ , was considered constant and equal to  $25[\text{W}\cdot\text{m}^{-2}\cdot\text{K}^{-1}]$  (summer) and  $15[\text{W}\cdot\text{m}^{-2}\cdot\text{K}^{-1}]$  (winter).

To be more precise, the calculated equivalent temperature is applied on the model surfaces, for which direct incidence of solar radiation occurs – at the roof and south facing oriented surfaces. For the floor and north facing oriented facades was applied the external air temperature (recorded during the experimental testing campaign).

As the measured solar radiation presents high entropy on the maximum peaks (because the inconstant solar incidence) and influences significantly, mainly the winter model, it was applied a filtering signal with smooth algorithm for the winter data. The used method of the smooth algorithm was the percentile filtering which takes into account 30 points and the percentile 65. This method works fairly well for signals that present “noise” localized at peaks, which is this case.

Other selection criterion was taken into account was the average temperatures. As the imposed conditions/temperatures at both compartments are similar, the temperatures average imposed and recorded into the compartments should be also similar. For the summer season, these were not undertaken because the average imposed temperatures were similar with the recorded in both compartments. Therefore, for the equivalent temperature of the winter season considering the exterior heat transfer convection coefficient,  $h_e$ , equal to  $25 [\text{W}\cdot\text{m}^{-2}\cdot\text{K}^{-1}]$  the temperature average was significantly lower than the average temperature recorded inside the compartments. The average temperatures of the reference and PCM compartment were  $17.11^\circ\text{C}$  and  $15.44^\circ\text{C}$ , respectively. Considering the initial equivalent temperature profile, the average temperature is  $13.35^\circ\text{C}$  and the maximum temperature peak reaches  $40.13^\circ\text{C}$ . These values represent unreal conditions that lead to greatest differences between the experimental and numerical model. Applying the filter signal to the solar radiation profile and subsequently adding to the equivalent temperature with  $h_e$  equal to  $15[\text{W}\cdot\text{m}^{-2}\cdot\text{K}^{-1}]$ , the average temperature of the equivalent temperature profile is  $16.39^\circ\text{C}$  and the maximum temperature value  $48^\circ\text{C}$ .

According to the previous definitions and equation (5.2), two equivalent temperatures profile were created: for the summer season (see Figure 89) and for the winter season (see Figure 90). The comparison of the initial equivalent temperature profile against the filtered profile of the winter season is also presented in Figure 90.

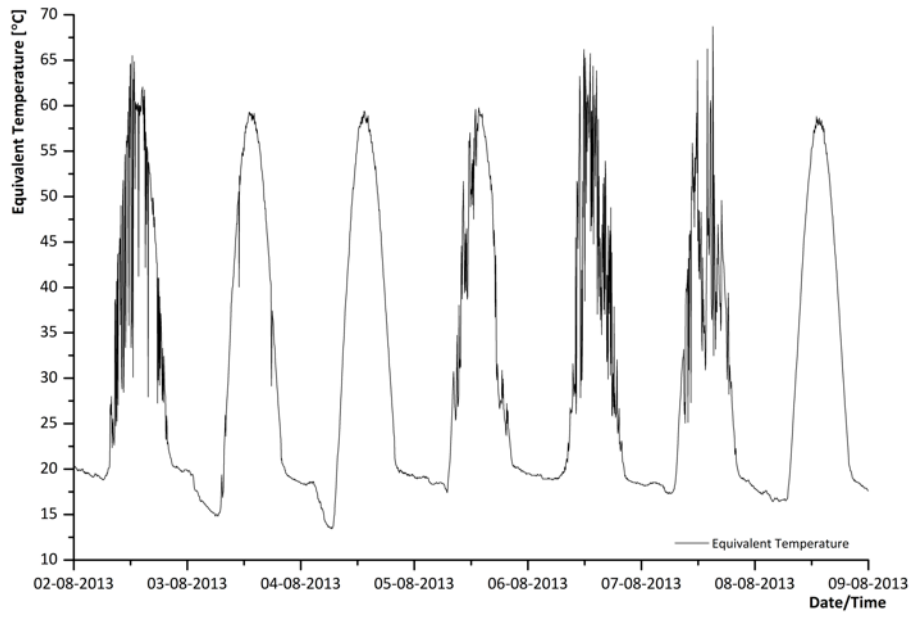


Figure 89 Equivalent temperature profile,  $T_{eq}$ , for the summer season

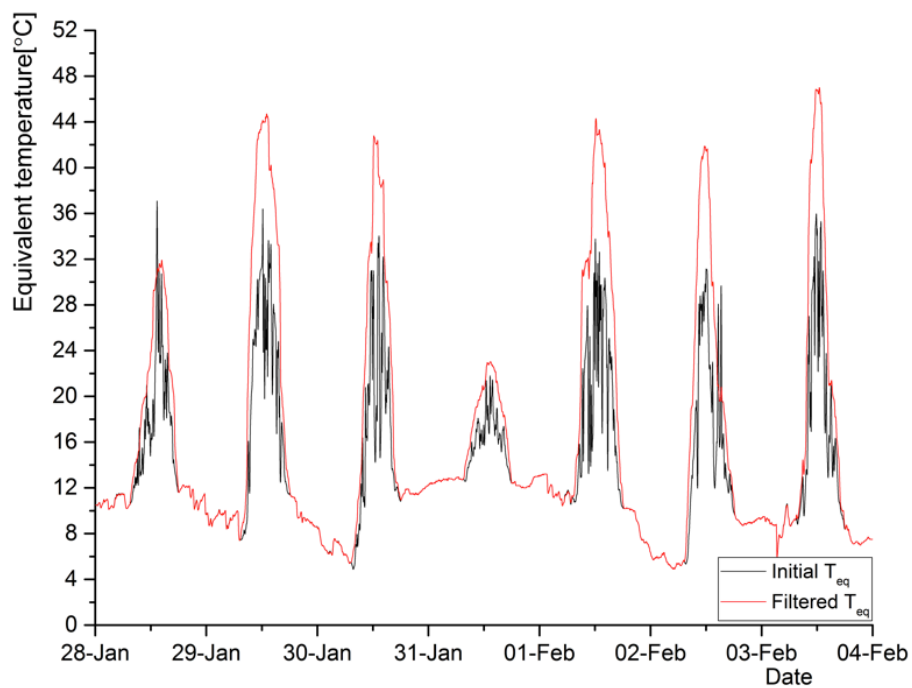


Figure 90 Equivalent temperature profile,  $T_{eq}$ , for the winter season

The equivalent temperature for the summer season ranges from 13 to 68°C and for the winter season from 5 to 47°C.

#### 5.4 Numerical definitions



### 5.4.1 Materials

According to the domains of the numerical models, the materials were selected and created. For the solid domains the input parameters needed to define the material were the density, specific heat and the thermal conductivity. For the fluid domain beyond the previous materials properties referred it was also introduced the viscosity, melting ranges and enthalpy.

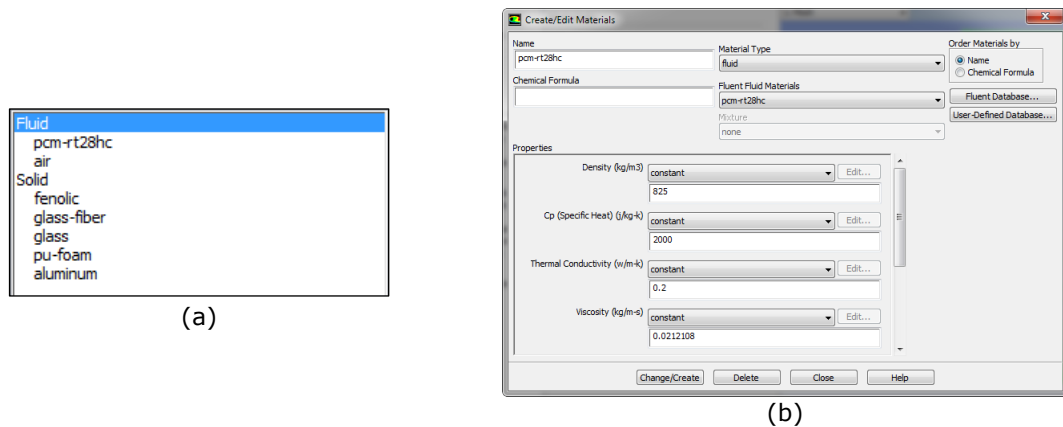


Figure 91 (a) List of materials; (b) Example of the PCM properties definitions

An example of the input materials parameters created and used for the numerical models is presented in Figure 91.a and the Figure 91.b (for the case for the compartment with PCM and without the insulation material on the aluminium blades). There are two materials defined and created as a fluid – air and PCM – and six other as solid – glass, glass-fibre, polyurethane foam (PU), phenolic, aluminium and XPS.

### 5.4.2 Cell zones and boundary conditions

For the 2D numerical model, eleven main cell zones were created and considered: *airgap1*, *floor*, *glass1*, *glass2*, *indoor\_space*, *macrocapsule*, *PCM* (or air, for the reference compartment), *roof*, *walln* and walls (*walln* - north and walls – south faced orientation) and *XPS* (for the models with the insulation material on window blades surfaces)(as shown in Figure 85). Figure 92.a shows the list of the cell zone conditions and Figure 92.b the boundary conditions of the numerical model.

The properties and the selected materials for each layer were created in the cell zone conditions menu. The material "air" was selected for the empty zones, which is the zones: "airgap1" (air gap of the double glazing), "indoor\_space" (indoor space of the compartments) and "empty" (interior of the macrocapsules for the reference compartment). The PCM is located inside of the macrocapsules

(PCM compartment) and besides considered and defined as fluid, when the PCM temperature is below the melting temperature of the PCM, this material is in the solid state. The window pane layers "*glass1*" and "*glass2*" is defined of glass and the "*XPS*" zone is the insulation material layer.

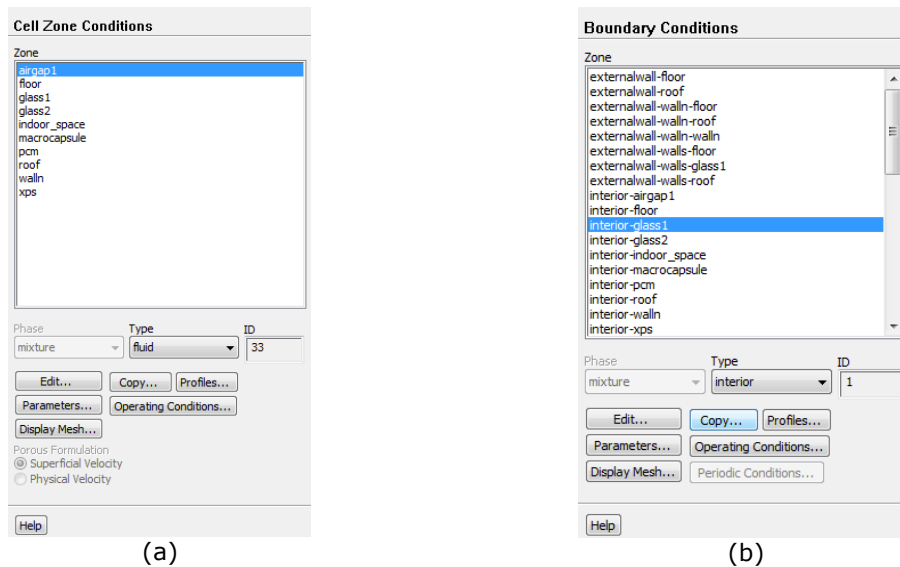


Figure 92 (a) Cell zones of the numerical models; (b) Boundary conditions of the numerical domains

The cell zones "*roof*", "*walls*" and "*walln*" are similar. As described before, these layers are composed mainly by polyurethane. The zone "*floor*" is also similar to the "*roof*" and "*walln*" zones, with addition of a phenolic layer material.

For these 2D models the boundary conditions are divided into two main types: walls and interior. The zones defined as interior are considered free-floating conditions zones, because any thermal conditions are applicable into these zones. Therefore the thermal behaviour of these zones is calculated according to the materials definitions of each zone.

According to the enabled numerical models and definitions of the ANSYS Fluent module it can be added thermal, physical and chemical conditions for these wall boundary types. Figure 93 shows the thermal conditions applied on the external surface of the "*glass1*" zone (which is the surface in contact with the external conditions). For this layer the selected material type is the glass and the thermal conditions applied was the temperature. With the thermal condition "Temperature" enabled, the "equivalent temperature" profile that was defined at the "Imposed conditions" subsection was selected. The equivalent temperature is the only parameter used on this surface, so the other available thermal conditions (wall thickness, heat generation rate and contact resistance) were left as default values.

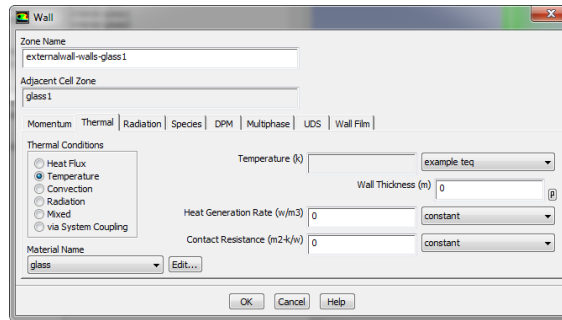


Figure 93 Boundary condition of the south-facing facade

The other three surfaces in contact with the external weather conditions (external surfaces of the zones: *roof*, *walln* and *floor*) were also defined. The thermal conditions applied on the “*roof*” external surface have the same conditions of the external surface of the “*glass1*” zone. For the external surfaces of the “*floor*” and “*walln*” was selected the convection thermal condition option. For these 2 latter boundaries were used the external air temperatures of the experimental testing campaign, instead of the equivalent temperature profile and was defined the convection coefficient of  $25[\text{W}\cdot\text{m}^{-2}\cdot\text{K}^{-1}]$ .

#### 5.4.3 Models, solidification and melting

To calculate and solve the heat transfer phenomenon of the numerical domains it was enabled the following options: “energy”, “viscous” and “solidification and melting” (see Figure 94).

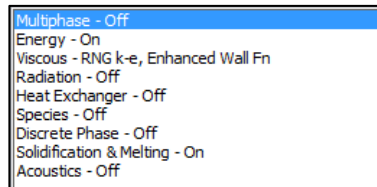


Figure 94 Selected models for the calculation process

The numerical calculation includes the heat transfer between the solid and fluid domains of the numerical model [190]. The heat transfer through the defined regions were calculated using the follow energy equation (eq. (5.3)):

$$\frac{\partial}{\partial t}(\rho E) + \nabla \cdot (\vec{v}(\rho E + p)) = \nabla \cdot \left( k_{eff} \nabla T - \sum_j h_j \vec{J}_j + (\bar{\tau}_{eff} \cdot \vec{v}) \right) + S_h \quad (5.3)$$

The first three terms on the right-hand side of equation (5.3) represents the energy transfer due to conduction, species diffusion and viscous dissipation. The  $S_h$  parameter includes the heat transfer from chemical reactions or other volumetric heat sources (if applicable) and the  $\bar{\tau}$  represents the stress tensor

parameter. The effective conductivity,  $k_{eff}$ , is the calculated conductivity ( $k+k_t$ ) resourcing to the material property and to the turbulent thermal conductivity ( $k_t$ ) that is defined by the selected turbulence model. The  $\vec{J}_j$  is the diffusion flux of species  $j$  and  $h$  the sensible enthalpy. The parameters  $\rho$ ,  $p$  and  $\vec{v}$  represent the mass density, the pressure and the overall velocity vector, respectively.

The energy,  $E$ , is calculated using the following equation:

$$E = h - \frac{p}{\rho} + \frac{v^2}{2} \quad (5.4)$$

where, for an ideal gas the sensible enthalpy,  $h$ , is calculated according to equation (5.5) and in the case of incompressible flow gas is calculated using equation (5.6).

$$h = \sum_j Y_j h_j \quad (5.5)$$

$$h = \sum_j Y_j h_j + \frac{p}{\rho} \quad (5.6)$$

The  $Y_j$  parameter is the mass fraction of species  $j$  and  $h_j$ , the enthalpy of the species, is calculated according to equation (5.7).

$$h_j = \int_{T_{ref,j}}^T c_{p,j} \cdot dT \quad (5.7)$$

The  $T_{ref}$  depends on the solver and the selected models. As the selected solver was pressure-based the default  $T_{ref}$  is 298.15K or 20°C is assumed.

The viscous model was enabled and the Re-Normalization Group "RNG k- $\epsilon$  (2 eqn)" selected (see Figure 95). The "RNG k- $\epsilon$ " model is similar to the "standard k- $\epsilon$ " model with substantial improvements – it is more accurate and more reliable, where the flow features include strong streamline curvature, vortices, and rotation are added. The "RNG k- $\epsilon$ " includes the following refinements:

- Additional term at the calculation equations that improves the accuracy for rapidly stained flows;
- Improves the swirling flows;
- Provides an analytical formula for the turbulent Prandtl number instead of the standard model that uses constant values;

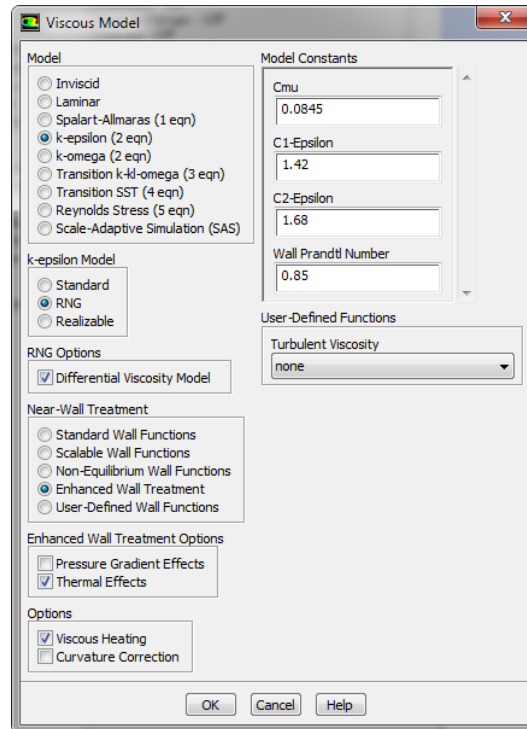


Figure 95 Viscous model definitions

For the models' constants were used the default values. The differential viscosity model was enabled to take into account the low-Reynolds number effects, because the studied model has near-wall regions in the domains.

To simulate the solidification and melting process, the solidification melting property function was enabled. For this feature other parameters were selected according to the PCM fluid characteristics. The momentum sink due to the reduced porosity in the mushy zone,  $S$ , calculated according to equation (5.8):

$$S = \frac{(1-\beta)^2}{(\beta^3 + \varepsilon)} \cdot A_{mush} \cdot (\vec{v} - \vec{v}_p) \quad (5.8)$$

Where  $\beta$  represents the liquid volume fraction,  $\varepsilon$  is a small constant (0.001) to prevent the division by 0,  $A_{mush}$  is the mushy zone constant set to 100000, that is the default value and  $\vec{v}_p$  is the pull velocity (solid velocity due to the pulling of solidified material out of the domain). The mushy zone constant measures the amplitude of the damping.

In this menu, it was selected to include pull velocities, as shown in Figure 96. This option takes into account the solidified material, as it is continuously withdrawn from the domain in the continuous casting process.

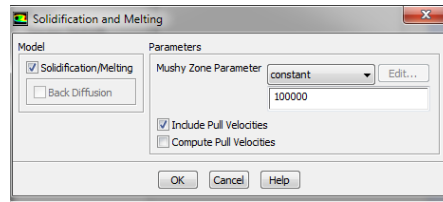


Figure 96 Solidification and melting menu

### 5.4.4 Solution methods and controls

During the simulated transient period, the PCM have multiphase state (liquid and solid). So, some parameters in the solution methods were changed in accordance to the calculation needs. The scheme selected for the calculations of the PCM model was the coupled, and the simple for the reference compartment. This coupled scheme is the most indicated for multiphase simulations. To improve the numerical calculations it was selected the Second Order Upwind for the special discretization of the Pressure, Momentum, Swirl Velocity and Energy as well as for the transient formulation option (see Figure 97.a). The Second Order Upwind is the Spatial Discretization option that provides high accuracy results of the computational calculations of the presented numerical model.

To improve the convergence of the numerical calculations it was used the high order term relaxation option and the values of the relaxation factor for the flow variables were changed to 0.9 (as shown in Figure 97.b). Some of the under relaxation factors at the solution controls menu were also changed from the default values to higher values, more precise for: pressure, momentum, turbulence dissipation rate and liquid fraction update as shown in Figure 97.c.

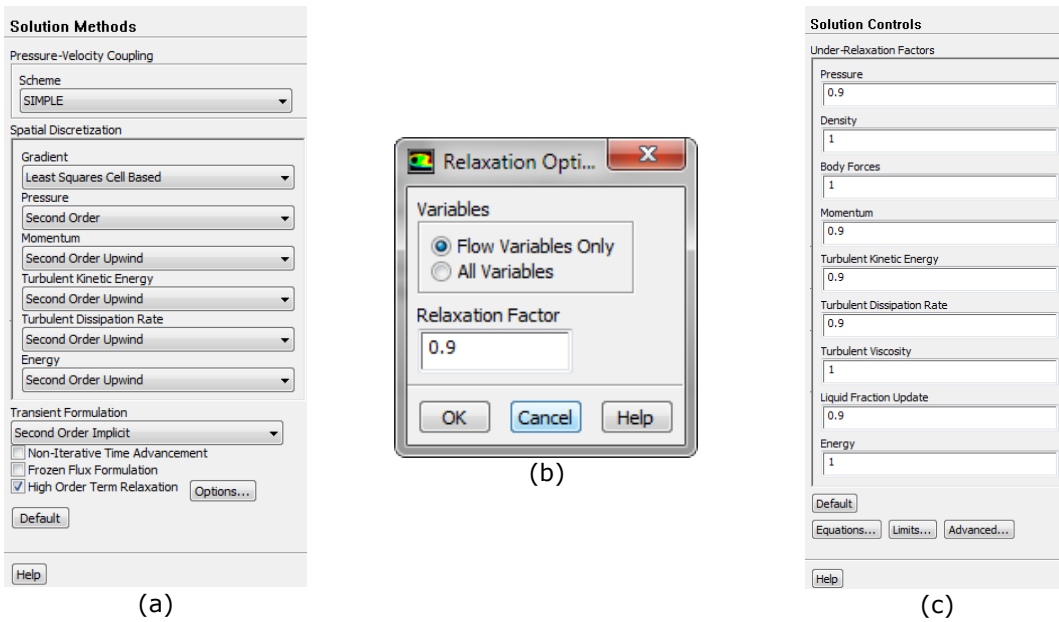


Figure 97 Definitions of the solution methods, (b) the relaxation option values and (c) solutions controls

#### 5.4.5 Solution initialization

Figure 98 presents the initial conditions for all domains of the reference numerical model. For the pressure, velocity and turbulence parameters it was used the default values (0 and 1). Therefore, as the internal temperature of the reference and PCM compartment is known (from the experimental testing campaign) the initial temperature of the models was changed. For the reference compartment the initial temperature was 295.4K or 22.25°C and for the PCM compartment was 297.13K or 23.98°C.

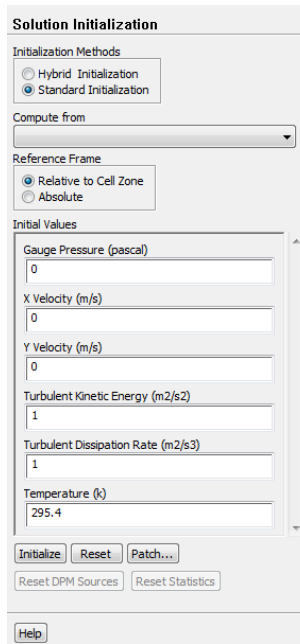


Figure 98 Menu of the solution initialization

#### 5.4.6 Calculation parameters

The last step before running the numerical calculations is the definitions of the “run calculation” menu (see Figure 99). The fixed time stepping method was selected with the time step sizes of 300s (or 5min) and the total time steps number of 2017 (which is equivalent to one week – 7 days).

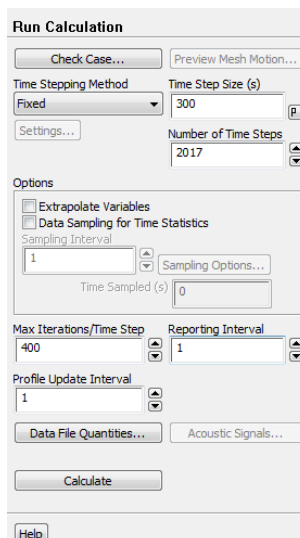


Figure 99 Calculation parameters of the 2D models

The size of the time steps of 5min was chosen to match the time step of the recorded data of the experimental testing campaign. The total number of time steps (2017) is equivalent to one week to compare with the experimental testing data ranging from the 2<sup>nd</sup> to the 9<sup>th</sup> of August.



### 5.4.7 Points of the numerical domains for the results analysis

To compare the indoor temperatures between the numerical and the experimental results it was defined three points in the interior domain of the numerical model (equivalent of the experimental testing probes location) (see Figure 100). Using these points the average temperatures were calculated and compared with the experimental data. In the following section, the temperatures profiles and thermal images of the numerical simulations are presented and also compared with the experimental data.

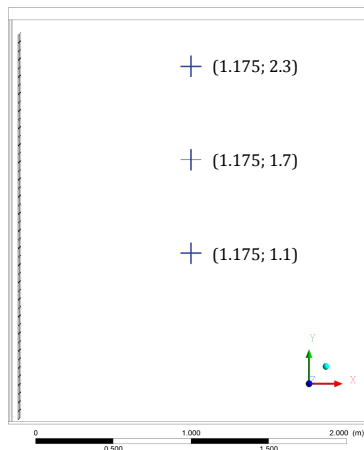


Figure 100 Point coordinates of the temperature results

## 5.5 Numerical results

### 5.5.1 Summer week

As explained and defined in sub-section 5.3 the numerical simulations were carried out resorting to the external weather data. The numerical results of the temperatures profiles between 2<sup>nd</sup> and 9<sup>th</sup> of August for both compartments are presented and compared in Figure 101.

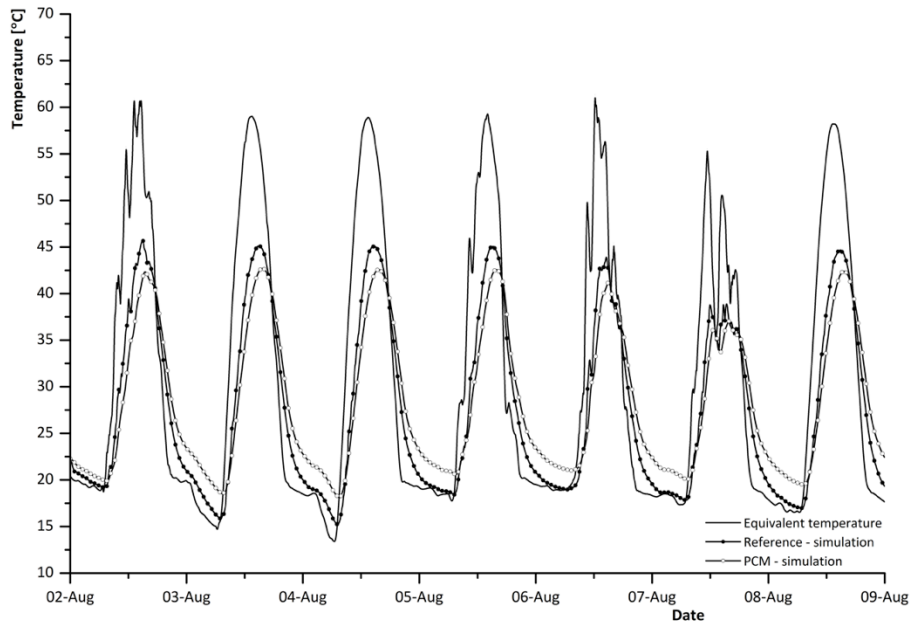


Figure 101 Temperature profiles in both compartments from the 2<sup>nd</sup> to 9<sup>th</sup> August

The results show that the indoor temperature amplitude of the PCM compartment is lower than the reference compartment. The thermal regulation by the PCM effect decreases the maximum indoor temperatures and increases the minimum indoor temperatures. During the warming period of the day (between 7h to 14h) the slope of the temperature profile of the PCM compartment is lower than the reference compartment (less steeper), which means that the PCM compartment will have a higher time delay between the imposed exterior temperature conditions and the indoor temperature. This feature is more significant when the indoor temperature reaches 25-27 degrees, because it is at this temperature range that the PCM begins the physical phase change. The PCM effect can be interpreted more clearly in Figure 102.

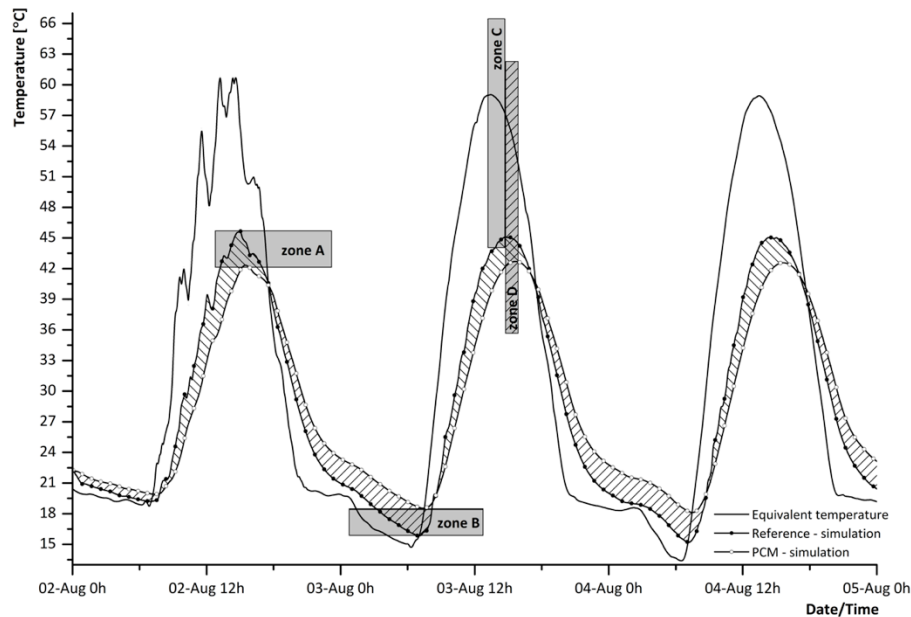


Figure 102 Temperature profiles in both compartments from the 2<sup>nd</sup> to the 5<sup>th</sup> of August

Analysing in detail the first three days of the simulation, the average temperature in the interior domain of the reference compartment ranges from 15°C to 46°C and for the PCM compartment ranges from 18°C to 42°C. The maximum temperature peak of the reference compartment is 46°C for the first day of simulation and the minimum was 15°C for the 4<sup>th</sup> August. Comparing the indoor temperatures of the PCM and reference compartment, the maximum temperature peak in the PCM compartment is 4°C lower (zone A) for the first day and the minimum temperature is higher 3°C (zone B) for the last day. Beyond the temperature regulation, that represents respectively an improvement of 8.7% for the day period and 16.7% for the night period, the PCM compartment increases significantly the time delay between the imposed exterior conditions and the internal domain. The maximum average temperature of the reference compartment is reached one hour after of the maximum imposed exterior condition, however the PCM compartment increases this feature up to two hours. However, for the night period the time delay between the imposed exterior conditions and the PCM compartment is not so significant. For this period the time delay between the PCM compartment and the minimum imposed temperature is reached one hour later and comparing with the reference compartment is about 30 minutes more. These results evidence the thermal regulation capacity of the PCM material.

The following figures (Figure 103 to Figure 107) present the indoor temperature contours of the reference and PCM compartments, for one selected day (3<sup>rd</sup> August). These results allow to compare more clearly the thermal behaviour inside each compartment on a daily cycle.

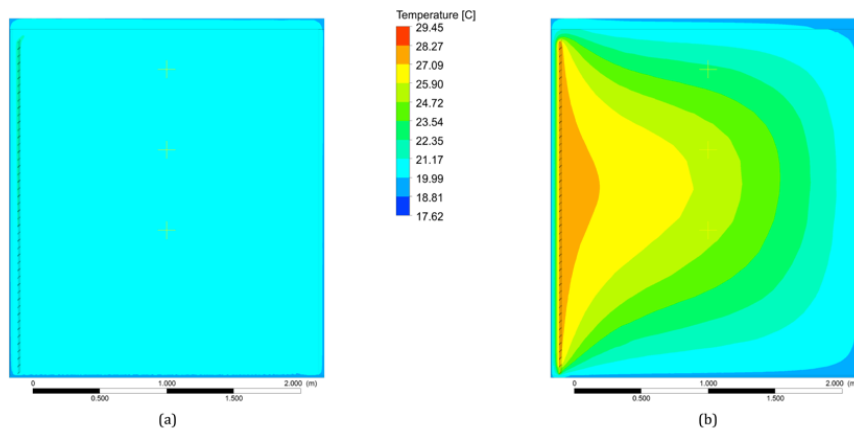


Figure 103 Temperature contours at 0h (3<sup>rd</sup> August) for the (a) reference compartment; (b) PCM compartment

Figure 103.a and (b) shows the temperatures contours at 0h for both compartments. The temperature inside of the reference compartment is constant and approximately 20°C, but the PCM compartment shows the effect of the phase change material. Analysing the PCM compartment, the imposed temperatures on the surrounding boundaries and the indoor temperatures are lower than the melting temperature of the PCM, so at this period the PCM is changing the physical state (from liquid to solid). This process is exothermic and the PCM is releasing the stored energy contributing to keep the indoor temperature of this compartment. The thermal contour of Figure 103.b reveals the PCM energy release and impact. At this specific time the maximum temperature difference between both compartments reaches 8°C nearest to the window shutter zone.

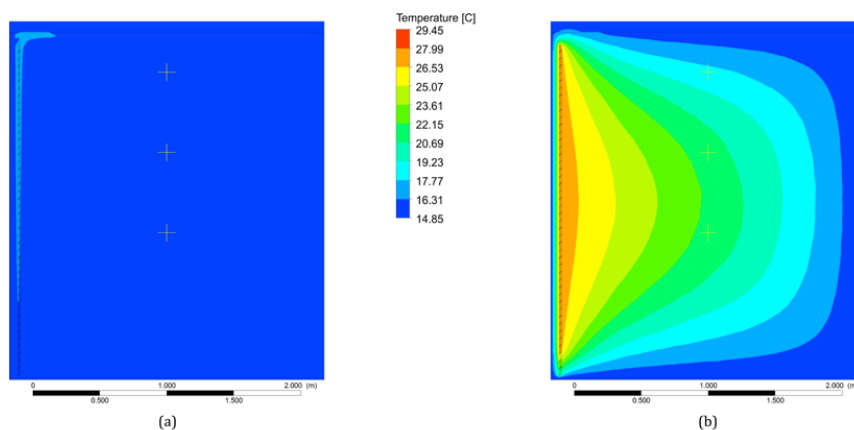


Figure 104 Temperature contours at 6h (3<sup>rd</sup> August) for the (a) reference compartment; (b) PCM compartment

Figure 104 shows the temperature contour at 6h for both compartments. The PCM compartment for this period keeps releasing energy and the temperature values closest to the window shutter range between 26°C and 27°C. The minimum

temperatures of the reference and PCM compartment are similar (15°C), however the reference compartment reveals the interior domain at low constant temperature.

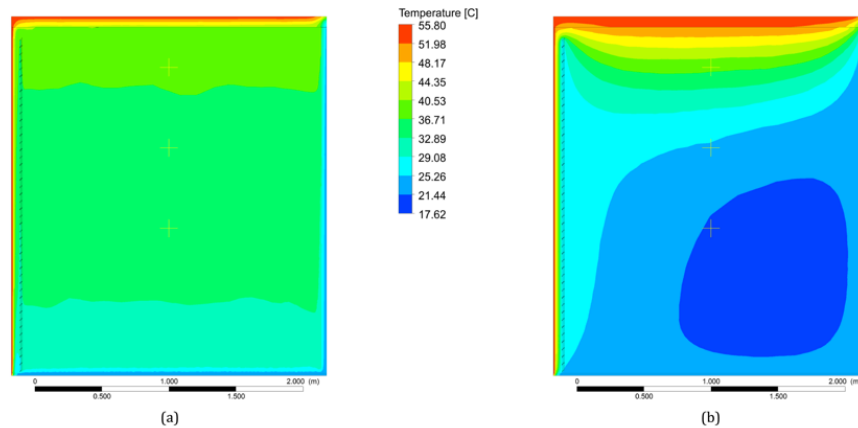


Figure 105 Temperature contours at 12h (3<sup>rd</sup> August) for the (a) reference compartment; (b) PCM compartment

Figure 105 presents the temperatures contours for noon (12h). At this time the temperature of the reference compartment is higher than the PCM compartment. The window shutter of the reference compartment, as expected, does not protect efficiently the indoor space from the exterior environment. The temperature contours of the reference compartment presents a quasi-uniform temperature with a strong and localised temperature stratification near to the internal roof surface (25°C to 40°C). Moreover, analysing the temperature contour of the PCM compartment it is clear that during this period, the imposed temperature on the roof and on the south wall surface contributes to increase the indoor temperature. The indoor temperatures and the imposed temperature on the mentioned surfaces are higher than the melting temperature of the PCM, so at this stage/time, the PCM is storing energy. During this endothermic process the PCM changes from the solid to liquid state and the latent heat capacity during this phenomenon allows the PCM to store a large quantity of energy, reducing the temperature increase inside the PCM compartment. The PCM compartment presents also temperature stratification ranging from 18°C to 30°C. Near the window shutter with PCM, as expected, is registered a better thermal behaviour compared with the others boundaries (walls and roof). The main solar energy gains occur through the roof, building up the indoor air temperature.

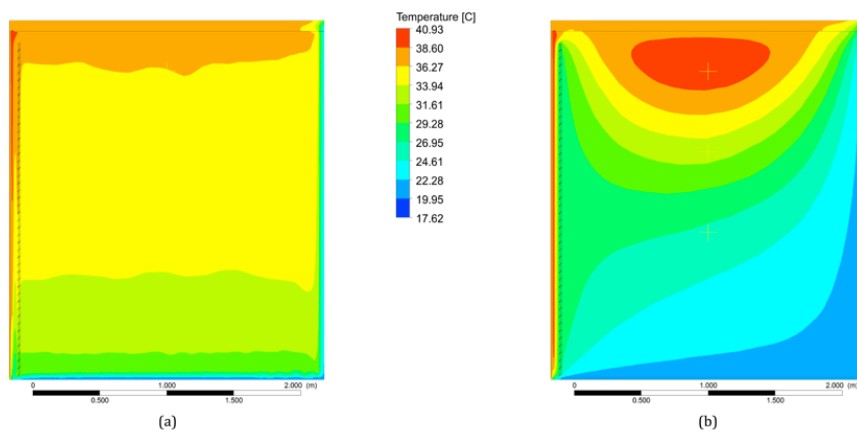


Figure 106 Temperature contours at 18h (3<sup>rd</sup> August) for the (a) reference compartment; (b) PCM compartment

The temperature contours for the 18h time step is presented in Figure 106. At this period the external air temperature and the solar radiation decrease, however the indoor temperatures of the compartments still remain high, mainly for the reference compartment. The indoor air temperature of the reference compartment, near to the roof internal surface, ranges from 36°C to 38°C, but at mid-height of the compartment keeps between 34°C and 36°C. As explained before, the external air temperature drops at this time, however the compartments increase the internal temperature throughout the day, keeping temperature high between 10h-20h. For the PCM compartment, the indoor temperature close to the roof surface ranges between 36°C and 40°C, and the indoor temperature is from 22°C to 34°C. The temperature near the window shutter with PCM to the interior domain, is between 27°C and 31°C, so at these temperatures the PCM starts to change from the liquid state to keeping a higher temperature range at this zone. However, according to the highest temperatures registered inside of PCM compartment it is expected that the PCM be completely melted between 12h (Figure 105.b) and 18h (Figure 106.b). During this period, when the PCM is in the liquid state the thermal behaviour is similar to a common material with sensible heat.

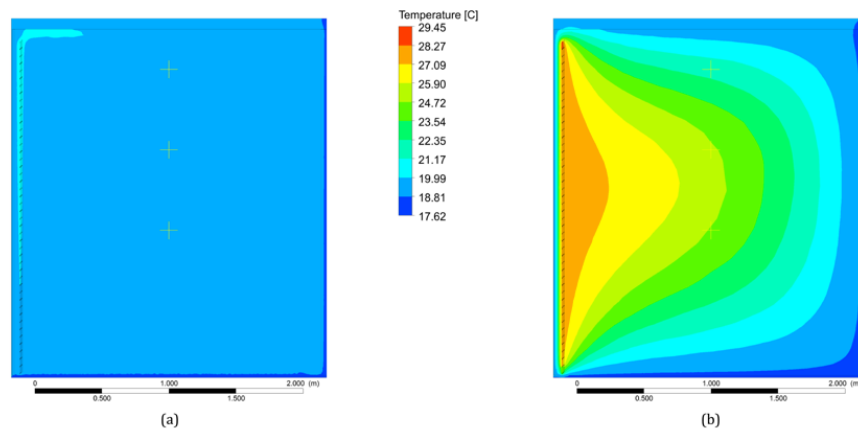


Figure 107 Temperature contours at 24h (3<sup>rd</sup> August) for the (a) reference compartment; (b) PCM compartment

Figure 107 presents a similar thermal behaviour as shown in Figure 103. This is at the end of a day cycle and at this time the PCM is releasing the stored energy, maintaining the indoor temperature of the PCM compartment.

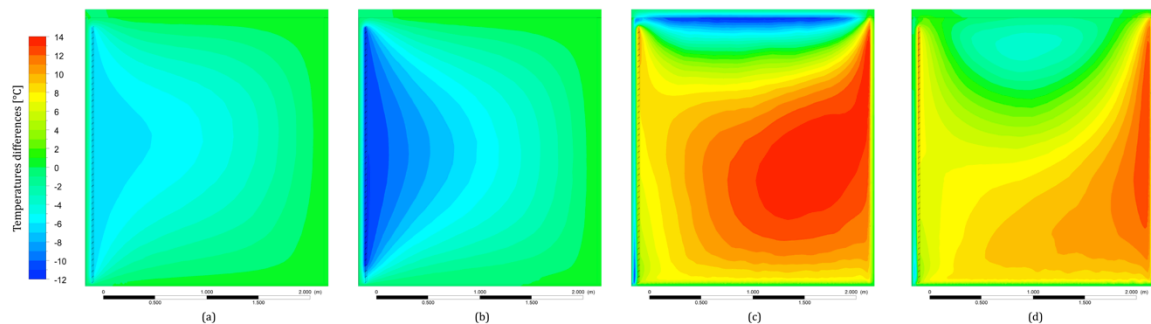


Figure 108 Contours of the temperatures differences between both compartments at (a) 0h; (b) 6h; (c) 12h, and (d) 18h

To understand clearly the indoor temperatures differences between both compartments, Figure 108 presents the contours of the temperatures difference between them for each time step. During the discharging period (when the PCM is releasing energy – from 18h to 6h) the indoor temperatures near to the window shutter are lower for the PCM compartment. The temperature difference between compartments during this period reached 11°C with the highest temperatures for the PCM compartment. During the charging period (when the PCM is storing energy – from 6h to 18h) the PCM presents a lower temperature values for the indoor domain. The temperatures nearest to the window shutter for the PCM compartment during this period are lower than the reference compartment. Near to the window shutter the temperature difference is 5°C to 9°C and at the mid-height of the indoor domain the maximum temperature difference is up to 13°C. However, during this charging period, the PCM compartment presents higher temperatures close to the internal roof surface. At 12h the PCM compartment

compared with the reference compartment presents a higher temperature up to 11°C and at 18h up to 6°C for the indoor space close to the internal roof surface. For thus, this phenomenon can be explained by the PCM storage capacity, as the PCM window shutter stores large energy quantities this boundary is more protected against the external imposed conditions. In consequence, the energy flux through the roof and the temperature stratification inside of the compartment near the roof domain are higher. The temperature difference on the peripheral boundary zones (roof, wall with north orientation and floor) is close to zero, as expected, since both models have the same imposed thermal conditions and external envelope layers composition.

### 5.5.2 Winter week

The numerical results of the temperatures profiles between 31<sup>th</sup> January and 4<sup>th</sup> February for both compartments are presented and compared in Figure 109.

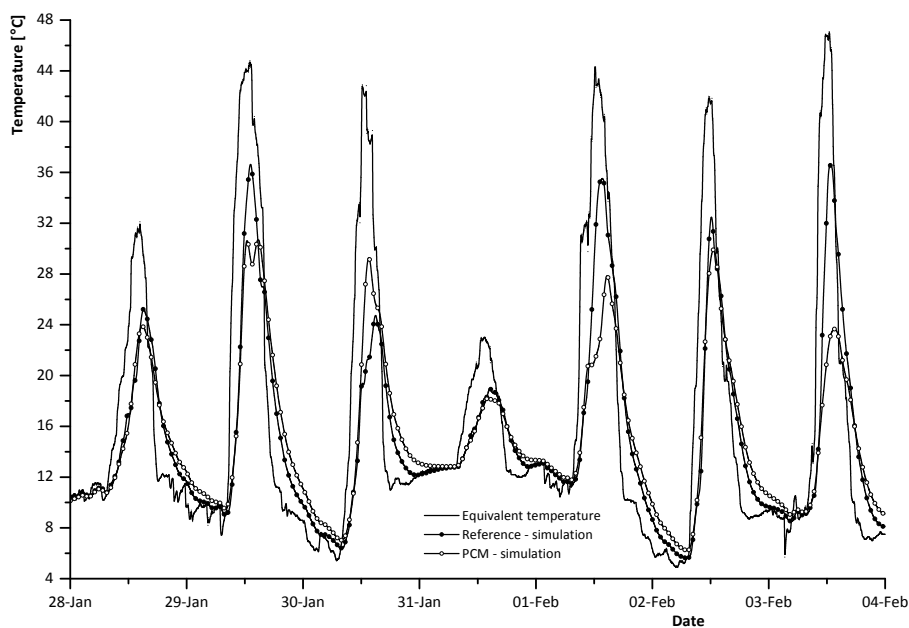


Figure 109 Temperature profiles in both compartments from the 31<sup>th</sup> January to 4<sup>th</sup> February

The indoor temperature profiles presented in Figure 109 reveal the benefits of the PCM introduction. For the simulated period, the maximum indoor temperature peaks of the PCM compartment are lower than the reference compartment, with the exception for the day 30<sup>th</sup> of January. Analysing the minimum temperatures, the difference between the PCM compartment and the reference compartment is not so significant. The minimum temperatures reached in the reference and PCM compartment are similar, however the temperature decreases faster for the reference compartment than the PCM compartment. Another significant



improvement from the PCM introduction is the time delay increment for both peaks, mainly for the maximum peak.

Figure 110, shows the temperatures profiles for the last three simulated days.

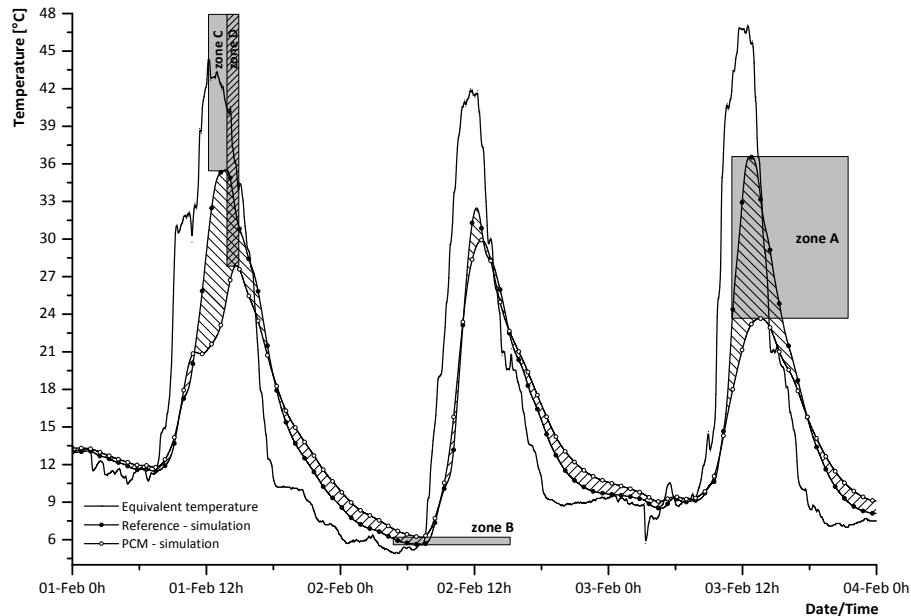


Figure 110 Temperature profiles in both compartments from the 1<sup>st</sup> to 4<sup>th</sup> of February

The zones A and B, represents the temperature difference between the models of the PCM and reference compartment. The zone C represents the time delay between the imposed equivalent temperature and the reference compartment and the zone D between the reference and the PCM compartment.

Analysing the zone A, the maximum indoor temperatures difference between the PCM and reference compartment is 12.9°C, which means that the maximum temperature peak in the PCM compartment is 23.65°C and on the reference compartment is 36.55°C. The minimum indoor temperatures reached in both compartments are similar. The reference compartment reaches 5.6°C and the PCM compartment 6.2°C, registering a temperature difference of 0.6°C (zone B).

The maximum indoor temperature on the reference compartment is reached at 13:42h, which is 1h:35min later than the maximum imposed temperature (Zone C). Comparing the time delay between the reference and the PCM compartment, the PCM compartment added 1h, which means that the maximum indoor temperature is reached approx. at 14:42h (Zone D).

Analysing the time delay between both compartments for the minimum indoor temperature, the time that the minimum temperatures are reached are similar, but in average, the PCM compartment increases 5 to 15min.

Therefore analysing the temperature profiles during the time that the outdoor temperatures drop (from 12:30 to 05:00), the thermal behaviour of the PCM compartment is more stable and constant (the indoor temperature in the PCM compartment decreases slowly and sweetly). These results show the PCM improvement during the daytime period, minimizing the faster temperature drop in this compartment.

The following figures present the indoor temperature contours for both compartments for one selected day (3<sup>rd</sup> of February). As the indoor temperatures on both models are similar between the 0h and 10h, it was chosen to compare a time range between 10h and 24h.

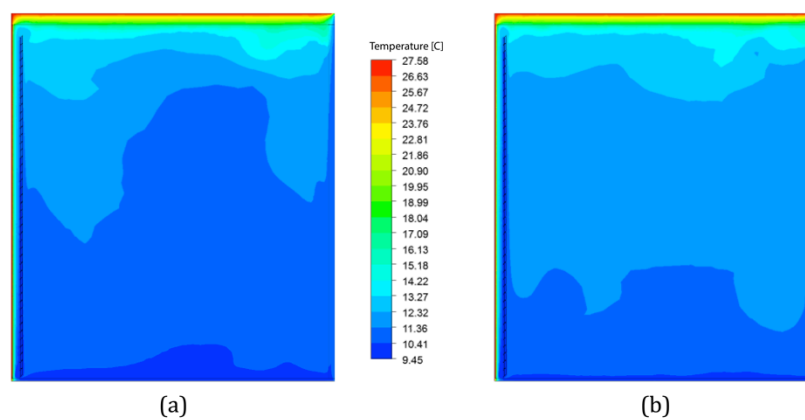


Figure 111 Temperature contours at 10h (3<sup>rd</sup> February) for the (a) reference model; (b) PCM model

Figure 111.a and Figure 111.b show the temperature contours for both models at 10h. At this time, the indoor temperatures of both models are similar but the PCM model presents a slightly higher temperature - up to 1°C. The temperature stratification at this time step is negligible and the solar radiation incorporated into the equivalent temperature definition - external boundary condition starts to be relevant.

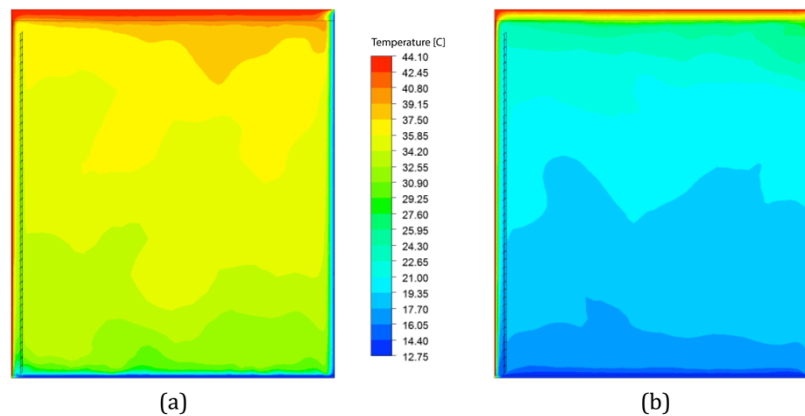


Figure 112 Temperature contours at 13h (3<sup>rd</sup> of February) for the (a) reference model; (b) PCM model

Figure 112 presents the temperatures profiles for the time period when the imposed boundary conditions are highest - the solar radiation and air temperature reaches the maximum peak. At this time, 13h, the reference model (Figure 112.a) presents significantly higher indoor temperatures comparing with the PCM model (Figure 112.b). The average temperatures at this time for the reference model is between 32.55°C and 39.15°C and on the PCM model is between 17.7°C and 25.95°C. As shown for both models, at this time step, the stratification of the indoor space is clear and more relevant for the air space between the window shutter and the double glazing unit.

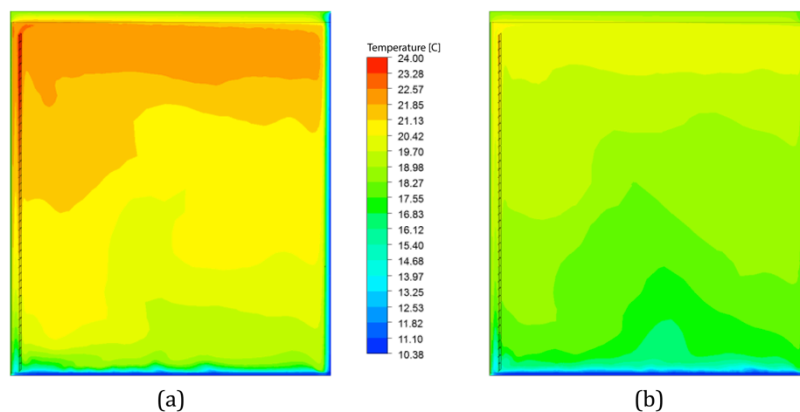


Figure 113 Temperature contours at 16h (3<sup>rd</sup> of February) for the (a) reference model; (b) PCM model

Figure 113 presents the temperatures contours at 16h. The indoor temperatures of both models are lower than the previous time step and the reference model (Figure 113.a) keeps the temperatures expressively higher than the PCM model (Figure 113.b). As expected, the temperature stratification for the reference model is higher than the PCM model. The PCM effect ensures the indoor temperatures for a longer period, dropping more slowly compared with the reference model. The reference model presents indoor temperatures between 16.83°C and 24°C, and the PCM model between 16.83°C and 20.46°C.

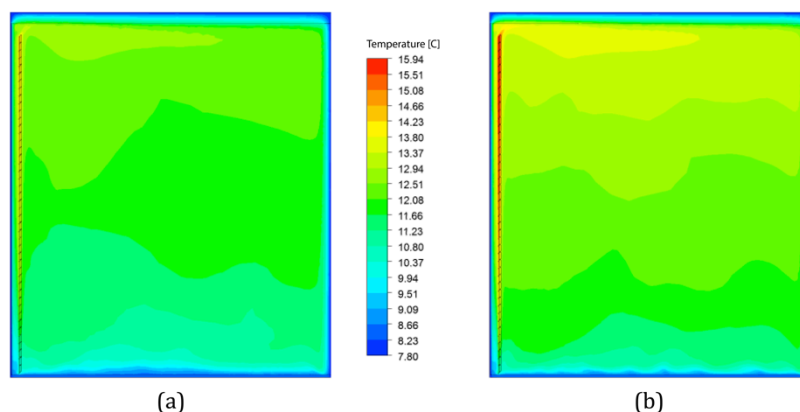


Figure 114 Temperature contours at 19h (3<sup>rd</sup> of February) for the (a) reference model; (b) PCM model

The temperature contours at 19h are presented in Figure 114.a for the reference model and in Figure 114.b for the PCM model. At this time step the external air temperature is lower and the solar radiation null, so the PCM has already released the stored energy, contributing to conserve the indoor temperatures higher. The temperatures close to the window shutter with PCM are higher than the reference model. Analysing the temperatures stratification, the PCM model shows a range between 11.23°C and 14.23°C and the reference model between 10.37°C and 12.94°C.

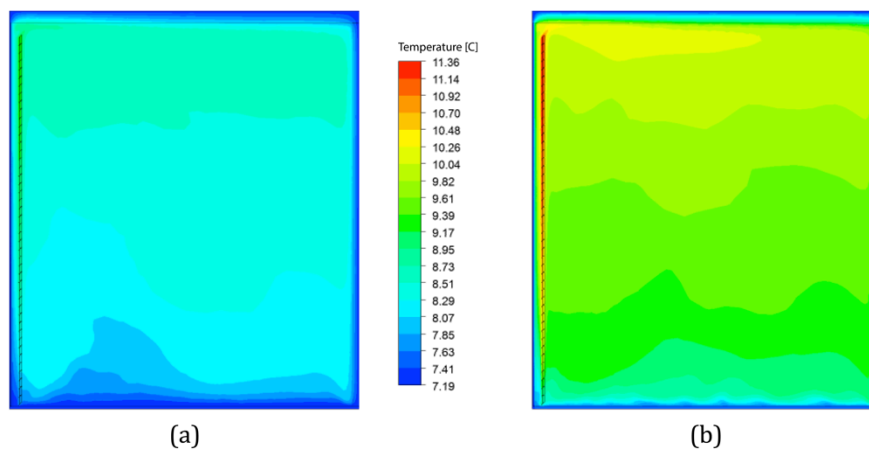


Figure 115 Temperature contours at 22h (3<sup>rd</sup> of February) for the (a) reference model; (b) PCM model

Figure 115 presents the indoor temperature contours for both models (with PCM - (a) and reference - (b)) for the time step that corresponds to 22h of the 3<sup>rd</sup> of February. The indoor temperature stratification for this period is insignificant - the reference model changes between 7.85°C and 8.51°C and on PCM model from 8.95°C to 10.04°C. At this time step, the indoor temperature for the PCM model keeps higher than the reference model, due to the previous PCM energy release which contributes to maintain the indoor temperatures higher.

To easily understand the indoor temperature differences between both models, Figure 116 shows the temperatures difference between the reference and PCM models.

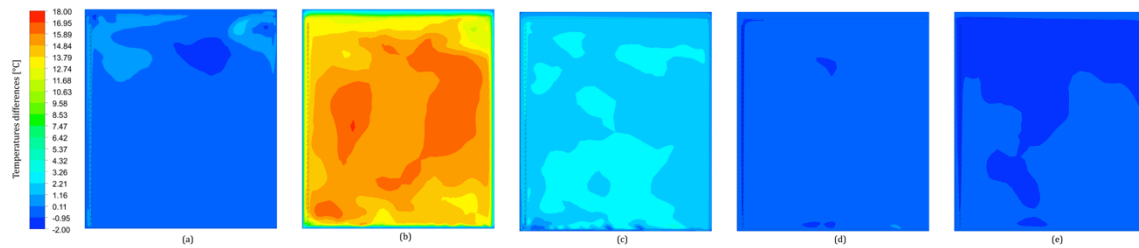


Figure 116 Contours of the temperatures differences between both compartments at (a) 10h; (b) 13h; (c) 16h; (d) 19h and (e) 22h

The main conclusions taken from each time step are:

- a) For this time step - 10h - the indoor temperatures differences between both models are mostly constant and range between  $-0.95^{\circ}\text{C}$  and  $0.11^{\circ}\text{C}$ , which means that indoor temperatures of the PCM model are higher than the reference model;
- b) At 13h time step the reference model presents higher temperatures than the PCM model. The difference is significant and ranges between  $12.74^{\circ}\text{C}$  and  $16.95^{\circ}\text{C}$ . For the PCM window shutter domain, the differences are also significant. The PCM model presents at the PCM domain a lower temperature up to  $15.89^{\circ}\text{C}$ ;
- c) For the 16h time step the indoor temperatures for the reference model are still higher than the PCM model. The temperature differences are between  $1.16^{\circ}\text{C}$  and  $3.26^{\circ}\text{C}$ ;
- d) Analysing the indoor temperatures on the reference compartment for this time step, 19h, it can be concluded that from the previous time step - 16h - the indoor temperatures for the reference model dropped faster than for the PCM model. The indoor temperatures for the reference model are lower or equal to the PCM model (difference between  $0.11^{\circ}\text{C}$  and  $-0.95^{\circ}\text{C}$ );
- e) For the last time step, 22h, the reference model has lower temperatures than the PCM model. In average, the most of the indoor domain is  $-2^{\circ}\text{C}$  than in comparison with the PCM model.

## 5.6 Numerical validation

The quantitative agreement of the measured indoor temperatures and the numerical calculated values were evaluated resorting to the most used statistical methods for these data analysis. It was evaluated the agreement between the numerical model and the experimental data resorting to the following criteria:

- Root mean square error (RMSE) [28, 191, 192];
- Percentage root mean square error (PRMSE) [28];

- Cumulative root mean square error (CVRMSE) [191-195];
- Mean bias error (MBE) [191, 192, 194, 195];
- Normative mean bias error (NMBE) [191, 193, 196];
- Goodness of fitness (GOF) [196];
- Correlation factor ( $R^2$ ) [28, 191];
- Box whisker mean (BWM) [191, 194, 195];
- Standard deviation [28];

These acceptance criteria are the most used for the building energy simulations. Considering the previous references, Table 18 summarizes the acceptable index values according to the based standards/guideline.

Table 18 Index calibration tolerances from the most used standards (based on [192, 193, 195])

Standard \ Index	ASHRAE 14 [191]	IPMVP [197]	FEMP [198]
CVRMSE <sub>hour</sub>	± 30%	± 20%	± 30%
CVRMSE <sub>month</sub>	± 15%		± 15%
MBE <sub>hour</sub>	± 10%	± 5%	± 10%
MBE <sub>month</sub>	± 5%	± 20%	± 5%

The Root Mean Square Error (RMSE) measures the variability between the experimental and numerical data. The Coefficient Variation of the Root Mean Square Error (CVRMSE) index quantifies and evaluates the dispersion between the experimental data and the simulated results. This index evaluates how well the simulated data fits with the experimental data and does not suffer from the cancellation effect as the MBE and NMBE indexes do. The follow equations (5.9), (5.10) and (5.11) define how the RMSE, the PRMSE and the CVRMSE indexes for the indoor temperatures comparison were calculated:

$$RMSE = \sqrt{\frac{1}{n} \sum_{i=1}^n (M_i - S_i)^2} \quad (5.9)$$

$$PRMSE = \sqrt{\frac{1}{n} \sum_{i=1}^n \left( \frac{M_i - S_i}{M_i} \right)^2} \quad (5.10)$$

$$CVRMSE = \frac{\sqrt{\frac{1}{n} \sum_{i=1}^n (M_i - S_i)^2}}{\bar{M}} \times 100 \quad (5.11)$$

where the  $S_i$  represents the temperature values of the numerical model and the  $M_i$  the recorded values of experimental campaign. The  $n$  represents the total number of values for the compared periods. For the compared period (between 2<sup>nd</sup> and 9<sup>th</sup> August)  $n$  is equal to 2016. For each recorded time step (each 5min) the difference between the experimental and numerical data is calculated and squared.

In addition, to validate the numerical results the average difference of the temperature values between the numerical and experimental data was calculated resorting to equation (5.12). The standard deviation,  $\sigma$ , was also analysed, according to equation (5.13).

$$|\bar{\Delta}| = \frac{1}{n} \cdot \sum_{i=1}^n |\Delta|_i \quad (5.12)$$

$$\sigma = \sqrt{\frac{1}{n} \cdot \sum_{i=1}^n (|\Delta|_i - |\bar{\Delta}|)^2} \quad (5.13)$$

where,  $|\Delta|_i$  is defined by equation (5.14):

$$|\Delta|_i = |S_i - M_i| \quad (5.14)$$

The Mean Bias Error compares the difference of the mean values between the experimental and numerical data as shown in equation (5.15). This is a non-dimensional value that can be presented in percentage and is a good indicator of the overall bias in the model. However, this index does not differentiate the positive and negative errors between them (offsetting errors), by other words this method has a cancelation effect because the positive bias offsets the negative bias.

$$MBE = \frac{\sum_{i=1}^n (M_i - S_i)}{\sum_{i=1}^n M_i} \quad (5.15)$$

The Normalized Mean Bias Error (NMBE), calculated in accordance to equation (5.16), compares the mean values of the experimental data with the simulated data and normalizes with the data of the mean experimental data. As the previous equations, the  $n$  represents the total number of values at the selected period and the  $M_i$  is the mean value of the experimental data. This statistical index is presented in percentage.

$$NMBE = \frac{\sum_{i=1}^n (M_i - S_i)}{n \times \overline{M_i}} \times 100 \quad (5.16)$$

The NMBE gives the perception of how close the numerical results are to the experimental data, however it presents the same weakness of the MBE in respect to the offsetting errors.

According to [196] the overall goodness of fit (GOF) can be calculated using equation (5.17):

$$GOF(\%) = \frac{\sqrt{2}}{2} \times \sqrt{NMBE^2 + CVRMSE^2} \quad (5.17)$$

### 5.6.1 Summer week

According to the previous equations the statistical indexes were calculated and the results are presented in Table 19.

Table 19 Values of the selected statistical indexes for the summer period analysed (2<sup>nd</sup> – 9<sup>th</sup> August)

Location	RMSE [°C]	PRMSE [%]	CVRMSE	$\sigma$ [°C]	MBE	NMBE [%]	GOF [%]
Reference Compartment	1.97	6.85	7.26	1.59	-0.02	-2.02	5.33
PCM compartment	2.43	9.62	8.95	1.70	-0.04	-3.94	6.91

Despite the assumptions and simplifications assumed for the 2D numerical model, the comparison of the numerical and experimental data demonstrates a good overall agreement.

The calculated statistical indexes values presented in Table 19 reveal a good agreement of the numerical and experimental indoor temperatures values. These statistical results of the PCM model are higher than the results of the reference compartment. The PRMSE over the testing period for the reference compartment is around 7% and increased slightly to 10% for the PCM compartment. The RMSE values for the reference compartment is about 2°C and increases to 2.4°C for the PCM compartment.

The standard deviation presents also a good accuracy of the tested methods, 1.6°C for the reference compartment and 1.7°C for the PCM compartment. Once again, the reference model presents better results (more accuracy) and this was expectable, because the PCM model is more complex to simulate, mainly due to the PCM phenomenon.



The Mean Bias Error (MBE) gives the average errors of the mean measured values. According [191, 194] to consider the model calibrated the hourly MBE values should be lower than 10%.

Cipriano, et al. [196] proposed a new procedure that has many similarities with Reddy [199] however the goodness of fit (GOF) criteria is twice more stringent than the previous one. This procedure can be used to calibrate building energy simulation models of real testing under indoor free-floating conditions. According [196] a GOF lower than 11% is recommended for trial agreement, so the overall results of the selected period present favourable GOF values.

Another property that shows better accuracy for the results of the reference compartment is the average of the correlation factor,  $R^2$ , which is presented in Figure 117. The correlation factor for the PCM compartment is 0.931 against 0.965 of the reference compartment. Observing Figure 117, that compares the recorded experimental indoor air temperatures with the simulated temperatures between 2<sup>nd</sup> and 9<sup>th</sup> August, for both compartments, it is evident that most of the data was well predicted. However, it is clear that the calculated temperatures have the tendency to be over predicted and this is more expressive during the charging period in the case of the PCM compartment. During this period, the PCM is storing energy and the PCM melting process contributes to increase this tendency. Another justification of this difference is due to the numerical model assumptions, which is represented by a 2D model. For example, the numerical model assumes perfect walls with constant thermal properties without any thermal bridges. In fact, this factor, along with others increase the indoor temperatures of the compartments, because they do not take into account the thermal losses that occur in the experimental model and the increase of the internal gains by the solar radiation during the day.

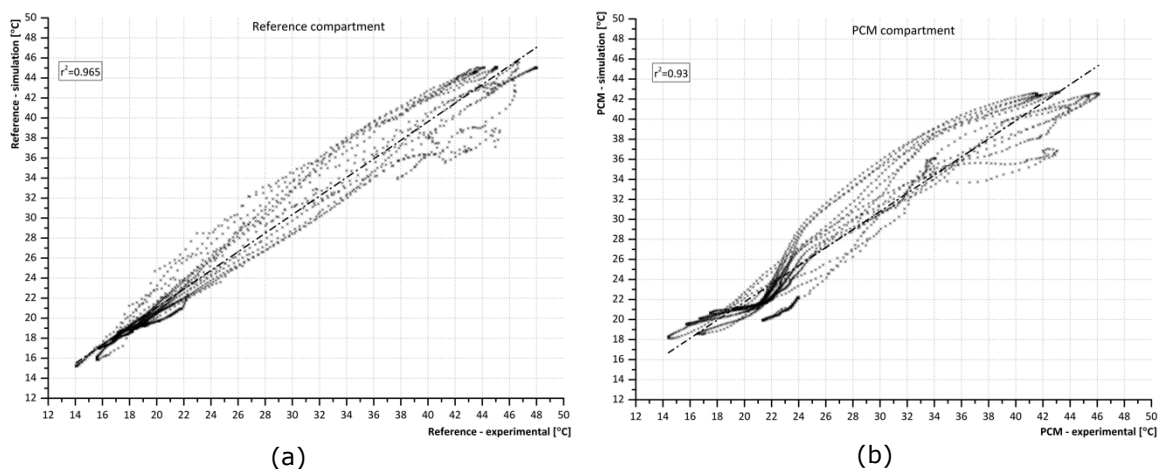


Figure 117 Experimental temperatures Vs. Numerical temperatures for the (a) Reference compartment (b) PCM compartment

Table 20 presents the calculated individual statistical indexes for the testing period. For each index, the results that present the best agreement between the experimental and numerical data are highlighted below:

Table 20 Statistical indexes for each testing day

Index	Compartment	02-Aug	03-Aug	04-Aug	05-Aug	06-Aug	07-Aug	08-Aug
RMSE [°C]	REF	0,98	1,82	2,32	1,45	1,64	2,67	2,37
	PCM	1,68	2,42	3,07	1,69	1,63	2,68	3,23
PRMSE [%]	REF	3,24%	6,92%	9,24%	4,75%	4,35%	7,66%	9,22%
	PCM	6,07%	8,89%	13,25%	6,73%	5,78%	9,74%	13,52%
STD	REF	0,64	1,41	1,87	1,03	1,33	2,31	1,92
	PCM	0,92	1,78	2,19	1,09	0,97	1,91	2,37
MBE	REF	0,01	-0,05	-0,08	0,01	0,02	0,02	-0,08
	PCM	0,04	-0,07	-0,11	-0,01	-0,01	-0,02	-0,11
NMBE [%]	REF	1,33	-5,46	-7,64	1,19	1,72	1,69	-8,01
	PCM	3,68	-6,56	-10,52	-1,22	-1,43	-2,17	-10,91
CVRMSE	REF	3,34	6,83	8,94	5,11	5,98	9,94	9,29
	PCM	5,69	9,02	11,92	6,01	5,95	10,03	12,62
GOF [%]	REF	2,55	6,18	8,32	3,71	4,40	7,13	8,67
	PCM	4,79	7,89	11,24	4,34	4,32	7,26	11,80

Analysing the results from Table 20, the three days that present the best agreement are 2<sup>nd</sup>, 5<sup>th</sup> and 6<sup>th</sup> of August. The 2<sup>nd</sup> of August is the day with the best fit, in accordance with the index statistical values. However, the 2<sup>nd</sup> of August is the first day of the numerical simulation and is constrained by the initial conditions of the numerical model.

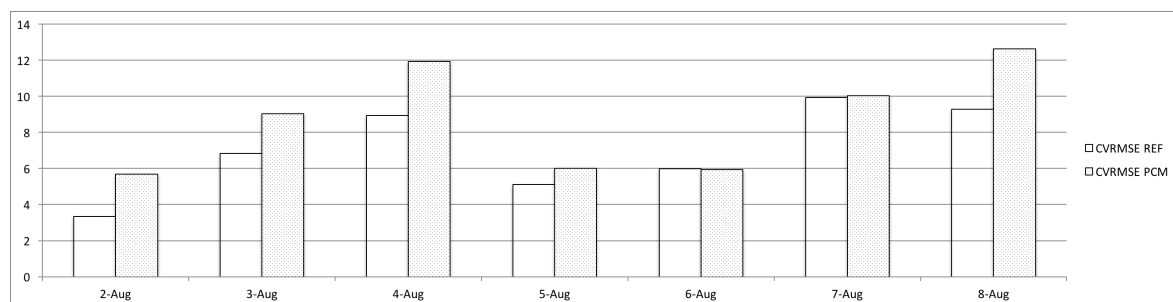


Figure 118 Plot of the daily Coefficient of Variation of the Root Mean Square Error

According [191, 194] the hourly CVRMSE should be lower than 30% for the model calibration. Analysing the CVRMSE index of both compartments (see Figure 118), the days that present best values are the 2<sup>nd</sup>, 5<sup>th</sup> and 6<sup>th</sup> August. For these days, the maximum CVRMSE index value is 6% and for the analysed period the days with highest error accumulation are 4<sup>th</sup> and 8<sup>th</sup> August that reach 12% for

the case of the PCM compartment. To conclude, results present a good overall agreement considering the CVRMSE limit values.

Figure 119 presents the daily Normative Mean Bias Error (NMBE) and it is clear the days with best agreement resorting to this index are: 2<sup>nd</sup>, 5<sup>th</sup>, 6<sup>th</sup> and 7<sup>th</sup> of August. The range from the 5<sup>th</sup> to the 7<sup>th</sup> August has the best fit, where the biggest difference is 2%. The results of the PCM compartment show a slight tendency for negative values, which means that during this period the most of times the calculated values are higher than the experimental data for the respective time step.

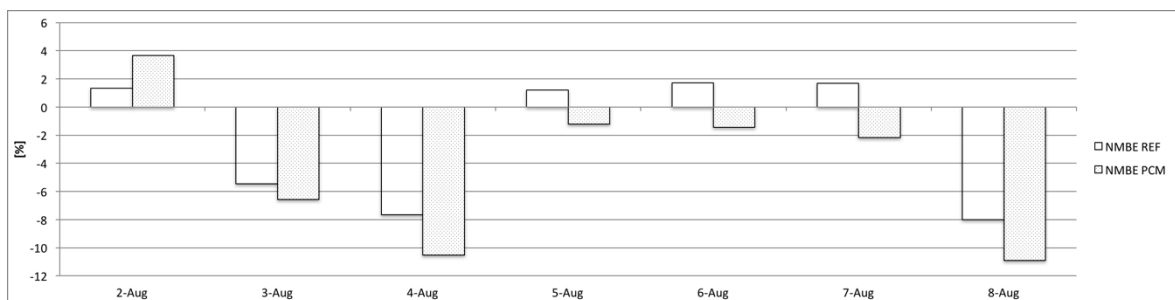


Figure 119 Plot of the daily Normative Mean Bias Error (NMBE)

According [196] that proposed this calibration procedure the results of the GOF index should be lower than 11%. Analysing the results presented in Figure 120, the most of the days show a good agreement (below 6-7%). The days that reveal a closer match to the measured data were the 2<sup>nd</sup>, 5<sup>th</sup> and 6<sup>th</sup> August. The 4<sup>th</sup> and 8<sup>th</sup> August for the PCM compartment attained a limit GOF value of 11%.

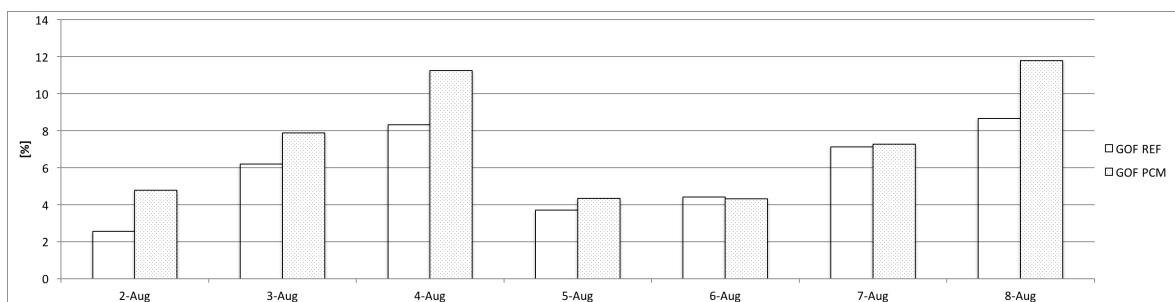


Figure 120 Plot of the daily Goodness of Fitness (GOF)

The box whisker mean (BWM) plots give a quick draw to analyse the temperatures of the reference and PCM compartments, allowing to compare the mean and the extreme values of the numerical simulations and experimental test values.

From Figure 121 and Figure 122 the main conclusions that can be taken are:

- The daily mean temperatures of the numerical and the experimental testing of the reference and PCM compartment are similar for most of the days. The last day (8<sup>th</sup> August) presents the highest difference and the 5<sup>th</sup> and 6<sup>th</sup> of August are the days with the most similar mean values;
- Considering the median line, the main conclusions are similar to the stated before, however, the reference compartment presented the best agreement between the numerical and experimental testing data and the PCM compartment presents a slight difference. For the reference compartment, the days with best fit were the 5<sup>th</sup> and 6<sup>th</sup> of August and for the PCM compartment were the 2<sup>nd</sup> and 6<sup>th</sup> of August. Analysing these results it can be also concluded that most of the data between 23°C to 26°C have a higher distribution and below this range a higher concentration;
- The reference compartment shows more similar minimum temperatures and has good agreement for each day, however analysing the maximum temperatures there is a high difference for the 7<sup>th</sup> August. For the PCM compartment most of the days presented an identical minimum and maximum temperatures;
- Analysing the results of the 2<sup>nd</sup> quartile of the reference compartment shows a best agreement between the numerical and the experimental testing. The numerical results of the PCM compartment reveal more points for this quartile than the experimental testing;
- Analysing the 3<sup>rd</sup> quartile, for most of the days the numerical and experimental data were similar. For both compartments, the three days that present higher differences between the numerical and experimental data are the 3<sup>rd</sup>, 4<sup>th</sup> and 8<sup>th</sup> of August, for which the numerical model reveals higher temperature range dispersion;
- As expected, the reference compartment presented higher whisker plots than the PCM compartment. This was expected, because this compartment has higher thermal amplitude and the thermal behaviour of this compartment changes faster, so it has more distributed values. A good example of this is the 2<sup>nd</sup> and 3<sup>rd</sup> quartiles that represent 50% of all data, where the temperatures range between 19 and 37°C for the reference compartment and 21°C to 34°C for the PCM compartment.

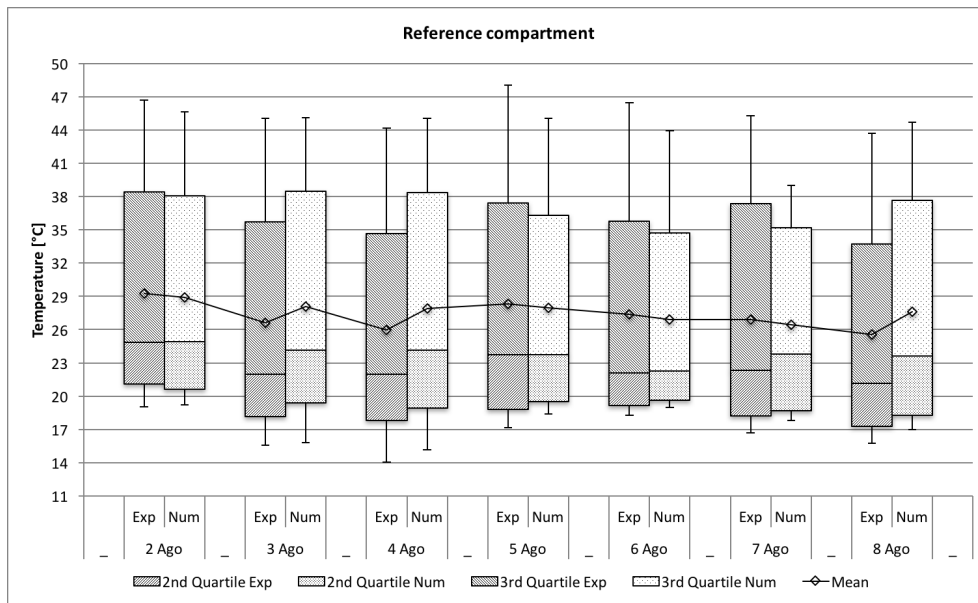


Figure 121 Box whisker mean (BWM) plot of the reference compartment

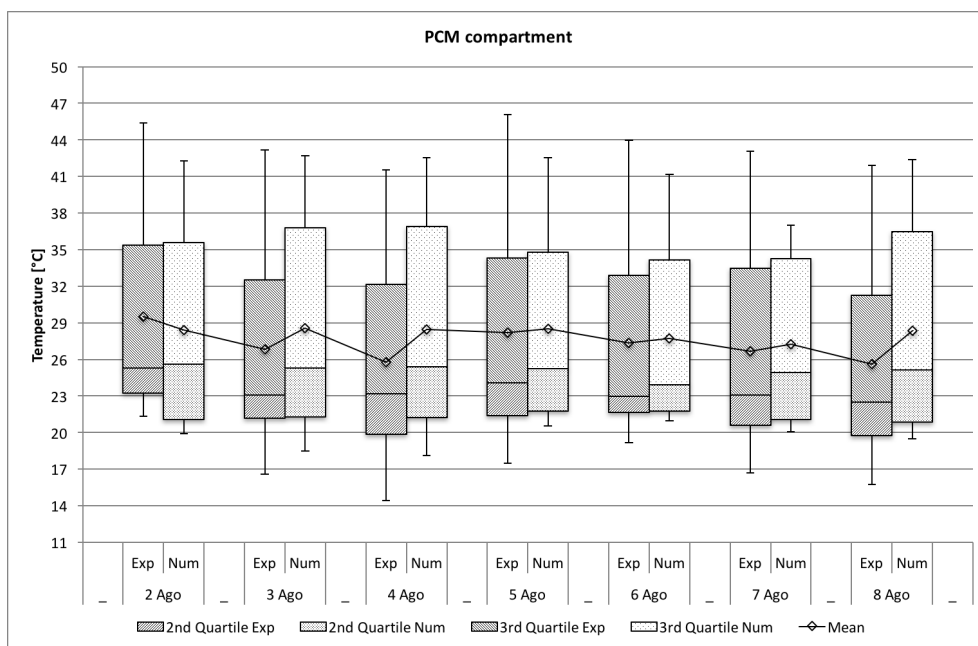


Figure 122 Box whisker mean (BWM) plot of the PCM compartment

Figure 123 presents the thermal behaviour of the temperature profiles between the numerical and the experimental testing. During the charging period, the numerical and experimental thermal profiles for both compartments are similar. For the discharging period the thermal profiles are similar, but for the PCM compartment there is a slight difference for the minimum temperature peak. The minimum numerical temperatures for the PCM compartment follow the experimental profile, however close of the minimum temperature peak the experimental values reach lower values than the numerical model.

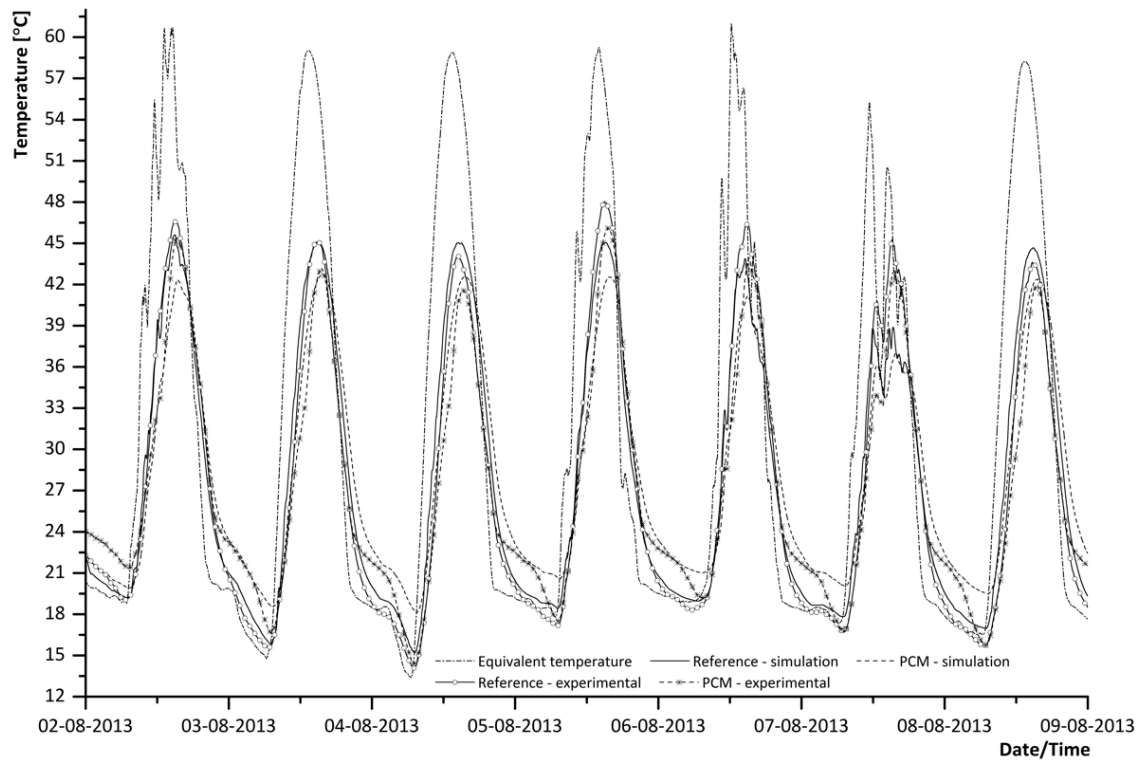


Figure 123 Comparison of the numerical results with the experimental data for the period between the 2<sup>nd</sup> and 9<sup>th</sup> of August

To compare in detail the numerical temperature obtained against the experimental data, Table 21 presents the values of the minimum and maximum indoor temperatures and their corresponding hour, the thermal amplitude and also the time delay between the PCM and reference compartments.

Table 21 Numerical versus experimental results

Indoor data		02 Aug		03 Aug		04 Aug		05 Aug		06 Aug		07 Aug		08 Aug	
		EXP	NUM	EXP	NUM	EXP	NUM	EXP	NUM	EXP	NUM	EXP	NUM	EXP	NUM
Reference	<sup>(1)</sup> Min Temperature	19.03	19.19	15.60	15.83	14.07	15.18	17.13	18.42	18.30	18.96	16.70	17.83	15.73	16.97
	<sup>(2)</sup> Max Temperature	46.70	45.65	45.07	45.10	44.17	45.05	48.03	45.07	46.47	43.94	45.30	38.99	43.67	44.69
	Amplitude <sup>(2)-(1)</sup>	27.67	26.46	29.47	29.27	30.10	29.87	30.90	26.65	28.17	24.98	28.60	21.16	27.93	27.72
	<sup>(3)</sup> <b>Time Min Temperature</b>	6:22	7:02	6:17	7:02	6:57	7:12	6:57	7:12	5:32	6:42	7:02	7:02	6:17	6:52
	<sup>(4)</sup> <b>Time Max Temperature</b>	14:47	15:02	14:32	14:42	14:17	14:22	15:02	15:12	15:02	14:32	15:17	14:42	14:42	14:52
PCM	<sup>(5)</sup> Min Temperature	21.35	19.91	16.60	18.53	14.40	18.12	17.50	20.59	19.15	21.01	16.70	20.07	15.75	19.49
	<sup>(6)</sup> Max Temperature	45.40	42.32	43.20	42.70	41.55	42.57	46.10	42.56	43.95	41.17	43.05	37.04	41.90	42.40
	Amplitude <sup>(6)-(5)</sup>	24.05	22.41	26.6	24.17	27.15	24.46	28.6	21.98	24.80	20.17	26.35	16.96	26.15	22.91
	<sup>(7)</sup> <b>Time Min Temperature</b>	7:02	7:22	7:02	7:22	7:02	7:32	7:02	7:32	7:37	7:22	6:57	7:22	6:47	7:22
	<sup>(8)</sup> <b>Time Max Temperature</b>	15:22	15:22	15:32	15:42	15:12	15:32	15:32	15:52	15:12	15:02	15:37	15:52	15:22	15:32
$T_{\min,PCM} - T_{\min,ref}$ <sup>(5)-(1)</sup>		2.32	0.72	1.00	2.70	0.33	2.94	0.37	2.17	0.85	2.05	0.00	2.24	0.02	2.52
$T_{\max,REF} - T_{\max,PCM}$ <sup>(6)-(2)</sup>		1.30	3.33	1.87	2.40	2.62	2.48	1.93	2.51	2.52	2.76	2.25	1.95	1.77	2.30
<b>Time delay for <math>T_{\min}</math></b> <sup>(7)-(3)</sup>		0:40	0:20	0:45	0:20	0:05	0:20	0:05	0:20	2:05	0:40	0:05	0:20	0:30	0:30
<b>Time delay for <math>T_{\max}</math></b> <sup>(8)-(4)</sup>		0:35	0:20	1:00	1:00	0:55	1:10	0:30	0:40	0:10	0:30	0:20	1:10	0:40	0:40

From the results shown in Table 21, some main conclusions can be taken relatively of the numerical and experimental results comparison:

- The minimum temperatures are similar, mainly for the reference compartment, where the higher difference registered was 1.29°C. However for the PCM compartment this difference was more expressive (between 1.44°C and 3.72°C);
- For the maximum temperatures, both models present a good agreement between the experimental and numerical data. For the reference and PCM compartment the temperatures differences reached 2.97°C and 3.54°C, respectively (except for the 7<sup>th</sup> August, where the differences for the maximum temperature peak reaches 6°C);
- For the reference compartment the minimum temperatures for the numerical model are mostly reached after the experimental testing (up to 60min). This same conclusion cannot be taken for the maximum temperatures, which ranges from +15min to -30min;
- For the PCM compartment both indoor peak temperatures (maximum and minimum) are first reached for the numerical model (except for the 6<sup>th</sup> August) and the time difference between them is mostly around 20min;
- Comparing the time delay that the PCM compartment presents comparatively to the reference compartment, the numerical and

experimental results are also similar. For the maximum indoor temperature peaks the difference between the numerical model and the experimental recorded data is almost between 0 and 15min and for the minimum temperature peaks the average difference is 15min.

According to the results of the statistical indexes, the best agreement between the experimental data and the numerical simulations is the 2<sup>nd</sup>, 5<sup>th</sup> and 6<sup>th</sup> of August. Figure 124 presents the indoor temperature comparison between the experimental and numerical model.

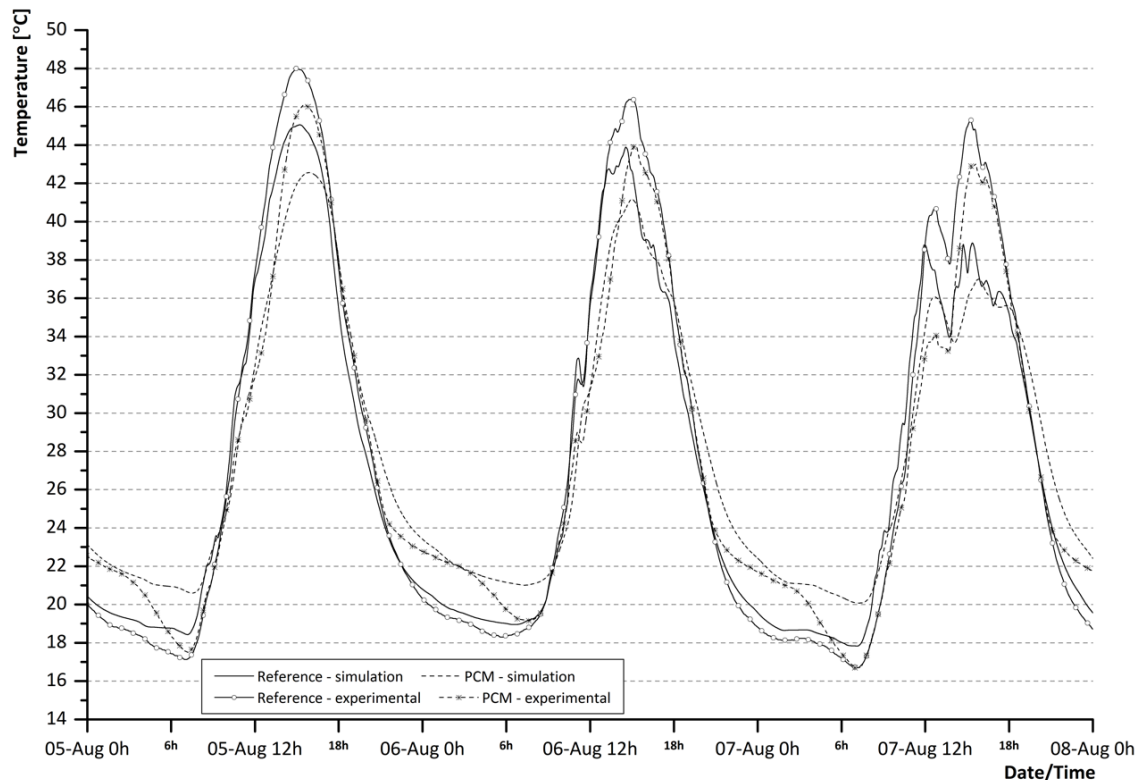


Figure 124 Comparison of the numerical and experimental data for the period of the 5<sup>th</sup> to the 8<sup>th</sup> August

Analysing the results of the reference compartment, the comparison between the indoor temperatures of the experimental data and the simulated data show a good agreement and a well-predicted model during this period. During the warming and cooling period of the day, the indoor temperatures of the experimental model fit with the indoor temperatures of the simulated model. Closest to the minimum temperatures, during the night, the numerical model presents a higher temperature than the real data recorded, however this is a slight difference (between 0 and 1°C). Analysing the maximum temperature peaks the experimental data presents a higher value that reaches a difference up to 3°C, compared with the simulated model.



The results of the PCM compartment for the selected period show a good agreement mainly during the warming period (daytime). During the night period, when the minimum indoor temperatures are reached, the temperature profile of the numerical model is slightly higher than the experimental model and can be up to 3°C. Considering maximum indoor temperatures of the PCM compartment the difference between the recorded data and the numerical results can be up to 5°C.

Analysing the time that the minimum and maximum temperatures are reached for both compartments, they are quite similar, so the time delay obtained between them is also similar.

Besides the similarity of temperature profiles for the warming and cooling period and the statistical indexes predicted a good agreement, the highest differences between models are observed for the minimum and maximum indoor temperatures peaks, mainly for the PCM compartment. For the numerical model, the PCM energy storage and release is not disturbed by losses or gains from the model boundaries, which clearly affect the experimental model. According to this, two main conclusions can be taken:

- During the night for the numerical model, when the minimum indoor temperatures are reached, the PCM releases the stored energy and maintains the indoor temperature between 21°C and 23°C, during about 6h. This energy release is most effective for the numerical model due to the model assumptions referred before;
- During the daytime period for the numerical model, when the maximum indoor temperatures are reached, the PCM stores energy contributing to attenuate the maximum temperatures and to minimize the indoor temperature drop. Once again, thermal bridges and air infiltrations affects the experimental testing contributing to increase the indoor temperatures of the compartments and justify the temperature differences between both models (experimental and numerical).

For the reference compartment, the temperature difference is minimized because there are no extra thermal storage or release as in the PCM compartment, so the slight differences of temperatures between the experimental and the numerical model can be explained by the previous reasons.

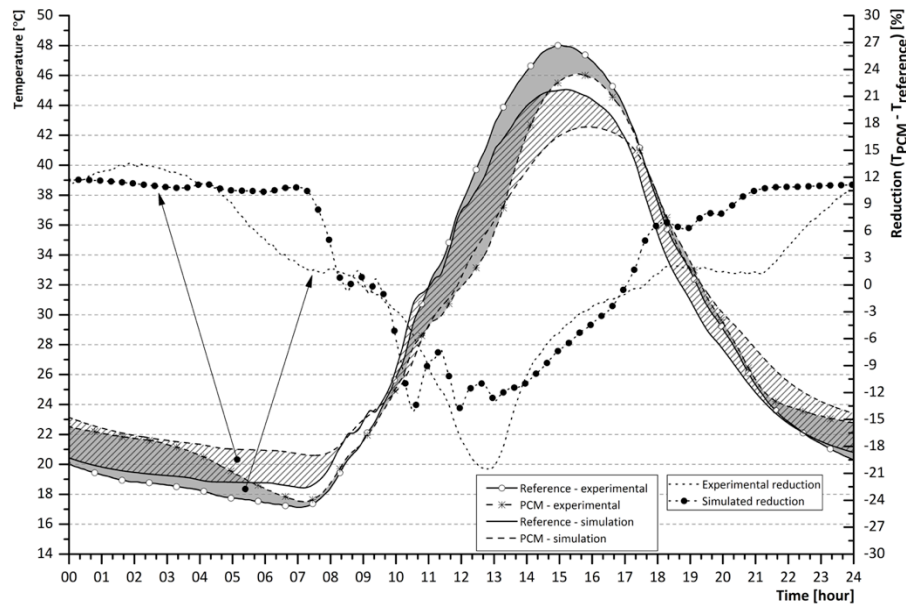


Figure 125 Thermal profiles for one day cycle (5<sup>th</sup> August)

Figure 125 presents the indoor temperatures profiles for the 5<sup>th</sup> August. The differences between the numerical and the experimental model are highlighted and the auxiliary y-axis shows the value of the temperatures differences between them. During this day the numerical model presents a thermal amplitude higher than the experimental model, which is 4°C for the reference compartment and 6°C for the PCM compartment. The minimum indoor temperature of the reference compartment is lower 1°C than the experimental model and the maximum temperature is higher 3°C than the numerical model. Analysing the PCM compartment, the numerical model presents the same behaviour, the minimum indoor temperature is higher 3°C and the maximum temperature is lower 3°C than the experimental recorded data. Comparing the time when the minimum and maximum indoor temperatures are reached, the numerical model presents slight differences. For the reference compartment, the minimum and the maximum indoor temperatures are reached 15min and 10min later than the numerical model and for the PCM compartment are reached after 30min and 20min respectively. Considering these results can be concluded that the numerical model increased the time delay between the PCM compartment and the reference compartment 15min for the minimum indoor temperatures and 10min for the maximum indoor temperatures, compared with the experimental recorded data.

### 5.6.2 Winter week

For the numerical validation, the experimental data of the winter results was treated as done before for the calculation of the equivalent temperature profile that was imposed on the external boundaries (roof and south walls) of the

numerical model. In this case, resorting to statistical commercial software was applied to the experimental data a filtering signal using the smooth algorithm with Fast Fourier Transform method (FFT) of 10 points. The filtered indoor temperature profiles compared with the measure data is shown in Figure 126.

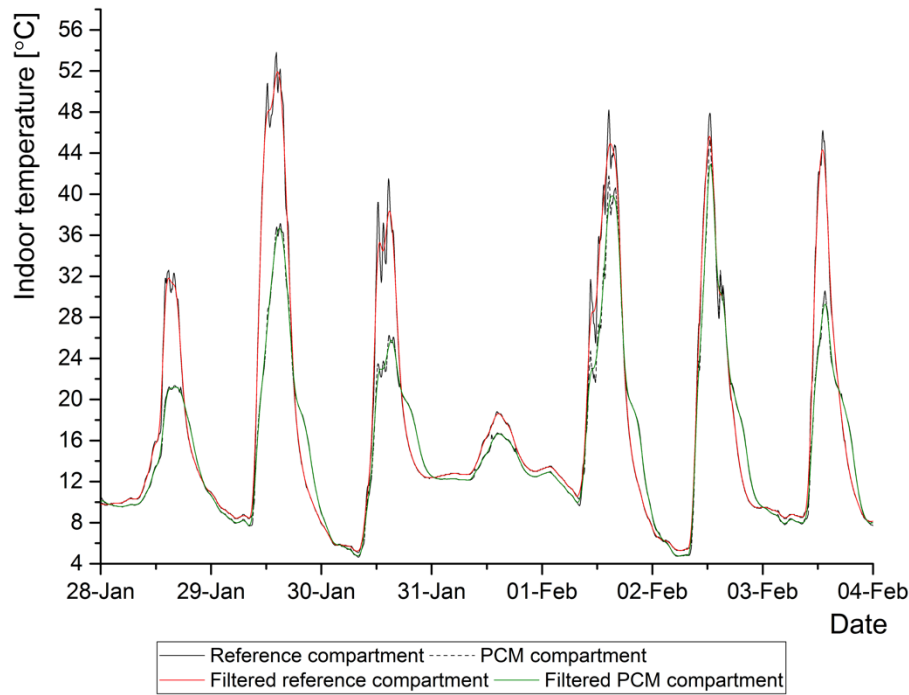


Figure 126 Filtered signal of the experimental indoor temperatures for the numerical comparison

According to the equations of the statistical indexes, presented at the beginning of this sub-section (sub-section 5.6), the overall statistical indexes for the winter period were calculated and presented in Table 22.

Table 22 Values of the selected statistical indexes for the analysed winter period (28<sup>th</sup> January to 4<sup>th</sup> February)

Location	RMSE [°C]	PRMSE [%]	CVRMSE	$\sigma$ [°C]	MBE	NMBE [%]	GOF [%]
Reference Compartment	5.30	16.49	30.96	4.55	0.12	12.33	23.56
PCM compartment	3.29	18.35	21.30	3.01	0.03	2.8	15.19

Despite the assumptions and simplifications assumed for the 2D numerical model, the comparison of the numerical and experimental data demonstrates a reasonable agreement. The CVRMSE and MBE indexes are in accordance with the standards ASHRAE 14 and FEMP for both models, however for the reference compartment values are near the limits. For the IPMVP [197] standard, the results of the overall CVRMSE are both higher than 20%, but the PCM model are close to the statistical agreement. In respect to the MBE index for the PCM compartment is in accordance with the limit values, but not for the reference compartment.

The correlation factor,  $R^2$ , was also calculated and analysed for both compartments. The reference and PCM compartment presents a correlation factor of 0.92 and 0.89 respectively.

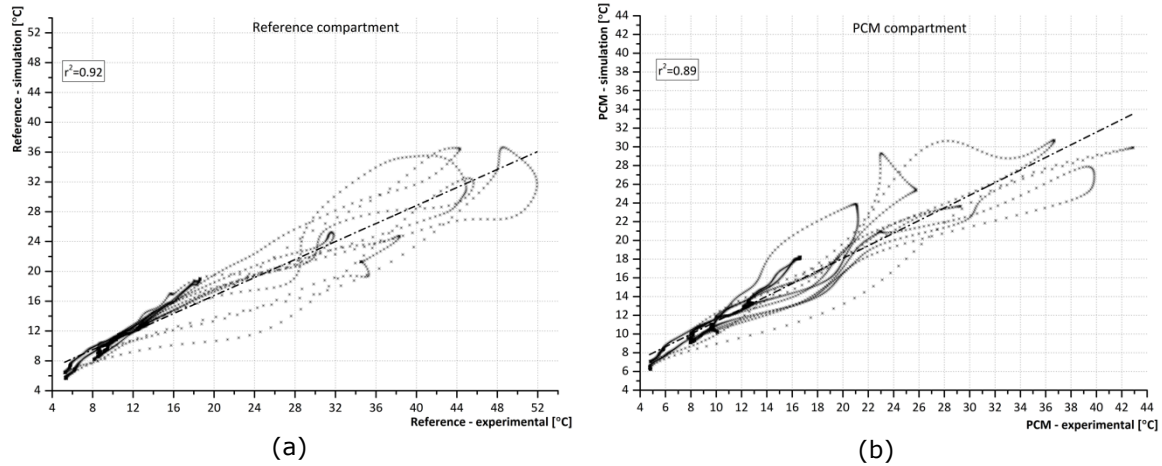


Figure 127 Winter results: experimental temperatures Vs. numerical temperatures for the (a) Reference compartment and (b) PCM compartment

Analysing the individual statistical indexes, which are presented in Table 23, three days were selected to discuss and compare the experimental data with the numerical calculated values.

Table 23 Statistical indexes for each testing day

Index	Compartment	29-Jan	30-Jan	31-Jan	01-Feb	02-Feb	03-Feb
RMSE [°C]	REF	8.91	6.15	0.25	5.43	5.86	2.77
	PCM	2.83	2.27	1.08	5.40	4.87	2.26
PRMSE [%]	REF	22.37	24.50	1.66	15.37	19.36	8.50
	PCM	16.82	26.83	7.57	17.81	24.35	14.53
STD	REF	7.76	5.10	1.91	4.52	4.86	2.45
	PCM	2.48	1.94	0.70	5.12	4.55	1.91
MBE	REF	0.22	0.17	-0.01	0.14	0.18	0.07
	PCM	0.02	-0.07	-0.07	0.15	0.14	0.04
NMBE [%]	REF	21.57	17.15	-0.58	13.62	18.25	7.04
	PCM	2.23	-6.60	-7.46	14.86	14.29	3.70
CVRMSE	REF	42.16	39.34	1.73	26.62	35.25	17.20
	PCM	16.40	16.67	7.97	27.86	29.23	16.07
GOF [%]	REF	33.49	30.35	1.29	21.15	28.07	13.14
	PCM	11.71	12.68	7.72	22.32	23.01	11.66

The first day (28<sup>th</sup> of January) was not considered because it is the first simulated day that is influenced by the initial conditions and by the model stabilization. Highlighted in Table 23 are presented the three days that presents best agreement, resorting to the selected statistical indexes. The 31<sup>th</sup> of January

and 3<sup>rd</sup> of February are the two days that presents best results for both compartments. The other day that shows best agreement for the PCM compartment is the 29<sup>th</sup> of January and for the reference compartment is the 1<sup>st</sup> of February.

Considering this results, the interval chosen to compare the calculated data against the experimental data was between 1<sup>st</sup> and 3<sup>rd</sup> of February. Besides the day with best agreement, the 31<sup>st</sup> of January, it was selected the 2<sup>nd</sup> day with best agreement to be used in the time period to compare the results. This decision was because *i)* the imposed conditions for the 31<sup>st</sup> of January are lower in comparison with the other days, so the indoor results for this day are more similar, *ii)* the 3<sup>rd</sup> of February is the day that presents agreement for all days, so in consequence it was chosen this day to be used in the time period and *iii)* the best time period possibilities are 1<sup>st</sup> to 3<sup>rd</sup> of February or 29<sup>th</sup> to 31<sup>st</sup> of January, however the latter presents more value discrepancies between both models. Due to these three reasons, the best continuous range to compare and to validate the numerical models is from 1<sup>st</sup> to 3<sup>rd</sup> of February.

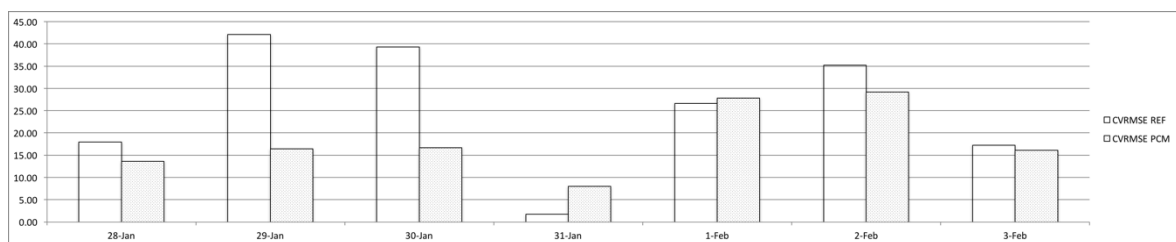


Figure 128 Plot of the daily Coefficient of Variation of the Root Mean Square Error

Analysing the CVRMSE index during the testing time (Figure 128), that should be lower than 30%, the last three days do not presents so high discrepancies results between the reference and the PCM compartment. For the reference compartment, these days presents best average results than the other days, however for the PCM compartment the first three days reveal better agreement.

Figure 129 presents the daily Normative Mean Bias Error (NMBE) and once again the last three days presents lower discrepancies between the results of the PCM and reference compartments. The results for the PCM compartment for the first days shows a slight tendency for negative values which means that during this period, most of times the calculated values are higher than the experimental data at this time step.

## 5.6 Numerical validation

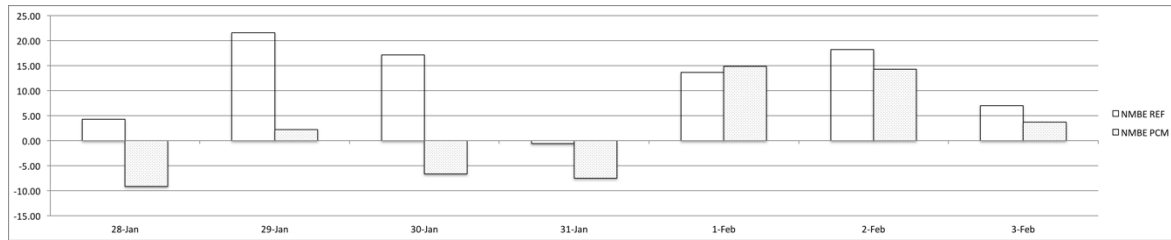


Figure 129 Plot of the daily Normative Mean Bias Error (NMBE)

The Figure 130, presents the goodness of fit (GOF) for the selected testing period. According [196] that proposed this calibration procedure, the results of the GOF index should be lower than 11%. Analysing the results presented in Figure 130, for the reference compartment, the most of the days presents higher GOF values, which means according to this statistical index this model is not calibrated. For the PCM compartment, the GOF statistical index for 1<sup>st</sup> and 2<sup>nd</sup> of February are higher than the acceptable value, however for the other testing days are in the limit.

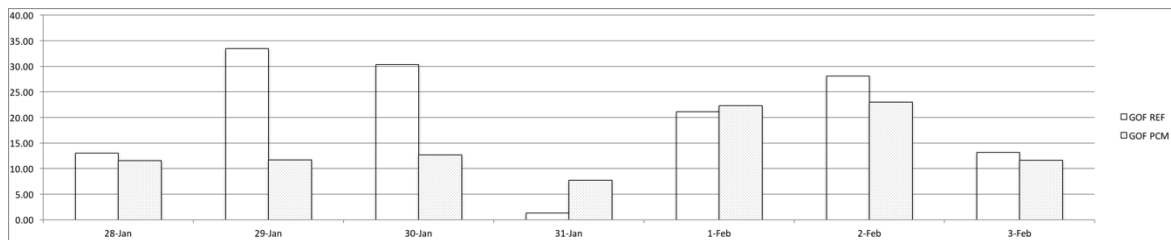


Figure 130 Plot of the daily Goodness of Fitness (GOF)

The box whisker mean (BWM) plots give a quick draw to analyse the temperatures of the reference and PCM compartments, allowing to compare the mean and the extreme values of the numerical simulations and the experimental testing.

From Figure 131 and Figure 132 the main conclusions that can be taken are:

- The most of the days, the mean temperatures values are higher for the experimental testing data than the numerical model (for both compartments). With the exception of the 31<sup>st</sup> of January for the reference compartment, for which the experimental and numerical analysis presents similar mean temperatures and for the PCM compartment the 30<sup>th</sup> of January for which the numerical model shows higher mean temperatures values;
- Considering the median line, the main conclusions are different. The reference compartment presents best agreement between the numerical and the experimental testing and the PCM compartment presents a slight difference without a conclusive tendency. Analysing these results it can be

also concluded that most of the data above  $\pm 12^{\circ}\text{C}$  have a higher distribution and below this range a higher concentration;

- Both compartments shows a similar minimum indoor temperature, however analysing the maximum temperatures the box whisker plots show a clear difference - the maximum temperatures are higher for the experimental testing data;
- Analysing the results of the 2<sup>nd</sup> quartile of the reference and PCM compartment the experimental and numerical model present similar results, mainly for the reference compartment;
- Analysing the 3<sup>rd</sup> quartile, the numerical and experimental model present similar results, mainly for the PCM compartment. For the reference compartment, the 29<sup>th</sup> of January shows significant results discrepancies for this quartile.

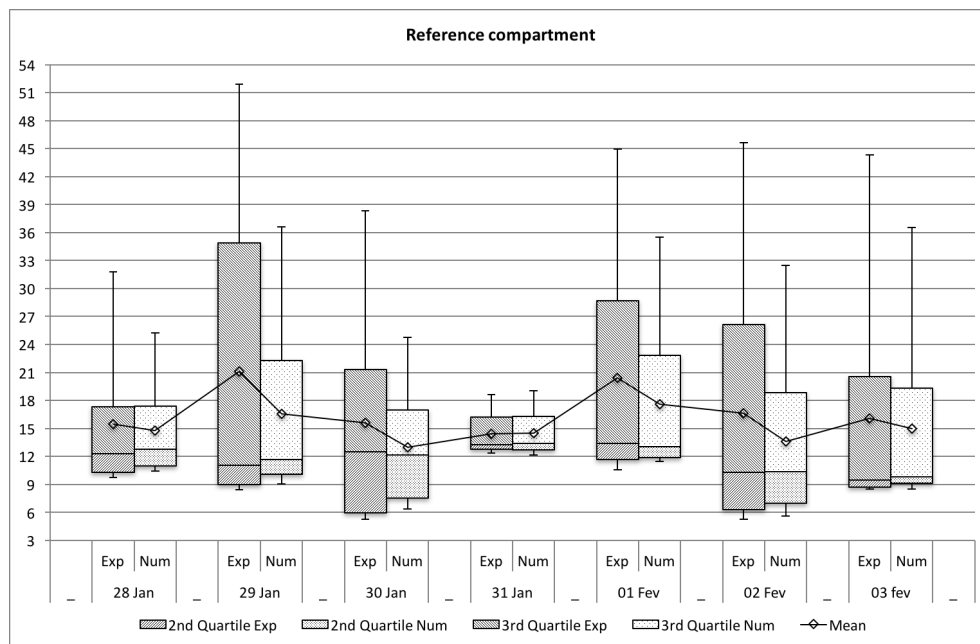


Figure 131 Box whisker mean (BWM) plot of the reference compartment

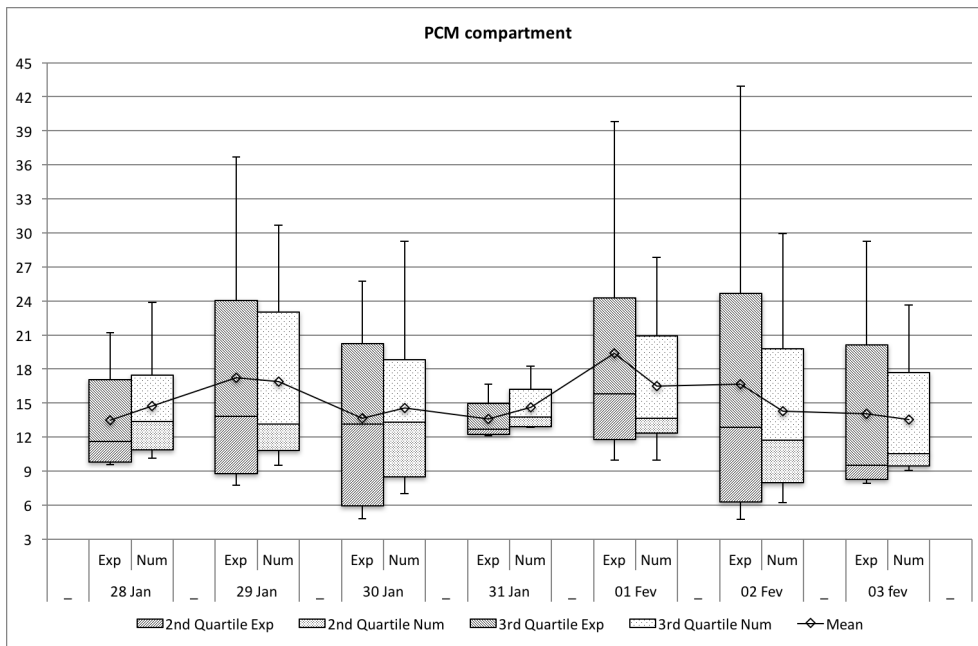


Figure 132 Box whisker mean (BWM) plot of the PCM compartment

Figure 133 presents the thermal behaviour of the temperatures profiles between the numerical and the experimental testing data.

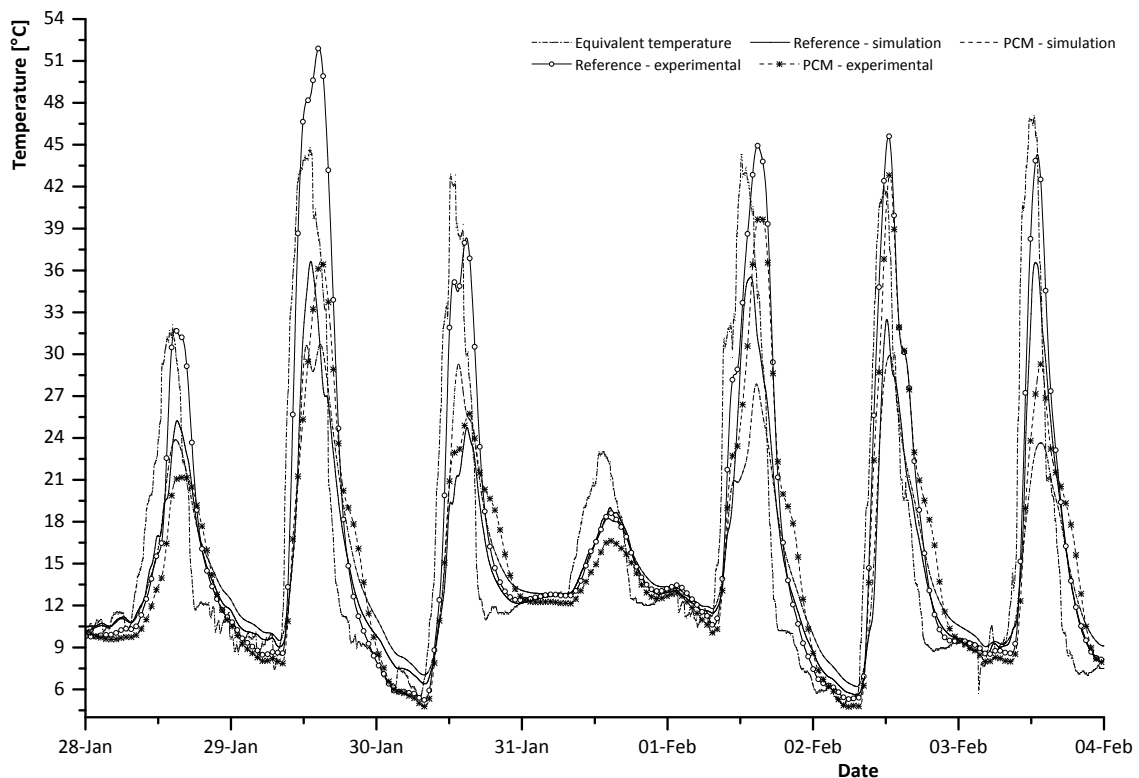


Figure 133 Comparison of the numerical results with the experimental data for the period between the 28<sup>th</sup> of January and 4<sup>th</sup> of February



The thermal behaviour of both temperatures profiles - numerical and experimental - are similar therefore it is clear the value differences between them. Another characteristic that stands out is that the equivalent temperature profile imposed to the numerical models is the most of the time lower than the recorded indoor temperatures. As described and discussed before, besides of the signal treatment which improved the equivalent temperature and approximate the imposed profile to the real conditions, this is not enough and the equivalent temperature still is lower than the measured indoor temperatures for the reference compartment.

The Table 24 presents in detail the measured and the numerical results for both compartments. It is presented the maximum and minimum indoor temperatures, the thermal amplitude and the time delay of the minimum and maximum indoor temperature for both compartments.

Table 24 Numerical versus experimental results

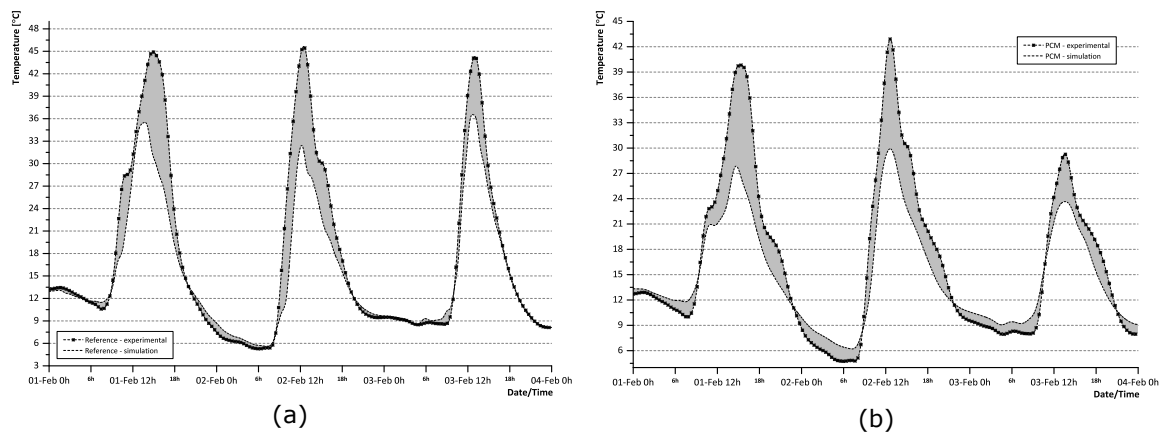
Indoor data		28 Jan		29 Jan		30 Jan		31 Jan		01 Feb		02 Feb		03 Feb	
		EXP	NUM	EXP	NUM	EXP	NUM	EXP	NUM	EXP	NUM	EXP	NUM	EXP	NUM
Reference	<sup>(1)</sup> Min Temperature	9.76	10.44	8.43	9.04	5.23	6.40	12.39	12.18	10.56	11.47	5.28	5.60	8.49	8.51
	<sup>(2)</sup> Max Temperature	31.82	25.23	51.93	36.64	38.34	24.75	18.63	19.01	44.93	35.53	45.65	32.49	44.31	36.55
	Amplitude <sup>(2)-(1)</sup>	22.06	14.80	43.49	27.60	33.11	18.35	6.24	6.84	34.36	24.06	40.37	26.88	35.82	28.04
	<sup>(3)</sup> Time Min Temperature	1:17	0:02	5:32	7:57	7:47	8:02	0:02	0:02	7:37	7:27	6:07	7:07	4:52	4:42
	<sup>(4)</sup> Time Max Temperature	14:47	15:07	14:27	13:07	14:47	14:57	14:32	14:32	14:52	13:42	12:27	12:12	12:57	12:37
PCM	<sup>(5)</sup> Min Temperature	9.57	10.14	7.74	9.50	4.78	7.03	12.14	12.83	9.97	11.78	4.74	6.20	7.93	9.05
	<sup>(6)</sup> Max Temperature	21.20	23.88	36.68	30.70	25.77	29.29	16.64	18.24	39.84	27.87	42.91	29.92	29.29	23.65
	Amplitude <sup>(6)-(5)</sup>	11.63	13.74	28.94	21.21	20.99	22.26	4.50	5.40	29.87	16.09	38.16	23.72	21.35	14.60
	<sup>(7)</sup> Time Min Temperature	4:27	0:02	8:17	7:57	7:57	7:52	7:52	5:17	7:42	7:27	5:57	7:12	4:42	4:27
	<sup>(8)</sup> Time Max Temperature	16:17	14:52	14:52	14:42	15:12	13:32	14:37	14:12	15:17	14:42	12:37	12:37	13:32	13:32
$T_{\min,PCM} - T_{\min,ref}^{(5)-(1)}$		-0.19	-0.30	-0.69	0.46	-0.45	0.63	-0.25	0.66	-0.60	0.31	-0.53	0.60	-0.56	0.55
$T_{\max,REF} - T_{\max,PCM}^{(6)-(2)}$		10.62	1.36	15.25	5.94	12.57	-4.54	1.99	0.78	5.09	7.66	2.74	2.57	15.02	12.90
<b>Time delay for <math>T_{\min}^{(7)-(3)}</math></b>		3:10	0:00	2:45	0:00	0:10	-0:10	7:50	5:15	0:05	0:00	-0:10	0:05	-0:10	-0:15
<b>Time delay for <math>T_{\max}^{(8)-(4)}</math></b>		1:30	-0:15	0:25	1:35	0:25	-1:25	0:05	-0:20	0:25	1:00	0:10	0:25	0:35	0:55

The main conclusions taken from the results shown in Table 24 are:

- The minimum temperatures reached for the numerical and experimental model are similar for the most of the days. The higher minimum temperature difference between the numerical and experimental model is 1.17°C for the reference compartment and 0.68°C for the PCM compartment;

- Analysing the maximum temperatures of the numerical and experimental models, the differences are more significant. The experimental model has maximum indoor temperatures up to 15°C for the reference compartment and up to 12°C for the PCM compartment;
- For the reference compartment the minimum temperatures on the numerical model are reached half of the times after the experimental testing (up to 90min). For the others 50% of the time, the minimum indoor temperatures for the numerical model is reached at the similar time of the experimental testing. For the PCM compartment the conclusions are similar;
- Comparing the time delay between the experimental and numerical models for the minimum indoor temperatures peaks, the reference compartment presents best agreement, mostly between 1<sup>st</sup> and 3<sup>rd</sup> of February where the maximum time delay difference between the experimental and numerical models is 5 to 15min. For the time delay of the maximum temperature peaks the differences between the numerical and experimental models are more expressive: from 15min to 1h:35min.

As explained before in this sub-section, according to the results of the statistical indexes, the interval period of three days to compare the indoor temperatures between the experimental and numerical models is between 1<sup>st</sup> and 4<sup>th</sup> of February. Figure 134 presents the indoor temperatures comparison between the experimental and numerical model.



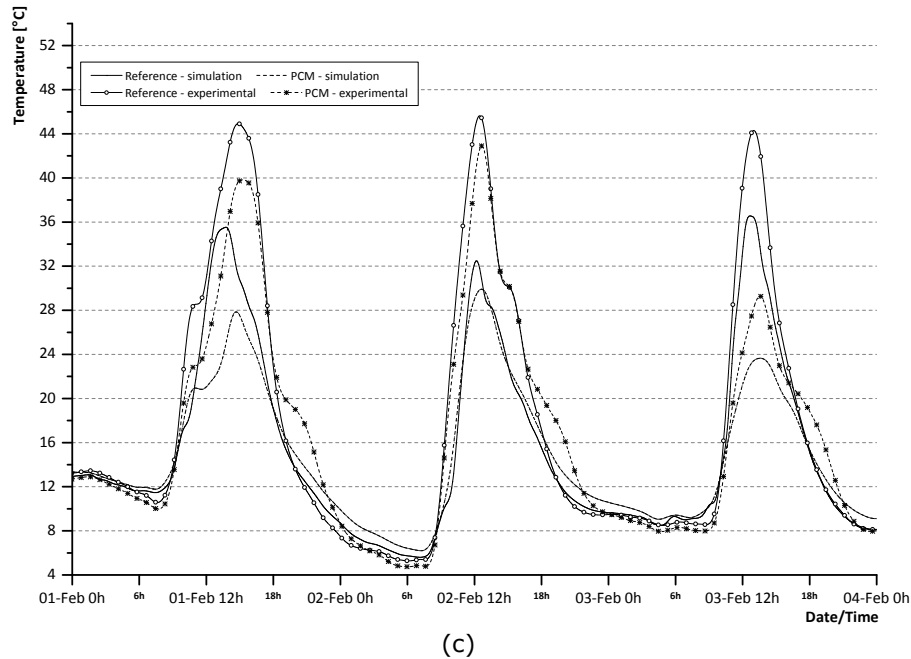


Figure 134 Comparison of the numerical and experimental data for the period of the 1<sup>st</sup> to 4<sup>th</sup> February: (a) for the reference compartment; (b) for the PCM compartment and (c) for both compartments

The temperature profiles of the experimental data compared with the simulated results show a similar thermal behaviour.

Analysing the results of the three days, Figure 134.a, the numerical results during the heating and cooling period are similar, however for the maximum indoor temperature peak the numerical model does not reach the same values of the experimentally recorded. For the time of the maximum indoor temperatures, the experimental model presents higher temperatures, up to 12°C. For the night period the differences are small - between 0°C and 1°C. The day that presents best agreement between the experimental and numerical model is the 3<sup>rd</sup> of February. For this day, the thermal behaviour is quite similar and the maximum difference that occurs is at the maximum temperature peak and equal to 6.5°C.

For the PCM compartment, Figure 134.b, the conclusions are similar to the reference compartment. The day with best agreement is the 3<sup>rd</sup> of February, where the maximum temperature difference is about 4.5°C and the worst the 2<sup>nd</sup> of February which the temperatures differences reaches 22°C. During the night period the minimum indoor temperatures are slightly different in comparison with the reference compartment. For the PCM compartment, the experimental model reaches less 2°C than the numerical model. During the temperature drop, the experimental model presents a slope difference between 30°C to 21°C. As the indoor temperatures for the experimental testing are higher than the obtained for the numerical models, the PCM effect is more clear for the experimental testing.

Comparing the numerical and experimental results of the indoor temperatures of both compartments for the selected period, Figure 134.c, the PCM compartment - as expected - presents lower thermal amplitude than the experimental compartment. Comparing the time delay between them, the PCM compartment increases slightly the time delay, as discussed and concluded before from the results of Table 24. For this time period the thermal behaviour of the numerical and experimental data are similar for both compartments, however the PCM model of the experimental testing presents a slope difference at the discharging period when the temperature reaches 22°C. This thermal behaviour is shown for the experimental testing because the indoor temperatures changes from 29°C to 43°C, so if the PCM melting temperature range is from 27°C to 29°C it is expectable that the PCM melting fraction is higher for the experimental testing than the numerical model. So, when the temperatures drops, the PCM of the experimental model releases more energy than the numerical model, leading to keep the indoor temperature higher and changing the temperature profile slope. For the numerical model the thermal energy release is more smoothen than the recorded experimental data.

Figure 135 presents in detail the day of the selected period that presents best statistical and thermal agreement - 3<sup>rd</sup> of February - and also the indoor temperature reduction for each time of the day.

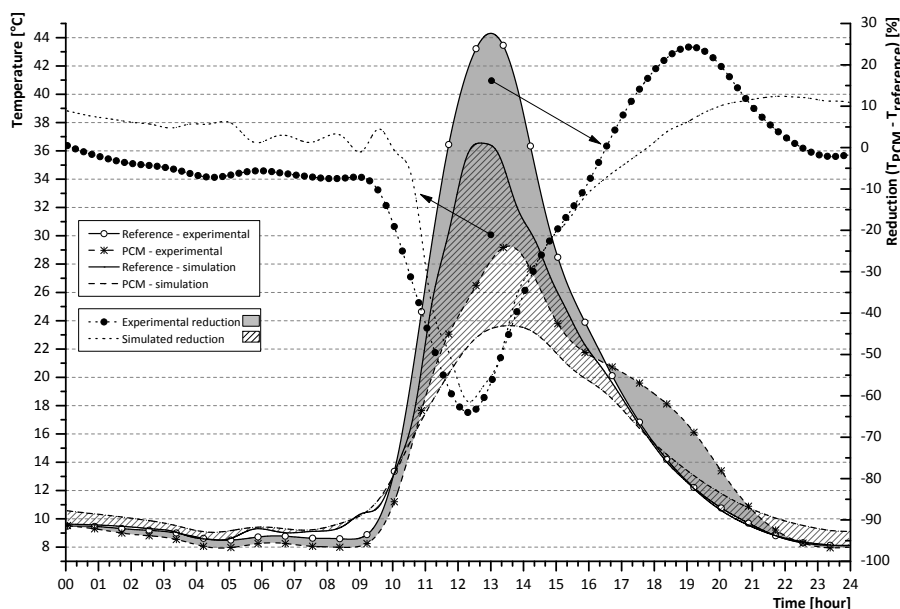


Figure 135 Thermal profiles for one day cycle (3<sup>rd</sup> of February)

The differences between the numerical and the experimental models are highlighted in Figure 135. The auxiliary y-axis shows the percentage value of the

temperatures reduction of each compartment for the numerical and experimental model.

Comparing the temperature reduction of the experimental and numerical models, for the first ten hours (0h to 10h) the experimental and numerical models presents similar temperature reduction between compartments. At this time period range, the temperature reduction for the experimental model is 0% to -5% and on the numerical model 0% to 10%. This results means that the PCM and reference model have the same indoor temperature when the reduction is 0%, but for the experimental comparison the PCM compartment presents lower temperatures (up to 5%) and for the simulation PCM model presents higher temperatures (up to 10%).

Analysing the daytime period - from 10h to 16h - the maximum temperature reduction for experimental and numerical models are similar. The temperature reduction from the PCM compartment is 65% for the experimental testing and 62% for the numerical model.

Comparing the time period between 16h to 24h the experimental reduction shows that the PCM compartment has lower temperatures than the reference compartment until 16:45. After this time, the PCM compartment presents higher temperatures, up to 25%. The temperatures differences between them reduce again and are similar close to 21:30. For the numerical simulation, the results are a slightly different. The PCM model presents lower temperatures until 17:45 and after this time shows higher temperature than the reference model - up to 12%.



# **CHAPTER 6**

## 6 Conclusions

The final remarks taken from the present work are presented in this section.

The main conclusions from each chapter are presented. The results from the experimental testing and from the numerical studies are highlighted.

---





## 6.1 Final remarks

The buildings external envelope has a crucial role in the energy efficiency of the buildings since the glazing is responsible for high-energy transfer (gains and losses). Poorly specified glazing solutions lead to the increase of energy demand and to thermal and visual discomfort conditions for occupants. In terms of energy efficiency and indoor air temperature asymmetry, these are issues presently object of high-end research and application for enhancing building envelope.

## 6.2 Past research and studies

The present dissertation presents many experimental and numerical studies, prototypes and commercial based solutions based on phase change materials (PCMs) that have been developed in last years to improve the thermal and energy efficiency of the building glazed envelope.

Taking into account the main results of the presented studies, the introduction of phase change materials in building glazing solutions and shading devices is an efficient strategy for improving the thermal energy storage capacity and the thermal inertia of these boundaries.

The main conclusions and systematic results taken from the presented research on PCMs integration into the glazing and shading devices can be abridged to:

- Increase of the indoor thermal comfort of the building and consequently of occupants satisfaction;
- Indoor thermal regulation of the indoor air temperature amplitude, reducing the maximum indoor air temperature and increasing the minimum indoor air temperature;
- Increase of the time delay between the imposed conditions (or external weather conditions) and the internal conditions. This fact, allows to store heat during the day and release during the night, leading to low daily temperature swing.

Besides the largely referred and acceded references of recent research and prototypes, consensually the authors opinion is there is a lack of effective commercial products resourcing to PCMs. In the last years, the funding on this research topic has been massive, so it is predicted that in the next few years more commercial based products will be available on the market. Therefore, more development and research activity for commercial PCM based products must be carried out, as well as cost-benefit analysis.

Still other research issues regarding PCM based or incorporated products applied to glazing and shading devices solutions, as the case for information about the life-cycle assessment, also known as life-cycle analysis (LCA), costs and the payback amortisation are lacking. As further work, a thorough literature review on this topic, comparing these features with other technological and typical buildings solutions is prominent.

### 6.3 Prototype definitions and development

The developed prototype was based on previous material selection, geometry optimization and PCM selection. The following was defined:

- The PCM selected for the experimental prototype was the RT28HC<sup>®</sup>. This is an organic paraffin that has the temperature range between 27°C and 29°C and a latent heat storage capacity of 245kJ.kg<sup>-1</sup>. The main disadvantage of this PCM is the volume expansion that can reach 12.5%;
- The aluminium material was chosen to build the window shutter blades since it is the most used material to build window shutters in Portugal and enhances the thermal behaviour of the PCM.

The tested window shutter prototype has 2.22m of height and 1.71m of length and is composed by 50 aluminium blades. One of the window shutter faces has insulation material and the window blades have the capacity to be rotated from 0 to 180°.

To fill the window blades with PCM - the shutter blade and the PCM material - was heated and the PCM introduced in the liquid state. To hermetically seal the ends of the window shutter blades it was used an aluminium cap that was glued with high temperature resistant silicon and epoxy glue.

### 6.4 Experimental results

The performance of a window shutter with phase change materials was experimentally tested at full scale. The PCM provided an additional thermal inertia capacity for this compartment that is recorded by the indoor air temperatures and heat flux results attained.

Based on the experimental campaign of two similar window shutter solutions oriented to the south - one considered as the reference and the other filled with PCM - during the summer and winter periods in a Mediterranean climate, the main results are exposed below.

#### 6.4.1 Summer week

During testing period of the experimental campaign, 2<sup>nd</sup> to 09<sup>th</sup> of August, the test cell was submitted to average solar radiation of 237 [W.m<sup>-2</sup>] to 306 [W.m<sup>-2</sup>]. The external air temperature ranges from 13°C to 25°C.

The following conclusions can be taken:

- During the charging and discharging process of the PCM, for each time step the window shutter with PCM can reduce the indoor compartment temperature about -22% to 18% (minimum and maximum value correspondently);
- The window shutter with PCM can decrease the maximum and minimum temperatures peaks about 6% and 11%, respectively. During this time, the use of PCM in the window shutter solution could increase 45min the time delay for the minimum temperature peak and one hour the time delay for the maximum temperature peak, compared to the reference compartment;
- The maximum value of the heat flux is 18 [W.m<sup>-2</sup>] for the reference compartment and 8 [W.m<sup>-2</sup>] in the compartment with the PCM shutter;
- The heat flux profiles shows the PCM thermal regulation effect over in the indoor temperatures;

#### 6.4.2 Winter week

The maximum indoor temperature of the compartment with the PCM shutter is 37.2°C, which is 16.6°C lower than the indoor air temperature of the reference compartment and is reached 1:15h later. Comparing the indoor temperatures over time, the reduction of temperature can reach 90% (when the indoor air temperatures increases) and up to 35% (when the indoor air temperatures drops). For the maximum indoor air temperature peak the difference between both compartments is 30% to 40%. However the minimum indoor air temperature peaks are similar, so for this situation the potential improvement of the PCM incorporation is null, proving that other features come into play such as thermal bridges losses, large glazing areas and thermal inertia. Therefore more work of the compatibility and the optimization of these different features are necessary.

The maximum and minimum heat flux measured on the internal partition wall of the reference compartment was 16 [W.m<sup>-2</sup>] and -8 [W.m<sup>-2</sup>], respectively. The compartment with the PCM shutter presents more steady results of the heat flux and the maximum heat flux recorded was 6.5 [W.m<sup>-2</sup>] and the minimum -3 [W.m<sup>-2</sup>].

The overheating inside of the test cell compartments was higher than the expected, therefore during the day the PCM melted completely and stayed in this condition too long that it allowed to increase the compartment internal air temperature above comfortable conditions. The thermal insulation level of the test cell should be improved because as shown in section 4.5.2 the thermal bridges losses are high as well as through the cell doors.

### 6.5 Numerical results

Despite the assumptions and simplifications assumed for the 2D numerical model, the results of the numerical model demonstrate a reasonable agreement. The CVRMSE and MBE indexes are in accordance with the standards ASHRAE 14 and FEMP for both models. For the IPMVP [197] standard, the results of the overall CVRMSE are both higher than 20%, but the PCM model are close to the statistical agreement.

#### 6.5.1 Summer week

The present results and analysed data, more precisely the indoor temperatures, heat transfer data and external weather conditions, are crucial for the numerical model validation and consequent parametric analysis.

According to the used criteria acceptance, the results of the numerical model presented good agreement and reliability, and the numerical model was considered as calibrated with well prediction data. Analysing the CVRMSE index of both compartments the days that present best values are 2<sup>nd</sup>, 5<sup>th</sup> and 6<sup>th</sup> August. For these days, the maximum CVRMSE index value is 6% and for the analysed period the days with highest error accumulation are 4<sup>th</sup> and 8<sup>th</sup> August that reach 12% for the PCM compartment. The standard deviation presents also a good accuracy of the tested methods, 1.6°C for the reference compartment and 1.7°C for the PCM compartment. A GOF lower than 11% is recommended for trial agreement. The overall results of the selected period present favourable GOF values. The correlation factor for the PCM compartment is 0.931 against 0.965 of the reference compartment.

The box whisker mean (BWM) plots give a quick draw to analyse the temperatures of the reference and PCM compartments, allowing to compare the mean and the extreme values of the numerical simulations and the experimental testing. According to the results and the box whisker mean plots the numerical model presents well-predicted data.

Resourcing to the numerical models, the PCM compartment presents overall better thermal behaviour compared with the reference compartment. For the first three days of the simulation that were analysed in detail, the average temperature in the interior domain of the reference compartment ranges from 15°C to 46°C and for the PCM compartment ranges from 18°C to 42°C, which means that the maximum temperature peak in the PCM compartment is lower up to 4°C and the minimum temperature is up to higher 3°C. Besides the temperature regulation, that represents respectively an improvement of 8.7% for the warming period and 16.7% for the night period, the PCM compartment increases significantly the time delay between the imposed exterior conditions and the internal domain. The maximum average temperature of the reference compartment is reached one hour after of the maximum imposed exterior condition and for the PCM compartment up to two hours. For the night period the time delay between the imposed exterior conditions and the PCM compartment is one hour, which is up to 30 minutes more comparing with the reference compartment.

#### 6.5.2 Winter week

The main conclusions taken from the numerical results are:

- The maximum indoor temperatures difference between the PCM and reference compartment is 12.9°C, which means that the maximum temperature peak on the PCM compartment is 23.65°C and on the reference compartment is 36.55°C;
- The minimum indoor temperatures reached in both compartments are similar. The reference compartment reaches 5.6°C and the PCM compartment 6.2°C, which is a temperature difference of 0.6°C;
- The maximum indoor temperature on the reference compartment is reached at 13:42h, which is 1h:35min later than the maximum imposed temperature. Comparing the time delay between the reference and the PCM compartment, the PCM compartment added 1h, which means that the maximum indoor temperature is reached approx. at 14:42h;
- Analysing the time delay between both compartments for the minimum indoor temperature, the time that the minimum temperatures are reached are similar, but in average, the PCM compartment increases 5 to 15min;
- The temperature profiles during the time that the temperatures are dropping (from 12:30 to 05:00), the thermal behaviour on the PCM compartment is more stable and constant (the temperature on the PCM compartment decreases slower and sweetly). These results show

the PCM improvement during the daytime period, minimizing the faster temperature drop in this compartment.

Comparing the numerical results with the experimental data, both compartments shows a similar minimum indoor temperatures, however analysing the maximum temperatures the box whisker plots shows a clearer difference - the maximum temperatures are higher on the experimental testing.

The minimum temperatures reached for the numerical models and on the experimental model are similar for the most of the days. The higher minimum temperature difference between the numerical and experimental model is 1.17°C for the reference compartment and 0.68°C for the PCM compartment.

Analysing the maximum temperatures on the numerical and experimental models, the differences are more significant. The experimental model has maximum indoor temperatures up to 15°C for the reference compartment and up to 12°C for the PCM compartment.

Comparing the time delay between the experimental and the numerical models for the minimum indoor temperature peaks, the reference compartment presents best agreement, mostly between 1<sup>st</sup> and 3<sup>rd</sup> of February where the maximum time delay difference between the experimental and numerical model is 5 to 15min. For the time delay of the maximum temperature peaks the differences between the numerical and experimental model are more expressive: from 15min to 1:35h.

## 6.6 Economic analysis

Analysing the results of the testing periods, the PCM melting and solidification process was reached completely for each day, which means that the PCM energy storage capacity was 245kJ.kg<sup>-1</sup> per day.

The total mass of PCM was calculated using the equation (6.1) and is equal to 29kg. Each window shutter blade was filled with 290g of PCM ( $m_{PCM,blade}$ ) is composed by 100 aluminium blades ( $N_{blades}$ ).

$$m_{t,PCM} = m_{PCM,blade} \cdot N_{blades} = 0.29 \cdot 100 = 29kg \quad (6.1)$$

Considering these two values (the total mass of PCM and the energy storage capacity of the PCM) the total energy storage from the windows shutters can be calculated:

$$E_t = \Delta h \cdot m_{t,PCM} = 245 \left[ \frac{kJ}{kg} \right] \cdot 29 [kg] = 7105 kJ \text{ or } 1.97 kWh \quad (6.2)$$

The total energy potential savings from the tested prototype is 1.97kWh per day. Using the price of the simple electricity rate ( $0.1684\text{€}\cdot\text{kWh}^{-1}$ ) from the energy supplier EDP - Portuguese electricity supplier, "Energias de Portugal" - the economic savings can be calculated:

$$Day_{savings} = E_t \cdot E_{price} = 1.97 \left[ \frac{kWh}{day} \right] \cdot 0.1684 \left[ \frac{\text{€}}{\text{€}} \right] = 0.3318 \left[ \frac{\text{€}}{day} \right] \quad (6.3)$$

Considering that the PCM window shutter on annual basis works completely (total charging and discharging cycles) during 40% of year, the potential savings per year is up to 48.44€, as calculated by equation (6.4):

$$Year_{savings} = Day_{savings} \cdot N_{days,year} \cdot 40\% = 0.3318 \cdot 365 \cdot 0.4 = 48.44\text{€} \quad (6.4)$$

The cost of the PCM was approximately  $6.5\text{€}\cdot\text{kg}^{-1}$ , therefore calculating the cost for the total mass of PCM used on the prototype (29kg), the total cost of the PCM was 188.5€.

Analysing the potential energy savings and the total cost of the PCM, the estimated payback time is 3 years and 10 months.

## 6.7 Future work

Using the acquired knowledge of this work, some recommendations and research topics are suggested for future work:

- Carried out a similar study, adding an active ventilation system. It is expected the use of a mechanical ventilation system can potentiate the PCM thermal behaviour and improve the PCM charging and discharging process;
- Using an energy analyser equipment to quantify the energy consumption of the HVAC system in both compartments (with and without PCM) to maintain the indoor temperature between a pre-establish temperature range;
- Using the numerical capacities, analyse the energy performance of the window shutter to optimize the PCM quantity, melting temperatures, latent heat capacity and shutter blades geometry (such as length, thickness and profile shape) and materials;

- Development of a numerical model combining PCMs with different melting temperatures to fill the aluminium blades and comparing with the single temperature PCM solution;
- Performing the life cycle assessment (LCA) and life cycle cost (LCC) of the developed PCM shutter solution;
- Carry out more numerical studies adding new variables and parameters, such as: overhangs, different testing locations, building typologies (thermal inertia) and test cell orientation;
- Carry out an experimental campaign in a real building environment (internal gains, lighting, equipment, occupation), i.e. office space, to evaluate the thermal regulation effect of the PCM shutter.



# **REFERENCES**



- 
- [1] O. Publishing, *World Energy Outlook 2012*. Paris, FRA: Organisation for Economic Cooperation and Development (OECD), 2012.
- [2] C. Koo, S. Park, T. Hong, and H. S. Park, "An estimation model for the heating and cooling demand of a residential building with a different envelope design using the finite element method," *Applied Energy*, vol. 115, pp. 205-215, 2/15/2014.
- [3] S. M. C. Magalhães and V. M. S. Leal, "Characterization of thermal performance and nominal heating gap of the residential building stock using the EPBD-derived databases: The case of Portugal mainland," *Energy and Buildings*, vol. 70, pp. 167-179, 2// 2014.
- [4] "Directive 2010/31/EU of the European Parliament and of the Council of 19 May 2010 on the energy performance of buildings," *Official journal - European Union legislation*, vol. 53, pp. 13-35, 2010.
- [5] J. Bosch, F. X. Johnson, E. Clément, R. Mertens, and N. Roubanis, *Panorama of Energy - Energy Statistics to Support Eu Policies and Solutions*: Office for Official Pubns of, 2009.
- [6] E. Union. (1995-2015). *European Commission Energy Topics*. Available: <https://ec.europa.eu/energy/en/topics/>
- [7] Oecd, *World Energy Outlook 2009*. Paris, FRA: Organisation for Economic Cooperation and Development (OECD), 2009.
- [8] F. Cappelletti, A. Prada, P. Romagnoni, and A. Gasparella, "Passive performance of glazed components in heating and cooling of an open-space office under controlled indoor thermal comfort," *Building and Environment*, vol. 72, pp. 131-144, 2014.
- [9] M. G. Gomes, A. J. Santos, and A. M. Rodrigues, "Solar and visible optical properties of glazing systems with venetian blinds: Numerical, experimental and blind control study," *Building and Environment*, vol. 71, pp. 47-59, 1// 2014.
- [10] J. Peng, L. Lu, and H. Yang, "An experimental study of the thermal performance of a novel photovoltaic double-skin facade in Hong Kong," *Solar Energy*, vol. 97, pp. 293-304, 11// 2013.
- [11] S. Ghoshal and S. Neogi, "Advance Glazing System - Energy Efficiency Approach for Buildings a Review," *Energy Procedia*, vol. 54, pp. 352-358, // 2014.
- [12] T.-P. Wang, L.-B. Wang, and B.-Q. Li, "A model of the long-wave radiation heat transfer through a glazing," *Energy and Buildings*, vol. 59, pp. 50-61, 4// 2013.
- [13] R. Baetens, B. P. Jelle, and A. Gustavsen, "Phase change materials for building applications: A state-of-the-art review," *Energy and Buildings*, vol. 42, pp. 1361-1368, Sep 2010.
- [14] L. F. Cabeza, A. Castell, C. Barreneche, A. de Gracia, and A. I. Fernández, "Materials used as PCM in thermal energy storage in buildings: A review," *Renewable and Sustainable Energy Reviews*, vol. 15, pp. 1675-1695, 2011.
-

- [15] H. Mehling and L. F. Cabeza, *Heat and cold storage with PCM : an up to date introduction into basics and applications*. Berlin, Germany: Springer, 2008.
- [16] M. R. Anisur, M. H. Mahfuz, M. A. Kibria, R. Saidur, I. H. S. C. Metselaar, and T. M. I. Mahlia, "Curbing global warming with phase change materials for energy storage," *Renewable and Sustainable Energy Reviews*, vol. 18, pp. 23-30, 2013.
- [17] M. a. Markets. (2009-2015). *Advanced Phase Change Material (PCM) Market worth \$1,472 Million by 2019*. Available: <http://www.marketsandmarkets.com/PressReleases/MarketsandMarkets-Global-Advanced-Phase-Change-Material-PCM-Market.asp>
- [18] M. a. Markets. (2009-2015). *Advanced Phase Change Material Market (PCM) worth \$1,150 Million By 2018*. Available: <http://www.marketsandmarkets.com/PressReleases/advanced-phase-change-material-pcm.asp>
- [19] S. Grynning, A. Gustavsen, B. Time, and B. P. Jelle, "Windows in the buildings of tomorrow: Energy losers or energy gainers?," *Energy and Buildings*, vol. 61, pp. 185-192, 6// 2013.
- [20] T. R. Nielsen, K. Duer, and S. Svendsen, "Energy performance of glazings and windows," *Solar Energy*, vol. 69, Supplement 6, pp. 137-143, 7// 2001.
- [21] M. K. Urbikain and J. M. Sala, "Analysis of different models to estimate energy savings related to windows in residential buildings," *Energy and Buildings*, vol. 41, pp. 687-695, 6// 2009.
- [22] A. Maccari and M. Zinzi, "Simplified algorithms for the Italian energy rating scheme for fenestration in residential buildings," *Solar Energy*, vol. 69, Supplement 6, pp. 75-92, 7// 2001.
- [23] A. Parekh, "Setting window energy efficiency levels in Canada," in *IEA-SHC Task 27 Performance of Solar Facade Components, Subtask A: Performance, Buildings Group*, ed. Ottawa, Canada: CANMET Energy Technology Centre, 2009.
- [24] *Energy performance of fenestration systems for residential buildings calculation procedure (ISO 18292:2011)*, 2011.
- [25] H. Ye, X. Meng, L. Long, and B. Xu, "The route to a perfect window," *Renewable Energy*, vol. 55, pp. 448-455, 7// 2013.
- [26] H. Ye, X. Meng, and B. Xu, "Theoretical discussions of perfect window, ideal near infrared solar spectrum regulating window and current thermochromic window," *Energy and Buildings*, vol. 49, pp. 164-172, 6// 2012.
- [27] B. L. Gowreesunker, S. B. Stankovic, S. A. Tassou, and P. A. Kyriacou, "Experimental and numerical investigations of the optical and thermal aspects of a PCM-glazed unit," *Energy and Buildings*, vol. 61, pp. 239-249, 6// 2013.
- [28] F. Goia, M. Perino, and M. Haase, "A numerical model to evaluate the thermal behaviour of PCM glazing system configurations," *Energy and Buildings*, vol. 54, pp. 141-153, 11// 2012.

- 
- [29] Y. A. Kara and A. Kurnuç, "Performance of coupled novel triple glass and phase change material wall in the heating season: An experimental study," *Solar Energy*, vol. 86, pp. 2432-2442, 9// 2012.
- [30] F. Goia, M. Perino, and V. Serra, "Improving thermal comfort conditions by means of PCM glazing systems," *Energy and Buildings*, vol. 60, pp. 442-452, 5// 2013.
- [31] H. Manz, P. W. Egolf, P. Suter, and A. Goetzberger, "TIM-PCM external wall system for solar space heating and daylighting," *Solar Energy*, vol. 61, pp. 369-379, 12// 1997.
- [32] K. A. R. Ismail and J. R. Henríquez, "Parametric study on composite and PCM glass systems," *Energy Conversion and Management*, vol. 43, pp. 973-993, 5// 2002.
- [33] K. A. R. Ismail, C. T. Salinas, and J. R. Henriquez, "Comparison between PCM filled glass windows and absorbing gas filled windows," *Energy and Buildings*, vol. 40, pp. 710-719, // 2008.
- [34] H. Weinläder, A. Beck, and J. Fricke, "PCM-facade-panel for daylighting and room heating," *Solar Energy*, vol. 78, pp. 177-186, 2// 2005.
- [35] F. Goia, M. Zinzi, E. Carnielo, and V. Serra, "Characterization of the optical properties of a PCM glazing system," *Energy Procedia*, vol. 30, pp. 428-437, // 2012.
- [36] S. Li, Y. Zhou, K. Zhong, X. Zhang, and X. Jin, "Thermal analysis of PCM-filled glass windows in hot summer and cold winter area," *International Journal of Low-Carbon Technologies*, November 13, 2013 2013.
- [37] F. Goia, L. Bianco, Y. Cascone, M. Perino, and V. Serra, "Experimental Analysis of an Advanced Dynamic Glazing Prototype Integrating PCM and Thermotropic Layers," *Energy Procedia*, vol. 48, pp. 1272-1281, // 2014.
- [38] F. Goia, M. Perino, and V. Serra, "Experimental analysis of the energy performance of a full-scale PCM glazing prototype," *Solar Energy*, vol. 100, pp. 217-233, 2// 2014.
- [39] F. Goia, "Thermo-physical behaviour and energy performance assessment of PCM glazing system configurations: A numerical analysis," *Frontiers of Architectural Research*, vol. 1, pp. 341-347, 12// 2012.
- [40] Y. A. Kara and A. Kurnuç, "Performance of coupled novel triple glass unit and pcm wall," *Applied Thermal Engineering*, vol. 35, pp. 243-246, 3// 2012.
- [41] L. Jain and S. D. Sharma, "Phase Change Materials for day lighting and glazed insulation in buildings," *Journal of Engineering Science and Technology*, 2009.
- [42] G. Diarce, A. Urresti, A. García-Romero, A. Delgado, A. Erkoreka, C. Escudero, *et al.*, "Ventilated active facades with PCM," *Applied Energy*, vol. 109, pp. 530-537, 2013.
-

- [43] K. A. R. Ismail and J. R. Henriquez, "Thermally effective windows with moving phase change material curtains," *Applied Thermal Engineering*, vol. 21, pp. 1909-1923, Dec 2001.
- [44] H. Weinlaeder, W. Koerner, and M. Heidenfelder, "Monitoring results of an interior sun protection system with integrated latent heat storage," *Energy and Buildings*, vol. 43, pp. 2468-2475, 9// 2011.
- [45] E. M. Alawadhi, "Using phase change materials in window shutter to reduce the solar heat gain," *Energy and Buildings*, vol. 47, pp. 421-429, 2012.
- [46] A. M. Borreguero, M. Luz Sánchez, J. L. Valverde, M. Carmona, and J. F. Rodríguez, "Thermal testing and numerical simulation of gypsum wallboards incorporated with different PCMs content," *Applied Energy*, vol. 88, pp. 930-937, 2011.
- [47] C. Chen, H. Guo, Y. Liu, H. Yue, and C. Wang, "A new kind of phase change material (PCM) for energy-storing wallboard," *Energy and Buildings*, vol. 40, pp. 882-890, 2008.
- [48] A. G. Entrop, H. J. H. Brouwers, and A. H. M. E. Reinders, "Experimental research on the use of micro-encapsulated Phase Change Materials to store solar energy in concrete floors and to save energy in Dutch houses," *Solar Energy*, vol. 85, pp. 1007-1020, 2011.
- [49] A. C. Evers, M. A. Medina, and Y. Fang, "Evaluation of the thermal performance of frame walls enhanced with paraffin and hydrated salt phase change materials using a dynamic wall simulator," *Building and Environment*, vol. 45, pp. 1762-1768, 2010.
- [50] G. Evola, L. Marletta, and F. Sicurella, "Simulation of a ventilated cavity to enhance the effectiveness of PCM wallboards for summer thermal comfort in buildings," *Energy and Buildings*, vol. 70, pp. 480-489, 2014.
- [51] M. A. Izquierdo-Barrientos, J. F. Belmonte, D. Rodríguez-Sánchez, A. E. Molina, and J. A. Almendros-Ibáñez, "A numerical study of external building walls containing phase change materials (PCM)," *Applied Thermal Engineering*, vol. 47, pp. 73-85, 2012.
- [52] T. Silva, R. Vicente, N. Soares, and V. Ferreira, "Experimental testing and numerical modelling of masonry wall solution with PCM incorporation: A passive construction solution," *Energy and Buildings*, vol. 49, pp. 235-245, 2012.
- [53] R. Vicente and T. Silva, "Brick masonry walls with PCM macrocapsules: An experimental approach," *Applied Thermal Engineering*, vol. 67, pp. 24-34, 6// 2014.
- [54] N. Zhu, Z. Ma, and S. Wang, "Dynamic characteristics and energy performance of buildings using phase change materials: A review," *Energy Conversion and Management*, vol. 50, pp. 3169-3181, 12// 2009.
- [55] M. Farid, "A review on phase change energy storage: materials and applications," *Energy Conversion and Management*, vol. 45, pp. 1597-1615, 2004.

- 
- [56] R. Cheng, X. Wang, and Y. Zhang, "Energy-Efficient Building Envelopes with Phase-Change Materials: New Understanding and Related Research," *Heat Transfer Engineering*, vol. 35, pp. 970-984, 2013.
- [57] V. V. Tyagi and D. Buddhi, "PCM thermal storage in buildings: A state of art," *Renewable & Sustainable Energy Reviews*, vol. 11, pp. 1146-1166, Aug 2007.
- [58] A. Sharma, V. V. Tyagi, C. R. Chen, and D. Buddhi, "Review on thermal energy storage with phase change materials and applications," *Renewable & Sustainable Energy Reviews*, vol. 13, pp. 318-345, Feb 2009.
- [59] A. A, "Low temperature latent heat thermal energy storage: Heat storage materials," *Solar Energy*, vol. 30, pp. 313-332, 1983.
- [60] S. M. Hasnain, "Review on sustainable thermal energy storage technologies, Part I: heat storage materials and techniques," *Energy Conversion and Management*, vol. 39, pp. 1127-1138, 8/1/ 1998.
- [61] M. Pomianowski, P. Heiselberg, and Y. Zhang, "Review of thermal energy storage technologies based on PCM application in buildings," *Energy and Buildings*, vol. 67, pp. 56-69, 12// 2013.
- [62] V. V. Tyagi and D. Buddhi, "PCM thermal storage in buildings: A state of art," *Renewable and Sustainable Energy Reviews*, vol. 11, pp. 1146-1166, Aug 2007.
- [63] B. Zalba, J. M. Marin, L. F. Cabeza, and H. Mehling, "Review on thermal energy storage with phase change: materials, heat transfer analysis and applications," *Applied Thermal Engineering*, vol. 23, pp. 251-283, Feb 2003.
- [64] V. V. Tyagi, S. C. Kaushik, S. K. Tyagi, and T. Akiyama, "Development of phase change materials based microencapsulated technology for buildings: A review," *Renewable and Sustainable Energy Reviews*, vol. 15, pp. 1373-1391, 2// 2011.
- [65] A. Sharma, V. V. Tyagi, C. R. Chen, and D. Buddhi, "Review on thermal energy storage with phase change materials and applications," *Renewable and Sustainable Energy Reviews*, vol. 13, pp. 318-345, Feb 2009.
- [66] D. Feldman, M. A. Khan, and D. Banu, "Energy storage composite with an organic PCM," *Solar Energy Materials*, vol. 18, pp. 333-341, 1989.
- [67] D. Feldman, D. Banu, D. Hawes, and E. Ghanbari, "Obtaining an energy storing building material by direct incorporation of an organic phase change material in gypsum wallboard," *Solar Energy Materials*, vol. 22, pp. 231-242, 1991.
- [68] G. Zhou, Y. Zhang, K. Lin, and W. Xiao, "Thermal analysis of a direct-gain room with shape-stabilized PCM plates," *Renewable Energy*, vol. 33, pp. 1228-1236, 2008.
- [69] S. Ahmet, "Form-stable paraffin/high density polyethylene composites as solid-liquid phase change material for thermal energy storage: preparation and thermal properties," *Energy Conversion and Management*, vol. 45, pp. 2033-2042, 2004.
-

- [70] M. Xiao, B. Feng, and K. Gong, "Preparation and performance of shape stabilized phase change thermal storage materials with high thermal conductivity," *Energy Conversion and Management*, vol. 43, pp. 103-108, 2002.
- [71] Y. P. Zhang, K. P. Lin, R. Yang, H. F. Di, and Y. Jiang, "Preparation, thermal performance and application of shape-stabilized PCM in energy efficient buildings," *Energy and Buildings*, vol. 38, pp. 1262-1269, 2006.
- [72] Y. Zhang, J. Ding, X. Wang, R. Yang, and K. Lin, "Influence of additives on thermal conductivity of shape-stabilized phase change material," *Solar Energy Materials and Solar Cells*, vol. 90, pp. 1692-1702, 2006.
- [73] D. W. Hawes and D. Feldman, "Absorption of phase change materials in concrete," *Solar Energy Materials and Solar Cells*, vol. 27, pp. 91-101, 1992.
- [74] T. Lee, D. W. Hawes, D. Banu, and D. Feldman, "Control aspects of latent heat storage and recovery in concrete," *Solar Energy Materials and Solar Cells*, vol. 62, pp. 217-237, 2000.
- [75] M. Pomianowski, P. Heiselberg, and R. L. Jensen, "Dynamic heat storage and cooling capacity of a concrete deck with PCM and thermally activated building system," *Energy and Buildings*, vol. 53, pp. 96-107, 2012.
- [76] D. W. Hawes, D. Banu, and D. Feldman, "Latent heat storage in concrete," *Solar Energy Materials*, vol. 21, pp. 61-80, 1990.
- [77] T.-C. Ling and C.-S. Poon, "Use of phase change materials for thermal energy storage in concrete: An overview," *Construction and Building Materials*, vol. 46, pp. 55-62, 9// 2013.
- [78] D. P. Bentz and R. Turpin, "Potential applications of phase change materials in concrete technology," *Cement and Concrete Composites*, vol. 29, pp. 527-532, 2007.
- [79] M. Hadjieva, R. Stoykov, and T. Filipova, "Composite salt-hydrate concrete system for building energy storage," *Renewable Energy*, vol. 19, pp. 111-115, 1// 2000.
- [80] A. K. Athienitis, C. Liu, D. Hawes, D. Banu, and D. Feldman, "Investigation of the thermal performance of a passive solar test-room with wall latent heat storage," *Building and Environment*, vol. 32, pp. 405-410, 1997.
- [81] P. Kauranen, K. Peippo, and P. D. Lund, "An organic PCM storage system with adjustable melting temperature," *Solar Energy*, vol. 46, pp. 275-278, // 1991.
- [82] R. J. Kedl, "Conventional Wallboard With Latent Heat Storage For Passive Solar Applications," in *Energy Conversion Engineering Conference, 1990. IECEC-90. Proceedings of the 25th Intersociety*, 1990, pp. 222-225.
- [83] J. B. Drake, "A study of the optimal transition temperature of PCM (phase change material) wallboard for solar energy storage," ORNL/TM-10210; Other: ON: DE88001522 United States Other: ON: DE88001522 Thu Feb 07 16:58:27 EST 2008 NTIS, PC A02/MF A01; 1. ORNL; EDB-87-168834 English, 1987.



- 
- [84] F. Kuznik, J. Virgone, and J. Roux, "Energetic efficiency of room wall containing PCM wallboard: A full-scale experimental investigation," *Energy and Buildings*, vol. 40, pp. 148-156, 2008.
- [85] G. Evola, L. Marletta, and F. Sicurella, "A methodology for investigating the effectiveness of PCM wallboards for summer thermal comfort in buildings," *Building and Environment*.
- [86] Y. Zhang, K. Lin, Y. Jiang, and G. Zhou, "Thermal storage and nonlinear heat-transfer characteristics of PCM wallboard," *Energy and Buildings*, vol. 40, pp. 1771-1779, 2008.
- [87] D. Feldman, D. Banu, and D. W. Hawes, "Development and application of organic phase change mixtures in thermal storage gypsum wallboard," *Solar Energy Materials and Solar Cells*, vol. 36, pp. 147-157, 1995.
- [88] F. Kuznik and J. Virgone, "Experimental investigation of wallboard containing phase change material: Data for validation of numerical modeling," *Energy and Buildings*, vol. 41, pp. 561-570, 2009.
- [89] L. Shilei, F. Guohui, Z. Neng, and D. Li, "Experimental study and evaluation of latent heat storage in phase change materials wallboards," *Energy and Buildings*, vol. 39, pp. 1088-1091, 2007.
- [90] F. Kuznik, J. Virgone, and K. Johannes, "In-situ study of thermal comfort enhancement in a renovated building equipped with phase change material wallboard," *Renewable Energy*, vol. 36, pp. 1458-1462, 2011.
- [91] F. Kuznik, J. Virgone, and J. Noel, "Optimization of a phase change material wallboard for building use," *Applied Thermal Engineering*, vol. 28, pp. 1291-1298, 8// 2008.
- [92] G. Zhou, Y. Yang, and H. Xu, "Performance of shape-stabilized phase change material wallboard with periodical outside heat flux waves," *Applied Energy*, vol. 88, pp. 2113-2121, 2011.
- [93] C. Hasse, M. Grenet, A. Bontemps, R. Dendievel, and H. Sallée, "Realization, test and modelling of honeycomb wallboards containing a Phase Change Material," *Energy and Buildings*, vol. 43, pp. 232-238, 2011.
- [94] N. Zhu, P. Hu, and L. Xu, "A simplified dynamic model of double layers shape-stabilized phase change materials wallboards," *Energy and Buildings*, vol. 67, pp. 508-516, 12// 2013.
- [95] H. E. Feustel and C. Stetiu, *Thermal performance of phase change wallboard for residential cooling application*. California, EUA: Lawrence Berkeley National Lab, C.A., 1997.
- [96] M. Ahmad, A. Bontemps, H. Sallée, and D. Quenard, "Thermal testing and numerical simulation of a prototype cell using light wallboards coupling vacuum isolation panels and phase change material," *Energy and Buildings*, vol. 38, pp. 673-681, 2006.
- [97] J. S. Kim and K. Darkwa, "Simulation of an integrated PCM-wallboard system," *International Journal of Energy Research*, vol. 27, pp. 215-223, 2003.
-

- [98] X. Xiao, P. Zhang, and M. Li, "Preparation and thermal characterization of paraffin/metal foam composite phase change material," *Applied Energy*, vol. 112, pp. 1357-1366, 12// 2013.
- [99] M. Xiao, B. Feng, and K. Gong, "Thermal performance of a high conductive shape-stabilized thermal storage material," *Solar Energy Materials and Solar Cells*, vol. 69, pp. 293-296, 10// 2001.
- [100] C. Y. Zhao, W. Lu, and Y. Tian, "Heat transfer enhancement for thermal energy storage using metal foams embedded within phase change materials (PCMs)," *Solar Energy*, vol. 84, pp. 1402-1412, 8// 2010.
- [101] M. Koschenz and B. Lehmann, "Development of a thermally activated ceiling panel with PCM for application in lightweight and retrofitted buildings," *Energy and Buildings*, vol. 36, pp. 567-578, 2004.
- [102] X. Wang and J. Niu, "Performance of cooled-ceiling operating with MPCM slurry," *Energy Conversion and Management*, vol. 50, pp. 583-591, 3// 2009.
- [103] E. M. Alawadhi, "Thermal analysis of a building brick containing phase change material," *Energy and Buildings*, vol. 40, pp. 351-357, 2008.
- [104] A. Castell, I. Martorell, M. Medrano, G. Pérez, and L. F. Cabeza, "Experimental study of using PCM in brick constructive solutions for passive cooling," *Energy and Buildings*, vol. 42, pp. 534-540, 2010.
- [105] J. M. Marín, B. Zalba, L. F. Cabeza, and H. Mehling, "Improvement of a thermal energy storage using plates with paraffin-graphite composite," *International Journal of Heat and Mass Transfer*, vol. 48, pp. 2561-2570, 6// 2005.
- [106] N. H. S. Tay, M. Belusko, and F. Bruno, "Designing a PCM storage system using the effectiveness-number of transfer units method in low energy cooling of buildings," *Energy and Buildings*, vol. 50, pp. 234-242, 7// 2012.
- [107] I. Cerón, J. Neila, and M. Khayet, "Experimental tile with phase change materials (PCM) for building use," *Energy and Buildings*, vol. 43, pp. 1869-1874, 2011.
- [108] L. Royon, L. Karim, and A. Bontemps, "Thermal energy storage and release of a new component with PCM for integration in floors for thermal management of buildings," *Energy and Buildings*, vol. 63, pp. 29-35, 8// 2013.
- [109] J. C. Kurnia, A. P. Sasmito, S. V. Jangam, and A. S. Mujumdar, "Improved design for heat transfer performance of a novel phase change material (PCM) thermal energy storage (TES)," *Applied Thermal Engineering*, vol. 50, pp. 896-907, 1/10/ 2013.
- [110] S. Álvarez, L. F. Cabeza, A. Ruiz-Pardo, A. Castell, and J. A. Tenorio, "Building integration of PCM for natural cooling of buildings," *Applied Energy*, vol. 109, pp. 514-522, 2013.
- [111] A. de Gracia, L. Navarro, A. Castell, Á. Ruiz-Pardo, S. Álvarez, and L. F. Cabeza, "Thermal analysis of a ventilated facade with PCM for cooling applications," *Energy and Buildings*, vol. 65, pp. 508-515, 2013.

- 
- [112] F. Kuznik, D. David, K. Johannes, and J.-J. Roux, "A review on phase change materials integrated in building walls," *Renewable and Sustainable Energy Reviews*, vol. 15, pp. 379-391, 2011.
- [113] P. A. Maldonado, L. F. Cabeza, and M. Medrano. (2011). *Application of Passive Thermal Energy Storage in Buildings Using PCM and Awnings*.
- [114] W. Xiao, X. Wang, and Y. Zhang, "Analytical optimization of interior PCM for energy storage in a lightweight passive solar room," *Applied Energy*, vol. 86, pp. 2013-2018, 2009.
- [115] M. N. A. Hawlader, M. S. Uddin, and M. M. Khin, "Microencapsulated PCM thermal-energy storage system," *Applied Energy*, vol. 74, pp. 195-202, 2003.
- [116] M. Rady, "Thermal performance of packed bed thermal energy storage units using multiple granular phase change composites," *Applied Energy*, vol. 86, pp. 2704-2720, 2009.
- [117] P. A. Maldonado, L. F. Cabeza, and M. Medrano, *Application of passive thermal energy storage in buildings using PCM and awnings*. Lérida, Spain: University of Lleida, 2011.
- [118] C. Y. Zhao and G. H. Zhang, "Review on microencapsulated phase change materials (MEPCMs): Fabrication, characterization and applications," *Renewable and Sustainable Energy Reviews*, vol. 15, pp. 3813-3832, 2011.
- [119] C. Voelker, O. Kornadt, and M. Ostry, "Temperature reduction due to the application of phase change materials," *Energy and Buildings*, vol. 40, pp. 937-944, // 2008.
- [120] D. David, F. Kuznik, and J.-J. Roux, "Numerical study of the influence of the convective heat transfer on the dynamical behaviour of a phase change material wall," *Applied Thermal Engineering*, vol. 31, pp. 3117-3124, 2011.
- [121] L. Cabeza, C. Castellon, M. Nogues, M. Medrano, R. Leppers, and O. Zubillaga, "Use of microencapsulated PCM in concrete walls for energy savings," *Energy and Buildings*, vol. 39, pp. 113-119, 2007.
- [122] P. Arce, C. Castellón, A. Castell, and L. F. Cabeza, "Use of microencapsulated PCM in buildings and the effect of adding awnings," *Energy and Buildings*, vol. 44, pp. 88-93, 2012.
- [123] M. Hunger, A. G. Entrop, I. Mandilaras, H. J. H. Brouwers, and M. Founti, "The direct incorporation of micro-encapsulated Phase Change Materials in the concrete mixing process - A feasibility study," in *CMS2009: Conference on Construction Material Stewardship - LIFECYCLE DESIGN OF BUILDINGS, SYSTEMS AND MATERIALS. Conference Proceedings*. vol. 323, ed Rotterdam (Netherlands): in-house publishing, 2009, pp. p.141-148.
- [124] D. N. Nkwetta and F. Haghghat, "Thermal energy storage with phase change material—A state-of-the art review," *Sustainable Cities and Society*, vol. 10, pp. 87-100, 2// 2014.

- [125] R. Parameshwaran, S. Kalaiselvam, S. Harikrishnan, and A. Elayaperumal, "Sustainable thermal energy storage technologies for buildings: A review," *Renewable and Sustainable Energy Reviews*, vol. 16, pp. 2394-2433, 2012.
- [126] X. Wang, Y. Zhang, W. Xiao, R. Zeng, Q. Zhang, and H. Di, "Review on thermal performance of phase change energy storage building envelope," *Chinese Science Bulletin*, vol. 54, pp. 920-928, 2009.
- [127] D. Zhou, C. Y. Zhao, and Y. Tian, "Review on thermal energy storage with phase change materials (PCMs) in building applications," *Applied Energy*, vol. 92, pp. 593-605, 4// 2012.
- [128] A. M. Khudhair and M. M. Farid, "A review on energy conservation in building applications with thermal storage by latent heat using phase change materials," *Energy Conversion and Management*, vol. 45, pp. 263-275, 2004.
- [129] P. Tatsidjodoung, N. Le Pierrès, and L. Luo, "A review of potential materials for thermal energy storage in building applications," *Renewable and Sustainable Energy Reviews*, vol. 18, pp. 327-349, 2013.
- [130] E. Osterman, V. V. Tyagi, V. Butala, N. A. Rahim, and U. Stritih, "Review of PCM based cooling technologies for buildings," *Energy and Buildings*, vol. 49, pp. 37-49, 2012.
- [131] N. Soares, J. J. Costa, A. R. Gaspar, and P. Santos, "Review of passive PCM latent heat thermal energy storage systems towards buildings' energy efficiency," *Energy and Buildings*, vol. 59, pp. 82-103, 4// 2013.
- [132] M. Zhang, M. A. Medina, and J. B. King, "Development of a thermally enhanced frame wall with phase-change materials for on-peak air conditioning demand reduction and energy savings in residential buildings," *International Journal of Energy Research*, vol. 29, pp. 795-809, 2005.
- [133] I. L. Wong, P. C. Eames, and R. S. Perera, "A review of transparent insulation systems and the evaluation of payback period for building applications," *Solar Energy*, vol. 81, pp. 1058-1071, 9// 2007.
- [134] H. Shahid and D. Naylor, "Energy performance assessment of a window with a horizontal Venetian blind," *Energy and Buildings*, vol. 37, pp. 836-843, 8// 2005.
- [135] Y.-C. Chan and A. Tzempelikos, "Efficient venetian blind control strategies considering daylight utilization and glare protection," *Solar Energy*, vol. 98, Part C, pp. 241-254, 2013.
- [136] D. Iyi, R. Hasan, R. Penlington, and C. Underwood, "Double Skin Facade: Modelling Technique and Influence of Venetian Blinds on the Airflow and Heat Transfer," *Applied Thermal Engineering*.
- [137] H. Simmler and B. Binder, "Experimental and numerical determination of the total solar energy transmittance of glazing with venetian blind shading," *Building and Environment*, vol. 43, pp. 197-204, 2// 2008.

- 
- [138] C. Tian, T. Chen, and T.-m. Chung, "Experimental and simulating examination of computer tools, Radlink and DOE2, for daylighting and energy simulation with venetian blinds," *Applied Energy*, vol. 124, pp. 130-139, 7/1/ 2014.
- [139] C. Oleskowicz-Popiel and M. Sobczak, "Effect of the roller blinds on heat losses through a double-glazing window during heating season in Central Europe," *Energy and Buildings*.
- [140] A. Tzempelikos and A. K. Athienitis, "The impact of shading design and control on building cooling and lighting demand," *Solar Energy*, vol. 81, pp. 369-382, 3// 2007.
- [141] A. R. Othman and A. A. M. Khalid, "Comparative Performance of Internal Venetian Blind and Roller Blind with Respects to Indoor Illumination Levels," *Procedia - Social and Behavioral Sciences*, vol. 101, pp. 542-553, 11/8/ 2013.
- [142] J. Yao, "Determining the energy performance of manually controlled solar shades: A stochastic model based co-simulation analysis," *Applied Energy*, vol. 127, pp. 64-80, 8/15/ 2014.
- [143] A. I. Palmero-Marrero and A. C. Oliveira, "Effect of louver shading devices on building energy requirements," *Applied Energy*, vol. 87, pp. 2040-2049, 6// 2010.
- [144] B. R. Hughes, J. K. Calautit, and S. A. Ghani, "The development of commercial wind towers for natural ventilation: A review," *Applied Energy*, vol. 92, pp. 606-627, 4// 2012.
- [145] G. Datta, "Effect of fixed horizontal louver shading devices on thermal performance of building by TRNSYS simulation," *Renewable Energy*, vol. 23, pp. 497-507, 2001.
- [146] G. A. Florides, S. A. Kalogirou, S. A. Tassou, and L. C. Wrobel, "Modeling of the modern houses of Cyprus and energy consumption analysis," *Energy*, vol. 25, pp. 915-937, 10// 2000.
- [147] E. S. Lee and A. Tavit, "Energy and visual comfort performance of electrochromic windows with overhangs," *Building and Environment*, vol. 42, pp. 2439-2449, 6// 2007.
- [148] I. O. f. Standardization, *ISO 7730: Moderate Thermal Environments - Determination of the PMV and PPD Indices and Specification of the Conditions for Thermal Comfort*: ISO, 1994.
- [149] *Indoor environmental input parameters for design and assessment of energy performance of buildings addressing indoor air quality, thermal environment, lighting and acoustics (BS EN 15251:2007)*, 2007.
- [150] P. O. Fanger, *Thermal comfort: analysis and applications in environmental engineering*. New York: McGraw-Hill, 1972.
- [151] S. Grynning, F. Goia, E. Rognvik, and B. Time, "Possibilities for characterization of a PCM window system using large scale measurements," *International Journal of Sustainable Built Environment*.
-

- [152] D. Christoffers, "Seasonal shading of vertical south-facades with prismatic panes," *Solar Energy*, vol. 57, pp. 339-343, 1996.
- [153] Y. Zhang, Y. Jiang, and Y. Jiang, "A simple method, the T-history method, of determining the heat of fusion, specific heat and thermal conductivity of phase-change materials," *Measurement Science and Technology*, vol. 10, p. 201, 1999.
- [154] I. Fluent, "ANSYS FLUENT 12.0: User's Guide," ed. Lebanon, N.H.: Fluent Inc., 2009.
- [155] A. Cannavale, F. Fiorito, D. Resta, and G. Gigli, "Visual comfort assessment of smart photovoltachromic windows," *Energy and Buildings*, vol. 65, pp. 137-145, 2013.
- [156] O. C. A. A. M. S. W. A. Univ. of Waterloo, *Calculating the solar heat gain of window frames*. United States: American Society of Heating, Refrigerating and Air-Conditioning Engineers, Inc., Atlanta, GA (US), 1999.
- [157] H. K. Joseph, "A New Method for Predicting the Solar Heat Gain of Complex Fenestration Systems I. Overview and Derivation of the Matrix Layer Calculation," *ASHRAE Transactions*, vol. 100, Part 1, 1993.
- [158] J. L. K. N. A. Wright, "TRANSACTIONS PAPERS - QC-06-001 Solar Absorption by Each Element in a Glazing/Shading Layer Array (RP-1311)," *ASHRAE transactions.*, vol. 112, p. 3, 2006.
- [159] J. H. Klems, "A New Method for Predicting the Solar Heat Gain of Complex Fenestration Systems-2. Detailed Description of the Matrix Layer Calculation," *ASHRAE transactions.*, vol. 100, p. 1073, 1994.
- [160] H. K. Joseph and L. W. Jeffrey, "Measurement of Bidirectional Optical Properties of Complex Shading Devices," *ASHRAE Transactions*, vol. 101, Part 1, 1995.
- [161] J. L. Wright, "Calculating Center-Glass Performance Indices of Windows," *ASHRAE transactions.*, vol. 104, p. 1230, 1998.
- [162] U. S. D. o. E. O. o. S. Lawrence Berkeley National Laboratory and I. Technical. (2000). *Solar Heat Gain Through Fenestration Systems Containing Shading Procedures for Estimating Performance from Minimal Data*. Available: <http://www.osti.gov/servlets/purl/834476-hO4bfp/native/>
- [163] D. K. Edwards, "Solar absorption by each element in an absorber-coverglass array," *Solar Energy*, vol. 19, pp. 401-402, 1977.
- [164] D. S. Yahoda, J. L. Wright, and Ashrae, *Methods for calculating the effective solar-optical properties of a venetian blind layer* vol. 111. Atlanta: Amer Soc Heating, Refrigerating and Air-Conditioning Eng, 2005.
- [165] T. Talmatamar, M. Alhabobi, Y. Sfaxi, and C. Awanto, "Analysis of solar radiation for sunlit glass shaded by vertical adjustable flat slats," *Renewable Energy*, vol. 6, pp. 663-671, 10// 1995.
- [166] *ISO 15099, Thermal performance of windows, doors and shading devices - Detailed calculations*. Geneva: ISO, 2003.

- 
- [167] J. L. J. Rosenfeld, W. J. Platzer, H. van Dijk, and A. Maccari, "Modelling the optical and thermal properties of complex glazing: overview of recent developments," *Solar Energy*, vol. 69, Supplement 6, pp. 1-13, 7// 2001.
- [168] S. Rheault and E. Bilgen, "Heat Transfer Analysis in an Automated Venetian Blind Window System," *Journal of Solar Energy Engineering*, vol. 111, pp. 89-95, 1989.
- [169] D. S. W. J. L. Yahoda, "Thermal and Solar Heat Gain Characteristics of Venetian Blinds - Methods for Calculating the Effective Longwave Radiative Properties of a Venetian Blind Layer," *ASHRAE transactions.*, vol. 110, p. 463, 2004.
- [170] H. Simmler, U. Fischer, and F. Winkelmann, "Solar-thermal window blind model for DOE-2," *Simulation Research Group internal report, Lawrence Berkeley National Laboratory, Berkeley, CA*, 1996.
- [171] EnergyPlus, *EnergyPlus engineering document: the reference to EnergyPlus calculations*. USA: U.S. Dep. Energy, 2005.
- [172] M. G. Gomes, A. M. Rodrigues, and J. A. Bogas, "Numerical and experimental study of the optical properties of venetian blinds," *Journal of Building Physics*, vol. 36, pp. 7-34, // 2012.
- [173] O. Merker, F. Hepp, A. Beck, and J. Fricke, "A new solar shading system with phase change material (PCM)," in *Proceedings of the World Renewable Energy Congress WII*, Cologne, Germany, 2002.
- [174] L. Zalewski, A. Joulin, S. Lassue, Y. Dutil, and D. Rouse, "Experimental study of small-scale solar wall integrating phase change material," *Solar Energy*, vol. 86, pp. 208-219, 2012.
- [175] L. Zalewski, M. Chantant, S. Lassue, and B. Duthoit, "Experimental thermal study of a solar wall of composite type," *Energy and Buildings*, vol. 25, pp. 7-18, 1997.
- [176] G. f. i. M. u. T. GESIMAT GmbH. Available: <http://www.gesimat.de>
- [177] G. G. Systems. (2015). *GlassX*. Available: <http://glassx.ch/>  
<http://www.glassxpcm.com>  
<http://www.greenliteglass.com/products/energy-saving-glass/glass-x-crystal.html>
- [178] N. Soares, J. J. Costa, A. Samagaio, and R. Vicente, "Numerical evaluation of a phase change material-shutter using solar energy for winter nighttime indoor heating," *Journal of Building Physics*, July 31, 2013 2013.
- [179] P. Brousseau and M. Lacroix, "Numerical simulation of a multi-layer latent heat thermal energy storage system," *International Journal of Energy Research*, vol. 22, pp. 1-15, 1998.
- [180] C. R. Chen, A. Sharma, S. K. Tyagi, and D. Buddhi, "Numerical heat transfer studies of PCMs used in a box-type solar cooker," *Renewable Energy*, vol. 33, pp. 1121-1129, May 2008.

- [181] C. R. Chen and A. Sharma, "Numerical Investigation of Melt Fraction of PCMs in a Latent Heat Storage System," *Engineering and Applied Sciences*, vol. 4, pp. 437-444, 2006.
- [182] M. Costa, D. Buddhi, and A. Oliva, "Numerical simulation of a latent heat thermal energy storage system with enhanced heat conduction," *Energy Conversion and Management*, vol. 39, pp. 319-330, 1998.
- [183] Y. Dutil, D. R. Rousse, N. B. Salah, S. Lassue, and L. Zalewski, "A review on phase-change materials: Mathematical modeling and simulations," *Renewable and Sustainable Energy Reviews*, vol. 15, pp. 112-130, 2011.
- [184] S. V. Patankar, *Numerical heat transfer and fluid flow*. Washington; New York: Hemisphere Pub. Corp. ; McGraw-Hill, 1980.
- [185] P. Verma, Varun, and S. K. Singal, "Review of mathematical modeling on latent heat thermal energy storage systems using phase-change material," *Renewable and Sustainable Energy Reviews*, vol. 12, pp. 999-1031, 5// 2008.
- [186] A. I. o. Aeronautics and Astronautics, *AIAA Guide for the Verification and Validation of Computational Fluid Dynamics Simulations*: American Institute of Aeronautics and Astronautics, 1998.
- [187] P. d. Santos and L. Matias, "Coeficientes de transmissão térmica de elementos da envolvente dos edificios," in *ITE 50*, 21 ed. Lisboa, Portugal: LNEC - Laboratório Nacional de Engenharia Civil, 2006.
- [188] T. Silva and R. Vicente, "Sistema de Proteção Solar," Portugal Patent PT 107310 A, 2015.
- [189] T. Silva, R. Vicente, F. Rodrigues, A. Samagaio, and C. Cardoso, "Development of a window shutter with phase change materials: Full scale outdoor experimental approach," *Energy and Buildings*, vol. 88, pp. 110-121, 2/1/ 2015.
- [190] I. ANSYS, "ANSYS Fluent 14.5: Theory Guide," vol. Release 14.5, ed. Canonsburg, US, 2012.
- [191] R. American Society of Heating and E. Air-Conditioning, *Ashrae guideline : measurement of energy and demand savings*. Atlanta, GA: ASHRAE, 2002.
- [192] D. Coakley, P. Raftery, and M. Keane, "A review of methods to match building energy simulation models to measured data," *Renewable and Sustainable Energy Reviews*, vol. 37, pp. 123-141, 2014.
- [193] R. Ruiz Flores and V. Lemort, "Calibration of Building Simulation Models: Assessment of Current Acceptance Criteria," in *8th International Conference Improving Energy Efficiency in Commercial Buildings (IEECB'14)*, Frankfurt, Germany, 2014.
- [194] M. Royapoor and T. Roskilly, "Building model calibration using energy and environmental data," *Energy and Buildings*, vol. 94, pp. 109-120, 5/1/ 2015.



- 
- [195] P. Raftery, M. Keane, and A. Costa, "Calibrating whole building energy models: Detailed case study using hourly measured data," *Energy and Buildings*, vol. 43, pp. 3666-3679, 2011.
- [196] J. Cipriano, G. Mor, D. Chemisana, D. Pérez, G. Gamboa, and X. Cipriano, "Evaluation of a multi-stage guided search approach for the calibration of building energy simulation models," *Energy and Buildings*, vol. 87, pp. 370-385, 1/1/ 2015.
- [197] M. International Performance, C. Verification Protocol, S. United, E. Department of, E. Office of Energy, E. Renewable, *et al.*, *International performance measurement & verification protocol. Volume I, Volume I*. [Washington, D.C.?]: Office of Energy Efficiency and Renewable Energy, U.S. Dept. of Energy, 2001.
- [198] S. United, E. Dept. of, E. Office of Energy, E. Renewable, S. United, E. Dept. of, *et al.* (2008). *Measurement and Verification (M&V) Guidelines for Federal Energy Projects, V3.0*. Available: <http://www.osti.gov/servlets/purl/1218089/>
- [199] T. A. Reddy, "Literature Review on Calibration of Building Energy Simulation Programs: Uses, Problems, Procedures, Uncertainty, and Tools (RP-1051)," *Transactions - American Society of Heating Refrigerating and Air Conditioning Engineers*, vol. 112, pp. 226-240, 2006.